SLAC – 321
UC – 34D
(E)

A SEARCH FOR SUPERSYMMETRIC ELECTRONS WITH THE MARK II DETECTOR AT PEP*

Bruce William LeClaire

Stanford Linear Accelerator Center
Stanford University
Stanford, California 94305

October 1987

Prepared for the Department of Energy
under contract number DE-AC03-76SF00515

Printed in the United States of America. Available from the National Technical Information Service, U.S. Department of Commerce, 5285 Port Royal Road, Springfield, Virginia 22161. Price: Printed Copy A09, Microfiche A01.

* Ph.D. Dissertation

Abstract

An experimental search for selectrons, the supersymmetric partner of the electron, has been performed at the PEP storage ring at SLAC using the Mark II detector. Supersymmetry is a theory based upon a symmetry between fermions and bosons, such that all ordinary fermions(bosons) have supersymmetric bosonic(fermionic) partners. This theory is very important in current theoretical attempts to construct a complete unified quantum field theory which incorporates all four forces: strong, electromagnetic, weak, and gravitational. However, all experimental searches for supersymmetric signals, including this one, have so far yielded negative results.

The experimental search done was based upon the following hypothetical reaction in e^+e^- interactions at PEP center of mass energies of 29 GeV:

$$e\,e \longrightarrow e\,\tilde{e}\,\tilde{\gamma} \hookrightarrow e\,\tilde{\gamma}\,.$$

In this reaction the selectrons, $\tilde{e}$, are assumed produced by the interaction of one of initial state electrons with a photon radiated from the other initial state electron. This latter electron is assumed to continue down the beam pipe undetected. The photon and electron then produce a selectron and a photino, $\tilde{\gamma}$, in the supersymmetric analog of Compton scattering. The photino is assumed to be the lightest supersymmetric particle, and as such, does not interact in the detector, thereby escaping detection very much like a neutrino. The selectron is assumed to immediately decay into an electron and a photino. This electron is produced with large $p_\perp$ with respect to the beam pipe, since it must balance the transverse momentum carried off by the photinos. Thus, the experimental signature of the process is a single electron in the detector with a large unbalanced transverse momentum.

No events of this type were observed in the original search of 123 pb^{-1}

of data, resulting in a cross section limit of less than 2.4×10^{-2} pb (at the 95% CL) within the detector acceptance. This cross section upper limit applies to any process which produces anomalous single electron events with missing transverse momentum. When interpreted as a supersymmetry search it results in a lower selectron mass limit of 22.2 GeV/c^2 for the case of massless photinos. Limits for non-zero mass photinos have also been calculated.

Acknowledgments

My experience at SLAC, and especially with the Mark II collaboration, has taught me much. I am indebted to the generous support that both have given me over the years. I have enjoyed working at SLAC, and feel fortunate to have participated in the PEP experimental program.

I had two advisors during my tenure as graduate student, and to each I owe many thanks. I wish to thank Bob Hollebeek for his advice and encouragement during the initial stages of my thesis work. The final attainment of my degree owes much to Jonathan Dorfan, whose encouragement was both timely and valuable.

The Mark II detector was largely complete when I first arrived. Its construction and maintainance was done by a large number of people, many of whom had come and gone before my arrival. To all of them I'd like to say "damn good job". The wealth of physics results produced at PEP attests to this. It was an honor to work with this group.

I would like to thank Dean Karlen, Spencer Klein, and Keith Riles for their help in proof-reading this thesis, and for many discussions on analysis. I have enjoyed working with each one of them, and wish them well.

It is my parents to whom I owe the largest debt. Their unfailing support throughout the years can never be repaid. They gave me encouragement for everything I did over the years– well, almost everything. They too did a "damn good job".

My introduction to high energy physics was largely due to Bernie Gittelman. He was my benefactor at Cornell, hiring me to work at the Wilson Synchrotron Laboratory. Without a doubt, his ability and willingness to argue things out with me, until I got it straight, has yet to be equaled. I will forever be grateful for the opportunities he provided me. I also wish to acknowledge another of my teachers, Al Silverman. His initial encouragement of my lab work reaffirmed a desire I've had since I was eight years old– to be an experimental physicist. He comes in

second only to Bernie in his ability to tolerate my infinite number of questions (asked during my first college level quantum mechanics class). Lastly, I would like to thank one more Cornell professor, N. David Mermin. He is an outstanding teacher, as I learned in his course on quantum mechanics. Prof. Mermin saw the world in a beautiful fashion; his physics showed it, as did his office (which had a harpsichord in it).

The person most responsible in laying the foundation of my education at SLAC was my former office mate, Larry Gladney. He taught me the ropes at Mark II, and was always willing to help solve any problem I brought to him. His help in the selectron analysis was indispensable. I miss the many office discussions we had, and can only say that I hope we work together again someday in the future. No doubt we will, for as Larry said, "It doesn't matter where you do your post-doc, so long as you end up at the SSC".

I would like to finish with an old physics joke. It goes something like this: A rather rich race horse owner hired a trainer, a chemist, and a physicist to develop the fastest horse. After a period of time they all gathered to present their work (somewhat akin to the yearly Moriond Conference). The trainer went first:

"This new exercise program we've developed should trim his time down ...."

The chemist then presented his results:

"I've developed a new nutrient additive that will increase the horse's muscle volume by ...."

At last the physicist got up to present his finding:

"Well, we've got the problem solved for a spherical horse."

I wish I could say as much.

Table of Contents

List of Tables

List of Figures

Notation

Natural units are used throughout, with $\hbar = c = 1$. The common unit for mass, energy, and momentum is therefore eV, and typically given in GeV. The context will make clear which quantity is being referred to.

Four vector notation will often be denoted by greek indices, such that (s.t.):

$$x^\mu = \begin{pmatrix} x^0 \\ x^1 \\ x^2 \\ x^3 \end{pmatrix} \equiv (x^0, x^i), \quad i = 1, 2, 3$$

where,

$$x^0 \equiv t, \qquad (x^i) \equiv \vec{\mathbf{x}}.$$

We use following time-like metric for flat spacetime:

$$g^{\mu\nu} = g_{\mu\nu} = \mathrm{diag}(1, -1, -1, -1)$$

s.t.,

$$x_\mu = g_{\mu\nu} x^\nu \equiv (x_0, x_i)$$

where,

$$x_0 = x^0 = t \quad \text{and} \quad (x_i) = -(x^i) = -\vec{\mathbf{x}}.$$

The scalar product is then given by:

$$x \cdot x = x^\mu x_\mu = g_{\mu\nu} x^\mu x^\nu = t^2 - |\vec{\mathbf{x}}|^2.$$

We denote the 4-gradient as follows:

$$\partial_\mu \equiv \frac{\partial}{\partial x^\mu} = (\partial_t, \nabla)$$

$$\partial^\mu \equiv \frac{\partial}{\partial x_\mu} = (\partial_t, -\nabla).$$

The Dirac equation is given by:

$$(i\partial\!\!\!/ - m)\psi = (i\gamma^\mu \partial_\mu - m)\psi = 0$$

where,

$$\{\gamma^\mu, \gamma^\nu\} = 2g^{\mu\nu}.$$

The left- and right-handed chiral spinors are given by the following projection operators:

$$\psi^{\mathrm{L}} \equiv \mathrm{P_L}\psi = \left(\frac{1-\gamma_5}{2}\right)\psi$$

$$\psi^{\mathrm{R}} \equiv \mathrm{P_R}\psi = \left(\frac{1+\gamma_5}{2}\right)\psi$$

where,

$$\gamma_5 = \gamma_5^\dagger \equiv i\gamma^0\gamma^1\gamma^2\gamma^3.$$

Finally, the Dirac adjoint spinor is given by:

$$\bar{\psi} \equiv \psi^\dagger \gamma_0.$$

Chapter 1. Theoretical Motivation

1.1 Introduction

The current theoretical picture of physics, which is often referred to as the standard model[1], is tremendously successful in its description of the world. The standard model does not, however, represent a complete unified theory of all the interactions in nature, and its shortcomings are well recognized[2]. Supersymmetry[3] is a recent theoretical idea which represents a potentially significant addition to our current understanding of the world. It offers many promising avenues in the attempt to construct a unified field theory of physics, and alleviates many of the shortcomings of the standard model.

Supersymmetry has yet to be experimentally confirmed[4]. Prompted by this fact, an experimental search for supersymmetric electrons, produced in e^+e^- collisions at center of mass energies of 29 GeV, was performed with the Mark II detector. The results of this search are discussed in subsequent chapters. This chapter contains a discussion of the theoretical motivation for supersymmetry, beginning with a description of the standard model, and ending with the phenomenology of the experimental signal used in the search presented here.

1.2 The Standard Model

Physics is an attempt to understand the most basic principles of nature, its innermost workings. Physicists are very lucky people, for nature appears to be guided by only a few such principles, written in the universal language of mathematics. Physics has a long history, dating back at least as far as the musings of Democritus in ancient Greece. But modern physics was not born until the sixteenth and seventeenth century, with the insights of Galileo and Newton. The eighteenth century saw the maturation of classical mechanics, and

the advent of the theory of classical electromagnetism. This was also a period of intense mathematical development, under the guidance of Gauss, Euler, Lagrange, Hamilton, Laplace, and Fourier, among others.

The early twentieth century gave birth to two major new conceptual frameworks: quantum mechanics, and relativity theory. They were brought together in 1928 by Dirac[5], and together with Maxwell's theory of electromagnetism, represent a body of knowledge sufficient to understand the interactions of atoms and molecules. In a sense, that is all the physics one needs to make up the world we know, since the electromagnetic interactions of atoms and molecules form the basis for all of chemistry, and ultimately biology. But for reasons still unknown, the world has structure going beyond atoms and molecules, and interactions which are not needed to hold atoms or molecules together†. It is this additional structure which physicists are compelled to explore.

During the 1940's theorists such as Schwinger, Feynman, and Tomonaga[6] created a complete quantum field theory of electrodynamics, referred to as QED. The central mathematical idea was that of a Lagrangian, which together with Hamilton's least action principle, gives rise to the field equations of motion. This formalism represented a simplicity and symmetry which was often overlooked during the next 30 years. By the 1940's the existence of the four forces of nature, gravitation, electromagnetic, weak, and strong was known. These four forces are still considered fundamental today, although we now recognize an intimate connection between the weak and electromagnetic forces. The 1940's also saw the set of known particles grow from the simple set of five known in the 1930's, *i.e.* protons, neutrons, electrons, photons, and neutrinos. We are all quite familiar with the first three as the constituents of the atom. The photon was known to be associated with the electromagnetic force. Pauli first postulated the existence

---

† Although these additional interactions may be necessary for the ultimate synthesis of atoms and molecules from the big bang.

of neutrinos, which are intimately connected with the radioactive decays due to the weak force. The discovery of two new particles, now known as the muon and the pion, lead to great excitement. The pion was known to be necessary to account for the strong force, as predicted by Yukawa. It is the strong force which is responsible for holding the protons and neutrons together in the nucleus of the atom. The muon, however, did not seem necessary, for they were not required by any theory, prompting one physicist to exclaim, "Who ordered *that*?!"[7]. This question is equally valid today.

The 1950's and 1960's saw an explosion of new particle discoveries, using cosmic ray experiments at first, and later, earth based accelerators such as cyclotrons, betatrons, and synchrotrons. Many new experimental techniques were developed and a wealth of data was collected. Theory suffered from an embarrassment of wealth, for a deep understanding of much of this data was still several decades away. Many avenues of investigation were explored during this period, and the state of confusion spawned many ingenuous theoretical ideas. However, not all lines of research were viable, nor were the viable avenues always recognized as such. None the less, great progress was made in several important areas. For instance, new quantum numbers like strangeness, which we now recognize as being carried by a new flavor of quark, were discovered during this period.

The 1950's also saw the concept of symmetry assume a central role in quantum physics. Symmetry provides a unifying view of the world, allowing many statements to be made without having to solve the equations of motion in full detail. Furthermore, symmetries guide the physicist in making the first guesses as to how the world works. It is interesting to note that the connection between symmetries and conserved quantities in mechanics was first discovered by Jacobi in 1842[8]. But it is only with the advent of quantum mechanics that symmetry assumes its true importance. The role of symmetry in quantum

Discovery	Primary Investigator	Year
X-rays	W. Röntgen	1895
Radioactivity	H. Becquerel	1896
Electron	J. J. Thomson	1896
Nucleus	E. Rutherford	1911
Positron	C. Anderson	1932
Neutron	J. Chadwick	1932
Muon	C. Anderson, S. Neddermeyer	1936
Pion	C. Powell	1947
Strange particles	G. Rochester, C. Butler	1947
Anti-proton	E. Segrè, O. Chamberlain	1955
Nucleon substructure	R. Hofstader	1961
Charm	B. Richter, S. Ting	1974
Tau	M. Perl	1975
Bottom	L. Lederman	1977
$W^{\pm}$, Z^0	C. Rubbia, S. van der Meer	1983

Table 1.1. Selected Chronology of Major Particle Discoveries. This table is by no means exhaustive, but it does include some of the major experimental discoveries in particle physics.

mechanics was fully formalized in the 1959 work of Wigner[9]. In the early 1960's Gell-Mann and Ne'eman purposed the eightfold-way[10], a symmetry scheme for the classification of baryons and mesons. The eightfold-way served as a basis for the quark model, which was independently proposed by Zweig and Gell-Mann in the mid-1960's[11–13]. Ironically, the 1950's also saw the downfall of an important symmetry, *i.e.* parity. The possibility of parity violation in weak interactions was first suggested in 1956 by Lee and Yang[14], and found soon afterwards in nuclear experiments[15]. In 1957, Marshak and Sudarshan[16], and

Feynman and Gell-Mann[17], introduced the V-A theory of the weak interaction, which incorporated parity violation. Another symmetry to fall was that of CP, which was experimentally found to be violated in 1964[18]. After the downfall of CP symmetry there were few guiding principles during this period, which some refer to as "the dark age of field theory"[19].

Ironically, the seeds of our current theoretical understanding of the world were planted at this time, in a seminal paper published in 1954 by Yang and Mills[20]. This paper was an attempt to understand the strong interactions via a SU(2) gauge theory. As such it was doomed to failure, because, as we now know, the strong interactions are governed by an SU(3) symmetry. However, this paper revitalized the idea of gauge symmetry, a symmetry which is possessed by the electromagnetic force, but whose importance to other interactions had previously been neglected. Because of the failure of Yang-Mills theory to understand the strong interaction the paper went neglected for many years. It also suffered from another apparent shortcoming; a gauge symmetric Lagrangian cannot contain any mass terms. This appeared to contradict a simple observational fact, *i.e.* particles have mass. Furthermore, barring confinement, all forces have infinite range if their force carriers are massless. Since the weak force was known to be short ranged, its force carriers must also be massive. Thus, the idea of gauge symmetry lay dormant for many years.

Gauge symmetry was rediscovered in the 1960's, and by the late 1970's became a central underpinning to our understanding of the world. The great success of this idea is represented in the Nobel prize winning work of Glashow, Weinberg, and Salam[21–23]. Their work incorporated the weak force into a gauge theory, by the synthesis of the electromagnetic and weak forces into the electroweak force. The discovery of neutral currents in neutrino detectors provided the initial experimental confirmation of this theory, followed later by sensitive parity violating experiments at SLAC, and culminated by the actual production

and detection of the W and Z° gauge bosons at CERN's Sp$\bar{p}$S facility[24–29]. The problem of generating massive bosons will be discussed below.

The standard model of the world was completed during the 1970's and 1980's. Gauge symmetry now assumed its role as the guiding principle for the form of particle interactions. The strong, weak, and electromagnetic forces are embedded in a $SU(3)_C \times SU(2)_L \times U(1)_Y$ gauge group. The color force is due to an $SU(3)_C$ color gauge group, with a strong coupling constant, α_s. The electromagnetic and the weak forces are embedded in a direct product of a $SU(2)_L$ weak isospin gauge group with a $U(1)_Y$ hypercharge gauge group. The electroweak force is governed by one coupling constant, α_{EM}. The gauge groups dictate the boson particle spectrum, with four spin 1 gauge bosons: γ, Z°, W^+, and W^-. These bosons are responsible for mediating the interactions between fermions. The non-Abelian nature of the $SU(3)_C$ and $SU(2)_L$ gauge groups imply that these bosons can have self-interactions, unlike the photon. This is because the non-Abelian gauge bosons carry the same charge that they couple to, unlike Abelian gauge bosons such as the photon.

The strong force is carried by 8 gluons, which couple to color fields. Quarks are fermion fields which carry color, and are found inside hadrons. Quarks are extraordinary in that they carry fractional charge, in units of 1/3 e. Hadrons are physical particles which interact strongly, but have no net color charge. They are known to come in two varieties, mesons, which have one quark and one anti-quark, and baryons, which have three quarks of different color. Thus, hadrons come in integer multiples of e. The gluons are massless, and the force is infinite ranged in a broken colored vacuum state. However, due to confinement, a broken colored vacuum can only exist stably inside hadrons. Confinement is a feature of the strong coupling force, and states that color fields can only exist in small regions of space, *e.g.* inside hadrons. Quarks and gluons move about relatively freely inside hadrons, with a force that becomes weaker the closer together they are. This feature of the

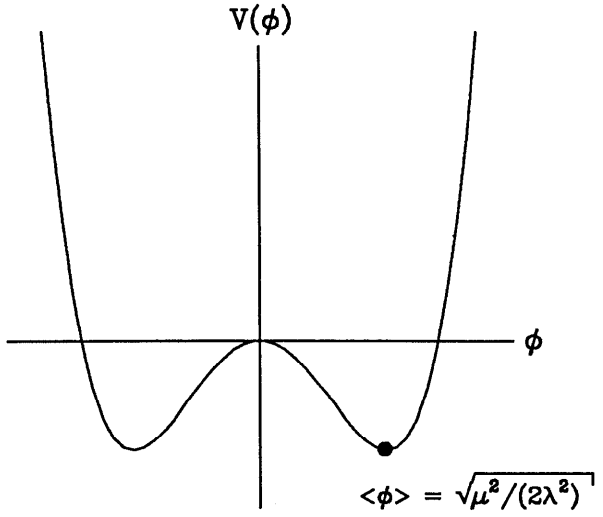

Figure 1.1. Higgs Potential. The Higgs potential, $V(\phi) = \lambda^2|\phi|^4 - \mu^2|\phi|^2$, is shown here for non-zero μ, λ. The potential has a minimum at non-zero field values, $|\langle\phi\rangle| = \sqrt{\mu^2/(2\lambda^2)}$. The Higgs potential always exhibits a degeneracy, as the double well above shows. We have picked one possible solution for definiteness.

theory is referred to as asymptotic freedom. However, the force grows without bound as the quarks and gluons are separated. The $SU(3)_C$ theory of the strong force therefore predicts that free quarks and gluons cannot be observed in the world, a prediction which must of course be experimentally verified. The strong force which acts between hadrons is seen to be a remnant of the strong force which is mediated by gluons. Because of confinement, colored gluons cannot be exchanged over long distances between hadrons. Instead, colorless objects such as pions must be exchanged, and since these mesons are massive this remnant strong force is short ranged. Thus, the gauge symmetry of the strong force is hidden at low energies.

The rediscovery of gauge symmetry was brought about by attempts to understand not the strong force, but the weak force. The electromagnetic and weak forces are unified in the standard model, governed by one coupling constant, α_{EM} , and one mixing angle, θ_W. A recently introduced theoretical idea, that of broken gauge symmetry, allows the weak bosons to acquire mass within the gauge

	Leptons		Quarks		
Fermions	$(e)_R$	$\begin{pmatrix}\nu_e\\ e\end{pmatrix}_L$	$(u_i)_R$	$(d'_i)_R$	$\begin{pmatrix}u_i\\ d'_i\end{pmatrix}_L$
	$(\mu)_R$	$\begin{pmatrix}\nu_\mu\\ \mu\end{pmatrix}_L$	$(c_i)_R$	$(s'_i)_R$	$\begin{pmatrix}c_i\\ s'_i\end{pmatrix}_L$
	$(\tau)_R$	$\begin{pmatrix}\nu_\tau\\ \tau\end{pmatrix}_L$	$(t_i)_R$	$(b'_i)_R$	$\begin{pmatrix}t_i\\ b'_i\end{pmatrix}_L$

	EM	Weak	Strong
Gauge Bosons	γ	Z° $W^\pm$	g_{ij}

Higgs Scalar H°

Table 1.2. Standard Model Particle Spectrum. All the particles which make up the standard model are shown above. With the exceptions of the Higgs and the top quark all have been experimentally observed. The fermions are grouped according to their weak interactions. Each row of leptons and quarks represents a generation. The subscripts, i and j, represent color indices for strongly interacting particles. The primes ($'$) on the d,s, and b quarks serve as a reminder that the weak interaction eigenstates are not the mass eigenstates. The fermion anti-particles have not been listed here.

structure of the electroweak force. The gauge symmetry breaking is accomplished by the Higgs mechanism[30]. In its simplest form, the Higgs is an particle which has a potential with quartic and quadratic terms,

$$V(\phi) = \lambda^2|\phi|^4 - \mu^2|\phi|^2,$$

so that its energy has a minimum for nonzero fields. Therefore, the Higgs field acquires a nonzero vacuum expectation value, about which the quantization of its modes is done. It is the vacuum which doesn't respect the gauge symmetry, as shown in Fig. 1.1. Using the Higgs mechanism, it is possible to begin with a manifestly $SU(2)_L \times U(1)_Y$ gauge invariant Lagrangian, and break the gauge symmetry so that the resulting effective Lagrangian contains 2 massive charged bosons, 1 massive neutral boson, and 1 massless neutral boson. In the Weinberg-Salam model, the charged bosons arise from the raising and lowering operators of $SU(2)_L$ coupling to the vacuum expectation value of a Higgs doublet, while the massive neutral boson results from the Higgs coupling to a mixture of the 3^{rd} component of weak isospin and hypercharge operators. This mixing is governed by the Weinberg angle. The orthogonal mixture obeys a $U(1)_{EM}$ symmetry which the broken vacuum does obey, so that this boson is massless. The $U(1)_{EM}$ coupling is to the electric charge operator, which is given by the following linear combination:

$$Q = \frac{1}{2}(\sigma_3 + Y).$$

The massless boson which couples to the above charge is the photon. The 3 massive bosons are the weak bosons, *i.e.* the W^+, W^-, and Z°. The W bosons couple to weak isospin charge, which is only carried by left-handed fermions. The Z° couples to a combination of weak isospin charge and hypercharge. Since the vacuum expectation value of the Higgs generates mass for all the weak bosons, the weak force is short ranged. In contrast the photon, being massless, has infinite range.

The weak force requires that fermions come in left-handed doublets, so that the left-handed electron and its neutrino belong to an isospin doublet. Since the right-handed electron is in an isospin singlet it carries different quantum numbers than the left-handed electron. Therefore, the left- and right-handed electrons have different couplings to the Z° , giving rise to interesting parity violating effects.

Similar statements apply to the muon and tau particles. The existence of right handed neutrinos, although not excluded by any feature of the theory, is still an open question. Quarks also come in left-handed doublets and right-handed singlets. Experimentally, it has been observed that a quark doublet exists for every lepton doublet. The doublets are grouped together into what are referred to as generations. There are three known generations, each having the identical couplings, while differing only in masses, see Table 1.2. Note however, that the top quark has yet to be experimentally observed. Thus we have a total of 73 fundamental fields when we count all the degrees of freedom (including handedness and color). Notice that even if the world only consisted of one generation there would still be 43 fundamental fields required.

The standard model is completed by the addition of two more features: the Higgs coupling to fermions, and the KM, or Koboyashi-Maskawa, matrix[31]. The non-zero vacuum expectation value for the Higgs field can also give rise to fermion masses via gauge invariant Yukawa couplings between the Higgs and fermions. The different masses are the result of different Yukawa couplings, which are free parameters in the standard model. The KM matrix is an extension of the Cabbibo angle to 3 generations of quarks. It is a 3×3 unitary matrix which takes mass eigenstates (such as the down, strange or bottom quarks) into weak eigenstates of the weak interactions. It can be conveniently parameterized by three real angles, $\theta_i (i = 1, 3)$, plus one complex phase angle, δ. The KM matrix, denoted by V, can then be written as follows:

$$V = \begin{pmatrix} c_1 & s_1 c_3 & s_1 s_3 \\ -s_1 c_2 & c_1 c_2 c_3 + s_2 s_3 e^{i\delta} & c_1 c_2 s_3 - s_2 c_2 e^{i\delta} \\ -s_1 s_2 & c_1 s_2 c_3 + c_2 s_3 e^{i\delta} & c_1 s_2 s_3 + c_2 c_3 e^{i\delta} \end{pmatrix}$$

where $c_i,\ s_i = \cos\theta_i,\ \sin\theta_i$.

This matrix is very important phenomenologically; for instance, it determines

interesting quantities such as the B meson lifetime. Furthermore, a non-zero phase angle, δ, gives rise to CP violation in the standard model†. The four angles are all free parameters within the context of the standard model.

In this form the standard model has been tremendously successful. QED is the most accurate physical theory known; the weak bosons have now been discovered as predicted, and the quark model has been able to classify the vast number of meson and baryon states into a concise spectroscopy. The observation of two and three jet structure in hadronic events at both e^+e^- and $p\bar{p}$ colliders provides experimental evidence of the validity of QCD. Admittedly, QCD has made few predictions which can be experimentally verified, but this is due only to the mathematical complexity of the theory, and not with any fundamental problem. A similar statement applies to turbulence, although no one doubts that the Navier-Stokes equation describes it.

Despite such accomplishments, the standard model is regarded as a stepping stone to a more complete theory of the world. As mentioned above, it contains a large number of fields, many of which seem to be unrelated to each other. It also involves many free parameters, 1 Weinberg angle, 4 KM angles, 10 Yukawa couplings, 1 electroweak coupling, and 1 strong coupling. The standard model has no answers to questions such as the number of generations, or if there are right-handed neutrinos. The standard model also fails to unify the four forces, instead, it has three: strong, electroweak, and gravity. The gravitational force is also not yet treated as a quantum force, it still only obeys the classical geometric equations of Einstein. The standard model is therefore widely viewed as a low energy effective Lagrangian of a more complete theory that is yet unknown.

---

† Note that δ does not appear in the mixing matrix until there are at least three generations of quarks. Therefore, this mechanism of CP violation cannot occur for models with only one or two generations. Another mechanism has been proposed where CP violation occurs because of a relative phase between several Higgs doublets. Recall, however, that the minimal standard model requires only one Higgs doublet.

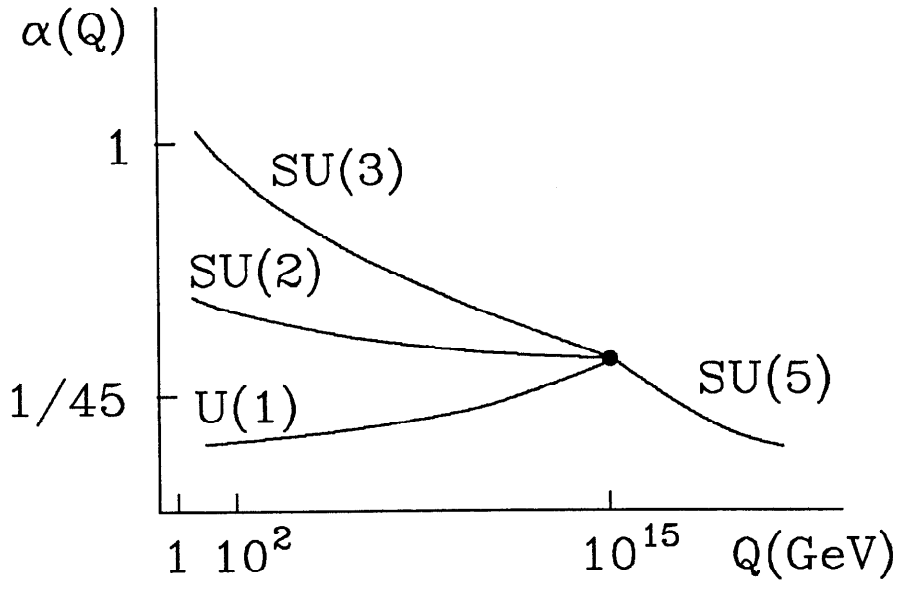

Figure 1.2. Running Coupling Constants in Grand Unified Theories. This figure shows the evolution of the 3 coupling constants in the SU(5) GUT model. The SU(5) symmetry is restored at a scale of 10^{15} GeV. Below that scale the world appears to be governed by three different groups. Actual extrapolations from low energy data do indeed suggest a convergence of the coupling constants at high energies, although not necessarily at a single point, see Ref. 32.

1.3 Towards a Grand Unified Theory - GUT Physics

The success of the Weinberg-Salam model has lead theorists into attempts to unify the electroweak and strong forces as well. Such attempts at a grand unified theory, or GUT, lead to predictions that are both pleasing, such as the value of the Weinberg angle, and startling, such as proton decay[33]. The original idea of grand unified theories was suggested by Pati and Salam[34]. Later, a model based upon SU(5) was proposed by Georgi and Glashow[35]. Essential to all GUT models is the embedding of the group $SU(3)_C \times SU(2)_L \times U(1)_Y$ inside a larger group. The embedding group is broken at some large energy scale, so that its symmetries are hidden at low energies. The critical feature allowing unification is the evolution of the coupling constants due to radiative corrections, a feature of all quantum field theories. These renormalization effects cause the constants to run, *i.e.* to depend upon the energy scale of the interaction. In GUT models,

the running coupling constants evolve until they are equal, this occurs at the unification scale, as shown in Fig. 1.2.

The most developed GUT model is based on SU(5), and it serves to illustrate various generic predictions of grand unified theories. SU(5) assigns the fermions in each generation to two representations, connecting quarks and leptons together in each representation. This synthesis allows for lepto-quark gauge bosons, derived from the SU(5) group, to mediate lepton–quark transitions. These bosons are affected by the broken symmetry and so acquire a mass on the order of the unification scale. Thus, lepton–quark transitions are exceedingly weak at low energy scales. However, these interactions allow baryon and lepton number to be violated. Among some of the predictions of SU(5):

- *Charge quantization.* Because the charge operator is a generator of SU(5), each representation must be electrically neutral. This provides the connection between electron and quark charge (there are three down quarks in the $\mathbf{5}^*$ representation, versus one electron).
- *The Weinberg angle.* This angle is viewed as a Clebsch-Gordan coefficient between the different coupling constants at high energy. SU(5) predicts $\sin\theta_W = 3/8$. Radiative corrections must be taken into account at lower energies in order to compare with the experimental value of $\sin\theta_W = 0.22$.
- *Quark-Lepton Masses.* Here again, the symmetry requires the masses of quarks and leptons to be equal, since they are grouped together in a single representation. Renormalizing to low energies gives the ratio of the b quark to the tau lepton mass in the range 2.7–3, which is what is observed. Since this renormalization depends on the number of flavors the success of the relation can be used to constrain the number to be less than 6. Unfortunately, these mass relations don't work as well for the lighter generations.
- *Proton Decay.* Due to the exchange of lepto-quark gauge bosons between

its valance quarks the proton will decay with $\tau_p \sim 4.5 \times 10^{29\pm1.7}$ years. Unfortunately for SU(5), present experimental results rule out proton decay lifetimes up to about 3.2×10^{32} years. Other GUT models predict longer protons lifetimes, so this is only a problem for minimal SU(5)[36].

- *Magnetic Monopoles.* Grand unified theories also suggest that magnetic monopoles could exist as special topological solutions for the Higgs field, as first worked out by 't Hooft and Polyakov[37].

Despite such successes grand unified theories suffer from several defects, some of which are inherited from the standard model. Whereas these theories explain why generations exist, *i.e.* why quarks and leptons come in matched sets, they still do not explain why more than one generation is needed. The large number of parameters in the standard model are essentially retained, including the important KM mixing angles. And gravity is still not incorporated into the theory (thus, GUT is somewhat of a misnomer) although the GUT scale is only four orders of magnitudes away from the Planck scale ($\sim 10^{19}$ GeV), which is where quantum gravity is expected to become important. But the most important problem for the construction of any GUT model is the incorporation into a single theory of two widely disparate scales, *i.e.* the GUT symmetry breaking scale (10^{15} GeV) and the electroweak symmetry breaking scale (10^3 GeV). This is the gauge hierarchy problem.

The gauge hierarchy problem centers around the decoupling of scalar masses from the fundamental scale of the gauge symmetry breaking. Gauge bosons connected with gauge groups remaining after symmetry breaking can remain light via gauge symmetry. Fermions can remain light because of chiral symmetry, a symmetry which the gauge breaking does not respect and therefore cannot couple to. But scalar bosons have no such principles to prevent them from acquiring large masses from radiative corrections involving loop diagrams or from tree level coupling to the additional Higgs which generate the GUT scale. The Higgs scalar

responsible for breaking the $SU(2)_L \times U(1)_Y$ cannot be allowed to acquire too large a mass, or else the weak bosons would acquire masses on the order of the GUT scale. The parameters of the theory can be adjusted to account for the 12 orders of magnitude difference, but this is regarded as somewhat unnatural.

1.4 Supersymmetry

Supersymmetry is a very vital and new extension to the standard model. It postulates a symmetry between bosons and fermions, such that every ordinary boson has a supersymmetric fermion partner, and every ordinary fermion has a supersymmetric bosonic partner. As with gauge symmetry, boson–fermion symmetries were initially pioneered in early attempts to understand the strong force in the 1960's. Ultimately, these attempts, which were known as the dual model of the pion, were destined to have limited success in understanding the strong force. None the less, the boson–fermion symmetry was appealing enough to encourage researchers, such as P. M. Ramond[38], and also A. Neveu and J. H. Schwarz[39], to continue work along these lines into the early 1970's. Supersymmetry itself was first formulated in 1971 by Y. A. Golfand and E. P. Likhtman of the Lebedev Physical Institute of Moscow[40]. It was independently developed in 1973 by D. V. Volkov and V. P. Akulov of the Physical-Technical Institute in Kharkov[41]. The first Lagrangian displaying both supersymmetric and gauge invariance was published by J. Wess of Karlsruhe University, and B. Zumino of CERN in 1974[42]. This work precipitated a more general interest in supersymmetry. The 1976 work of P. Fayet[43]presented the first model in which a realistic model of electroweak theory, incorporating the Higgs mechanism, was made supersymmetric. It is models such as these which of greatest interest to the experimentalist, and form the basis for the search described below.

All supersymmetric particles have the identical gauge couplings as their partners, and, in an unbroken supersymmetry, the same mass. The gauge

hierarchy problem is entirely alleviated in unbroken supersymmetry due to the perfect cancellation between fermion(boson) and super partner boson(fermion) loop corrections. Since there are no known supersymmetric particles, supersymmetry must be broken. In this case the loop corrections largely cancel, but a residual proportional to the mass difference of the superpartners, Δm, remains. If the Higgs mass is to remain below 1 TeV due to supersymmetry, then the supersymmetric particles must not be much heavier than this scale (they can of course be lighter).

Supersymmetry has other properties which are also quite appealing. Because its operators are based upon a graded Lie algebra, *i.e.* an algebra with non-commuting Grassman numbers, supersymmetry allows a connection between the Poincarè group of space-time transformations, and internal groups. The non-commuting nature of its algebra is absolutely necessary to overcome the "No-Go" theorem of Coleman and Mandula[44], which forbids any connection between Poincarè and internal symmetries for quantum field theories with a finite number of particles and commuting algebras. The simplest supersymmetric theory contains a self-conjugate operator, Q_α, which has spin 1/2. This operator transforms bosons to fermions and fermions to bosons; it is the supersymmetry operator. It has the following algebraic relations with the space-time rotation and translation operators, $M^{\mu\nu}$ and P^μ:

$$
\begin{aligned}
[Q_\alpha, M^{\mu\nu}] &= i(\sigma^{\mu\nu} Q)_\alpha \\
[Q_\alpha, P^\mu] &= 0 \\
\{Q_\alpha, \bar{Q}_\beta\} &= -2(\gamma_\mu)_{\alpha\beta} P^\mu \ .
\end{aligned}
$$

The last relation is potentially the most interesting, it shows that two successive supersymmetric transformations give rise to a translation in space-time. This offers the possibilities of incorporating gravity into the theory, by making supersymmetry a local symmetry, thereby introducing a new gauge field. Since

translations are part of the Poincarè group, and since the classical theory of local Poincarè symmetry is the theory of general relativity, this new gauge field must be the graviton, the quantum of gravity. Such theories are known as supergravity and are generally better behaved mathematically, with regards to divergences, than other attempts at models of quantum gravity. Finally, we mention in passing, that superstrings, a model of particles based upon a new dynamics, *i.e.* that of strings versus point particles, often contain supersymmetry. Superstrings are another promising theoretical concept of the 1980's which grew from preliminary work in the 1950's involving strong interactions[45].

Realistic models of supersymmetry, with a plethora of new phenomena, have been extensively developed in the last few years. Although initial models attempted to treat some of the known particles as supersymmetric partners of other known partners[41], this was later realized to be impossible†. Therefore, since no superpartners are already known, the minimal supersymmetric extension of the standard model leads to a doubling of the number of fundamental fields, see Table 1.3. Note that the Higgs sector has been enlarged to include two Higgs doublets. This is necessary since a single Higgs doublet can only generate masses for down-like quarks, *i.e.* those with charge $-1/3\ e$, without destroying supersymmetry. It should be pointed out that Table 1.3 lists the particle spectrum before supersymmetry is broken. This means that the final mass eigenstates may involve mixing between the original weak eigenstates. Because such mixing involves details of the model used to the generate symmetry breaking, few general statements can be made. Experimental searches, such as the one presented here, must typically make very restricted assumptions about the model they are testing, since the experimental signatures often depend upon the details of the model, such as mixing.

---

† Recall Dirac's initial attempt to interpret the positron solution of his wave equation as the proton.

Conventional Particles	⟵ Supersymmetric Partners ⟶ Weak Eigenstates	Name	Spin
$l = e, \mu, \tau$	$\tilde{l}_L$, $\tilde{l}_R$	sleptons	0
$\nu = \nu_e, \nu_\mu, \nu_\tau$	$\tilde{\nu}$	sneutrinos	0
$q = u, d, s, c, b, t$	$\tilde{q}_L$, $\tilde{q}_R$	squarks	0
g	$\tilde{g}$	gluinos	1/2
γ	$\tilde{\gamma}$	photino	1/2
Z^0	$\tilde{Z}^0$	zino	1/2
$W^\pm$	$\widetilde{W}^\pm$	wino	1/2
$H^0_{1,2}$, $H^+_{1,2}$	$\tilde{H}^0_{1,2}$, $\tilde{H}^+_{1,2}$	higgsino	1/2

Table 1.3. Supersymmetric Particle Spectrum. This table lists the particle content of the minimal supersymmetric extension of the standard model.

Many phenomenological models of supersymmetry introduce a new quantum number, R, which is multiplicatively conserved. All ordinary particles have R = +1, while their superpartners have R = −1. The R-number is given in terms of baryon number, lepton number, and spin as follows:

$$R = (-1)^{3B + 3L + 2S} .$$

R-parity can be broken by non-zero vacuum expectation values for some neutral scalar superpartner, such as the sneutrino, but this would lead to lepton number non-conservation. For instance, the process $\tilde{\nu} \rightarrow \nu + \gamma$ would be allowed if R-parity were violated. Although strong R-parity violation can be ruled out by lepton number conservation at low energies, weak R-parity is allowed. This is mentioned here because, although R-parity can safely be assumed in accelerator experiments, its weak violation can be significant for early cosmology[46].

R-parity conservation has several implications. It implies that superpartners must be created or destroyed in even numbers. Thus, accelerator experiments

must have energies large enough to be able to produce at least two superpartners in a collision process. Then, once a superpartner is created it always decays to another, lighter, superpartner. This process ends with the lightest superpartner particle, which is absolutely stable. If the lightest superpartner were charged, or had strong interactions, its relics from the big bang would have condensed out into galaxies in the form of heavy isotopes. Terrestrial searches have ruled out such heavy isotopes to a level to exclude the expected abundance from big bang produce by at least 5 orders of magnitude. Thus, the lightest superpartner must be neutral, and is often assumed to be the photino (or a mixture of the photino and higgsino).

1.5 Missing Energy- The Experimental Signal of Supersymmetry

Assuming that the photino is the lightest superpartner allows us to make several statements relevant to experimental searches about the photinos interactions with matter. Photinos can interact with bulk matter via t-channel exchange of quarks or squarks, or by the s-channel fusion of the photino and quark into a squark. The explicit form of the cross section is given in Haber and Kane[47]. It is of the order of the cross section for neutrino interactions with bulk matter (mostly due to the fact that neutrinos must exchange heavy gauge bosons to interact, while photinos must exchange or create heavy squarks). Thus, beam dump experiments can look for photino interactions in a fashion similar to searching for neutral current interactions of neutrinos. Collider experiments, on the other hand, can view photinos as non-interacting particles. This means that the most prominent signal of supersymmetry production will be missing energy, resulting from the escaping photinos that are the ultimate decay end products. Recall also that at least two photinos will escape since at least two superpartners were produced.

We now turn to the process which was the basis for the experimental search described here. It was originally suggested in a 1980 paper by G.R. Farrar and

P. Fayet[48] and first calculated in a 1982 paper by M.K. Gaillard, I. Hinchliffe, and L. Hall[49]. The search was based upon the following hypothetical reaction:

$$e\,e \longrightarrow e\,\tilde{e}\,\tilde{\gamma}$$
$$\hookrightarrow e\,\tilde{\gamma}\,.$$

In this reaction the selectron, $\tilde{e}$, is assumed produced by the interaction of one of initial state electrons with a quasi-real photon radiated from the other initial state electron. This latter electron is assumed to continue down the beam pipe undetected. The photon and electron then produce a selectron and a photino, $\tilde{\gamma}$, in the supersymmetric analog of Compton scattering. The photino is assumed to be the lightest supersymmetric particle, and as such, does not interact in the detector, thereby escaping detection very much like neutrinos. The selectron is assumed to immediately decay into an electron and a photino. This electron is produced with large $p_\perp$ with respect to the beam pipe, since it must balance the transverse momentum carried off by the photinos. Thus, the experimental signature of the process is a single electron in the detector with a large unbalanced transverse momentum. This signature has several advantages:

- Because the initial state radiated photon carries energy into the reaction selectrons with mass greater than the beam energy can be produced, unlike pair production searches.
- The experimental signature, *i.e.* a single electron, is very clean, and the detector response to electrons can be studied quite well.
- Finally, the large missing $p_\perp$ allows for very good background rejection, as will be extensively discussed later.

Chapter 2. The PEP Storage Ring

2.1 SLAC

The Stanford Linear Accelerator Center (SLAC) is a national laboratory funded by the U.S. federal government. Although closely affiliated with Stanford University, SLAC maintains its own administration. Its campus is even separate from Stanford's. Never the less, there is close cooperation between the two institutions. In fact, SLAC grew out of the early accelerator work done at Stanford, especially that of Hansen, Ginzton, Varian, and Hofstader[49]. A brief chronology of SLAC is presented in Table 2.1. SLAC is one of the few major high energy physics facilities in the world. As such, it draws physicists from the international community, as well as from across the United States. SLAC also has a strong theory group, whose close interaction with experimentalists provides for a very simulating intellectual environment.

2.2 The Linear Accelerator

The heart of SLAC is its two mile accelerator (which is actually 10,000 feet long). It provides high energy electrons and positrons to the various experimental facilities. During the early days of SLAC most of the beams went to fixed target experiments. Fixed target physics played a less important role at SLAC after the advent of storage rings. The linear accelerator, however, still played a very important role as the injector for these machines. It currently plays an especially central role in the new machine, the Stanford Linear Collider, which is just now (September 1987) coming online. This project will allow the Z° gauge boson to be studied in detail at an e^+e^- machine for the first time. Major modifications of the accelerator have been made to accommodate this new machine. The rest of this section describes the accelerator at the time of the thesis experiment (1980–1984), and so will be in the past tense.

SLAC CHRONOLOGY

April 1957	Proposal for two mile accelerator submitted by Stanford University to federal government.
September 1961	U.S. Congress approves project.
April 1962	Contract signed by U.S. Atomic Energy Commission and Stanford University.
July 1962	Construction begins.
March 1964	Original proposal for SPEAR.
May 21, 1966	First beam transmitted over the entire two miles of accelerator.
July 13, 1966	Positrons accelerated.
November 1966	Physics experiments begin.
August 1970	SPEAR funding from SLAC general funds approved.
April 28, 1972	Colliding beams at SPEAR.
February 1974	PEP proposal agreement reached between SLAC and LBL.
June 1977	PEP construction begins.
September 1980	Colliding beams at PEP.
Late 83, early 84	SLC funding approved (in stages).
October 1983	SLC formal construction begins.
March 1987	Electrons and positrons simultaneously reach SLC interaction point.

Table 2.1. A Selected Chronology of SLAC's History.

The linear accelerator, or linac, was a disk-loaded, traveling wave accelerator. The accelerating structure was made of copper, in 10 foot sections. The linac was comprised of a total of 952 of these sections. Each 10 foot section consisted of 87 cavities, plus two couplers. The RF energy was fed in one end, and taken out to an external load on the other end. The disks were chosen to be 0.230 inches thick,

SLAC LINAC PARAMETERS

Accelerator length	10000 feet
Length between feeds	10 feet
Number of accelerator sections	952
Operating frequency	2856 MHz
Phase shift per cavity	$2\pi/3$
Number of klystrons	238
Average peak power per klystron	25 MW
AC power	$\simeq$ 28 MW
Maximum repetition rate	360
RF pulse length	2.5 μs
Filling time	0.83 μs
Maximum electron intensity	10^9 pps
Maximum positron intensity	10^8 pps
Accelerating gradient without SLED I	8.2 MeV/m
Accelerating gradient with SLED I	11.5 MeV/m
Maximum energy without SLED I	23.8 GeV
Maximum energy with SLED I	33.3 GeV
Electron energy spread	$\pm$0.3%
Positron energy spread	$\pm$0.5%

Table 2.2. SLAC Linac Parameters. These parameters refer to the accelerator as configured for PEP running in 1980. SLED I refers to a technique used to increase delivered power by pulse compression, see Ref. 50.

in a compromise between maximizing shunt impedance while maximizing heat transference and minimizing electrical breakdowns. The cavity and iris diameters varied across the section in order to achieve a constant gradient structure. The radius varied from 3.29 inches at the input end to 3.22 inches at the output end

(a 2% variation). The iris diameter varied from 0.90 inches to 0.63 inches (a 30% variation). The group velocity varied linearly across the section, varying from $0.020\,c$ to $0.007\,c$. The shunt impedance in turn varied from 53 to 60 MΩ/m. The RF power to the accelerator was supplied by 238 klystrons; each klystron supplying four 10 foot sections. The linac used three different klystrons: a 20 and 30 MW, and a latter design of 38 MW. The average power supplied was about 25 MW. Other machine parameters can be found in Table 2.2. A complete account of the accelerator, circa 1967, can be found in Ref. 51.

2.3 The PEP Storage Ring

PEP, which stands for Positron Electron Project, was the second e^+e^- storage ring constructed at SLAC. PEP was originally proposed in 1971 as a e^+e^- machine with a maximum center of mass energy of 30 GeV[52]. An electron–proton option was also envisioned during the early conceptual design of the machine. The final design was for a e^+e^- storage ring with a maximum center of mass energy of 36 GeV[53]. Construction on the machine began in 1977, and was completed in 1979. PEP began operations in fall of 1980. The Mark II detector began taking data in January 1981. PEP operated steadily until February 1986, at which time it was temporary shut down while SLC began its commissioning phase. The data used to perform the search presented here was taken over a more limited range of time, from September 1981 until June 1983. During this time PEP delivered the 123 pb^{-1} of integrated luminosity used in the selectron search. Although PEP could obtain a maximum beam energy of 18 GeV with its 5.5 MW of RF power, it was operated at a constant center of mass energy of 29 GeV throughout in order to maximize luminosity.

PEP has a 2.2 km circumference ring with a twelve-fold symmetric machine lattice. It had a hexagonal layout, with an interaction region at the center of each of the six straight sections of the machine. This design helped to isolate the experiments from the bending magnets, thereby reducing synchrotron radiation

backgrounds in the experimental halls. The Mark II detector was located at region 12 (the regions were numbered 2—12 in a clockwise fashion). PEP had three counter-circulating bunches of positrons and electrons, each carried about 5 ma of current. The beams collided every 2.4 μs. The physical overview of PEP is shown in Fig. 2.1.

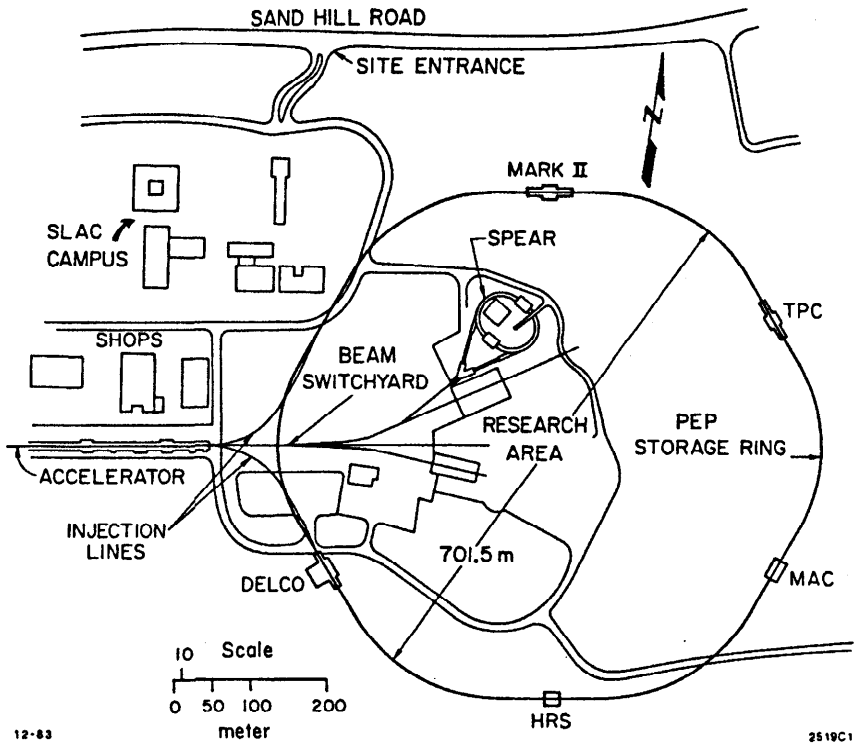

Figure 2.1. Overview of SLAC site.This figure shows the experimental area at SLAC at the time of PEP installation. It has since been enlarged to the east for the new SLC machine.

The RF power was fed in at three places on the ring, in regions 4, 8, and 12. The RF accelerating structures were 8 feet long, with 5 coupled cavities per section. Each RF station contained eight of these sections, which were powered by four 500 kW klystrons. The RF operated at 353 MHz. The average loss of energy per turn in the machine for each particle, due to synchrotron radiation, was 24 MeV.

The beams were supplied by the 2 mile linear accelerator in a synchronized pulsed injection mode. The beam lifetimes were variable, but had an average lifetime of about 4 hours (determined largely by the 10^{-8} torr vacuum). The beams could be replenished in a top-off mode, or they could be dumped and fresh bunches injected. The beams were separated during injection. The betatron oscillation damping time at PEP was 9 ms for beam energies of 14.5 GeV. Occasionally, noisy beams would also be separated in order to allow the operators to resteer the beams, and then recollided.

PEP's luminosity, L, could be parameterized as follows:

$$\mathrm{L} = \frac{\mathrm{I}^2}{4\pi \mathrm{N}_b f \epsilon_x \beta_y^*} \ ,$$

where,

- I is the machine current,
- f is the repetition rate,
- N_b is the number of brunches (3 for PEP),
- ϵ_x is the horizontal emittance (1.2×10^{-7} m-rad),
- β_y^* is the vertical beta function.

The vertical beta function was lowered from 26 cm to 11 cm during the second period of running, in September 1981, by moving the final focusing quadrupoles closer to the interaction region. This configuration resulted in record luminosities[54], with peak luminosities reaching 3.2×10^{31} $\mathrm{cm}^{-2}\mathrm{s}^{-1}$, or equivalently, integrated luminosities of 1 pb^{-1} per day, by Spring 1983. The machine configuration parameters at this time are shown in Table 2.3. The luminosity collected by the Mark II experiment at PEP is shown in Table 2.4.

Parameter	Name	Value
ν_x	Horizontal Betatron Tune	21.25
ν_y	Vertical Betatron Tune	18.19
β_x^*	Horizontal Beta Function	3.0 m
β_y^*	Vertical Beta Function	0.11 m
$\Delta\nu_x$	Horizontal Tune Shift	0.050
$\Delta\nu_y$	Vertical Tune Shift	0.046
σ_x^*	Horizontal Beam Size	4.8×10^{-4} m
σ_y^*	Vertical Beam Size	6.5×10^{-5} m
σ_z^*	Longitudinal Beam Size	1.7×10^{-2} m
ϵ_x	Horizontal Emittance	1.17×10^{-7} m-rad
ϵ_y	Vertical Emittance	5.2×10^{-9} m-rad
I_{max}	Maximum current per beam	24.8 ma
L_{peak}	Peak Luminosity	3.2×10^{31} cm^{-2}s^{-1}
L_{avg}	Average Luminosity	1 pb^{-1} /day

Table 2.3. PEP Configuration in Spring 1983. The beam dimensions at the interaction point are given by σ_x^* and σ_y^*.

Runs	Dates	Cycle	$\int L dt$ (pb^{-1})
6510 7404	1/25/81 6/29/81	Spring 81	14.52
8011 8201	10/29/81 12/21/81	Fall 81	1.63
8210 9099	3/13/82 6/15/82	Spring 82	18.15
9122 9557	10/24/82 12/31/82	Fall 82	8.25
9558 11472	1/06/83 6/30/83	Spring 83	100.01
11473 12059	10/03/83 12/22/83	Fall 83	15.94
12068 13311	1/12/84 4/30/84	Spring 84	62.64
Total Integrated Luminosity			221.1

Table 2.4. Luminosity Accumulated by the Mark II at PEP. This table shows the luminosity acquired by the PEP 5 experiment in the years from 1981 to 1984. Note that a 5% systematic error should be attached to all luminosities.

Chapter 3. Detector Description

3.1 History

The Mark II detector was a direct descendant of the Mark I detector*. Both detectors shared the distinction of having been premier general purpose detectors when they were first built. Furthermore, both operated at the SPEAR† storage ring, contributing greatly to the understanding of the rich physics available there. The Mark I detector took data at SPEAR from 1973 to the summer of 1976. It was replaced by the Mark II detector in 1977. The Mark II detector took data at SPEAR from spring of 1978 until the spring of 1979. The Mark II detector was subsequently moved to the PEP storage ring in the summer of 1980. It is one of the nine high energy physics experiments to operate at PEP. Because of its experience at SPEAR the Mark II detector was able to record and analyze high quality data shortly after the PEP storage ring turned on, in the fall of 1980. Due to the maturity of the experiment, the Mark II group was one of the first to publish physics results at PEP.

The general design of the Mark II detector was that of a cylindrical detector with its axis of symmetry coinciding with the vacuum beam pipe of PEP. The main strengths of the apparatus were its high resolution charged particle tracking, together with its very good electromagnetic calorimetry. It also provided for adequate muon coverage, with muon detection over 45% of 4π solid angle. The soundness of this design is evidenced by the evolution of the detector from SPEAR (Mark I/Mark II) to PEP (Mark II) to SLC§ (Mark II Upgrade). The latter detector is the successor to the Mark II detector at PEP, and will be one of the

---

* It is amusing to note that the name Mark I was assigned to the detector only after the Mark II detector was built. The Mark I was previously known as the SLAC-LBL Magnetic Detector.

† SPEAR stands for Stanford Positron Electron Asymmetric Ring.

§ SLC stands for Stanford Linear Collider.

first detectors to study the properties of the Z^0 neutral gauge boson in detail[55]. The evolution of the detector has focused on the methods and hardware used for charged particle tracking. The Mark I used a magnetostrictive spark chamber[56]. The Mark II detector in turn used a drift chamber design[57], helping to pioneer a technique which is so pervasive in detector design today. Furthermore, the Mark II detector at PEP also pioneered the design of high precision vertex chambers[58] which have contributed so importantly to lifetime measurements, along with their concurrent improvement in momentum resolution for charged tracks. The Mark II Upgrade detector has a beautiful new drift chamber[59] which has already been used to take data at PEP, in preparation for SLC.

The detector description in this thesis concerns the Mark II apparatus in its most mature stage at PEP. In this configuration the detector consisted of a central system of vertex chamber, drift chamber, time of flight counters, lead-liquid argon electromagnetic calorimeter, and muon chambers. These systems essentially covered the region from $-.70 \leq \cos\theta \leq .70$, where θ is the polar angle measured with respect to the beam pipe ($\theta = 0$ defines the direction of travel of the electron beam). The detector coverage in azimuthal angle, ϕ, was close to 100% of 2π. The coordinate system used by the Mark II detector at PEP is shown schematically in Fig. 3.1. The detector also had two endcap electromagnetic calorimeters and a small angle tagging system for coverage of the forward and backward regions. All of these systems will be discussed in the following sections.

Unfortunately for the analysis presented here, the Mark II detector suffered from a lack of complete solid angle coverage, or hermiticity. This point will be discussed in much greater detail later. Detectors built after the Mark II tend to have better solid angle coverage. Examples of such detectors are the MAC and ASP experiments here at SLAC, and the UA1 detector at CERN. This has come with the realization that particle searches play an important role in probing and testing the Standard Model, and that one of the most important signatures of

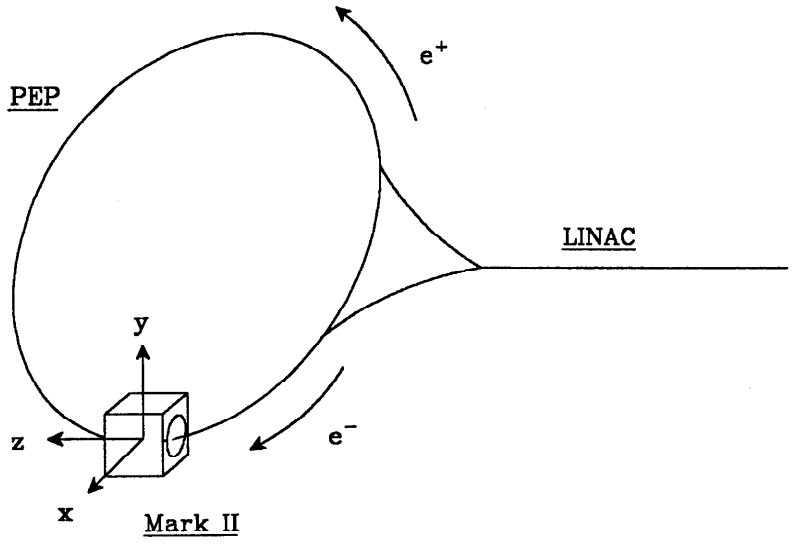

Figure 3.1. Mark II Coordinate System. The origin of this coordinate system was fixed at the center of the drift chamber. All detector components were surveyed into position with respect to the drift chamber.

new physics is missing energy. It is satisfying to note that this thesis represents one of the first searches for supersymmetry that has emphasized this point.

3.2 Overview

The Mark II detector, shown in Figs. 3.2 and 3.3, consisted of many subsystems each of which functioned to obtain complementary information about the particles arising from the initial electron-positron interaction. All of these subsystems gathered information from the electromagnetic interaction of the subatomic particles with bulk matter. This is generally true of all high energy physics detectors[60]. Ultimately, all the Mark II detector subsystems amplified this interaction into macroscopic electrical signals which were read out by the data acquisition system. These signals were treated either digitially† or as analog signals‡. The analog signals were read out as voltages on capacitors[61] which

† *E.g.* the proportional wire chambers in the muon system were treated as either being hit or not.

‡ *E.g.* the charge collected on the lead strips in the lead-liquid argon calorimeter was processed as an analog signal.

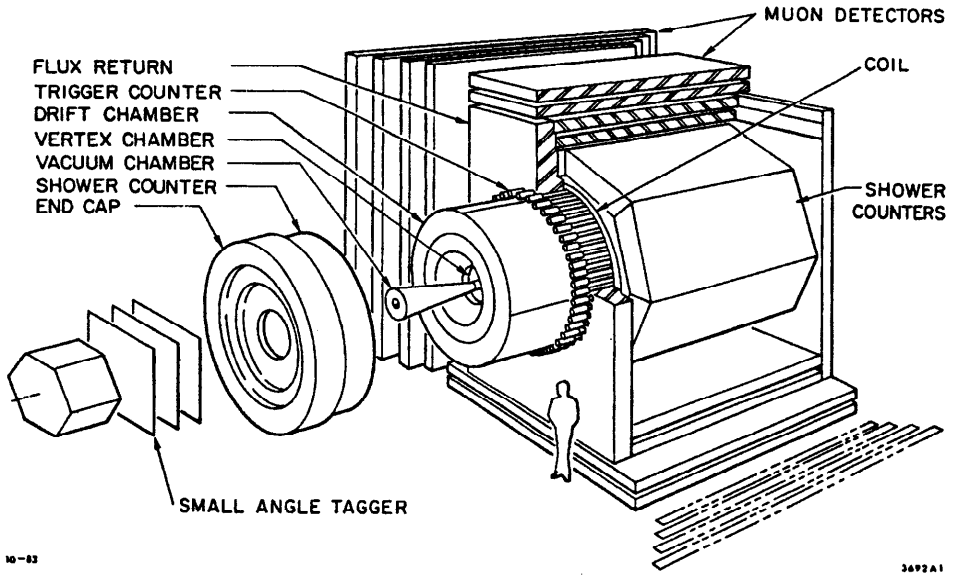

Figure 3.2. Mark II Isometric Overview. Note that the endcap support stand is not shown in this figure. The scale is given by the human figure.

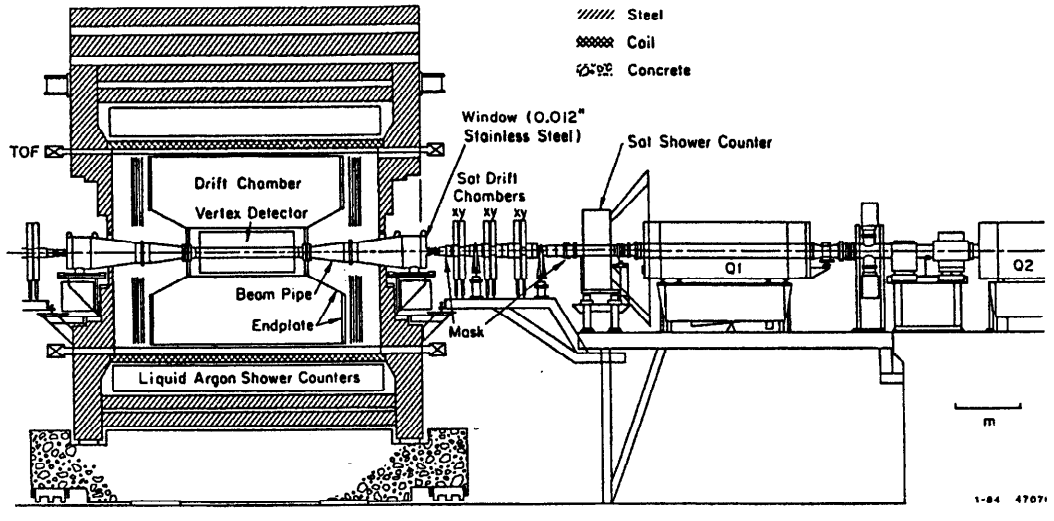

Figure 3.3. Side View of Mark II. This view shows the SAT system. The final focusing quadrupoles in the mini-β configuration can also be seen.

were subsequently digitized for readout by the data acquisition system. One of the biggest advantages of reading out the detector information electronically was that a fast triggering scheme could be used to minimize detector dead-time. This is vital for detectors operating in a storage ring environment since the beam crossing repetition rate is extremely high. There was a beam crossing every 2.45 μs at PEP, corresponding to a repetition rate of 408 kHz.

The experimental setup of almost all high energy physics experiments today require the detector to be isolated from personnel during data taking because of the radiation hazard presented by the beams. Storage rings typically have a large amount of synchrotron radiation present due to the constant circular acceleration of the beams. Therefore, no personnel were allowed in the PEP storage ring when beams were present. The Mark II experimenters were allowed access to the detector only during periods when there was no beams in the machine, and only under the strict supervision of the PEP safety personnel during such times. Normally, the Mark II detector was isolated by a thick shielding wall of concrete, and was inaccessible.

Since the Mark II detector was an electronic detector which was isolated from the experimenters during data taking, most of the signals from the detector were brought out on various cables. These cables were in turn brought into the LEACH (Local Electronics And Cryogenics House) for signal processing and data acquisition. Due to the inaccessibility of the detector only the minimum of electronics were placed in the interaction hall with the detector. Only when it was absolutely necessary were the electronics placed in the interaction hall (*e.g.* the preamps for the drift chamber sense wire signals were placed right next to the drift chamber in order to minimize pickup noise). The LEACH was therefore an integral part of the detector, serving to supervise data acquisition. In fact the LEACH was actually physically connected to the Mark II detector via various cables, gas and cryogenic lines, and pumping. The LEACH was accessible to the

experimenters during data taking. This allowed experimenters the opportunity to quickly service any failed electronic components in it.

The Mark II experiment was generally run from what was known as the control room, although it could also be controlled from the LEACH. The control room was adjacent to the LEACH, and housed the VAX 11/780 computer, along with display panels and the consoles used to run the experiment. The experimental data taking was supervised by one to two physicists working in eight hour shifts. Typically, there were three shifts per day. The experiment was run by a process on the VAX computer. When the electronic trigger processing (described in more detail below) selected an event the VAX computer would gather the data via a CAMAC† interface directly onto the VAX's unibus. The data was recorded onto magnetic tape in what was known as raw data format. This meant that only minimal data reduction was done (typically only that done by the BADC‡ microprocessors). The raw data tapes were then processed by an IBM 3033 and/or an IBM 3081 mainframe computer. A later section will discuss the off-line analysis. Data taking was very automatic when all went well. On these days the physicist(s) main duty would be to mount new tapes as the data was collected. Each event recorded onto tape was tagged with a run and record number. The run number was a unique number associated with a block of data acquisition, while the record number tagged events within a run. Each run was started and ended manually from the display panel. The physicists on shift were also responsible for calibrating the electronics once per shift, running a shift check to observe the hardware status, and monitoring the accumulated histograms for each run. They were also expected to quickly troubleshoot and fix any hardware or software problems that developed on shift.

---

† CAMAC stands for Computer Automated Measurement And Control. It is a electronics standard for data acquisition. SLAC CAMAC operated with clock times in integer multiples of 1.6 ms.

‡ BADC stands for Brilliant Analog to Digital Converter, see Ref. 62.

The detector components will be described in general in the following sections, after which a section on triggering and data acquisition will follow. This chapter will concentrate on the hardware design and performance of the Mark II, while the next chapter will describe the general data analysis that was done utilizing the various components. Table 3.1 shows the central detector's composition, listing each component's thickness in terms of radiation lengths (X_0), see also Figs. 3.2 and 3.3.

3.3 Vertex Chamber

The entire data set used in this analysis was taken after the Mark II vertex chamber[58] (VC) was installed, in the fall of 1981. The vertex chamber was a high precision, high density drift chamber which was placed as closely to the beam pipe as possible. The inner wall of the vertex detector was in fact the beam pipe, see Fig. 3.4. The vertex chamber design sought to maximize tracking resolution in a number of ways. Since the tracking resolution depends on both the number of measurements and the lever arm over which the measurements are made, the vertex chamber wires were collected into two bands of collection wires, or sense wires. The inner band consisted of four closely spaced, concentric layers of wires which were placed as near the beam pipe as possible, at an average radius of 11.4 cm. The outer band consisted of three closely spaced concentric layers of wires placed as near the outer chamber wall as possible, at an average radius of 31.2 cm. The inner chamber wall, *i.e.* the beam pipe, was constructed mainly of beryllium (a low Z metal), 1.4 mm thick, in order to minimize multiple Coulombic scattering effects. The chamber was 1.26 meters in length. Figure 3.5 shows the details of the beam pipe construction.

The cell design consisted of a sense wire, which was used to collect the ionization electrons, and field wires, which carried the high voltage used to collect and amplify the ionization left by high energy particles passing through the gas. Guard wires were also used to prevent crosstalk between cells and to help

Component	Inner Radius	Thickness	Material	X/X_0
X-ray shield	7.3	0.005	Ti	0.001
Beam pipe	7.62	0.142	Be	0.004
Insulator	7.76	0.005	Mylar	-
Ground Shield	7.8	0.002	Al	-
VC Gas	7.8	27.1	Ar,Eth	0.002
VC Outer Shell	35	0.178	Al	0.020
Lexan	37.1	0.32	Lexan	0.009
DC Gas	37.4	113	Ar,Eth	0.009
DC Outer Shell	150.3	0.64	Al	0.071
TOF	151.1	2.5	Pilot F	0.064
Coil	159	14	Al	1.4
Shower Counter	180	41	Pb-Ar	14
Hadron Filter 1	235	22.9	Fe	13.0
Hadron Filter 2	269	22.9	Fe	13.1
Hadron Filter 3	306	29.8	Fe	12.1
Hadron Filter 4	351	24.4	Fe	13.1

Table 3.1. Mark II Central Detector Components. This table shows the material encountered by a particle as it moved away from the interaction point at normal incidence. The numbers for the hadron filters are for the top wall of the muon system only, the other sides are similar. All dimensions are in centimeters.

electrostatic stability. The drift cell radius was 0.53 cm. The sense wires were 20 μm diameter thick gold plated tungsten wires, and the field and guard wires were 150 μm diameter thick gold plated aluminum wires in the inner band, and gold plated beryllium-copper wires in the outer band. A section of the chamber's wire pattern is shown in Fig. 3.6. All together there were 825 cells in the chamber; 270 in the inner band, and 555 in the outer. See Table 3.2 for details. The vertex

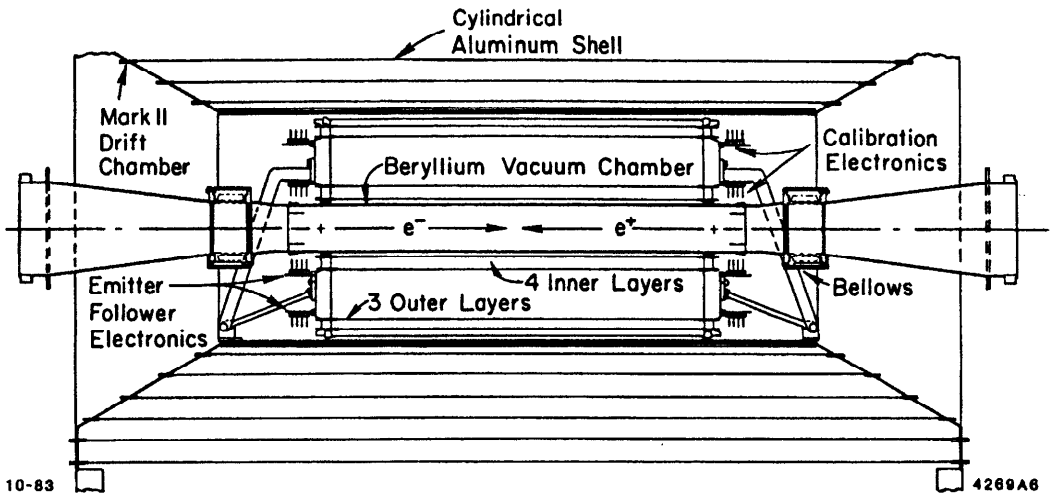

Figure 3.4. Mark II VC Construction. The overall mechanical design and placement of the vertex chamber is shown here. The vertex chamber sat inside the drift chamber, whose first few layers are also shown here.

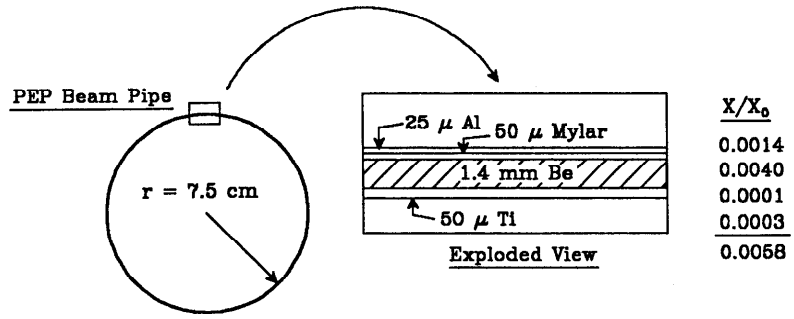

Figure 3.5. Mark II Beam Pipe. This figure shows the PEP beam pipe construction after the vertex chamber was installed. The inner layer of Ti was used as a shield against low energy synchrotron photons. The layer of Al was used as a ground shield against chamber pickup of the beam charge and was insulated from the Be by the mylar.

chamber design had the advantage of simplifying mechanical and electrical design while maximizing the tracking information obtained.

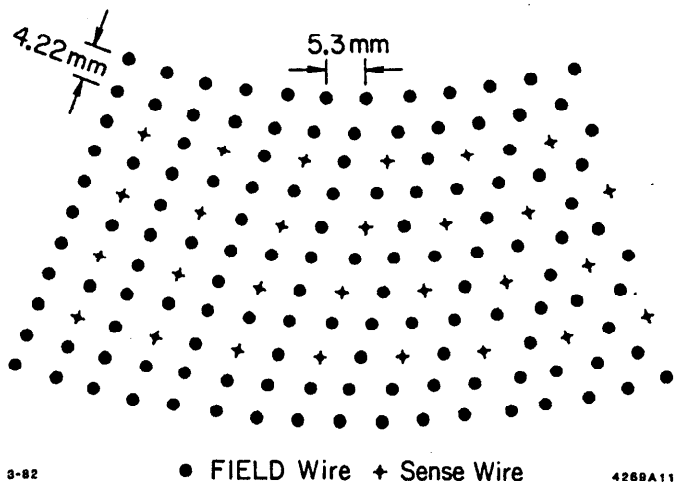

Figure 3.6. VC Wire Pattern. This figure shows the wire pattern for the inner band of the vertex chamber.

Band	Layer	Radius (cm)	Cells
Inner	1	10.1223	60
	2	10.9658	65
	3	11.8093	70
	4	12.6528	75
Outer	5	30.3668	180
	6	31.2103	185
	7	32.0538	190

Table 3.2. Vertex Chamber Construction. There were 270 wires in the inner band and 555 in the outer. The overall length of the chamber was 1.26 meters.

To improve the resolution of each space-time measurement from a cell the following was done:

- All wires were located as precisely as possible, to an accuracy of $\simeq 25$ μm.
- High resolution electronics were used, with a timing resolution of $\simeq 250$ ps.
- The voltage was set for a high gain, V = 2.250 kV. This resulted in a drift velocity of approximately 50 μm/ns.

- The gas pressure was kept stable, P = 15.50 ± .05 psia.
- A high gain, relatively fast gas was used. The original mixture was argon/ethane in a 50/50 mix by volume†.

The preamps and calibration electronics were mounted directly onto the outside of the vertex chamber. The gain was equalized throughout the chamber, and one space-time relation was used for the entire chamber (with the exception of a small section of the chamber which developed problems during operation). The voltage threshold was set to 400 μV. A block diagram of the readout electronics is shown in Fig. 3.7. The readout electronics were calibrated by sending pulse pairs with varying length delays directly onto the sense wires and monitoring the ADC† counts vs. the time delays. The average spatial resolution for the entire chamber was 95 μm.

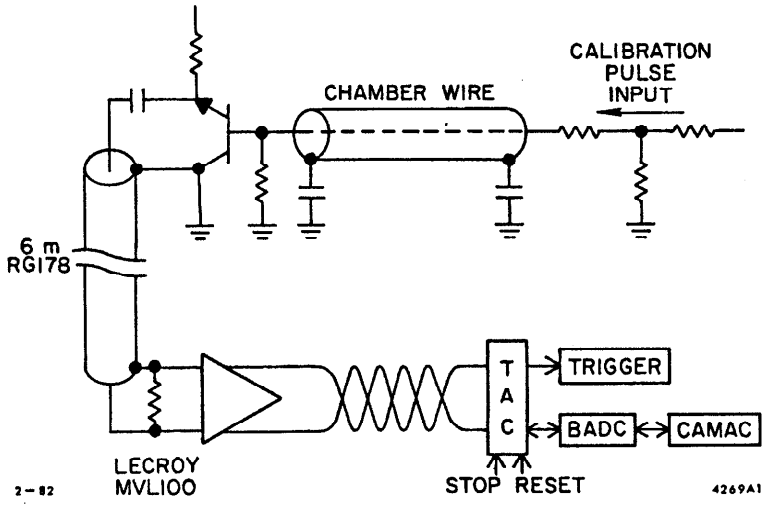

Figure 3.7. VC Electronics. This figure shows a schematic of the VC readout electronics. The sense wires were attached to emitter followers whose output was taken to the LEACH for further processing.

---

† After one and half years of running it was found necessary to add isopropyl alcohol to the gas mixture, at a level of 1.5% by volume, to inhibit dark currents and chamber aging.

† ADC stands for Analog to Digital Converter.

3.4 Drift Chamber

The Mark II drift chamber[63,57] (DC) was a cylindrical chamber which had 16 layers of sense wires starting at an inner radius of 41.36 cm and extending to an outer radius of 144.77 cm. The chamber endplate consisted of two pieces; a conical inner piece with a flat outer rim‡, and a flat annular ring which sat outside the conical piece. There were sixteen layers of wires in the drift chamber. The first six layers were on the conical section (four on the cone, two on the rim), while the outer endplate section had ten layers. The flat endplates were made of aluminum hexcel (7.62 cm thick), the conical section was made of solid aluminum. The hexcel design was chosen to withstand the large tension due to the wires with a minimum of material. The inner cylindrical wall of the chamber was composed of Lexan (a clear plastic); this allowed visual inspection of the chamber when the endcap calorimeter doors were removed. The outer cylindrical can was made of six 6.25 mm thick aluminum plates which were wrapped in fiberglass for torsion relief. The overall chamber construction is shown in Fig. 3.8.

The wires were strung alternating between axial, $+3°$ stereo, and $-3°$ stereo with respect to the beam pipe. This allowed the tracking algorithms to obtain z information as well as azimuthal information. Altogether there were 6 axial layers and 10 stereo layers. For historical reasons the layers were numbered from 6 to 21. Various layers were used in the charged track trigger, which will be described in a later section.

There were two cell designs used in the chamber construction; a small cell, which was used for six layers on the conical section of the endplate, and a large cell, which was used for the layers in the hexcel portion of the chamber. The large

‡ The conical section accommodated the compensating magnets of the SPEAR storage ring. These magnets were used to cancel the $\int \vec{\mathbf{B}} \cdot d\vec{l}$ contribution of the Mark II solenoid in order to prevent the beam's synchrotron and betatron oscillation modes from coupling to each other. The final PEP design did not require these magnets.

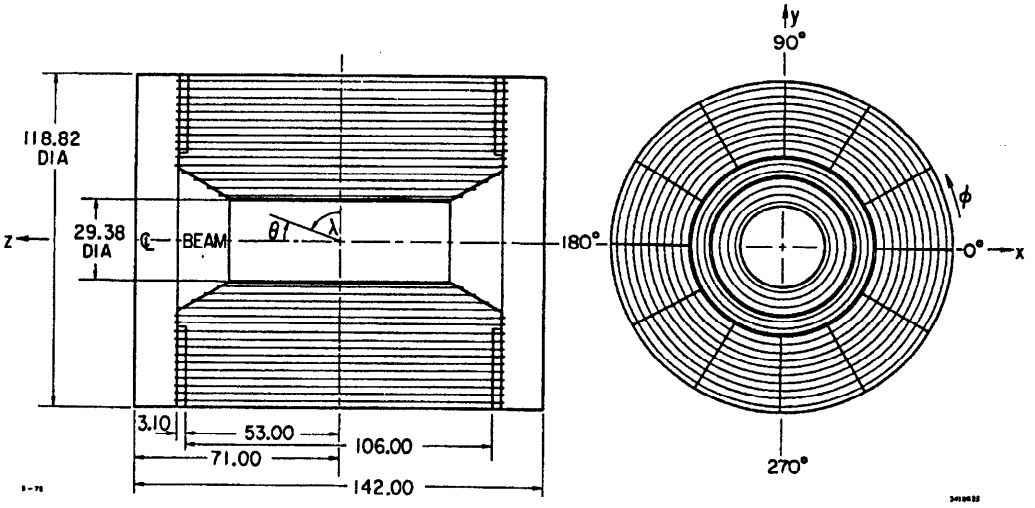

Figure 3.8. Mark II DC Construction. The drift chamber construction and coordinate system is shown here. Note that all dimensions are in inches.

cells were used in the outside of the drift chamber where the track density was small. The small drift cell radius was 0.902 cm, and the large drift cell radius was 1.803 cm, see Fig. 3.9. The wire pattern in the chamber repeated every 30° in azimuth (such that all the field wires line up in each layer). A 30° cell pattern is shown in Fig. 3.10. The field wires were placed at constant azimuth so that the cells were slightly trapezoidal rather than rectangular. The height of the cell was fixed at 1.20 cm for all layers. There were 3204 drift cells in the entire chamber. See Table 3.3 for details.

All the wires in the original construction were silver plated beryllium-copper (95% Cu, 5% Be). Each sense wire was surrounded by 6 field wires. The sense wires had a 38.1 μm diameter, the field wires had a 152 μm diameter. This material was chosen because it allowed a large elongation ($\simeq$ 40% for a 38μm thick wire) under a tension well below its tensile strength (3.05×10^6 g/cm^2). The chamber was originally strung at a minimal tension and then brought to uniform tension throughout by moving the endplates apart.

A 50/50 gas mixture,by volume, of argon/ethane was chosen for operation.

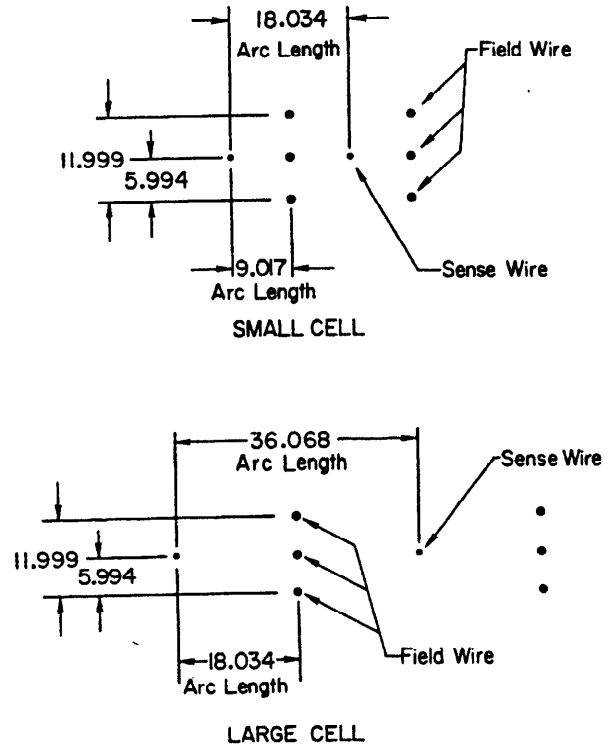

Figure 3.9. DC Cell Geometry. The geometry for both the large and small drift chamber cells is shown. Note that the dimensions are in millimeters.

The small cells were operated at a voltage of 2.85 kV and the large cells at 3.40 kV (except the outermost layer which was kept at 3.8 kV) during most of the data collection†. This meant that the large cells were operated below the drift velocity saturation point while the small cells were operated only slightly above saturation. The space-time relation for the large cells was very complicated due to the nonlinearities in the electric fields. An extensive iterative program for obtaining the correct constants for the parameterization of the space-time relation was an integral part of the Mark II data analysis. We will return to this point later.

The drift chamber electronics were very similar to those used for the vertex

† However, during the Fall of 1983 the DC began to glow badly, and it was necessary to lower the voltage to 3.2 kV in the large cells.

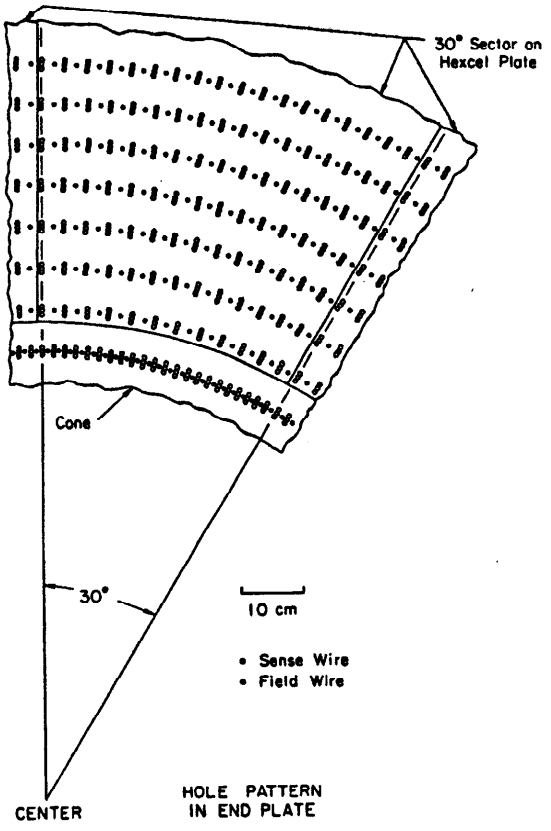

Figure 3.10. DC Cell Pattern. A 30° section of the drift chamber is shown here.

chamber, except they had a slightly worse timing resolution of $\simeq$ 350 ps. The preamps for the sense wire signals were placed on the outside of the detector, and the preamp output was cabled into the LEACH for signal processing. The discrimator threshold voltage was set at $\simeq$ 500 μV. A block diagram of the readout electronics is shown in Fig. 3.11. The DC readout electronics were calibrated with pulse pairs exactly like the VC, with the exception that the calibration pulses were capacitively coupled to the field wires which in turn were capacitively coupled to the sense wires. The resulting average spatial resolution for the entire chamber was 200 μm.

3.5 Time of Flight

The Mark II time of flight system, or TOF, consisted of 48 plastic scintillators

Cell Size	Layer	Radius	Length	Angle	Cells
Small	6	41.36	198.41	0	144
	7	48.26	222.29	+3.12	168
	8	55.15	246.17	−2.90	192
	9	62.04	270.05	0	216
	10	68.94	278.64	+2.90	240
	11	75.83	278.64	−2.90	264
Large	12	82.72	264.16	0	144
	13	89.62	264.16	+3.07	156
	14	96.51	264.16	−3.07	168
	15	103.40	264.16	0	180
	16	110.30	264.16	+3.07	192
	17	117.19	264.16	−3.07	204
	18	124.08	264.16	0	216
	19	130.98	264.16	+3.07	228
	20	137.87	264.16	−3.07	240
	21	144.77	264.16	0	252

Table 3.3. Drift Chamber Construction. Note that all dimensions are in centimeters. The angle refers to the stereo angle and is in degrees. Length refers to the active length of the sense wires. The layer number also gives the number of high voltage segments.

placed at an average radius of 1.51 m from the beam pipe. The scintillators were made of Pilot F, and measured 343 cm × 20.3 cm × 2.5 cm. The scintillators were cut in a rhomboidal fashion so that there was no clear crack between scintillators for tracks travelling radially from the interaction point. The scintillators covered the polar region of $|\cos\theta| \leq 0.75$. The light from the scintillator was brought out on both ends by lucite light guides and feed into two inch diameter photomultiplier

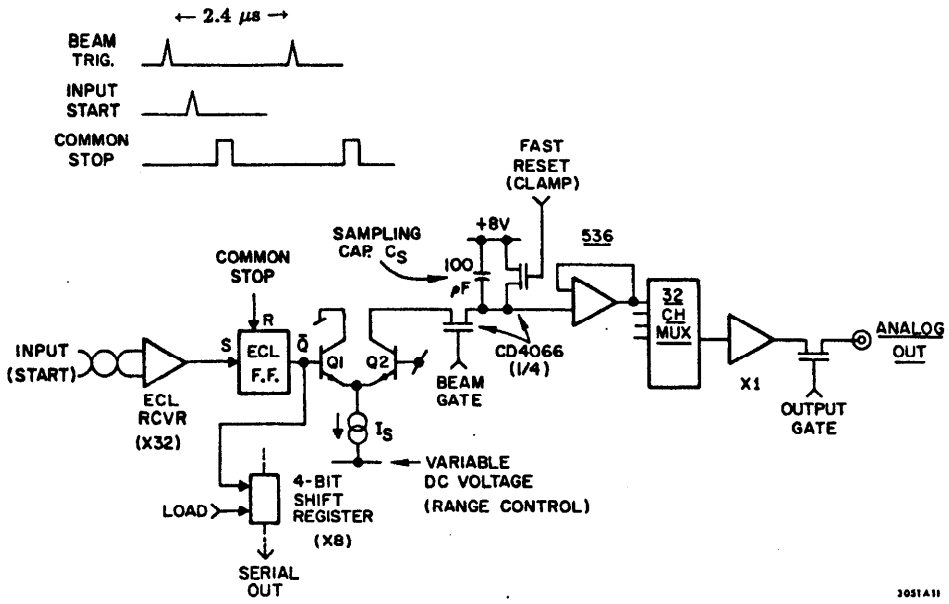

Figure 3.11. DC Electronics. This schematic shows the DC readout electronics. The timing information was gotten by ramping down the voltage on a capacitor.

tubes (Amperex XP2230)†. The photomultiplier output was split 20% into electronics which measured the charge integral signal, and 80% into timing electronics. Two discriminator levels were used for the timing, thus a total of three measurements were made. A block diagram of the readout electronics is shown in Fig. 3.12. The three measurements were used to make slewing corrections to the timing information. The system was periodically calibrated by sending laser pulses via optical fibers to the scintillator. The laser pulse intensity could be adjusted with various filters.

The efficiency for a charged track to fire a TOF counter was $\simeq 99\%$. Due to degradation with age and radiation damage the TOF timing resolution was only 340 ps for Bhabha electrons at PEP, compared to 270 ps for Bhabhas at SPEAR. For Bhabha electrons at PEP, where the charged particle was highly relativistic,

† It should be mentioned that 3 of the 48 TOF counters were read out on only one side after the magnet accident (described in the next section).

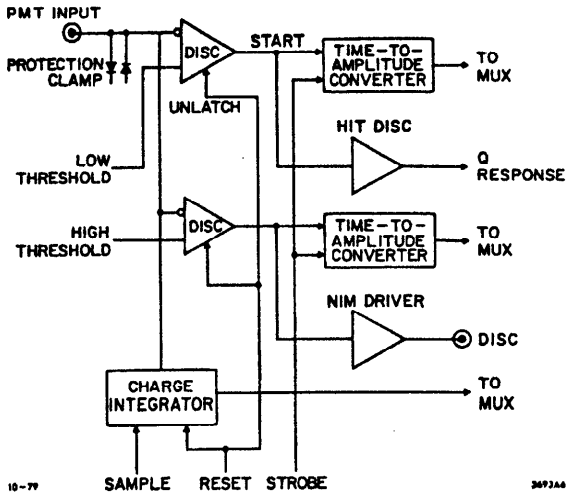

Figure 3.12. TOF Electronics. This schematic shows the readout electronics for the TOF system.

the TOF times varied between roughly 5 and 7 ns depending on the flight path.

The main role of the TOF system in this analysis is for the elimination of cosmic events. The particle identification capacity of the TOF system at PEP was much worse than that at SPEAR (mainly because SPEAR operated at lower energies). Most analyzes at PEP did not use the TOF system for particle identification. However, the TOF system played a very important role in the charged particle trigger, as will be described below.

3.6 Magnet

A solenoidal magnet was placed at a radius of 1.6 m. This magnet was constructed of hollow aluminum conductor, 4.4 cm × 2.4 cm in cross section, with an inner hole of 1.3 cm × 1.0 cm for carrying cooling water. The conductor was wrapped in fiberglass insulator, tightly wound into two layers, and epoxied in place. A heat shield was placed between the magnet and the TOF system. The TOF, DC, and VC systems all sat inside the magnet. During the early operation of Mark II at PEP the magnet suffered a short between the inner and the outer layer of conductor so that current went in only about 1/3 of the length of the

magnet, jumped the short, and traveled back out the magnet. In order to recover any use of the magnet it was necessary to float the inner layer of conductor, so that only the outer layer carried current. This reduced the magnet field strength by a factor of two.

The magnetic field provided by the solenoid was crucial to the momentum measurement done by the central tracking chambers. The field strength along the axis of symmetry was 2.35 kG, for the operating current of 2300 A (the magnet had a resistance of 1/8 Ω). The field was originally mapped out by a Hall probe, to an accuracy of $\simeq 0.2\%$, and modeled by a polynomial expansion in r and z. The overall field strength was monitored throughout data taking by a NMR‡ device. The magnetic flux was returned through the endcap, the flux return iron, and the two iron hadronic absorbers used in the top and bottom muon walls.

3.7 Lead-Liquid Argon Electromagnetic Calorimeter

The Mark II lead-liquid argon[64] (LA) calorimeter was outside the magnet coil, sitting at a radius of 180 cm. The LA system consisted of eight identical modules, measuring 380 cm long × 180 cm wide × 30 cm deep. The eight modules were arranged in an octagonal fashion about the beam pipe, and covered about 50 square meters for a solid angle coverage of $\simeq 65\%$ of 4π. The polar angle coverage was roughly over the region of $|\cos\theta| \leq 0.72$. The azimuthal angle coverage was about 88% of 2π, allowing for the 2.7° in ϕ of dead region near the module edges.

The calorimeter was constructed in layers; first a solid plane of showering material, then a gap filled by the liquid argon, then a plane formed by strips of the showering material. The liquid argon was used as an ionizing medium while the strip planes were used to collect the ionization. The first two layers of the LA module were made of 1.6 mm thick aluminum, separated by 8 mm of liquid argon, and formed what was known as the massless gap (or trigger gap). It was

‡ NMR stands for Nuclear Magnetic Resonance.

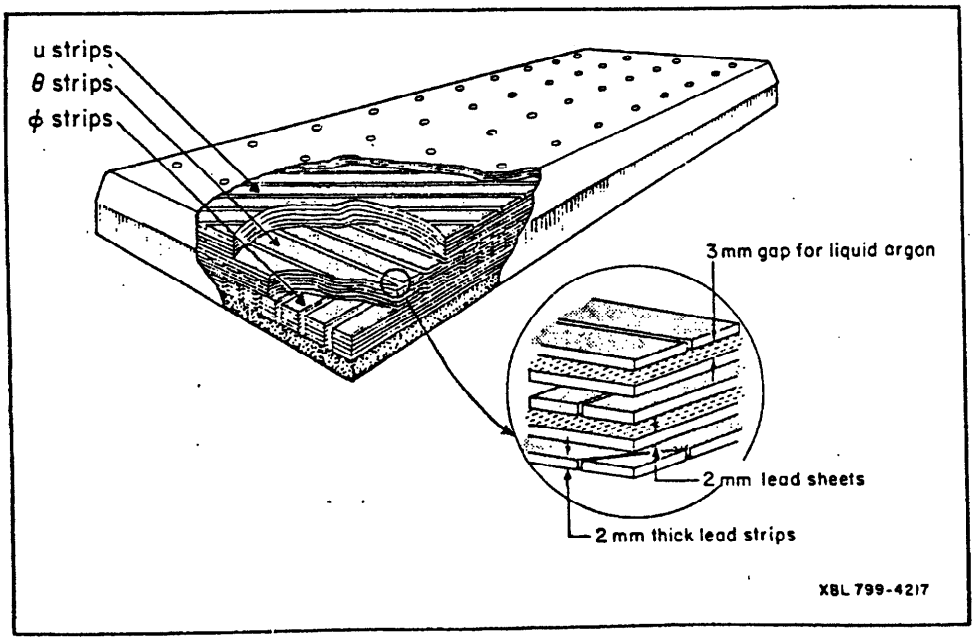

Figure 3.13. Mark II LA Module Construction. This figure shows one of the eight LA calorimeter modules in an exploded view.

only $\simeq 0.10\%$ radiation lengths thick. It was designed to minimize the probability of initiating a shower in order to detect showers that initiated in the magnet coil rather than the calorimeter. There were 36 strips read out in the trigger gap. They were held at $\simeq$ 10 kV.

The rest of the module was made up of 2 mm thick lead planes alternating with 3 mm liquid argon gaps. The lead was strengthened with 5% antimony. There were 37 layers altogether, for a shower sampling every 0.4% of a radiation length. All the odd numbered layers were solid planes of lead, all the even numbered layers were planes formed by lead strips, see The solid planes were held at ground, the collection strips at 3.5 kV. Altogether the system was about 14.5 radiation lengths thick at normal incidence angle.

The lead strips came in three varieties; which were known as the F, T, and U strips. The F strips (for fi, a corruption of phi) were orientated along the beam direction, the T strips (for theta) were orientated at 90°, and the U strips

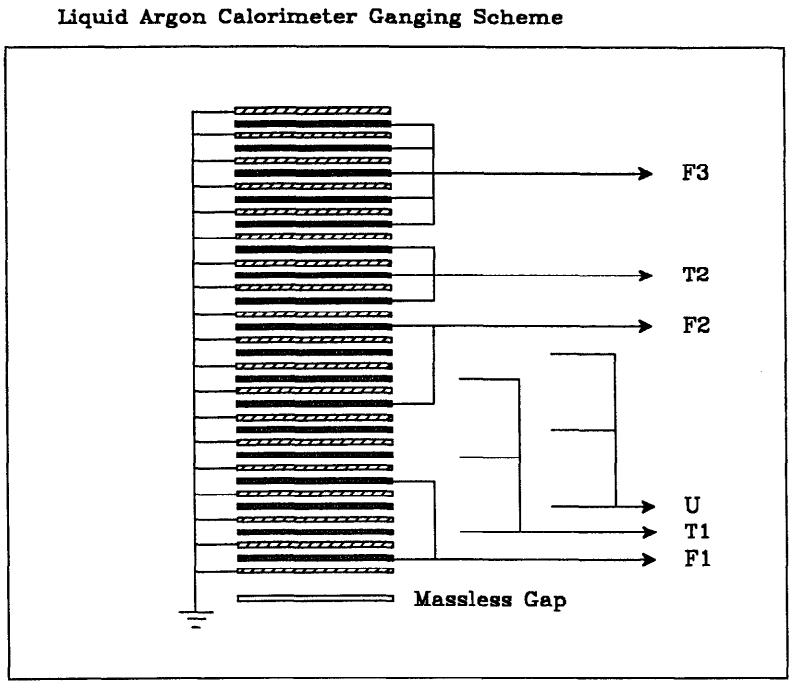

Figure 3.14. Liquid Argon Calorimeter Ganging Scheme.This figure shows the vertical gang scheme used to reducethe number of channels read out by the LA system.

were orientated at 45° to both the F and T strips. The U strips provided non-redundant readout information when multiple showering tracks entered a module. Of the eighteen strip layers, nine had F strips, six had T strips, and three had U strips. The F and T strips were 3.49 cm wide, the U strips were a factor of $\sqrt{2}$ wider, *i.e.* 4.94 cm, to facilitate construction of the support structure. The first layers, where the shower position resolution was most sensitive, alternated cyclically between F, T, and U strips. Thereafter only T and F layers were used since their construction was simpler. Altogether there were 1152 lead strips in each module. In order to economize on the readout electronics the strips were ganged in depth, and in some cases, within the layer. The vertical ganging is shown in Fig. 3.14. Thus, every F strip in layer 2 was electrically connected in parallel with the corresponding strip in layer 8 forming what was know as the F1 readout. The layer readout was then grouped into a F1, F2, and F3 readout in ϕ, a T1 and T2 readout in θ, and a U readout for ambiguity resolution. Within the T2 layer,

"Layer"	Coordinate	Width(cm)	Channels/Module
Trigger Gap	ϕ	3.7	36
F1	ϕ	3.7	38
T1	θ	3.7	100
U	u	5.0	56
F2	ϕ	3.7	40
T2	θ	7.4	52
F3	ϕ	3.7	40

Table 3.4. LA Calorimeter Readout. This table details the LA readout.

where spatial resolution was not critical, the strips were ganged horizontally in pairs (except the edge strips) to reduce the number of T2 readout channels from 100 to 52. With the U layers, the last ten strips at each end were paired off in order to approximate a constant capacitance per channel. With ganging the number of channels per module was 362, see Table 3.4 for more details.

The entire assembly was cooled to about 88° K. The module itself was cryogenically sealed and had liquid nitrogen cooling pipes attached to its back face. Special supports, which allowed the lead to expand and contract during cool-down or warm-up, were used to hold the lead in place. Special feedthoughs, which minimized heat losses, were used to carry the electronic signals out from the LA system to the LEACH. The cool-down period for the modules was three days. The cost per day of maintaining the module temperatures was $\simeq$ \$250/day. This can be compared to the cost of $\simeq$ \$2000/day of powering the solenoidal magnet.

The charge was collected on the strips and preamplified and integrated over $\simeq$ 460 ns by SHAM (Sample and Hold Analog Module) modules. The analog signals from the SHAM's were then sent to an ADC for readout to the VAX. The SHAM signals from the first few ganged layers were summed and used in an energy trigger, as will be discussed below. A schematic of the LA readout

electronics is shown in Fig. 3.15. The LA electronics were calibrated by injecting precise amounts of charge onto the strips and monitoring the readout.

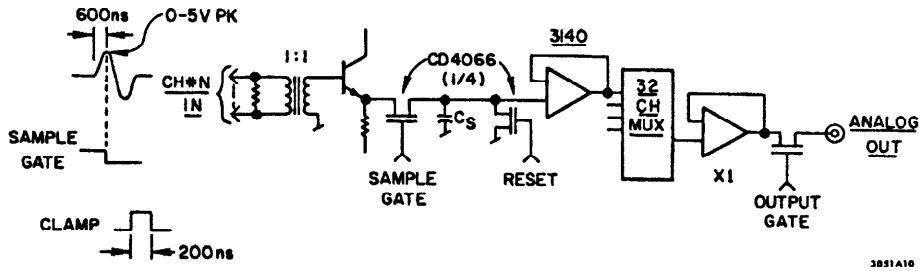

Figure 3.15. LA Electronics. This figure shows a schematic of the LA readout electronics.

The energy resolution of the LA systems was $\sigma_E/E \simeq 14.5\%/\sqrt{E}$ (E in GeV).

3.8 Muon System

The Mark II muon detection system at PEP consisted of four walls placed at the top, bottom, left, and right side of the beam pipe, at a distance of about 235 cm from the interaction point. Each wall consisted of four layers of hadron absorber (typically steel) alternating with four layers of proportional wire chambers (PWC's). The solid angle coverage varied from $\simeq$ 55% of 4π at the innermost layer to $\simeq$ 45% at the outermost. Table 3.5 shows the muon system construction.

The PWC's in the first layer were orientated to measure polar angle, while the outer three layers measured azimuthal angle. The PWC's were triangularly shaped in order to maximize track detection efficiency (*i.e.* no cracks between PWC's), see Fig. 3.16. They were made from extruded aluminum modules, each module having eight PWC's. The 45μm gold plated tungsten sense wires were spaced 2.5 cm apart. The 2.5 cm spacing roughly corresponded to the extrapolation error due to tracking error and multiple Coulombic scattering when projecting a charged track from the inner detector through the muon system. The wires were

	East Wall		Top Wall		West Wall		Bottom Wall	
	D	T	D	T	D	T	D	T
Layer	(m)	(g/cm^2)	(m)	(g/cm^2)	(m)	(g/cm^2)	(m)	(g/cm^2)
1	3.2	182	2.5	182	3.2	182	2.5	182
2	3.6	184	2.8	184	3.6	184	2.8	184
3	4.0	244	3.2	239	4.0	239	3.2	244
4	4.5	196	3.6	184	4.5	184	3.6	244
Total		806		789		806		854

Table 3.5. Mark II Muon System Construction. The muon system geometry is shown here. D refers to the perpendicular distance from the wall to the interaction point, T refers to the thickness of the hadronic absorber (in g/cm^2). The nuclear interaction length for iron is 132 g/cm^2. The East Wall was placed on outside of the PEP storage ring ($+x$ axis), the West Wall on the inside ($-x$ axis).

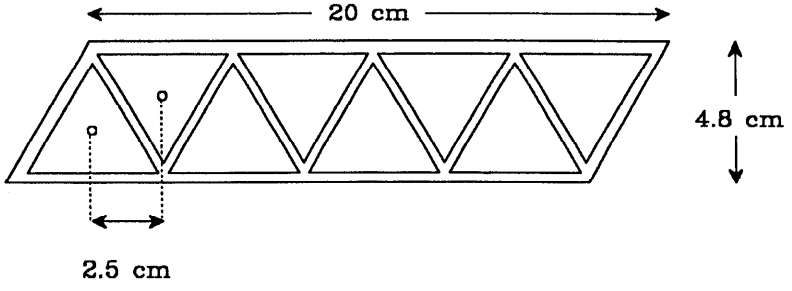

Figure 3.16. Muon PWC geometry. The PWC's for the muon system were made of extruded aluminum module; each module had eight tubes as shown above.

operated at a voltage of about 2 kV with a gas mixture of 95% argon and 5% CO_2 by volume.

3.9 Endcap Calorimeter

The forward and backward regions of the Mark II detector were covered by the endcap (EC) calorimeter. This component was a lead-proportional wire

calorimeter, consisting of two sheets of lead, 1.3 cm thick (*i.e.* 2.3 radiation lengths thick), alternating with two layers of proportional wire chambers. The usual tube PWC design, where the signal is read off a wire which is surrounded by a conducting chamber, was not used here. Instead, the PWC design consisted of a plane of 20μm gold plated tungsten wires, spaced every 4 mm, surrounded on both sides by a plane of G-10, which was supported by hexcel. The G-10 plane face nearest the wires was painted with strips of silver. These strips were held at -2.6 kV. The shower electrons were collected by the tungsten wire, avalanching in the Argon/Ethane gas mixture (50/50 by volume) as they neared the wire. This electron avalanche in turn caused an induced image charge signal on the silver strips which was readout by electronics very similar to the LA electronics. The strip patterns provided the positional resolution of the showers. There were four planes of strips, two for each plane of wires. The first pair of strips measured θ and ϕ. The second pair of strips were cut into a logarithmical geometry, where the strip geometry was given by $r = e^{\pm\phi}$ and so provided addition positional and ambiguity resolution. The strip width varied over the module, but was on the order of a few cm across. The endcap geometry is shown in Fig. 3.17.

Historically, the original Mark II endcap calorimeter was to have been a lead-liquid argon system with the strip geometry described above. One LA endcap was in fact built and used at SPEAR. Due to scheduling and budgeting difficulties the other endcap had the design described above. This design proved superior to the LA design for measuring low energy photons (*e.g.* it had fewer fake photons due to noise) and was adopted. Only the lead-PWC design was used at PEP.

The polar angle coverage of the endcaps was roughly over the region $0.76 \leq |\cos\theta| \leq 0.96$. The azimuthal angle was completely covered except for a break $4.2 \leq \phi \leq 5.2$ where a "keyway" was cut out for the support stand. The resolution of the system was $\sigma_E/E \simeq 50\%/\sqrt{E}$ (E in GeV) for electromagnetic showers. The relatively poor resolution of the endcap, plus the finite probability of photon

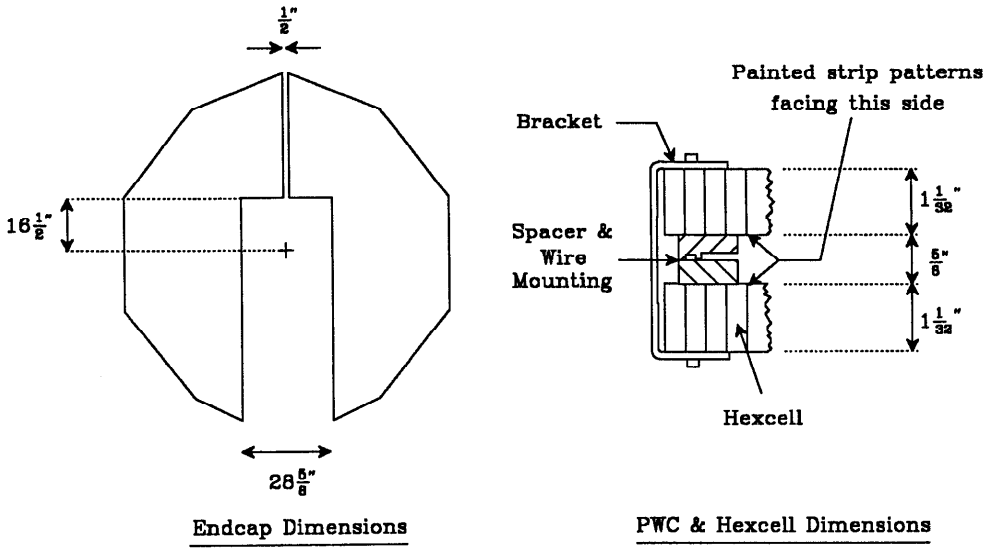

Figure 3.17. Endcap Construction. The left side of this figure shows the outside dimension of the endcap geometry. The active region was about an inch inside the perimeter. Each endcap consisted of two halves. The right side of the figure shows the PWC and hexcel design (wires not shown).

nonconversion in it ($\simeq 2.5\%$), greatly inhibited its use in all Mark II PEP analysis. The analysis discussed here only used the system as a veto (as will be discussed later).

3.10 Small Angle Tagger

The small angle tagger[65–67] (SAT) provided coverage down to very small polar angles in the forward and backward regions of the Mark II. The SAT system was used to monitor electrons at very small angles; which was especially useful for high statistics measurements of luminosities, and for tagging two photon physics events. The SAT system was made up of two modules, one placed in the forward region of the detector, the other in the backward region. Each SAT consisted of three layers of planar drift chambers, four large scintillator hodoscopes (known as the gross counters), four small precision placed scintillator hodoscopes (known as the precise counters), four small scintillator hodoscopes (know as the acceptance counters), and a lead scintillator calorimeter. The gross, precise, and acceptance

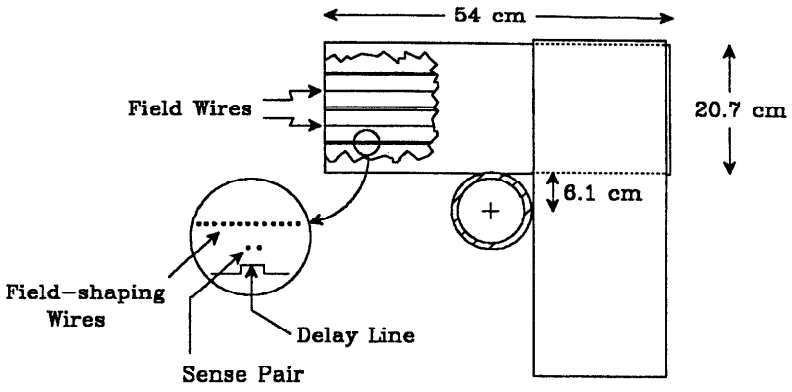

Figure 3.18. SAT Drift Chamber Construction. This figure shows two of the four planar drift chambers which formed one of the three sets of SAT drift chambers.

counters were used to monitor luminosity and to provide trigger signals. The SAT system was optimally designed for the detection of just one electron track per module and covered the angular region from 21 to 82 mradians in polar angle.

The drift chamber system consisted of three sets of four planar drift chambers. The first set of chambers was slightly smaller than the second two since it was placed closer to the interaction region. The four chambers were arranged in a rectangular fashion around the beam pipe, overlapping at the corners. The four chambers were paired off such that each pair were placed on opposite sides of the beam pipe. The first pair were oriented along the y coordinate, the second pair along the x coordinate. Each chamber had two field wire and three pairs of sense wires, see Fig. 3.18. The sense wires were paired in order to resolve the left-right ambiguity (*i.e.* which side of the wire the charged track passed through). The sense wires were read out with an inductive delay line in order to obtain spatial resolution along the wire length. A hit wire had a 300 μm resolution in the drift distance measurement, and a 0.5 cm resolution in the position measurement along its length. The optimal position resolution was obtained for tracks which passed through the overlapping corners of the chambers. The detection efficiency for each drift chamber layer was better than 99%.

The SAT calorimeter was made of alternating layers of lead and NE114 plastic

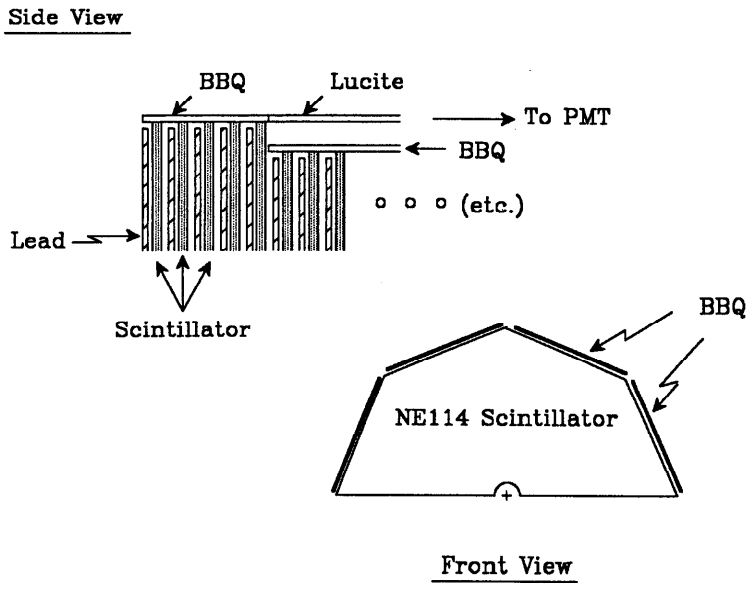

Figure 3.19. SAT System Calorimeter. This figure schematically shows the construction of a SAT lead-scintillator calorimeter module. The SAT system had four such modules, two on either side of the central detector.

scintillator. The lead sheets were 0.64 cm thick (*i.e.* 1.14 radiation lengths thick). The scintillator layers were each 1.27 cm thick. Altogether there were eighteen layers of lead and scintillator. Each SAT half had an upper and a lower calorimeter section. Each section was shaped as a half octagon with a hole cut in the center for the beam pipe. The scintillation light was collected by pieces of BBQ wave shifter which ran along the length of the entire assembly. The light was taken out on pieces of lucite light pipe and sent to PMT's, see Fig. 3.19. Each calorimeter section was read out by eight PMT's; four PMT's read out the front portion and four read out the back portion. This readout geometry gave a more uniform response for electrons entering at different points on the calorimeter face. The measured energy resolution was $\sigma_E/E \simeq 15.5\%/\sqrt{E}$ (E in GeV).

3.11 Beam Position Monitor

Two beam position monitors (BPM's) were located on either side of the Mark II detector at 4.9 m from the interaction point, just inside the final focusing

quadrupoles. The BPM's were installed at the same time the VC was installed. They consisted of 4 copper buttons spaced 90° apart which measured an induced charge every time the beams passed by. The ratio of induced voltages on opposite buttons provided a measure of the beam position. The four buttons therefore provided a measurement of the beam's position in two orthogonal coordinates. The beam position at the interaction point was found by interpolation from the beam position at the BPM's.

The electrical signals from the BPM's were taken out on 100 feet of RG223 cable to a pulse shaper and then fed into an ADC. At each 4 minute interval during data taking 32 voltage measurements were made for each of PEP's three bunches. These measurements were averaged and recorded onto magnetic tape. The short term resolution of the system was $\simeq 50\mu$m. The system was subject to long term drifts. This system was used by experimenters doing lifetime measurements to reject runs where the PEP operators "steered" the beams. Most analyzes used a run averaged beam position, based upon finding the event vertex over a large statistics data sample. This method used the tracking chamber information for positional information. The selectron analysis presented here is insensitive to such details.

3.12 Trigger and Data Acquisition Systems

The Mark II trigger[67–70] was a very flexible, versatile, fast electronic system which allowed the experiment to operate with very little dead-time while logging out interesting physics events at almost 100% efficiency. The flexibility of the trigger allowed the experimenters to compensate for hardware problems that developed in the detector during data taking. The trigger was versatile enough to be reconfigured for different event topologies in a quick and easy fashion. A particularly interesting case of this was the trigger used for this analysis, the so called selectron trigger. This trigger was never used at SPEAR, nor was it used during the first two years of data taking at PEP. Yet, when it was realized that single electrons provided an interesting physics signature the trigger reconfiguration was done within a few weeks. The Mark II triggered upon a variety of different criterion which involved charged tracks and/or calorimetric energy in the central detector, and showering electrons in the SAT system.

The Mark II trigger system used for data taking† was based upon a two level trigger. The first level was known as the primary trigger and was used to process the detector front end data very quickly upon each beam crossing (roughly every 2.4 μs at PEP). If the detector data was interesting enough to satisfy the primary trigger then the secondary trigger electronics were used to further process the data in order to decide whether the event should be logged to tape. While e^+e^- storage rings provide much cleaner environments than fixed target or $p\bar{p}$ machines they are never the less still plagued by uninteresting background events, such as coincident cosmic rays and beam-gas interactions. Noise is also present in the e^+e^- environment, and is generated by various sources, such as electronic pickup of the beam, 60 Hz line pickup, and synchrotron radiation photons (which generated stray hits in the wire chambers). The purpose trigger system selected

† This excludes the cosmic ray trigger which was useful for monitoring purposes when PEP was running without beams.

interesting events arising from e^+e^- interactions while filtering out as many background events as possible. The trigger had to perform in the presence of noise, accruing the minimum amount of dead-time. The dead-time arose from the trigger processing and data acquisition times. The present of noise complicated the job of the hardware track finding.

The primary trigger was dead-time free because of the bunched structure of the beams. It used simple selection criteria in order to obtain high efficiency and speed. If the primary trigger was not satisfied, the data acquisition system was reset and ready to take new data within 200 ns. The requirement that the primary trigger was dead-time free is given by:

$$\tau_c + \tau_{pt} + \tau_r < \tau_{bx}$$

where,

- τ_c was the maximum hardware collection time (*e.g.* the maximum drift time in the wire chambers),
- τ_{pt} was the primary trigger processing time,
- τ_r was the data acquisition reset time,
- τ_{bx} was the time between beam crossings.

This condition was easily met at PEP.

The primary trigger signal was used by the Master Interrupt Controller, or MICKEY, to decide whether to generate a reset and input gate signal to the data acquisition system or to delay them while the secondary trigger processing occurred. If the secondary trigger was satisfied then the reset and input gate signals were further delayed until after complete data acquisition had occurred. The detector dead-time was given by:

$$R_{pt} \cdot \tau_{st} + R_{st} \cdot \tau_{da}$$

where,

R_{pt} was the primary trigger rate, $\simeq$ 1.5 kHz at PEP,

R_{st} was the secondary trigger rate, $\simeq$ 3.0 Hz,

τ_{st} was the secondary trigger processing time $\simeq$ 34 μs,

τ_{da} was the data acquisition time $\simeq$ 40 ms.

The dead-time at PEP was roughly 7% for the typical 3 Hertz trigger.

The primary trigger was generated in one of three ways; by the charged tracking, by the calorimeter, or by the SAT system. The charged primary trigger was generated by a coincidence of a beam crossing signal (BX) and a drift chamber majority (DCM) signal. The DCM signal was generated by first grouping the drift cells in the vertex and drift chambers by layer. The TOF system phototubes were also grouped together as a "layer" as well. If any cell within a layer was hit, *i.e.* had a signal over threshold, then that layer was considered hit. If any TOF tube had a time compensated latch, *i.e.* such that the two photomultipliers had signals above threshold with times consistent with a real track passing through the scintillator‡, then the TOF layer was considered to have been hit. It should be mentioned that the TOF layer requirement provided the cosmic ray rejection with its tight timing gate ($\simeq$ 30 ns). The layer signals were fed into a programmable memory lookup module (MLM) whose output generated the DCM signal, and depended on the conditions the experimenters decided satisfied the primary charged trigger. This programmability allowed the primary trigger to be adjusted during running to compensate for chamber problems and the like, so that the primary trigger always operated at essentially 100% efficiency. A typical DCM required all of following

‡ The condition was relaxed for the three tubes which had to be disabled because of the magnet short. Their single photomultiplier signal was treated as a time compensated latched signal by the trigger.

conditions to be true:

≥ 2 *out of* 4 Inner VC layers,

≥ 1 *out of* 3 Outer VC layers,

≥ 2 *out of* 4 Inner DC layers (6-10),

≥ 1 *out of* 3 Mid-inner DC layers (11-13),

≥ 1 *out of* 3 Mid-outer DC layers (14-16),

≥ 2 *out of* 4 Outer DC layers (17-21),

≥ 1 *out of* 48 TOF time compensated latches.

The calorimetric primary trigger was generated by either the TED trigger or the SED trigger. Both of these triggers used the ADC raw energy sum from the calorimeter modules' front end electronics as input. This involved only the collection strips from the front portion of the liquid argon modules, *i.e.* excluding the T2 and F3 ganged layers (the total module was not used to reduce incoherent noise). The endcap modules used the sum of the logarithmic strips plus twice the phi strips (for technical reasons the theta strips were left out of the trigger). The TED trigger was generated when two LA or endcap calorimeter modules had energies above threshold. The LA energy threshold was $\simeq$ 1 GeV, the endcap threshold was $\simeq$ 2.5 GeV. Showering tracks which passed the threshold requirement were known as D-tracks. The TED trigger can be stated as requiring $N_D \geq 2$. The SED trigger was based upon an OR'ed condition of the sum of raw ADC energy over all eight LA modules and the sum of the two endcap raw ADC energies. The threshold was about 0.70 GeV in the LA system and 1.0 GeV in the endcap system. It should be mentioned that both the SED and TED triggers were vetoed when line synchronous noise was picked up. The last primary trigger was the SAT primary trigger. This trigger could be generated under a number of different conditions but typically required two collinear shower modules above threshold ($\simeq 1/2\ E_B$), plus two collinear gross scintillator counters and at least one

precise-acceptance telescope. Because of the large number of low angle Bhabha events this trigger was typically pre-scaled by a factor of 16.

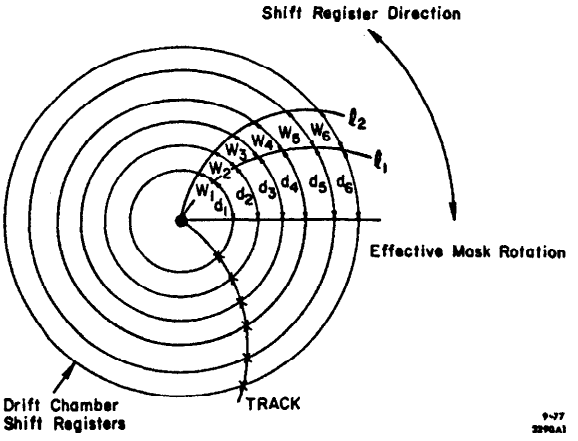

Figure 3.20. Hardware Road Definition. This figure illustrates how a hardware road is defined. Hit wires falling between arcs l_1 and l_2 are used to form a bit pattern which in turn is used to determine if a hardware track is present. This diagram shows the situation at SPEAR, the road definition at PEP was slightly more complicated in order to narrow the angular width of the road at small radii. This improved the rejection of background tracks which originated at large radii from the beam. See Ref. 71 for details.

The secondary trigger began processing after the primary trigger was satisfied. The calorimeter and SAT secondary triggers were automatically generated when their primary trigger requirements were satisfied. The secondary trigger's main purpose was to find hardware tracks in the central wire chambers. Hardware tracks were found by a special pattern recognition processor which operated in about 34 μs. They worked with the hit wires, and ignored the wire's associated timing information. Basically, the hardware tracks were based upon "roads", where a road is defined in Fig. 3.20 The master clock, operating at 10 MHz, moved the roads 2π around the entire chamber in units of one drift cell†

† To be accurate the road was moved one cell at a time only in the layer (21) with the largest number of cells (252). The other layers were clocked at a slower rate so that the road's average angular velocity was the same for all layers. A special widener for hit cells

(plus some overlap at the end to prevent any inefficiency). Twenty four curvature modules were used to find the tracks, half for positive curvatures, and half for negative curvatures. Each curvature module searched a different road, where a road is analogous to a momentum band. Two different roads were used for B-tracks, which looked for high momentum tracks in the innermost layers of the tracking chambers. Eleven different roads were used for A-tracks, such that the largest curvature found corresponded to about 130 MeV tracks. The curvature modules were programmed to use two different criteria (A or B) in their track finding. If a curvature module fired it communicated this information to one of the two track counter modules (A or B). The different track counter modules counted the number of tracks found by the curvature modules. In practice, only the A-track counter was used in the trigger. The track definitions were programmable, and changed over the course of data taking, but the following requirements were typical for the A-trigger:

≥ 2 *out of* 4 Inner VC layers,

≥ 4 *out of* 7 DC layers (6,7,9,15,18,19,20),

≥ 2 *out of* 4 Outer DC layers (18,19,20),

≥ 1 *out of* 1 TOF time compensated latch.

The track counter modules recorded the azimuthal position of the track, and eliminated double counting at the overlap region of the road's sweep over the chamber. The secondary charged trigger was satisfied when two distinct hardware tracks were found.

At this point all the basic features of the trigger have been discussed. The primary trigger was in reality a simple OR gate in a NIM logic crate, where

---

was used to allow tolerance for this effect in the pattern recognition. This necessitated an anti-chatter interval to be used to avoid double counting tracks, which in turn meant that the hardware would miss double tracks which were too close together. See Ref. 68 for details.

each system (SAT, tracking, and calorimeter) generated its own primary trigger signal. This primary trigger went into MICKEY, the Master Interrupt Controller. MICKEY was responsible for generating a WAIT signal when the primary trigger was fired, else it generated a RESET signal. The MICKEY module had twelve inputs into it. The tracking system had 6 inputs, two for each track counter. The calorimeter system had 3 inputs, as did the SAT system. Two of the tracking inputs counted the number of hardware A-tracks which were found, and used them in the charged trigger (the input saturated at 3 if more than 3 A-tracks were found). Similarly, two of the calorimeter inputs counted the number of number of modules above threshold (where again, the inputs saturated after 3). The other calorimeter input into MICKEY was used for the SED trigger. MICKEY used a programmable memory lookup table to determine whether the secondary trigger was satisfied. A charged secondary trigger was generated by MICKEY when two or more A-tracks were found. The TED calorimeter secondary trigger was generated for the case where two or more LA or endcap calorimeter modules fired.

The selectron trigger was implemented in May 1982, by reprogramming MICKEY to also generate a secondary trigger for one charged track, in combination with one calorimeter module firing. The primary trigger did not have to change, since it was ready generated by the DCM signal (as well as being backed up by the SED trigger for high energy electrons after its installation in the trigger). The Mark II detector was the first storage ring experiment to operate with a single electron trigger.

The Mark II data acquisition system was based upon CAMAC, and a system overview is shown in Fig. 3.21. The Mark II system was highly multiplexed and extensively utilized a device known as a Brilliant Analog to Digital Converter (BADC), for collecting, compacting, and transferring data to the CAMAC highway. The BADC's were programmable microprocessors which addressed each

hardware channel. The BADC's greatly simplified data collection in a number of ways. Firstly, they ignored all data channels whose signals fell below a given threshold, or pedestal. Secondly, they stored individual constants for each channel for correcting and converting the data into "physics units", *e.g.* the times for the wires chambers were read out in units of 0.1 ns by the BADC. There were roughly 30,000 constants stored by the BADC's which never had to be used by the offline analysis program, although these constants were of course made available to it. The corrected data value for a channel, Q_i', was generated from the raw data value, Q_i, when the channel was above its pedestal, ϵ_i, by the formula:

$$Q_i' = \alpha_i(Q_i - \delta_i) + \beta_i(Q_i - \delta_i)^2.$$

The constants, $\alpha_i, \beta_i, \delta_i$ and ϵ_i were generated frequently by calibrations and stored in the BADC. The ultimate data transfer to the VAX 11/780 was done under the direction of the VCC, or VAX CAMAC Channel. This device connected the VAX Unibus to CAMAC. The VAX Unibus operated at a maximum speed of 0.7 Mbytes/sec. This was the limiting cycle time for the system.

System interrupts (CAMAC LAM's or Look At Me's) were handled by the System Interrupt Module (SIM), which was in the system CAMAC crate. The SIM was connected to Remote Interrupt Modules (RIM's) by a daisy chain coaxial cable. The RIM's monitored the crate LAM's in addition to having six front panel inputs. The RIM's communicated with the SIM via a serial protocol. The SIM was polled by the VCC when it was not transferring data. The SIM could then communicate an interrupt to the VAX, which would then process and clear it.

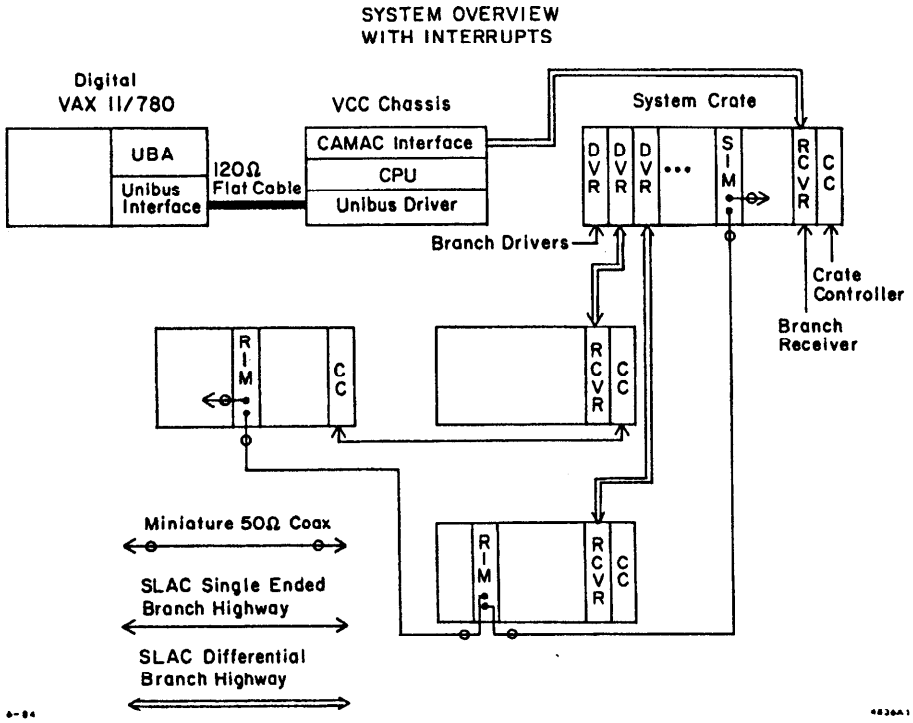

Figure 3.21. Mark II Data Acquisition System. The Mark II CAMAC system and VAX interface.

Chapter 4. Offline Analysis and Tracking Code

4.1 Overview

The Mark II offline analysis[72] was done in two steps: production and user analysis. The production jobs filtered and processed the raw data in a standard fashion, under the supervision of a program known as PASS2. Those events which survived the PASS2 cuts were written onto PASS2 tapes for general use. The PASS2 production code contained the standard Mark II tracking routines. These routines processed the hardware system information stored in the raw data. PASS2 did the charged particle tracking, calorimeter shower finding, TOF timing corrections, muon tracking, and SAT tracking. PASS2 was also responsible for associating the different subsystem information together for each track in an event. For example, a showering electron would have its shower information associated with its drift chamber information, and a muon would have the muon system information associated with its drift chamber information. The PASS2 program also filtered out non-physics events such as high voltage shorts, beam-gas and beam-wall events, etc.

The Mark II data structure was logically organized into different data types which were kept in a linked list. One data type contained the raw data for the event. Another contained the PASS2 information, which included a tracklist of information for each particle found in the event. This tracklist contained the available drift chamber tracking, shower, TOF, muon, and SAT information for each track. The PASS2 analysis program was responsible for filling in this information.

All of the tracking routines used empirically derived constants to convert the raw data into final physics quantities. These constants were determined by stand alone programs by iteratively fitting raw data distributions. The people responsible for the different subsystems would run constants finding programs

to determine the optimal constants for a given block of runs. These constants were then used by the PASS2 routine for tracking these blocks of runs†. The importance of finding optimal constants cannot be overemphasized although our we will not discuss them in more detail.

There existed another type of production job which used the PASS2 data to make event selection cuts. This allowed a further condensation of data onto DST's (Data Summary Tapes). The DST cuts were more restrictive than the PASS2 cuts and tended to select hadronic, Bhabha, gamma-gamma, and two prong muon events. All of the Mark II hadronic analyzes used the DST data sets (which were often small enough to be stored on disk). Most of the low-multiplicity analyzes used the PASS2 tapes because the DST cuts often had low efficiency for these event categories. Since the DST production code merely outlined a set of selection criteria and did not do any tracking it more closely resembled a user's EVANAL program (see below) than the PASS2 production code, although in practice the DST program also called PASS2 for retracking the events with the most up to date values of the detector constants. The analysis presented in this thesis did not use the DST data sets for the event selection, instead, the results presented here are based upon analysis of the PASS2 data tapes.

The typical Mark II user would run their analysis program using the PASS2 tracklists as input. The user would link a standard analysis library (M2LIB TXTLIB) which contained the routines which supervised and ran the analysis. Since the analysis library routines the bookkeeping work (such as tape I/O, etc.) the user could immediately concentrate on the physics quantities in the tracklist. A main program (M2MAIN) read in events from tape or disk, and filled all the

† Originally, the Mark II analysis consisted of PASS1 and PASS2 production passes with the PASS1 program being responsible for both finding the optimal constants and prefiltering poor quality events out of the data. The constants finding job was later done by individual subsystem stand alone programs, while the prefiltering job was later done by CHUKIT (see the next section).

common blocks with the tracklist information. The raw data for an event was also read into a large array (IRAW) for possible use. After each event was read in the main program called a subroutine, EVANAL, that was provided by the user for their individual analysis.

Due to its importance, the PASS2 program will be described in more detail in this chapter. The discussion is not intended to be definitive, but will provide a brief description of the Mark II tracking routines and offline analysis. More extensive treatments of selected topics will be referenced. Since the single electron signal is extremely sensitive to the PASS2 processing this chapter will serve as a necessary introduction to the PASS2 routines which impact on the single electron search. Later chapters will further discuss certain of these routines. The EVANAL program used in the selectron data analysis will also be discussed in the following chapters. The rest of this chapter will concentrate on PASS2, whose routines and control flow are shown in Fig. 4.1. Only the routines most relevant to the selectron analysis will be described here, *i.e.* the hardware filter, charged tracking and shower reconstruction routines. All the tracking routines are described in Table 4.1. The other subroutines are described in Table 4.2. Finally, the ECODE-SUBCOD event classification scheme can be found in Table 4.3. Tables 4.2 and 4.3 can be found at the end of this chapter.

4.2 Hardware Filter

CHUKIT was a filter routine which utilized the hardware information stored in the raw data to make event selection cuts. It was designed as a much faster replacement to a previous filter known as PASS1. Unlike the older PASS1 filter, which called tracking routines that could consume large amounts of CPU time for junk events, CHUKIT made no tracking calls. This was important in view of the fact that $\simeq$ 90% of the raw data consisted of junk events. CHUKIT, which was sometimes referred to as the hardware filter, made the following cuts:

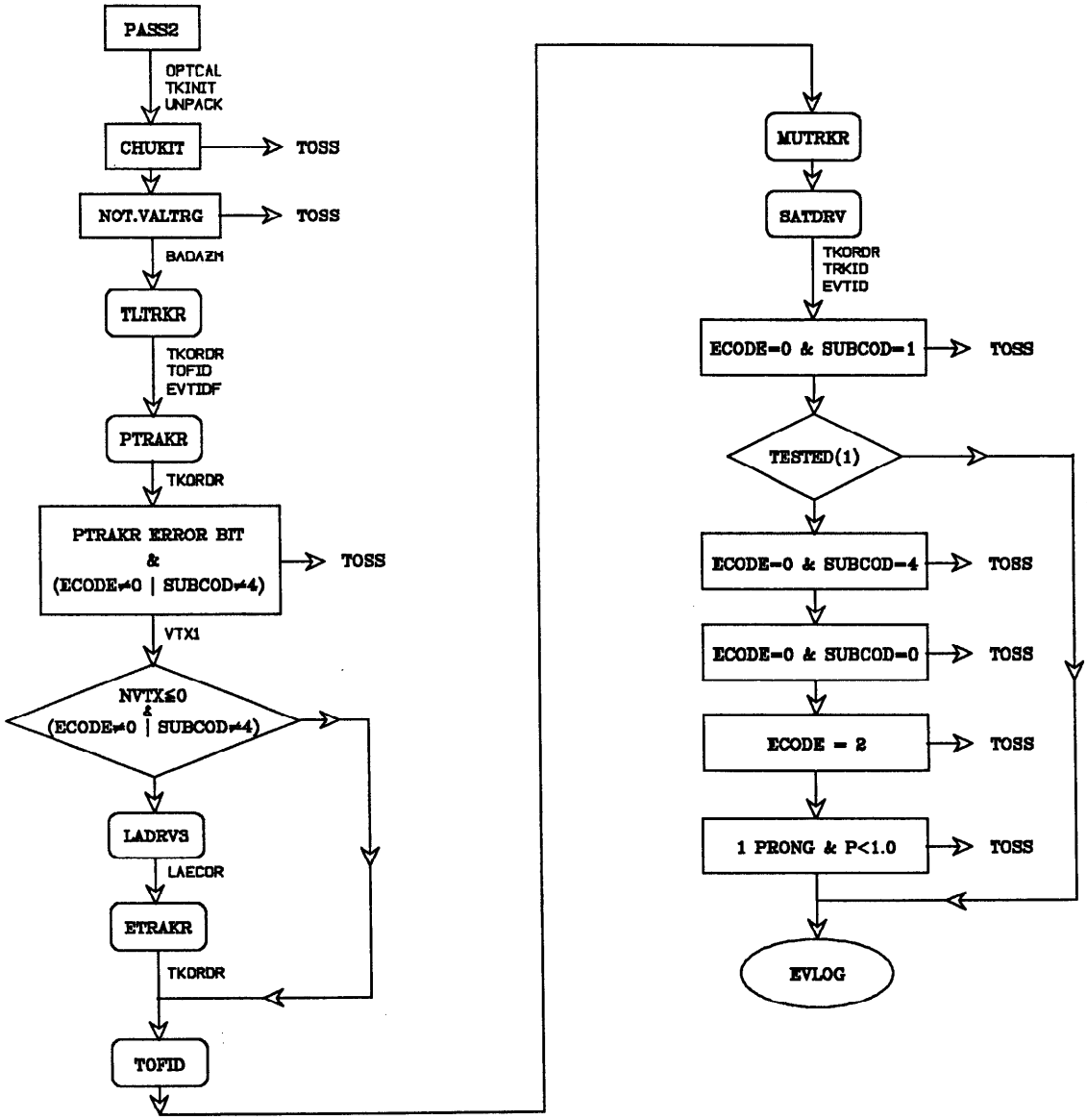

Figure 4.1. Mark II PASS2 Production Code. This figure shows the PASS2 routines and control flow for analyzing events from their raw data. Routines which made selection cuts are shown in boxes, tracking routines are shown in rounded boxes, and logic branch points are shown in diamonds. EVLOG was the routine which recorded a fully PASS2'ed event onto tape. See the text and table 4.1 for a discussion of the tracking routines, see Table 4.2 for the other PASS2 routines. Lastly, see Table 4.3 for a discussion of the ECODE-SUBCOD event classification scheme. Tables 4.2 and 4.3 are at the end of this chapter.

PASS2 TRACKING ROUTINES

Subroutine	Description
TLTRKR	A first pass track finding routine which used the curvature modules for pattern recognition and simple circle fits for track fitting.
TOFID	This routine takes the TOF times and applies the final corrections to them.
PTRAKR	The final charged track finding program. It used piecewise helical track fitting.
LADRV3	Shower reconstruction driver for LA and endcap calorimeters.
ETRAKR	Routine for finding charged tracks which go into the endcaps but were missed by PTRAKR. Associated endcap information with the tracks it found.
MUTRKR	Projects charged tracks from the central drift chambers into the muon chambers looking for linkage with muon hits.
SATDRV	Found the charged tracks in SAT drift chambers. Associated SAT calorimetric energy, if any, with these tracks.

Table 4.1. PASS2 Tracking Subroutines. This table contains a list of the subroutines responsible for tracking in the various hardware subsystems (where tracking can also mean shower reconstruction and timing corrections). These routines formed the heart of the Mark II production code.

- *Selectron Cut.* All events with $N_A = 1$ & $E_{LA} < 4.0$ were tossed. All events with $N_A = 1$ and averaged curvature module within 1.7 units of zero curvature (in curvature module units) were saved; otherwise the 1 A-track events were tossed. The curvature cut is roughly equivalent to a 450 MeV momentum cut.
- *High Multiplicity Cut.* All events with $N_A \geq 4$ were saved.
- *Nonadjacent TED Cut.* Events with $N_A = 0$ and only 1 nonadjacent set of latched LA modules were tossed, all other TED events without any A-tracks were saved.

- *Total Energy Cut.* All events with $N_A \geq 2$ & $E_{SUM} \geq 1.5$ were saved.
- *Tagged SAT Cut.* All events with $N_G \geq 2$ & $E_{SAT} \geq 1.0$ were saved.
- *Coplanar A-track Cut.* All events with at $2 \leq N_A \leq 3$ and at least one A-track with averaged curvature module within 1.7 units of zero curvature, separated by at least 2.14 radians in ϕ from any other A-track, were saved.

N_A refers to the number of A-tracks found by the hardware trigger in the above.

The A-tracks were found with 22 curvature modules, numbered from 1 to 22, which were ordered sequentially from large positive curvature to large negative curvature. The curvature modules covered equal bands of $1/p$ space, where p is the track momentum in GeV. Each curvature module covered 1.379 GeV^{-1} in inverse momentum space, *i.e.* a curvature module unit. Thus, the highest momentum modules roughly covered the region $0.725 \leq p \leq \infty$. The low momentum cutoff for the curvature modules was 60 MeV. Note that several adjacent curvature modules would typically fire for a single track since the charged trigger had a built-in redundancy The raw data recorded all the curvature module read outs for each event. An unbiased hardware estimate of the track's inverse momentum was found by averaging the number of the curvature modules which fired for it and subtracting 11.5 (12 was actually used in the code). The clock time at which the A-track was found was also recorded in the raw data. This time could be directly converted into an azimuthal angle for the track.

CHUKIT used several of the energy quantities available in the raw data. The first of these, E_{LA} (E in GeV), was the raw energy over all eight LA modules. This sum omitted the energy in the back portion of the module, in the T2 and F3 ganged layers. Another calorimetric energy sum, E_{SUM}, was the LA energy sum plus the endcap energy sum. Finally, the quantity E_{SAT} was the energy sum in the SAT system calorimeters.

The impact of the CHUKIT filter on this analysis will be discussed in the next chapter. As is evident, this filter played an important role in selecting the

final data sample available on the PASS2 tapes.

It is very important in particle searches to ensure full efficiency in getting the events from the detector to the final analysis. Almost as importantly as having a fully efficient trigger is having fully efficient analysis cuts, including those made by the production code. This point will be returned to in the next chapter.

4.3 Charged Particle Tracking

Charged particle tracking[63,73] was done in the central drift chambers (DC and VC) by two routines, TLTRKR and PTRAKR†. TLTRKR was used as a first pass to associate DAZM's‡ with a track. TLTRKR used the hardware information from the curvature modules to guide its pattern recognition algorithm and a simple circle fit to find tracks. It had a modest track finding efficiency of 70% and was used primary to help make PTRAKR's job easier. PTRAKR was the final tracking program and gave the highest track finding efficiency, $\sim$ 99%, together with the best momentum resolution. It used a 2 dimensional histogram to do its pattern recognition (one dimension was curvature, the other azimuthal angle). Once the DAZM's for a track were associated, either by TLTRKR or by PTRAKR's own pattern recognition utility, a linear least squares fit to piecewise sections of helixes was done. The piecewise helical approach allowed PTRAKR to account for inhomogeneities in the magnetic field, dE/dx energy losses and multiple scattering effects. The distance scale of the helical pieces was given by the distance between drift chamber layers. There were 6 parameters used to describe the track. One accounted for any multiple Coulombic scattering at the interface between the vertex and drift chambers by allowing for a small kink in the track at this point. The other five parameters described the particle's trajectory

† Another routine, SUPTRK, for SUPer TRacKer, was used in some analyzes instead of PTRAKR. It differed mostly in its pattern recognition algorithms. It was nonstandard, however, and was not used in this analysis.

‡ DAZM stands for Drift AZiMuth. It refers to hit VC or DC sense wires.

at the point of closest approach to the DC origin (which could be "swum" to any point on the tracks trajectory). These parameters, $\{\phi,\ \tan\lambda,\ \kappa,\ \xi,\ \eta\}$, had the following significance:

ϕ was the azimuthal angle of the tangent direction.

$\tan\lambda$ was the tangent of the dip angle, $\lambda = \pi/2 - \theta$.

κ was the track curvature which is given by $1/p\cos\lambda$.

ξ was point of closest approach projected onto the axes perpendicular to both the track direction and the magnetic field.

η was point of closest approach projected onto the direction of the magnetic field.

The drift chamber defined the coordinate system used for charged particle tracking. The two parameters, ξ and η, gave the point of closest approach to the DC origin.

PTRAKR produced an error matrix for each track it found, based upon the expected positional resolution of each measurement (*i.e.* DAZM). The positional resolution depended on where in the drift cell the track went and its direction of motion. This dependence necessitated an iterative approach to track finding in PTRAKR. Up to 23 total space point measurements could be made using both the drift and vertex chambers. The overall transverse momentum resolution, for particles going through all layers in the chambers, was given by

$$\sigma_{p_\perp}/p_\perp = \sqrt{(0.02)^2 + (0.01p_\perp)^2}.$$

The constant term in the square root represents the Coulombic multiple scattering contribution.

4.4 Liquid Argon Shower Reconstruction

The lead-liquid argon calorimeter served two main purposes: to detect photons, and to separate electrons from charged hadrons and measure the

electron's shower energy. The tracking routine responsible for both LA and endcap shower reconstruction[74] was LADRV3. Only the LA reconstruction will be described here, the endcap algorithms were similar.

The dual purpose of the calorimeter translated into two reconstruction algorithms. The first was to associate shower energy with charged tracks. This was done by utilizing the charged tracking information from the central drift chambers. Thus, in PASS2, LADRV3 is called after PTRAKR. The charged track shower reconstruction began by projecting all charged tracks found in an event into the LA system. The algorithm started by finding the largest pulse height sum for 2 or 3 adjacent strips (depending on layer) in a layer. All contiguous strips adjacent to these strips were then added in. If the distance from the largest pulse height to the projected position of the charged track was less than some maximum distance (determined empirically), then the energy in these groups of strips was associated with the charged track. It should be noted that a minimum ionizing particle was expected to deposit 200-400 MeV of energy in a LA module from dE/dx losses.

The second reconstruction technique worked independently of the charged track information and did its own pattern recognition to find clusters of strips which formed photons. Several different algorithms were used because of the desire to maintain good efficiency for detecting low energy photons with the minimum of fakes. Fake photons could easily be found in the LA system because of fluctuations above threshold in the electronic noise on the readout channels. Recall that the threshold for the LA channels was 1 σ of the rms spread in pedestal noise. Incoherent correlated up fluctuations could give rise to fake clusters which simulated real low energy photon events. Typical rms noise fluctuations (in units of collected energy) were 0.3-0.4 MeV in the massless gap, 2.5-3.0 MeV in F3, and 0.8-1.2 in the other layers. Real photons with an energy of 200 MeV typically deposited energies of $\sim$ 2 MeV/channel, photons above 1 GeV deposited energies above 10 MeV/channel. The basic cluster algorithm would find unassociated

strips with signals above 2 σ in noise and build groups on either side. The group building would end if any of the following was true:

- A blank channel was found (one blank channel was allowed if it was a dead channel) or a "valley" between peaks.
- The module boundary was reached.
- A maximum (energy dependent) number of strips have been associated in the group.
- A signal of less than 2 σ_{noise} was found. This strip would still be added to the group if the group had less than the maximum allowed.

The group energy centroid and width were then calculated from the pulse height measurements.

These groups were then used in the shower reconstruction. Several different algorithms were used for photon finding (four in total). The main algorithm for finding photons (over 80% of the photons were found with this algorithm) was as follows:

- A crossing of F1 and/or F2, U, and T1 strips, forming what was called a cluster. The crossing tolerance was gotten by requiring the F and T crossing be within 1.5 strip widths of the hit U strip (3 strip widths in the corners of the module where the U strips were ganged).
- The energy sum over the F, U, and T layers used in finding the cluster, E_{sum}, was required to satisfy $E_{sum} > 7\ \text{MeV} + N_{channels} * 1\text{MeV}$. $N_{channels}$ was the number of channels used in finding the cluster.

Other algorithms were used which attempted to compensate for down fluctuations in energy deposition in a layer while requiring the correlations in lateral and longitudinal shower development found in real showers. These algorithms will not be described here, they can be found in Ref. 74. The energy corrections for ionization loss, radiative loss in the coil, and leakage out the back of the module are described there as well. The average resolution of the liquid argon calorimeter was given by $\sigma_E/E \simeq 14.5\%/\sqrt{E}$ (E in GeV).

PASS2 NON-TRACKING ROUTINES

Subroutine	Description
OPTCAL	Corrected the ϕ position of the drift chamber wires.
TKINIT	Initialized program memory prior to track finding.
UNPACK	Unpacked the raw data into various common blocks from the I/O buffer.
CHUKIT	Hardware filter for fast event selection based on raw data information.
VALTRG	Used to validate event trigger with the trigger programmed into MICKEY. Useful for online monitoring during data taking.
BADAZM	Eliminated bad dazms from the tracking pool. These dazms either had unphysical times or too many dazms adjacent within the layer. The latter case signifies an electronics problem.
TKORDR	Sorted the tracklist so that charged tracks came first, and neutrals last.
EVTIDF	Similar to EVTID, in fact, it was an entry in EVTID. Classified events according to multiplicity, topology, and particle content. Set ECODE and SUBCOD. Note that EVTIDF set ECODE, SUBCOD to (0,4) for 0 prong TED triggers.
VTX1	Found the primary event vertex by searching within a large fiducial volume centered on DC zero (which should be have been near the IP or interaction point).
LAECOR	Applied energy corrections to showers tracks found by LADRV3.
TRKID	Provided a set of weights for the particle id based upon the available subsystem information.
EVTID	See EVTIDF description. Also see the Table 4.3.
TESTED	Checked for a TED trigger with two back to back latched TED modules.

Table 4.2. PASS2 Non-tracking Subroutines. This table shows all the subroutines in PASS2 that were not driver routines for the hardware subsystems.

ECODE/SUBCOD/EVID CLASSIFICATION SCHEME

ECODE	SUBCOD	EVID	MNEMONIC	DESCRIPTION
0 GARBAGE	0	0	NO VTX	other no vertex
	1	0	BM BURP	beam burp, no vertex
	2	0	NO TRIG	illegal trigger (VALTRG=.FALSE.)
	3	0	COPL 2B	>1 B tracks, 2 of which are coplanar to 20 degrees, no vertex
	6	0	FLT LRGZ	all TLTRKR prongs with $-0.3 < z < 0.3$ m, NCHRG = NATRKS, filtered
1 COSMIC	0	0	GOOD TDC	good cosmic - good tdc's
	1	0	NO TDC	assumed cosmic: collinear with bad tdc's
	2	0	> 2P	good cosmic in 3 or more prong
	3	0	1P IR	cosmic with 1 prong in I.R.
	4	0	LRGE ANG	acollinearity angle between 10 and 57 degrees, cosmic time
	5	0	1P NONIR	cosmic with 1 prong not in I.R.
	6	0	FLT CSMC	good cosmic found with TLTRKR, filtered
2 WALL	0	0	2P PIPE	2 prongs with vertex at pipe radius
	1	0	> 2P PIPE	3 or more prongs with vertex at pipe
	2	0	1P PIPE	1 prong with vertex at pipe
	3	0	LARGE Z	any number of prongs, $-0.3 < z < 0.3$ m
	4	0	LARGE R	any number of prongs, $r > 1.4$ m
	5	0	NP PIPE	all neutral prong, vertex at pipe

Table 4.3. ECODE-SUBCOD Classification Scheme. This table shows the ECODE-SUBCOD event classification scheme used by Mark II. The ECODE provided six general event categories which were further divided by the SUBCOD. Note that EVID was set to 3 for any event with a SAT secondary Bhabha trigger (G-bit in MICKEY).

ECODE	SUBCOD	EVID	MNEMONIC	DESCRIPTION
3 EE QED	0	1	NORM EE	normalizing bhabha
	1	0	OTHR EE	2 e's, good tdc's, not normalizing
	2	0	CHG2/TDC	2 e's, bad tdc's or charge 2
	3	0	> 2P	multiprong bhabha
	4	0	E-X	2 prongs, coplanar, 1 e
	5	0	GAM GAM	γ opposite converted γ, or all γ's
	6	0	1P LOST	1 e prong with shower opposite
	7	0	QED NOLA	normalizing QED-type event, not in LA fiducial volume
	8	3	SAT EE	G bit is only bit on in secondary trigger
4 MU PAIR	0	2	NM MU MU	normalizing μ pair
	1	0	OT MU MU	other μ pair, 2 collinear prongs, not normalizing
	2	0	MU-X	2 coplanar prongs: 1 μ, other non-e
	3	0	1P LOST	1 prong with a non-e LA track opposite
	4	0	> 2P	multiprong μ-pair
5 HADRON	0	0	> 2P	3 or more prongs in I.R.
	1	0	NCOPL 2P	noncoplanar charge-0 2-prong, not e's
	2	0	CHRG2 2P	charge-2 2-prong
	3	0	NEUT,+1P	1 or more neutral prongs in I.R., not all γ's, or 1 prong plus neutrals
	4	0	> 2P+XTRA	3 or more prongs in I.R. plus extra nearby prongs
	5	0	2P+XTRA	2 prongs in I.R. plus extra nearby prongs or coplanar charge-0 2-prong with neutral
	6	0	1P+XTRA	1 prong in I.R. plus extra nearby prongs

Table 4.3 (Continued).

ECODE	SUBCOD	EVID	MNEMONIC	DESCRIPTION
6 UNKNOWN	0	0	VTX FAIL	poor xyz match for 2 prongs or vertex fit failed for > 2 prongs
	1	0	1P	1 prong in I.R.
	2	0	4-6 NCOP	noncoplanar 2-prong with $4 < r < 6$ cm
	3	0	R>15 cm	vertex at $r > 15$ cm
	4	0	4-6 NP	3 or more prongs with $4 < r < 6$ cm
	5	0	4-6 COPL	coplanar 2-prong with $4 < r < 6$ cm
	6	0	COSMIC?	probable cosmic (collinear pair with no tdc information in a multiprong or collinear charge-2 2-prong with no tdc information)
	7	0	0-4 2P	coplanar charge-0 2-prong, no e or μ, or 1-prong with opposite-charge nearby track coplanar with it
	8	0	NEUT	1 converted γ in I.R. or any number of neutral prongs not in I.R. or pipe

Table 4.3 (Continued).

Chapter 5. Selectron Monte Carlo Generator

5.1 The Physics of Single Selectron Production

The original reference for this process is the 1982 paper by M.K. Gaillard, I. Hinchliffe, and L. Hall[48]. This paper was used in the original selectron search[76], published by the Mark II collaboration in 1983. These early results were limited by the assumption of massless photinos. A 1984 paper by T. Koyayashi and M. Kuroda[77] calculated single selectron production as a function of both selectron and photino masses. This latter paper served as the source for all the cross section equations used in the construction of the selectron Monte Carlo generator described below.

5.1.1 Kinematics

The kinematics of single selectron production and detection center around the process $e^- + \gamma \rightarrow \ \tilde{e}^- + \tilde{\gamma}$ (note– charge conjugate processes are implied throughout this discussion). The photons are radiated off the positrons, and, using the Weiszäcker-Williams approximation[78]†, have the following energy spectrum:

$$\mathrm{F}(y)\,dy = \frac{\alpha}{\pi y}\left[1 + (1-y)^2\right] \ln\left(\frac{\mathrm{E_B}}{m_e}\right) dy$$

where,

$\mathrm{F}(y)\,dy$	is the number of photons in the interval dy
y	is the fraction of incident energy carried off by the photon, such that $\mathrm{E}_\gamma = y\mathrm{E_B}$
$\mathrm{E_B}$	is the beam energy
m_e	is the electron mass (which is hereafter neglected in comparison to the selectron or photino masses, $m_{\tilde{e}}$ and $m_{\tilde{\gamma}}$, respectively).

† Also known as the EPA or equivalent photon approximation.

Notice that for small values of y, $F(y)$ has the typical $1/k$ bremsstrahlung spectrum. The photons travel in the same direction as the incident as the incident radiating particle, which is taken to be the $+z$-axis for positrons†, in our treatment of the Weiszäcker-Williams approximation‡.

The photon and electron may be thought to fuse into an intermediate state with invariant mass $\sqrt{\hat{s}}$, where $\hat{s} = ys$, s being the center of mass energy squared of the original electron–positron system. This intermediate state then undergoes a two-body decay into a selectron and photino. In the collision center of mass frame (the CM frame), the intermediate state is at rest and the selectron and photino come out back to back with a fixed momentum given by:

$$|\hat{\mathbf{p}}| = \frac{1}{2}\sqrt{\frac{\lambda s}{y}}\,. \qquad \left(\begin{array}{c}\text{Note - all quantities in CM frame are denoted with hats,}\\ \text{and all 3-vectors are denoted by boldface letters.}\end{array}\right)$$

We take λ to be a dimensionless function of the dimensionless quantities: y, $\chi_{\tilde{e}} = m_{\tilde{e}}^2/s$, and $\chi_{\tilde{\gamma}} = m_{\tilde{\gamma}}^2/s$, as follows:

$$\lambda = \lambda(y, \chi_{\tilde{e}}, \chi_{\tilde{\gamma}}) = (y - y_+)(y - y_-)$$

---

† Note that this convention is standard in most Monte Carlos, but opposite the actual situation in the Mark II detector.

‡ Although this assumption is in widespread use in the literature (*e.g.* in Refs. 48, 77, and 79), it is overly restrictive, as was pointed out by D. Karlen after the completion of this work. A better approximation would allow the photon to have finite q^2, *i.e.* to be radiated at an angle with respect to the incident direction. The formula for this case is derived in Ref. 80. When the photon's angle is integrated out, we arrive at the following integrated photon energy spectrum:

$$F(y) = \frac{\alpha}{\pi}\left[\frac{[1+(1-y)^2]}{y}\ln\left(\frac{q^2_{\max}}{q^2_{\min}}\right) - 2m_e^2 y^2\left(\frac{1}{q^2_{\min}} - \frac{1}{q^2_{\max}}\right)\right].$$

The maximum q^2 is determined by the veto angle for the positron. Since the Mark II SAT system veto was at 2°, the above formula indicates that the photon spectrum was overestimated by 40%.

where,

$$y_+ = (\sqrt{\chi_{\tilde{e}}} + \sqrt{\chi_{\tilde{\gamma}}})^2$$
$$y_- = (\sqrt{\chi_{\tilde{e}}} - \sqrt{\chi_{\tilde{\gamma}}})^2$$

and,

$$y_+ \geq y_- \ .$$

This is a convenient form to use because it emphasizes the dependence on y explicitly. For instance, the above form automatically gives the threshold value of y for selectron–photino production, $y \geq y_+ \equiv y_{\rm thres}$, since for $|\hat{\mathbf{p}}|$ to be real we must have $\lambda \geq 0$.

The collision center of mass system is related to the lab frame by Lorentz boost along the $-z$-axis with boost parameters given by:

$$\beta = \frac{1-y}{1+y} \qquad \gamma = \frac{1+y}{2\sqrt{y}} \ .$$

Notice that for $y = 0$, $\beta = 1$ as expected when m_e is set to zero, and that for $y = 1$, $\beta = 0$ since the lab frame is the same as the CM frame. The two frames have different views of the collision, see Fig. 5.1 (a) and (b).

The 4-momentum of the incident particles in the two systems are as follows:

$$p_e = (\mathrm{E_B},\ 0,\ 0,\ -\mathrm{E_B}) \qquad p_\gamma = (y\mathrm{E_B},\ 0,\ 0,\ y\mathrm{E_B})$$
$$\hat{p}_e = (\sqrt{y}\,\mathrm{E_B},\ 0,\ 0,\ -\sqrt{y}\,\mathrm{E_B}) \qquad \hat{p}_\gamma = (\sqrt{y}\,\mathrm{E_B},\ 0,\ 0,\ \sqrt{y}\,\mathrm{E_B}).$$

Of more use are the Mandelstram variables $\hat{s}$, $\hat{t}$, and $\hat{u}$, which enter into the

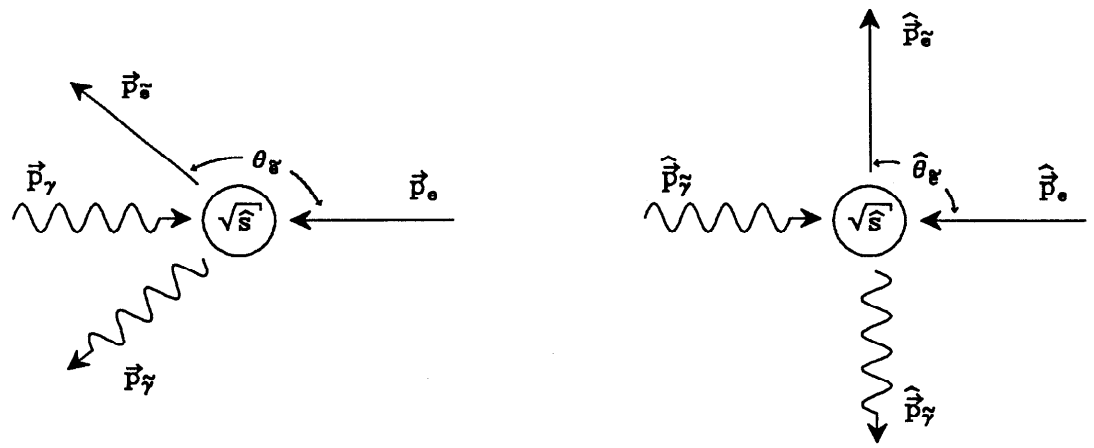

a) LAB frame b) CM frame

Figure5.1. Single Selectron Production in Lab and CM Frames.

invariant matrix elements. These relativistic invariants are given by:

$$\begin{aligned}
\hat{s} = (p_e + p_\gamma)^2 = (p_{\tilde{e}} + p_{\tilde{\gamma}})^2 &= ys \\
\hat{t} = (p_{\tilde{e}} - p_\gamma)^2 = (p_{\tilde{\gamma}} - p_e)^2 &= m_{\tilde{e}}^2 - \sqrt{ys}(\hat{\mathrm{E}}_{\tilde{e}} - |\hat{\mathbf{p}}_{\tilde{e}}| \cos\hat{\theta}_{\tilde{e}}) \\
&= m_{\tilde{e}}^2 - y\sqrt{s}(\mathrm{E}_{\tilde{e}} - |\mathbf{p}_{\tilde{e}}| \cos\theta_{\tilde{e}}) \\
\hat{u} = (p_{\tilde{e}} - p_e)^2 = (p_{\tilde{\gamma}} - p_\gamma)^2 &= m_{\tilde{e}}^2 - \sqrt{ys}(\hat{\mathrm{E}}_{\tilde{e}} + |\hat{\mathbf{p}}_{\tilde{e}}| \cos\hat{\theta}_{\tilde{e}}) \\
&= m_{\tilde{e}}^2 - y\sqrt{s}(\mathrm{E}_{\tilde{e}} + |\mathbf{p}_{\tilde{e}}| \cos\theta_{\tilde{e}}).
\end{aligned}$$

Because of the well known relation,

$$\hat{u} + \hat{s} + \hat{t} = m_{\tilde{e}}^2 + m_{\tilde{\gamma}}^2 + m_e^2 + m_\gamma^2 \approx m_{\tilde{e}}^2 + m_{\tilde{\gamma}}^2,$$

the three variables are not independent, and $\hat{u}$ can be eliminated in favor of $\hat{s}$ and $\hat{t}$. Whereas $\hat{s}$ is strictly a function of y (and of s), the $\hat{t}$ variable is a function of y and $\cos\hat{\theta}_{\tilde{e}}$ (or $\cos\theta_{\tilde{e}}$), and so contains all the angular dependence. Notice also that the $\hat{t}$ variable connects the selectron and photon, or alternatively the photino and electron, as does the t-channel Feynman graph (with the virtual selectron connecting the external lines).

The selectron Monte Carlo produces the particles according to the CM frame distributions. However, the differential cross section given in equation 7 of Kobayashi and Kuroda is written in terms of the lab frame variables. And although the total cross section (a relativistic invariant) given in equation 6 of the above paper is the same for both frames, the angular distributions in the two frames differ. In order to extract the angular distribution in the CM frame then, a further understanding of the collision kinematics is necessary.

For photons of a given energy, or equivalently, fixed y, the differential cross section can be written as $d\sigma_y/d\cos\theta\,(\cos\theta, y)$, or as $d\hat{\sigma}_y/d\cos\hat{\theta}\,(\cos\hat{\theta}, y)$, depending upon which coordinate system is used. (The angles and cross sections without explicit subscripts for particle identification hereafter refer to the selectron). Of course, $d\sigma_y = d\hat{\sigma}_y$ since the Lorentz boost is along the incident particle's direction. The subscript y reminds us that we are talking about photons at a fixed energy. In order to convert $d\sigma_y/d\cos\theta\,(\cos\theta, y)$ into $d\hat{\sigma}_y/d\cos\hat{\theta}\,(\cos\hat{\theta}, y)$ not only must the angle mapping $\cos\theta \rightleftharpoons \cos\hat{\theta}$ be known, but so must the Jacobian of the angle transformation. This Jacobian, J, will be a function of angle and boost, the latter being equivalent to y, so that we have

$$J(\cos\theta, y) = \left|\frac{d\cos\hat{\theta}}{d\cos\theta}\right| .$$

Then, using the chain rule we have†

$$\frac{d\sigma_y}{d\cos\theta} = \left|\frac{d\cos\hat{\theta}}{d\cos\theta}\right| \frac{d\hat{\sigma}_y}{d\cos\hat{\theta}} = J(\cos\theta, y)\frac{d\hat{\sigma}_y}{d\cos\hat{\theta}} .$$

† There is one subtlety which should be mentioned. For certain values of y and $\cos\theta$ the mapping from lab frame angle to CM frame angle is double valued. This is because the momentum ellipse in the lab frame is completely in one hemisphere and a ray drawn at a fixed angle will cross it twice (although the lab momenta will be different the angles will be the same). This fact is used in Kobayashi and Kuroda's paper but is not commented upon directly. All equations which follow that involve this double valued transformation are understood to have a sum over both CM angles.

The total selectron production cross section is then found by summing the product of the photon flux with the differential cross section, at a given energy, over the kinematically allowed region. This gives the following form for the selectron differential cross section:

$$\begin{aligned}\frac{d\sigma}{d\cos\theta}(\cos\theta) &= \int_{y_{\min}}^{1} dy\, \mathrm{F}(y)\, \frac{d\sigma_y}{d\cos\theta}(\cos\theta, y) \\ &= \int_{y_{\min}}^{1} dy\, \mathrm{F}(y)\, J(\cos\theta, y) \frac{d\hat{\sigma}_y}{d\cos\hat{\theta}}(\cos\hat{\theta}, y).\end{aligned}$$

The exact expression for the Jacobian can be found in the discussion of two body kinematics in Appendix A. Since we know the form of $J(\cos\theta, y)$ we can compare the above formula with equation 7 of Kobayashi and Kuroda in order to extract the angular differential cross section in the CM frame.

The kinematic cutoff, $y_{\min}$, is not only a function of particle masses, but also of selectron angle, $y_{\min} = y_{\min}(\cos\theta, \chi_{\tilde{e}}, \chi_{\tilde{\gamma}})$. Its exact form is of interest in itself, and is derived in the appendix, however, it is not relevant to the actual construction of the selectron Monte Carlo. The same is true of the Jacobian. The appendix contains a deeper discussion of the two body collision process, however, our discussion ends at this point since we now know how to extract $d\hat{\sigma}_y/d\cos\hat{\theta}$ from the Kobayashi and Kuroda paper.

5.1.2 Production Cross Sections

The total production cross section is found in equation 6 of Kobayashi and Kuroda. It has the following form:

$$\sigma_{\mathrm{tot}} = \int_{y_{\mathrm{thres}}}^{1} dy\, \mathrm{F}(y) \frac{\alpha^2\pi\sqrt{\lambda}}{2sy^2}\left[1 + 7\left(\frac{m_{\tilde{e}}^2 - m_{\tilde{\gamma}}^2}{\hat{s}}\right) + 4\frac{(m_{\tilde{e}}^2 - m_{\tilde{\gamma}}^2)(\hat{s} + m_{\tilde{e}}^2 - m_{\tilde{\gamma}}^2)}{\hat{s}\sqrt{\lambda s^2}} \times \ln\left|\frac{\sqrt{\lambda s^2} - (\hat{s} + m_{\tilde{e}}^2 - m_{\tilde{\gamma}}^2)}{\sqrt{\lambda s^2} + (\hat{s} + m_{\tilde{e}}^2 - m_{\tilde{\gamma}}^2)}\right|\right]$$

where,

$$\hat{s} = ys, \qquad \chi_{\tilde{e}} = m_{\tilde{e}}^2/s, \qquad \chi_{\tilde{\gamma}} = m_{\tilde{\gamma}}^2/s$$

$$y_+ = (\sqrt{\chi_{\tilde{e}}} + \sqrt{\chi_{\tilde{\gamma}}})^2, \quad y_- = (\sqrt{\chi_{\tilde{e}}} - \sqrt{\chi_{\tilde{\gamma}}})^2, \quad y_{\text{thres}} = y_+$$

$$\lambda = \lambda(y, \chi_{\tilde{e}}, \chi_{\tilde{\gamma}}) = (y - y_+)(y - y_-)$$

$$\mathrm{F}(y) = \frac{\alpha}{\pi y}\left[1 + (1-y)^2\right] \ln\left(\frac{\mathrm{E_B}}{m_e}\right).$$

As mentioned in the section on kinematics, we can extract the differential cross section with respect to CM frame variables from equation 7 of Koybayashi and Kuroda, even though they give the cross section in terms of lab frame variables. Thus, conforming with the notation introduced in the last section, we have:

$$\frac{d\hat{\sigma}_y}{d\cos\hat{\theta}} = \frac{\alpha^2\pi\sqrt{\lambda}}{2sy^2}\left(1 + \frac{\hat{t} + m_{\tilde{e}}^2 - 2m_{\tilde{\gamma}}^2}{\hat{s}} + \frac{2(m_{\tilde{e}}^2 - m_{\tilde{\gamma}}^2)(\hat{s} + m_{\tilde{e}}^2 - m_{\tilde{\gamma}}^2)}{\hat{s}(\hat{t} - m_{\tilde{e}}^2)} + \frac{2m_{\tilde{e}}^2(m_{\tilde{e}}^2 - m_{\tilde{\gamma}}^2)}{(\hat{t} - m_{\tilde{e}}^2)^2}\right).$$

Since we are in the CM frame the kinematic threshold does not depend on the angle of the selectron, its value is simply the constant y_{thres}. Thus the differential cross section in the CM frame is:

$$\frac{d\hat{\sigma}}{d\cos\hat{\theta}}(\cos\hat{\theta}) = \int_{y_{\text{thres}}}^{1} dy\, \mathrm{F}(y) \frac{d\hat{\sigma}_y}{d\cos\hat{\theta}}(\cos\hat{\theta}, y)\,.$$

It should be remarked here that this y integration is done numerically in the selectron Monte Carlo with the QAGS integrator (see reference in Monte Carlo Technique section).

The above cross section was used to generate the Monte Carlo events, and so, all the events were generated in the CM frame and then boosted back into the lab frame. This procedure was far superior to generating the events directly in the lab frame for several reasons:

- The form of the differential cross section is much simpler in the CM frame; in fact, the cross section in the lab frame uses the angle Jacobian, which is divergent near the kinematic threshold. So, even though this divergence is cancelled by the $\sqrt{\lambda}$ threshold factor, a straight-forward numerical integration over y is not possible (this was tried).
- The lab frame threshold factor, $y_{\min}$, depends on angle and is somewhat involved.
- The lab frame selectron momentum is double valued for certain values of y and $\cos\theta$ (there are two solutions on the momentum ellipse).
- Most importantly, the presence of the Jacobian function prevents an analytic integration over $\cos\theta$ for the lab frame differential cross section, whereas the CM frame differential cross section can be integrated directly over $\cos\hat{\theta}$.

These facts are mentioned here because of their relevance to the current discussion of kinematics, but they somewhat anticipate the discussion of the section on Monte Carlo construction.

At this point another very important point should be made. The above cross sections are only for $\tilde{e}_R$ production, that is, only for selectrons which are the partner of the right-handed helicity state of the electron. Kobayashi and Kuroda decided, with a certain loss of generality, that $m_{\tilde{e}_R} \ll m_{\tilde{e}_L}$, where $\tilde{e}_L$ is the supersymmetric partner of the left-handed helicity state of the electron. In order for this experimental search to be as general as possible both the mass degenerate case, $m_{\tilde{e}_R} = m_{\tilde{e}_L}$, and the mass nondegenerate case, $m_{\tilde{e}_R} \ll m_{\tilde{e}_L}$, were considered. Since $\tilde{e}_R^-$ only couples to e_{R}^-, and $\tilde{e}_L^-$ only couples to e_{L}^-, both initial and final states for $\tilde{e}_R^-$ and $\tilde{e}_L^-$ production will be different, so that the two cross sections are to be added for the degenerate mass case (*i.e.* no interference). The left and right partners have the same differential cross section if they have the same masses. This is due to a combination of parity and rotational invariance,

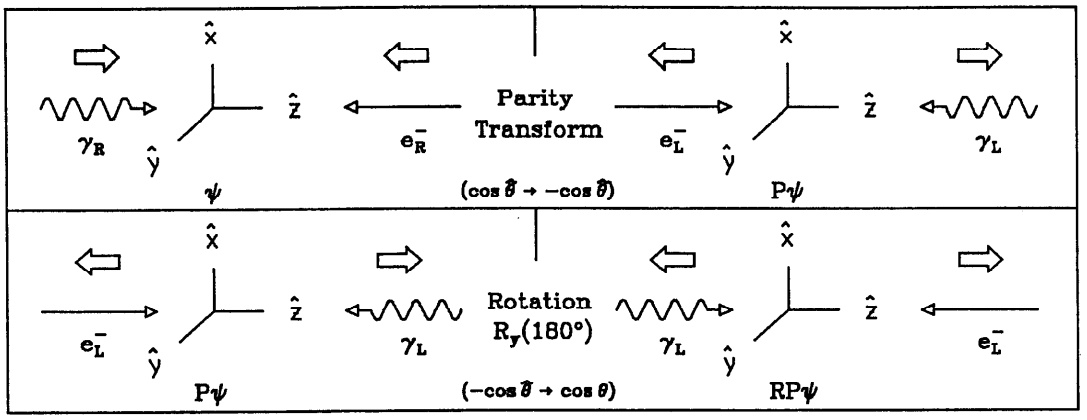

Figure 5.2. Mirror Inversion of Selectron Production. The upper half of the diagram shows a parity transformation on an l initial state with a right-handed electron. The helicity (or spin), shown by the large arrow, reverses under this transformation. The lower half of the diagram shows a rotation of 180° about y of the parity transformed state. The final state is then the mirror image of the initial state and involves a left-handed electron. Note that polar angles remain invariant.

i.e. mirror invariance. Parity is an invariant in supersymmetry (SUSY), unless additional interactions, such as $SU(2)_L$, give $\tilde{e}_R$ and $\tilde{e}_L$ different masses. Thus, starting with an incident e_R^-, we can do a mirror transformation and get e_L^- traveling in the same direction. Hence, the final states will also be related by a mirror transformation, and if the reaction is invariant under such a transformation the angular distribution must be the same, since a mirror transformation with respect to the y-z plane leaves $\cos\theta$ invariant, see Fig. 5.2.

The angular distributions themselves are not necessarily symmetric in $\cos\hat{\theta}$ however, because the initial states do indeed have a direction attached to them. This leads to a definite asymmetric angular distribution for both $\tilde{e}_R$ and $\tilde{e}_L$. From this feature of SUSY a general property of Yukawa couplings can be shown (where a Yukawa coupling means that a scalar particle comes off the fermion line; here the scalar particle is the selectron and the fermion line is the electron-photino line). We begin by comparing QED with SUSY. The analogy between the two theories is well known, but it is not applicable to the spin structure of the vertices,

only to the strengths of the couplings. Hence, while the QED vertex is helicity preserving, the SUSY vertex is helicity reversing. To show this, consider the two theories, with the two processes given by the two different interaction Lagrangians:

$$\begin{array}{lll} \text{QED} & e^- \to e^- + \gamma & \mathcal{L}_{\text{int}} = -e\bar{\psi}_e \gamma_\mu \chi_e A^\mu \\ \text{SUSY} & e^- \to \tilde{e}^- + \tilde{\gamma} & \mathcal{L}_{\text{int}} = -e\bar{\psi}_{\tilde{\gamma}} \chi_e \varphi_{\tilde{e}} \end{array}$$

Where χ is the initial state spinor wave function, ψ is final state spinor wave function, and A is the photon field, while φ is the scalar field. Note that in the QED vertex the fermions are joined by a gamma matrix, whereas this is not the case for the SUSY vertex. Therein is the essential difference in the spin structure of the two theories.

Next suppose that the incoming electron is right-handed, then we can write χ_e^{R} for its wave function. For ultra-relativistic particles the right-handed chiral projection operator is $(1+\gamma_5)/2$, where γ_5 is the hermitian pseudo-scalar operator. Then we can examine the helicity structure of the QED vertex by introducing the projection operator into $\mathcal{L}_{\text{int}}$ and looking only at spinor components (recall that γ_5 anticommutes with γ_μ):

$$\begin{aligned} \bar{\psi}_e \gamma_\mu \chi_e^{\text{R}} &= \bar{\psi}_e \gamma_\mu \left(\frac{1+\gamma_5}{2}\right) \chi_e^{\text{R}} = \bar{\psi}_e \left(\frac{1-\gamma_5}{2}\right) \gamma_\mu \chi_e^{\text{R}} \\ &= \psi_e^\dagger \gamma_0 \left(\frac{1-\gamma_5}{2}\right) \gamma_\mu \chi_e^{\text{R}} = \psi_e^\dagger \left(\frac{1+\gamma_5}{2}\right) \gamma_0 \gamma_\mu \chi_e^{\text{R}} \\ &= \left[\left(\frac{1+\gamma_5}{2}\right) \psi_e\right]^\dagger \gamma_0 \gamma_\mu \chi_e^{\text{R}} = \bar{\psi}_e^{\text{R}} \gamma_\mu \chi_e^{\text{R}} \,. \end{aligned}$$

And so, the helicity preserving nature of the QED vertex is apparent. On the other hand, the SUSY interaction Lagrangian is due to a Yukawa coupling and not a vector coupling. Therefore, no gamma matrices can appear in $\mathcal{L}_{\text{int}}$ since the fields have no space-time indices to contract against. For SUSY, $\mathcal{L}_{\text{int}} = -e\bar{\psi}_{\tilde{\gamma}} \chi_e \varphi_{\tilde{e}}$,

and the two fermions are the photino and the electron. Now, this is not the true interaction Lagrangian since the selectron comes in two varieties, $\tilde{e}_R^-$ and $\tilde{e}_L^-$, which couple to different electron wave functions. Thus, we should have written $\mathcal{L}_{\rm int} = -e(\bar{\psi}_{\tilde{\gamma}}\chi_e^{\rm R}\varphi_{\tilde{e}_R} + \bar{\psi}_{\tilde{\gamma}}\chi_e^{\rm L}\varphi_{\tilde{e}_L})$ down immediately. But I wanted to keep the analogy with QED clear up till now, when the difference becomes immediately obvious; there is no extra γ_μ factor to anti-commute with, so the chirality operator changes handedness in going from intial to final state operators, for instance:

$$\bar{\psi}_{\tilde{\gamma}}\chi_e^{\rm R}\varphi_{\tilde{e}_R} = \bar{\psi}_{\tilde{\gamma}}^{\rm L}\chi_e^{\rm R}\varphi_{\tilde{e}_R}.$$

So, Yukawa couplings involve a helicity flip, unlike vector couplings.

This structure of SUSY has some important consequences on the experimental search. Suppose we have an electron and photon collide to produce a photino and selectron, and suppose further that we only consider the forward and backward scattering of the selectron. Since the final state contains a scalar and spin-$\frac{1}{2}$ object going back to back, it must have an angular momentum of $\frac{1}{2}\hbar$. If a $\tilde{e}_R$ is produced the incident electron must be right-handed and so, from angular momentum considerations the incoming photon must be polarized with the same handedness. Thus, we have the two cases shown in Fig. 5.3.

The photino's helicity is also determined from angular momentum considerations. However, when the helicity-flip nature of SUSY is considered process (a) is seen to be disallowed, and process (b) allowed. This explains the angular distribution observed for massless photinos seen in Fig. 5.4.

To finish this section I would like to point out another unusual feature in the angular distribution for low mass selectrons. Recall that there are two Feynman graphs leading to single selectron production, see Fig. 5.5. The origin of the terms

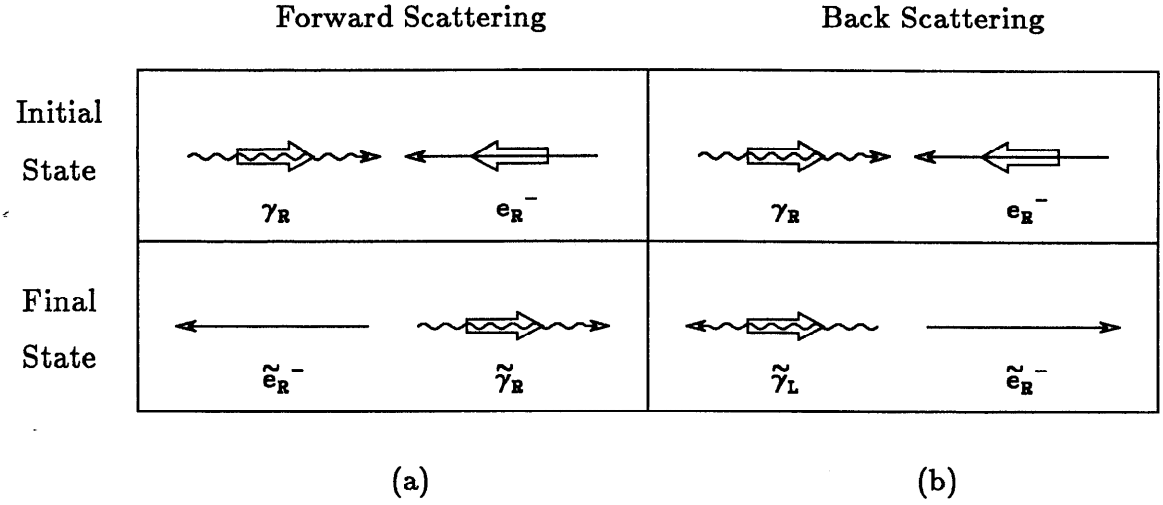

Figure 5.3. Forward–Backward Selectron Production. The helicities of initial and final states in selectron production. Two cases are considered, forward and backward production of $\tilde{e}_R^-$. The wide arrows show the helicities of all particles involved.

in $d\hat{\sigma}_y/d\cos\hat{\theta}$ can be traced to these two graphs as follows:

$$\frac{d\hat{\sigma}_y}{d\cos\hat{\theta}} = \frac{\alpha^2\pi\sqrt{\lambda}}{2y^2 s}\Bigg(\underbrace{1+\frac{\hat{t}+m_{\tilde{e}}^2-2m_{\tilde{\gamma}}^2}{\hat{s}}}_{\text{s-channel}} + \underbrace{\frac{2(m_{\tilde{e}}^2-m_{\tilde{\gamma}}^2)(\hat{s}+m_{\tilde{e}}^2-m_{\tilde{\gamma}}^2)}{\hat{s}(\hat{t}-m_{\tilde{e}}^2)}}_{\text{s- and t- channel interference}} + \underbrace{\frac{2m_{\tilde{e}}^2(m_{\tilde{e}}^2-m_{\tilde{\gamma}}^2)}{(\hat{t}-m_{\tilde{e}}^2)^2}}_{\text{t-channel}}\Bigg)$$

Note that $\hat{t}-m_{\tilde{e}}^2 = -\sqrt{\hat{s}}\,(\hat{\mathrm{E}}_{\tilde{e}} - |\hat{\mathrm{p}}_{\tilde{e}}|\cos\hat{\theta})$, so that the interference term is always negative, unlike the pure s- and t-channel terms which are always positive, when $m_{\tilde{e}} > m_{\tilde{\gamma}}$. Now, for small values of $m_{\tilde{e}}$ the selectron can be extremely relativistic, so that as $\cos\hat{\theta} \to +1$, we have $(\hat{t}-m_{\tilde{e}}^2) \to -\hat{p}_{\tilde{e}}/(m_{\tilde{e}}^2\sqrt{\hat{s}})$. This allows the t-channel contributions to become substantial. In fact, the angular distribution can decrease as $\cos\hat{\theta} \to +1$, due to the interference term, only to increase as $\cos\hat{\theta}$ gets even closer to $+1$, due to the eventual dominance of the pure t-channel term. Thus the angular distributions can show an interesting structure, see Fig. 5.6.

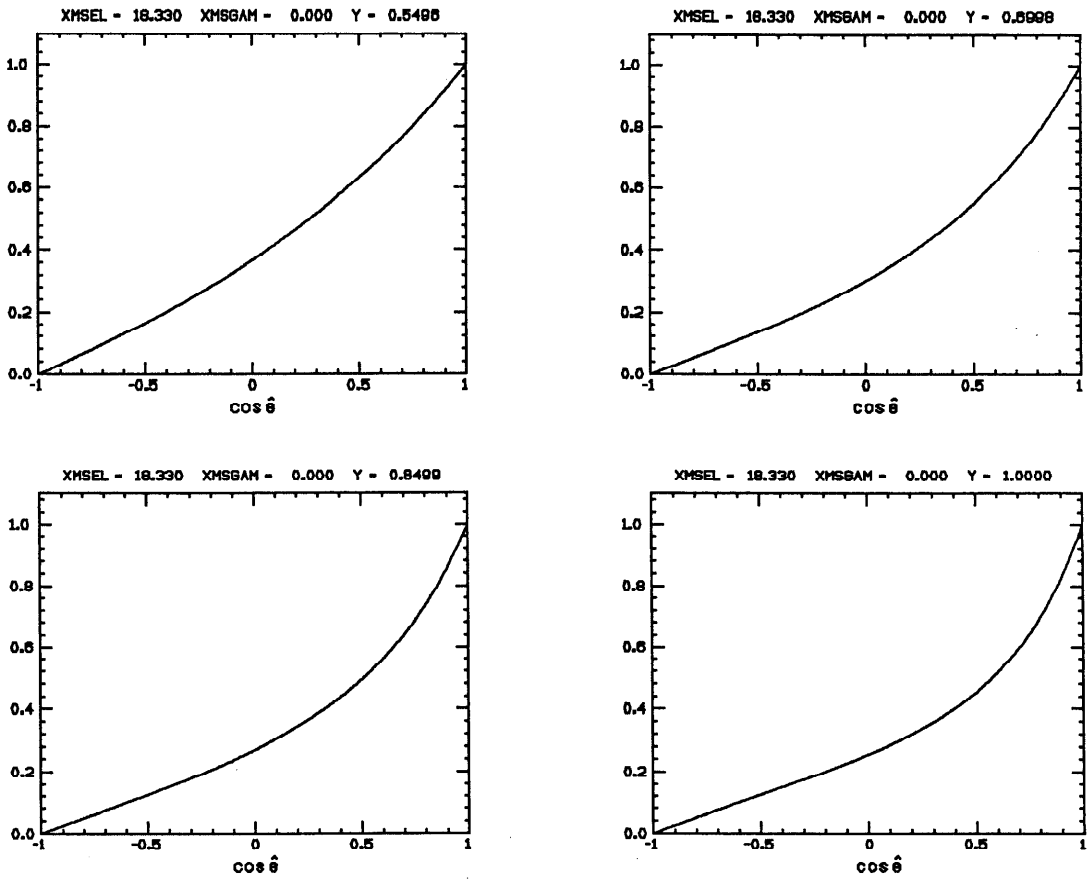

Figure 5.4. Relative Angular Distribution for Right-Handed Selectrons. These four graphs show the function $d\hat{\sigma}_y/d\cos\hat{\theta}(\cos\hat{\theta}, y)$ normalized to $d\hat{\sigma}_y/d\cos\hat{\theta}(\cos\hat{\theta} = 1, y)$ for four different values of y. The y values range from the y_{thres} to 1. The mass settings for the SUSY particles are $m_{\tilde{e}} = 18.330$ GeV, $m_{\tilde{\gamma}} = 0.0$ GeV. Since the photino is massless the full effect of the helicity suppression is apparent and all the distributions go to zero for $\cos\hat{\theta} = -1$.

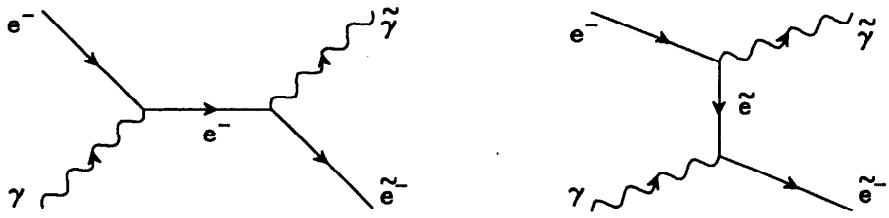

a) s-channel b) t-channel

Figure 5.5. Feynman Graphs for Single Selectron Production.

5.2 Construction of the Selectron Monte Carlo

5.2.1 Technique

The standard inversion technique was used throughout the selectron Monte Carlo in order to maximize efficiency. This was possible only because the events were generated in the CM frame where the distribution $d\hat{\sigma}_y/d\cos\hat{\theta}$ could be analytically integrated over $\cos\hat{\theta}$. The integration over y was done numerically using the QAGS integrator from SLAC Computing Service's NAPL library[81]. The actual execution of the inversion technique borrowed in large part from the Berends-Kleiss Monte Carlo code. In order to establish my notation let me briefly review the inversion method.

The problem in 1^{-D} (1-dimension) is as follows, given a probability distribution $f(x)$, how does one use it to generate simulated events much like the occurrence of events in the real world, which come in pseudo-randomly according to the probability function $f(x)$. The inversion method takes $f(x)$ and creates an integrated function $\mathcal{F}(x)$,

$$\mathcal{F}(x) = \int_{x_{\rm low}}^{x} f(x')\,dx' \qquad x_{\rm low} \le x \le x_{\rm up}.$$

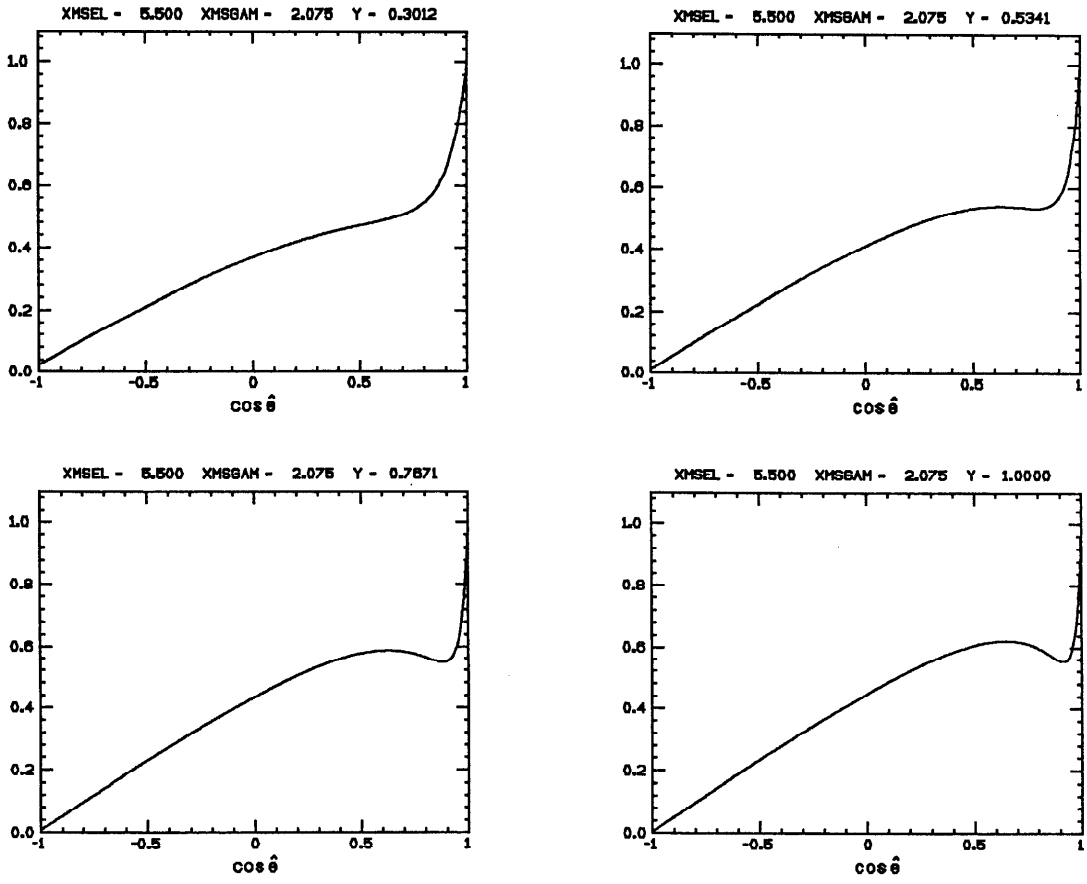

Figure 5.6. Relative Angular Distribution for Right-Handed Selectrons. These four graphs are analogous to those shown in Fig. 5.4, only here the mass settings for the SUSY particles are $m_{\tilde{e}} = 5.500$ GeV, $m_{\tilde{\gamma}} = 2.075$ GeV. The interesting feature of these plots is the appearance of the interference between s- and t-channel Feynman graphs, as mentioned in the text. As an aside notice that the distributions do not necessarily go to 0 as $\cos\hat{\theta} \to 0$ since the photino has finite mass and need not be ultra-relativistic.

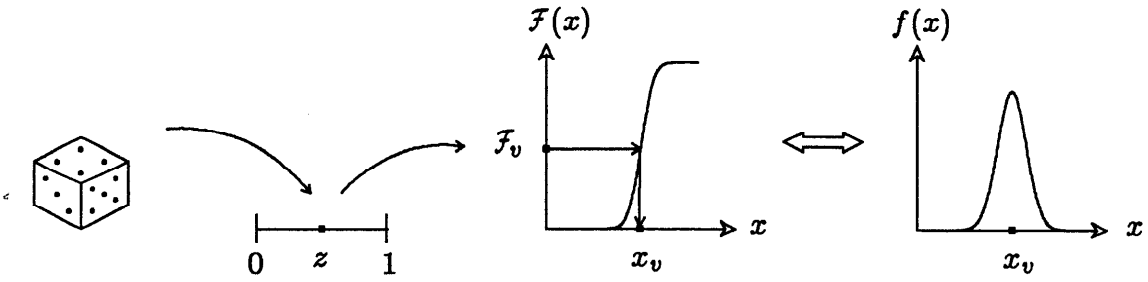

Figure 5.7 Monte Carlo Generation by Inversion Technique. This figure illustrates the method discussed in the text. The probability function is a Gaussian which is then integrated to generate $\mathcal{F}(x)$. Note that the scales between $f(x)$ and $\mathcal{F}(x)$ are not the same.

Notice that x_{low} and x_{up} have been introduced, they define the range of x, and are allowed to be infinite. It is apparent that $\mathcal{F}(x) = 0$ for $x = x_{\text{low}}$, and that $\mathcal{F}(x)$ must be a monotonically increasing function since $f(x) \geq 0$ for all allowed x.

The process of event generation is relatively simple once $\mathcal{F}(x)$ is known. First, map the interval [0,1] onto $[\mathcal{F}(x_{\text{low}}), \mathcal{F}(x_{\text{up}})]$. Then throw a random number, z, from 0 to 1, which maps into a value $\mathcal{F}_v = \mathcal{F}(x_v)$. Now you know $\mathcal{F}_v$. Then the question is how to invert the function $\mathcal{F}$ to get x_v, which you don't know. If $\mathcal{F}(x)$ is particularly simple then $\mathcal{F}^{-1}$ may be known. If not then numerical methods must be applied. This procedure tells you how to generate one event, and may be repeated until the needed statistics are generated. Once this is done the x distribution will be properly generated according to $f(x)$. The entire process is shown in Fig. 5.7.

For a problem in $2^{\text{-D}}$ the solution becomes more complicated. However, given the probability function, $f = f(x, y)$, the generation of events in x-y space is still possible by the inversion technique. Now two integrated probability distributions

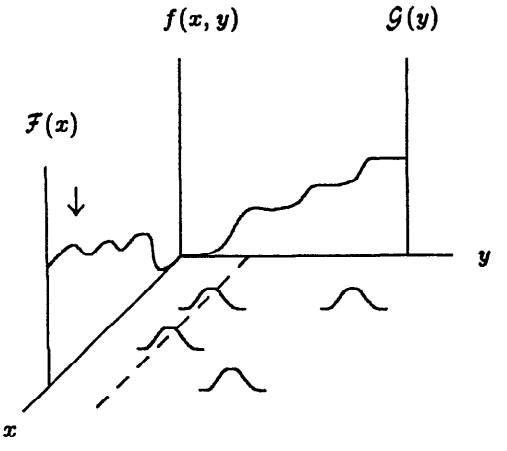

Figure 5.8. This figure shows the obvious, why the two integrated probability functions cannot be used in event generation. Shown is the function $f(x,y)$ plus $\mathcal{G}(y)$ (in the y-z plane) and $\mathcal{F}(x)$ (in the x-z plane). The dotted line shows a given value of y chosen in event generation and the arrow indicates a value of x which $\mathcal{F}(x)$ could wrongly choose for this y value.

may be obtained:

$$\mathcal{F}(x) = \int_{x_{\rm low}}^{x} dx' \int_{y_{\rm low}}^{y_{\rm up}} dy'\ f(x',y')$$

$$\mathcal{G}(y) = \int_{y_{\rm low}}^{y} dy' \int_{x_{\rm low}}^{x_{\rm up}} dx'\ f(x',y').$$

Note the following important fact, that if you integrate over the entire range of one of the variables, you get the probability distribution of the *other* variable. This reduces the problem to the one-dimensional problem, ***but only for generating the one variable.*** Thus, the function $\mathcal{F}(x) = \int_{x_{\rm low}}^{x} dx' \left[\int_{y_{\rm low}}^{y_{\rm up}} dy' f(x',y')\right]$ can be used to generate x by the inversion method. Of course, nothing is special about x, and $\mathcal{G}(y)$ can be used to generate y, it is merely a question of which variable you generate first. So, for definiteness, let's just generate y first. Having done so we cannot use $\mathcal{F}(x)$ to generate x since that's just plain wrong -see Fig. 5.8.

Instead, we must use $f(x,y)$ at a fixed value of y, where the value $y = y_v$, has been generated from $\mathcal{G}(y)$. So what happens here is that the inversion method in 1^{-D} is applied on the probability function, $f_y(x) = f(x,y_v)$. Thus, $\mathcal{F}_y(x)$ can be generated and x_v then determined.

The practicalities of real event generation should be discussed at this point. Whenever direct analytic integration over a variable is not possible numerical

integration must be used, and so a binning procedure together with interpolation is necessitated. This may be tolerable in 1^{-D} , but the procedure can become prohibitively costly in time for more dimensions. If that is the case I suggest you get to know $f(x,y)$ very well, if it is sufficiently flat the sampling procedure may work, if not, then it is imperative to find a function $g(x,y)$ which is integrable and yet is similar in behavior to $f(x,y)$. Then you can use the inversion technique on g to generate the events, and the sampling technique on the function $h = f/g$ in deciding to keep them. This can greatly improve the event generation efficiency versus direct use of the sampling technique with $f(x,y)$. Of course, the smarter you are in finding an integrable function g which best mimics f, the more efficient will be your Monte Carlo.

5.2.2 Event Generation

The selectron Monte Carlo events were generated for a given setting of $m_{\tilde{e}}$ and $m_{\tilde{\gamma}}$. Initially, there were three variables to generate: y, $\cos\hat{\theta}$, and $\hat{\varphi}$, where the angles refer to the selectron in the collision center of mass frame. The first variable generated was y, which used the probability function $\mathrm{F}(y)\hat{\sigma}_y$, given by,

$$\mathrm{F}(y)\hat{\sigma}_y = \mathrm{F}(y)\int_{-1}^{+1} d\cos\hat{\theta}\,\frac{d\hat{\sigma}_y}{d\cos\hat{\theta}}\,.$$

This function is found in explicit form as the integrand of equation 6 in Kobayashi and Kuroda:

$$\mathrm{F}(y)\hat{\sigma}_y(y) = \mathrm{F}(y)\frac{\alpha^2\pi\sqrt{\lambda}}{2y^2 s}\left[1+7\left(\frac{m_{\tilde{e}}^2-m_{\tilde{\gamma}}^2}{\hat{s}}\right)+4\frac{(m_{\tilde{e}}^2-m_{\tilde{\gamma}}^2)(\hat{s}+m_{\tilde{e}}^2-m_{\tilde{\gamma}}^2)}{\hat{s}\sqrt{\lambda s^2}}\right.$$
$$\left.\times\ln\left|\frac{\sqrt{\lambda s^2}-(\hat{s}+m_{\tilde{e}}^2-m_{\tilde{\gamma}}^2)}{\sqrt{\lambda s^2}+(\hat{s}+m_{\tilde{e}}^2-m_{\tilde{\gamma}}^2)}\right|\right].$$

This was used to generate the function $\mathcal{F}(y_i)$:

$$\mathcal{F}(y_i) = \int_{y_{\mathrm{thres}}}^{y_i} dy' F(y')\hat{\sigma}_y(y'), \quad y_i = y_{\mathrm{thres}}+(i-1)\frac{(1-y_{\mathrm{thres}})}{100}, \quad i = 1,2,\ldots,101.$$

The binning of the y values was of course necessary because numerical integration was needed. The integrated function was linearly interpolated in order to create a smooth continuous function in y. This size binning was deemed adequate and needed only 100 calls to QAGS. The continuous function, $\mathcal{F}(y)$, was used to determine the event value y by the now familiar inversion technique.

The determination of y fixed both the momentum of the selectron in the CM frame and the boost from the CM frame back to the lab. The latter was accomplished by the following 4×4 Lorentz transformation matrix:

$$\Lambda^{\mu}{}_{\nu} = \begin{pmatrix} \gamma & 0 & 0 & -\gamma\beta \\ 0 & 1 & 0 & 0 \\ 0 & 0 & 1 & 0 \\ -\gamma\beta & 0 & 0 & \gamma \end{pmatrix} \qquad \text{s.t.} \qquad p^{\mu} = \Lambda^{\mu}{}_{\nu}\, \hat{p}^{\nu} \, .$$

Next the direction of the selectron, in the CM frame, was needed in order to determine the components of $\hat{p}$:

$$\hat{p} = \begin{pmatrix} \sqrt{|\hat{\mathbf{p}}|^2 + m_{\tilde{e}}^2} \\ |\hat{\mathbf{p}}| \sin\hat{\theta} \cos\hat{\varphi} \\ |\hat{\mathbf{p}}| \sin\hat{\theta} \sin\hat{\varphi} \\ |\hat{\mathbf{p}}| \cos\hat{\theta} \end{pmatrix} .$$

The angle $\hat{\varphi}$ is easy to generate, $\hat{\varphi} = 2\pi z$, where z is a random number between 0 and 1. The polar angle is more involved since it depends on the collision dynamics. Returning to the discussion of generating events in a 2^{-D} space; we see here that since there is no $\hat{\varphi}$ dependence in the differential cross section the probability density is a function of y and $\cos\hat{\theta}$ alone. Thus, using the notation of the last section,

$$f(x,y) \longrightarrow \mathrm{F}(y) \frac{d\hat{\sigma}_y}{d\cos\hat{\theta}}(\cos\hat{\theta}, y).$$

Now we have already generated y, and in order to generate $\cos\hat{\theta}$ we must integrate the above at fixed y, and so, letting $x = \cos\hat{\theta}$,

$$\mathcal{F}_y(x) = \int_{-1}^{x} dx' \, \mathrm{F}(y) \frac{d\hat{\sigma}_y}{dx}(x', y) = \mathrm{F}(y) \int_{-1}^{x} dx' \, \frac{d\hat{\sigma}_y}{dx}(x', y).$$

And it turns out that the above can be integrated term by term in the CM frame.

$$\begin{aligned}\mathcal{F}_y(x) = \mathrm{F}(y) \frac{\alpha^2 \pi \sqrt{\lambda}}{2y^2 s} \Bigg[& \frac{1}{2}(x+1) + \frac{1}{\hat{s}} \left\{ \frac{3}{2}(m_{\tilde{e}}^2 - m_{\tilde{\gamma}}^2)(x+1) + \frac{1}{4}\sqrt{\lambda s^2}(x^2-1) \right\} \\ & + \frac{4(m_{\tilde{e}}^2 - m_{\tilde{\gamma}}^2)(\hat{s} + m_{\tilde{e}}^2 - m_{\tilde{\gamma}}^2)}{\hat{s}\sqrt{\lambda s^2}} \ln \left| \frac{\hat{s} + m_{\tilde{e}}^2 - m_{\tilde{\gamma}}^2 - x\sqrt{\lambda s^2}}{\hat{s} + m_{\tilde{e}}^2 - m_{\tilde{\gamma}}^2 + x\sqrt{\lambda s^2}} \right| \\ & + \frac{8m_{\tilde{e}}^2 (m_{\tilde{e}}^2 - m_{\tilde{\gamma}}^2)(x+1)}{4\hat{s}m_{\tilde{e}}^2 + (1-x)\left(\lambda s^2 + \sqrt{\lambda s^2(\lambda s^2 + 4\hat{s}m_{\tilde{e}}^2)}\right)} \Bigg].\end{aligned}$$

Notice that, for $x = 1$, the above becomes the integrated probability function used to generate y, as it should. This function was inverted in order to generate $\cos\hat{\theta}$.

At this point I should mention some of the detailed techniques used in the selectron Monte Carlo. The function inversion was done by code taken from the Berends-Kleiss Monte Carlo, specifically, the subroutine EVGENH. Basically, you give it a monotonically increasing function $\mathcal{F}(x)$, and a function value $\mathcal{F}_v = \mathcal{F}(x_v)$, plus the bounds on x, $x_{\mathrm{low}} \leq x \leq x_{\mathrm{up}}$, and it returns x_v. The inversion procedure utilized a binary search, which was possible because $\mathcal{F}(x)$ is a monotonic function of x. The algorithm adds a little more sophistication after roughly 10 or so steps through the binary search, for it also utilizes Newton's method. In fact, it proceeds by binary search only initially, and then oscillates between Newton's method and a few steps of a binary search.

I should also mention that the random number generation was done with code borrowed from the Berends-Kleiss Monte Carlo. The numbers were generated

in double precision format within the fortran function DRN. Ultimately, the generation was based upon a NAPL library routine, RAN6A, which generates single precision random numbers. For completeness, I might add that the number 137 was used as the seed.

Having gotten to this point, the rest of the procedure is relatively easy, since it centers around the decay $\tilde{e}^- \rightarrow e^- + \tilde{\gamma}$. The selectron's 4-momentum in the lab is known at this point, and using its direction cosines, $\hat{\mathbf{u}} = \hat{\mathbf{p}}/|\hat{\mathbf{p}}|$, a Lorentz boost matrix from the selectron center of mass system to the lab frame can be constructed (note- here β and γ refer to the selectron kinematic quantities as seen in the lab frame):

$$\Lambda^{\mu}{}_{\nu} = \begin{pmatrix} \gamma & \gamma\beta u_1 & \gamma\beta u_2 & \gamma\beta u_3 \\ \gamma\beta u_1 & 1+(\gamma-1)u_1^2 & (\gamma-1)u_1u_2 & (\gamma-1)u_1u_3 \\ \gamma\beta u_2 & (\gamma-1)u_1u_2 & 1+(\gamma-1)u_2^2 & (\gamma-1)u_2u_3 \\ \gamma\beta u_3 & (\gamma-1)u_1u_3 & (\gamma-1)u_2u_3 & 1+(\gamma-1)u_3^2 \end{pmatrix}.$$

Again we have a two body decay, and again a monoenergetic spectrum of the decay products in the rest frame of the decaying object. This time we have a decaying scalar particle and so, in its rest frame, the decay electrons are distributed isotopically. Thus, knowing the above matrix makes the selectron decay trivial, and so, the final 4-momentum of the electron in the lab frame is obtained.

5.2.3 Event Selection

At this point the event is fully generated and awaits analysis cuts. A subroutine named ERRDO subjected the final state electron to the QED background cuts. The acceptance for electrons resembles the state of Nevada in the E_e-$\cos\theta_e$ plane, see Fig. 5.9. A complete discussion of how this region was determined can be found in the next chapter. Events which place the final state electron into this region are accepted as candidate events, and are summed into

a counter, $\mathcal{N}_{\rm cand}^{\rm MC}$. A total number of events, $\mathcal{N}_{\rm tot}^{\rm MC}$, are generated. The effect of the acceptance cuts can be related to an efficiency for finding candidate events η,

$$\eta = \mathcal{N}_{\rm cand}^{\rm MC}/\mathcal{N}_{\rm tot}^{\rm MC} .$$

The total number of generated events, plus the total production cross section, $\sigma_{\rm tot}$, can be used to determine the integrated luminosity used in the selectron Monte Carlo,

$$L^{\rm MC} = \mathcal{N}_{\rm tot}^{\rm MC}/\sigma_{\rm tot} .$$

The experimental search used a total integrated luminosity of $L^{\rm exp} = 123.4$ pb^{-1}. Thus, the total number of selectron candidate events, $\mathcal{N}_{\rm cand}^{\rm exp}$, expected for a given value of $m_{\tilde{e}}$ and $m_{\tilde{\gamma}}$ in the experimental search is:

$$\mathcal{N}_{\rm cand}^{\rm exp} = 2\,\eta\sigma_{\rm tot}L^{\rm exp}.$$

The factor of 2 is introduced here to account for the charge conjugate process which are not included in $\sigma_{\rm tot}$.

The statistical error enters into the determination of η, which in turn is dependent on the error in $\mathcal{N}_{\rm cand}^{\rm MC}$. So, taking $\mathcal{N}_{\rm cand}^{\rm MC}$ to have Poisson errors we have:

$$\triangle\mathcal{N}_{\rm cand}^{\rm MC} = \sqrt{\eta(1-\eta)\,\mathcal{N}_{\rm tot}^{\rm MC}} \qquad \Rightarrow \qquad \triangle\eta = \frac{\triangle\mathcal{N}_{\rm cand}^{\rm MC}}{\mathcal{N}_{\rm tot}^{\rm MC}} = \sqrt{\frac{\eta(1-\eta)}{\mathcal{N}_{\rm tot}^{\rm MC}}}.$$

And as usual, if $\triangle\eta$ is to be decreased by a factor of 2 then the statistical sample, i.e. $\mathcal{N}_{\rm tot}^{\rm MC}$, must be increased by a factor of 4. The error on the number of candidates in the experimental search is then,

$$\triangle\mathcal{N}_{\rm cand}^{\rm exp} = 2\,\sigma_{\rm tot}L^{\rm exp}\sqrt{\frac{\eta(1-\eta)}{\mathcal{N}_{\rm tot}^{\rm MC}}} .$$

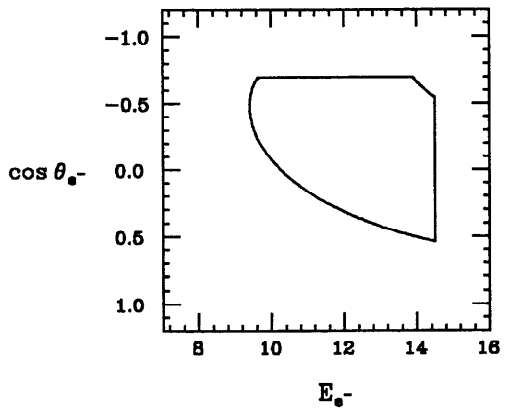

Figure 5.9. Single electron acceptance for the Monte Carlo. Candidate events must have final state electrons fall within the enclosed region. Positrons have the same acceptance but with $\cos\theta \rightarrow -\cos\theta$.

The selectron Monte Carlo was fine-tuned further in order to optimize its efficiency. By observing the y and $\cos\hat{\theta}$ distributions of the candidate events, i.e. those events passing the acceptance cuts, it was found that, for certain values of $m_{\tilde{e}}$ and $m_{\tilde{\gamma}}$, only very restricted ranges of y and $\cos\hat{\theta}$ gave rise to the candidate events. Hence, if the entire kinematically allowed range was used to generate events a tremendous amount of time would be wasted on making events which would never pass the cuts. Therefore, the Monte Carlo was modified so that it would only generate events in a restricted region of y, where $y_{\rm thres} < y_{\rm low} \leq y \leq 1$. By trial and error the lower bound, $y_{\rm low}$, for the candidate y distributions was determined, such that the y distribution of the candidate events died off before $y_{\rm low}$. This allowed the efficiency of the Monte Carlo candidate event generation to be greatly increased. Then the event generation used exactly the same formalism as before, only the y integrations began at $y_{\rm low}$ and not $y_{\rm thres}$. This yielded an effective total cross section:

$$\sigma_{\rm eff} = \int_{y_{\rm low}}^{1} dy \mathrm{F}(y)\sigma_y(y).$$

The luminosity for the Monte Carlo sample is thus given by $L^{\rm MC} = \mathcal{N}_{\rm tot}^{\rm MC}/\sigma_{\rm eff}$.

The number of events expected in the experimental search is then:

$$\mathcal{N}_{\rm cand}^{\rm exp} = \frac{2L^{\rm exp}}{L^{\rm MC}}\mathcal{N}_{\rm cand}^{\rm MC} = 2\,\sigma_{\rm eff}L^{\rm exp}\frac{\mathcal{N}_{\rm cand}^{\rm MC}}{\mathcal{N}_{\rm tot}^{\rm MC}} = 2\,\eta\sigma_{\rm eff}L^{\rm exp}.$$

Note that it is very important not to expect any candidate events with $y < y_{\rm low}$. This form for $\mathcal{N}_{\rm cand}^{\rm exp}$ resembles the previous form except that $\sigma_{\rm tot}$ is replaced by $\sigma_{\rm eff}$. The error on this number is also of the same form as before, but with the substitution of $\sigma_{\rm eff}$ for $\sigma_{\rm tot}$. Then,

$$\triangle\mathcal{N}_{\rm cand}^{\rm exp} = 2\,\sigma_{\rm eff}L^{\rm exp}\sqrt{\frac{\eta(1-\eta)}{\mathcal{N}_{\rm cand}^{\rm MC}}}\,.$$

The fact that $\triangle\mathcal{N}_{\rm cand}^{\rm exp}$ can be decreased by this method was due to $\sigma_{\rm eff}/\sigma_{\rm tot} \ll 1$, and not necessarily by the $\sqrt{\eta(1-\eta)}$ factor, (which could actually go the wrong way).

Chapter 6. Experimental Analysis

6.1 Single Electron Selection Cuts- Part 1

6.1.1 Isolation Cuts

The search criteria used to select candidate events in this analysis divided naturally into two categories– those designed to find and isolate single electron events, and those primarily designed to eliminate the QED background. The Mark II detector was well adapted for the detection of single electrons over the regions of solid angle where the coverage of its drift chamber and liquid argon calorimeter coincided. Unfortunately, such coverage did not extend over all solid angles. Not only was the detector uninstrumented at very low angles with respect to the beam pipe, but there were also regions at large angles that were calorimetrically uninstrumented, or poorly (with respect to this analysis) instrumented. This lack of coverage allowed background processes, predominantly from QED sources, to mimic the single electron signal of selectron decay because of undetected final state particles, especially undetected photons. The following list of experimental event selection criteria, or cuts, were designed to take advantage of the strengths of the detector in order to maximize the hypothetical selectron signal, while minimizing the background signal. We begin by describing the selection and isolation cuts.

The selection and isolation cuts can be further divided into two categories– those which were based upon the raw data, and those that used fully reconstructed track quantities, *i.e.* the PASS2 data, in their cuts. The following cuts outline those made on the raw data:

1.) The event trigger was required to satisfy the selectron trigger, *i.e.* $N_A = 1$, $N_D = 1$. This translates to the hardware finding one charged track and one LA shower above threshold. Refer to the detector description chapter for more details.

2.) The total raw energy sum over all the LA modules was required to be greater than 4 GeV.

3.) The total energy in any SAT calorimetric module, E_{SAT}, was required to satisfy $E_{SAT} \leq 3$ GeV. This cut eliminated many low angle Bhabha scattered electrons.

4.) The total number of drift chamber hit wires was required to be less than 50. This cut was designed to eliminate high voltage breakdown events, and cosmic ray showers. A typical track usually had between 10 and 14 hits in the drift chamber.

These cuts had the advantage of being very efficient for finding real single electron events while taking very little processing time on the computer. For electrons in the final acceptance the efficiency of these cuts was close to 100%. This will be discussed in a subsequent section.

The next set of cuts depended upon the event having been analyzed by the PASS2 analysis routines. These routines calculated the various physics quantities used in the following set of cuts:

5.) The offline tracking routines had to find one and only one charged track in the event.

6.) The total momentum of the charged track, p_{tot}, was required to satisfy $p_{tot} \geq 2$ GeV.

7.) The charged track was required to originate at the interaction point. Its distance of closest approach in the plane perpendicular to the beam axis, r_m, was required to satisfy $r_m \leq 5$ cm for the charged track. Its distance of closest approach along the beam axis, z_m, was required to satisfy $z_m \leq 15$ cm†.

---

† The z cut was more generous since the beams are much longer in z then they are wide, and also because of the poorer z resolution (vs. x-y resolution) of the tracking chambers.

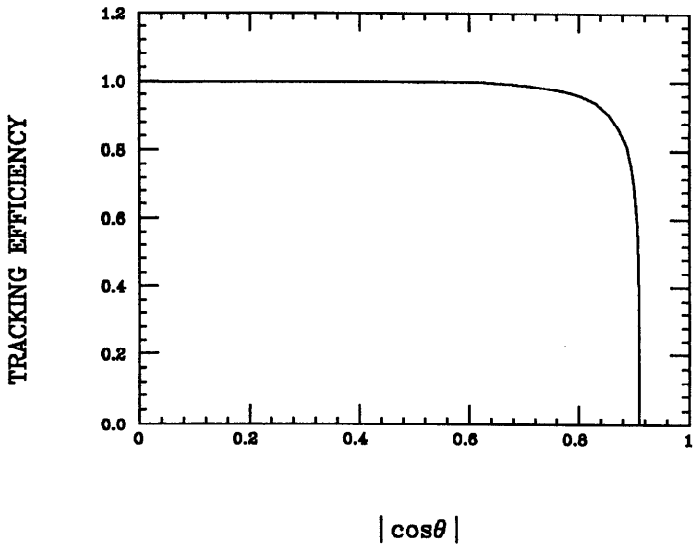

Figure 6.1. Tracking Efficiency vs. $|\cos\theta|$. Shown here is PTRAKR track finding efficiency as a function of track inclination for isolated tracks. Note the rapid fallout of tracking efficiency at 30°. This figure is taken from M. Levi's thesis[82]

8.) The charged track's reconstructed LA energy, E_{LA}, must be such that $E_{LA} \geq 5.8$ GeV.

9.) The charged track must be within the fiducial volume of the liquid argon system. Thus, it must have $|\cos\theta| \leq 0.70$ and $\delta\phi_{gap} > 2.7°$ from the azimuthal cracks in the liquid argon system.

10.) The event must pass DAZCUT (described below). This cut eliminated events which had a low angle electron exiting out the ends of the tracking chambers, especially the vertex chamber.

11.) No photons with $E_{LA} \geq 300$ MeV were allowed in the event unless they were within 36 cm of the charged track. This cut allowed for electrons to bremsstrahlung in the detector material without being rejected.

DAZCUT was a routine used to find track stubs in the vertex chamber from very low angle charged tracks (down to 10°). It was possible for charged tracks coming off at $\sim 10°$ to exit out the end of the vertex chamber without passing through any of the central drift chamber. Such tracks were never found by the

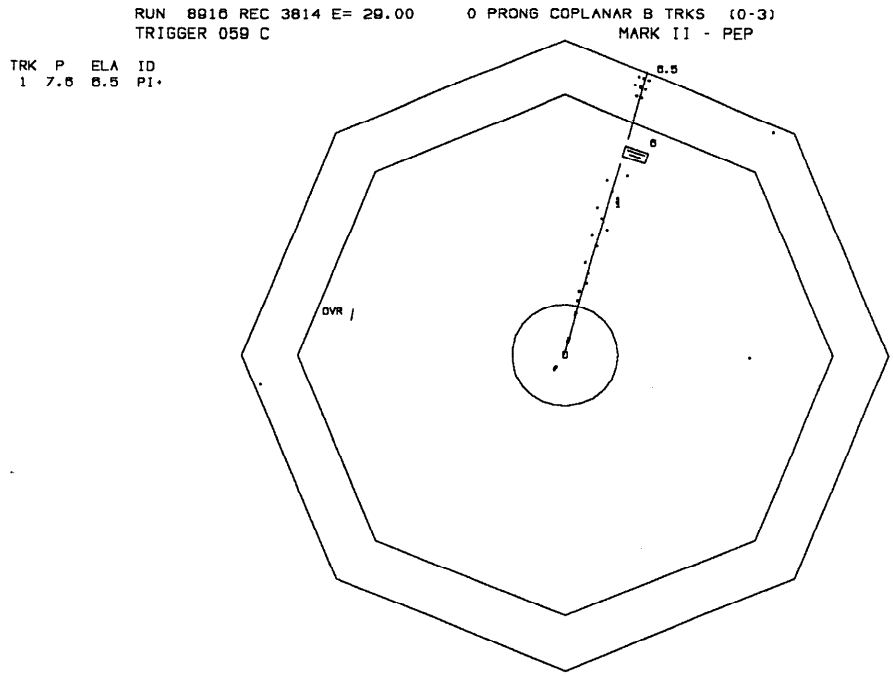

Figure 6.2. Drift Chamber View of DAZCUT Rejected Event. This event display shows a typical single electron event in the Mark II. This view shows the VC, DC, TOF, and LA systems in an x-y view. The small dots scattered along the track trajectory show hit VC or DC wires when the track is in the wire chambers, and hit LA strips when it is in the calorimeter.

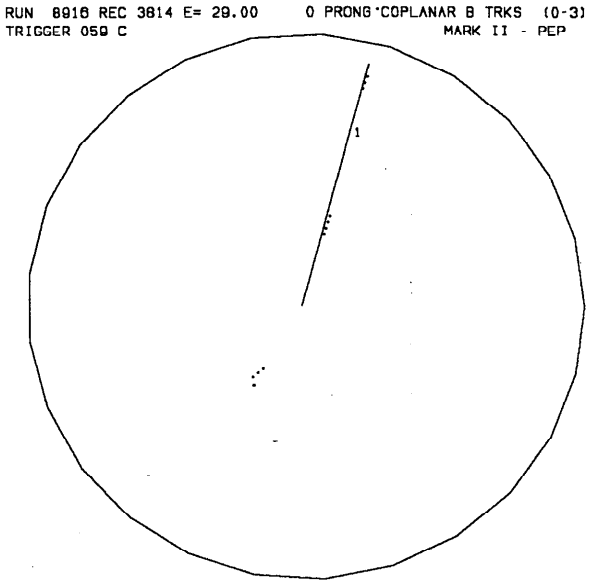

Figure 6.3. Vertex Chamber View of DAZCUT Rejected Event. This view shows the single electron traversing the VC. Note that all 7 layers of the VC fired for this track. Even more importantly, note that opposite the found track are four aligned hits in the inner band of the VC. These hits are in all probability due to a low angle electron escaping out the VC endplate.

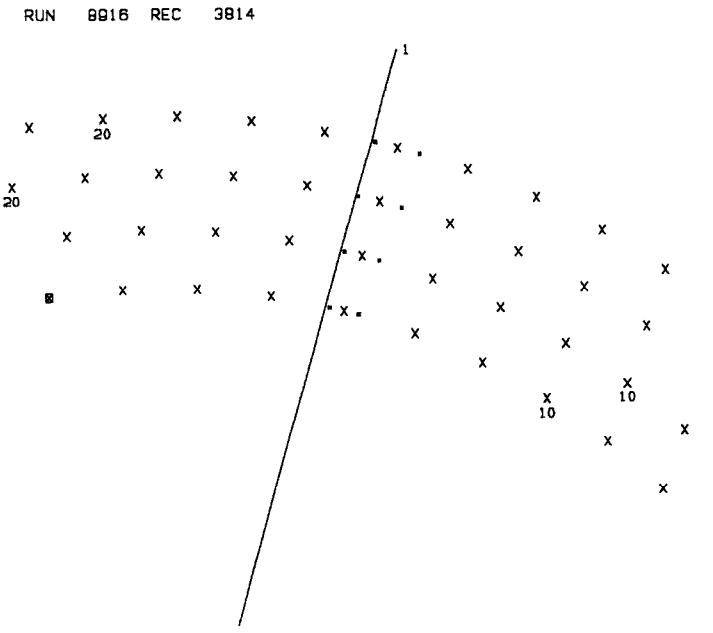

Figure 6.4. Magnified VC View I of DAZCUT Rejected Event. This is a closeup view of the inner band of wire in the VC. Each sense wire is represented by a "×", while the left-right solutions from the space-time relation for hit wires are shown by an "∗". The fitted track trajectory is also drawn. Note the alignment of the four hits (LLLL).

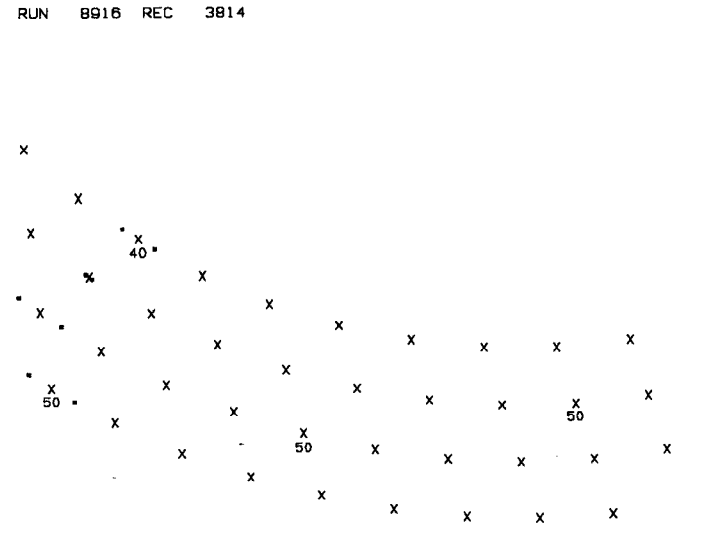

Figure 6.5. Magnified VC View II of DAZCUT Rejected Event. This view is analogous to the above, except that it is centered 180° opposite the found track. The normal track fitting routines did not find a track here since only four wires were hit. The alignment of the four hits (LRRL) for the track stub can be clearly seen (wires 40, 43, 46, 50 in layers 1–4).

Mark II's main track finding routine, PTRAKR. In fact, PTRAKR often failed to even find tracks which had stubs in the drift chamber due to falling efficiency as the number of wire hits decreased (PTRAKR required an absolute minimum of 7 hit wires in the drift chamber) as can be seen in Fig. 6.1. DAZCUT was designed to compensate for this deficiency by utilizing the special topology of the single electron, or selectron, event sample. Since the track associated with a stub was expected to balance the $p_\perp$ of the seen electron DAZCUT's search for stubs was confined to a narrow region of 30° in ϕ, centered opposite the seen electron. The event was rejected if there were three or more hits in layers 1-4 of the vertex chamber, counting one hit/layer at most. Noise hits were assumed random, and so seldom lined up as DAZCUT required. Figures 6.2–6.5 show various display plots of an event where DAZCUT was used.

The cuts mentioned above confined all particles other than the detected charged prong either to uninstrumented regions of the detector or to the 2° cone around the beam axis in the forward and backward regions. The cuts were applied to the data set collected from May 1982 until June 1983, covering runs 8838–9099 and 9364–11472†. The above cuts yielded 763 events from 123 pb^{-1} of data. These events will hereafter be referred to as the summary selectron sample, or summary sample for short. Additional cuts were applied to this summary sample, including a special cut designed to eliminate the lowest order QED background. This latter cut was determined by studying the background sources, and the gaps in the electromagnetic calorimetry. Events which passed the QED background cut were also handscanned to obtain the final selectron candidate sample. These cuts will be described in a later section. We must stop at this point, however, to discuss the QED background in greater detail due to its profound effect on the analysis.

---

† The excluded runs were rejected because the DC was operating at less than full voltage.

6.2 QED Background

6.2.1 Mark II Photon Detection

The major sources of background in this search were QED processes, in particular, $ee\gamma$ events (from the reaction $e^+e^- \rightarrow e^+e^-\gamma$) where only one electron is detected, the other electron goes down the beam axis, and the gamma falls into a gap in the electromagnetic calorimetry or a region with significant inefficiency for detecting photons.

Recall that the Mark II detector had three EM calorimetric systems: the LA, EC, and SAT systems. The fiducial acceptance for the LA and EC systems can be seen in Fig. 6.6. This scatter plot shows all tracks, charged and neutral, taken from a large data sample, which have calorimetric energy associated with them. The portion of the plot with $|\cos\theta| \lesssim 0.72$ represents the LA system's coverage. The rectangular geometry of the eight LA modules, when projected onto spherical coordinates, gives rise to the scalloped pattern observed. The thin depleted vertical strips represent the gaps in ϕ between the modules. For $0.72 \lesssim |\cos\theta| \lesssim 0.75$ there is no calorimetric coverage since this region is between the two systems and is therefore uninstrumented. This region is hereafter referred to as the "crack"; all other regions will be referred to differently. The crack played an important role in determining the analysis flow of the summary sample.

The EC system provided coverage for $|\cos\theta| \gtrsim 0.75$. The endcap's outer boundary was cut in a circular pattern as can be seen by the straight line defining its lower acceptance edge in the scatter plot. The inner boundary of the endcap system (with respect to the beam pipe) was cut in a square pattern for purposes of construction, and this is also apparent from the plot. The rather large uninstrumented region around $\phi = 3\pi/2$ is referred to as the "keyway". It is due to the support stand of the endcaps. The thin uninstrumented region at

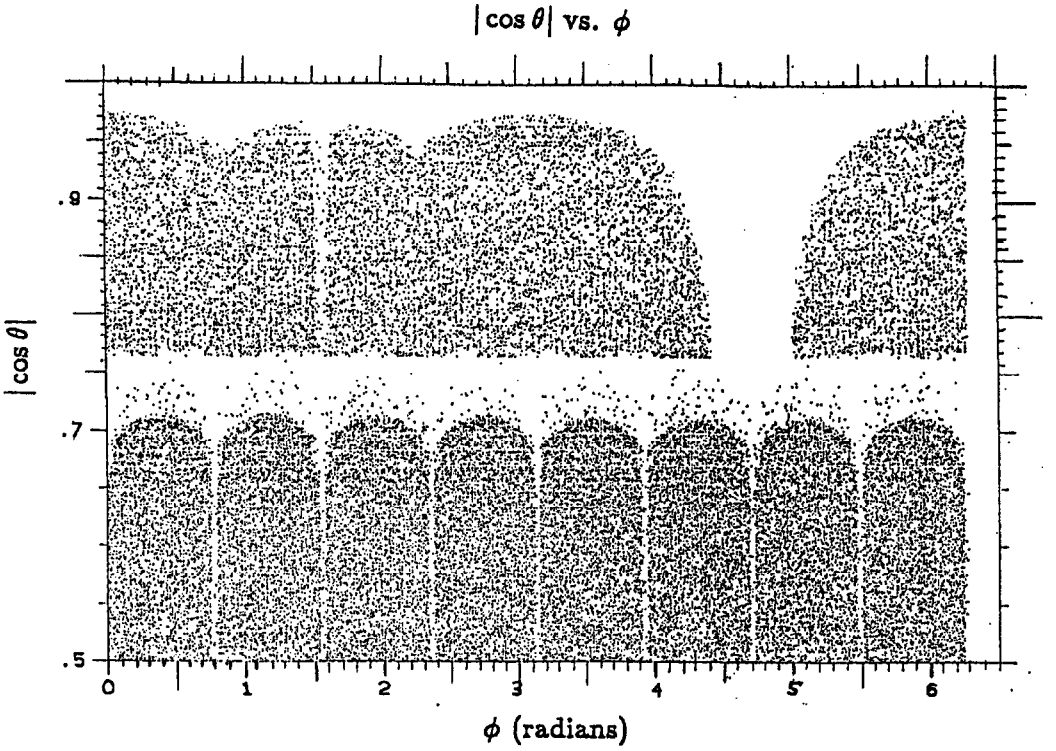

Figure 6.6. Liquid Argon and Endcap Calorimetric Acceptances. This scatter plot shows the fiducial volumes of the LA and EC systems. It was made from charged and neutral tracks which were associated with calorimetric energy, and it is the charged tracks which populate the region between the LA and EC systems ($0.72 \lesssim |\cos\theta| \lesssim 0.75$). See the text for a full discussion.

$\phi = \pi/2$ represents the gap between the two halves of the endcap module. As can be seen, there were many gaps in the solid angle coverage of the Mark II detector.

The endcap system also suffered from being only 2.3 radiation lengths thick at normal incidence. This can be compared to the LA system, which was 14.5 radiation lengths thick at normal incidence. Using EGS[75], it was determined that a photon with reasonably high energy (several GeV) had a 2.5% probability of passing through the endcap without converting, and thereby escaping detection†.

† Historically, the PWC design was not intended to be permanently used in the final endcap design. Due to the disappointing performance of the LA endcaps (which would have had the same thickness as the LA barrel), however, the PWC design was selected for use at

It is an unfortunate fact that the Mark II calorimetry allowed photons many avenues of escaping detection. The large number of events in the summary event sample demonstrates this all too well. None the less, the detector deficiencies provided an exciting experimental challenge; and one that could fortunately be met.

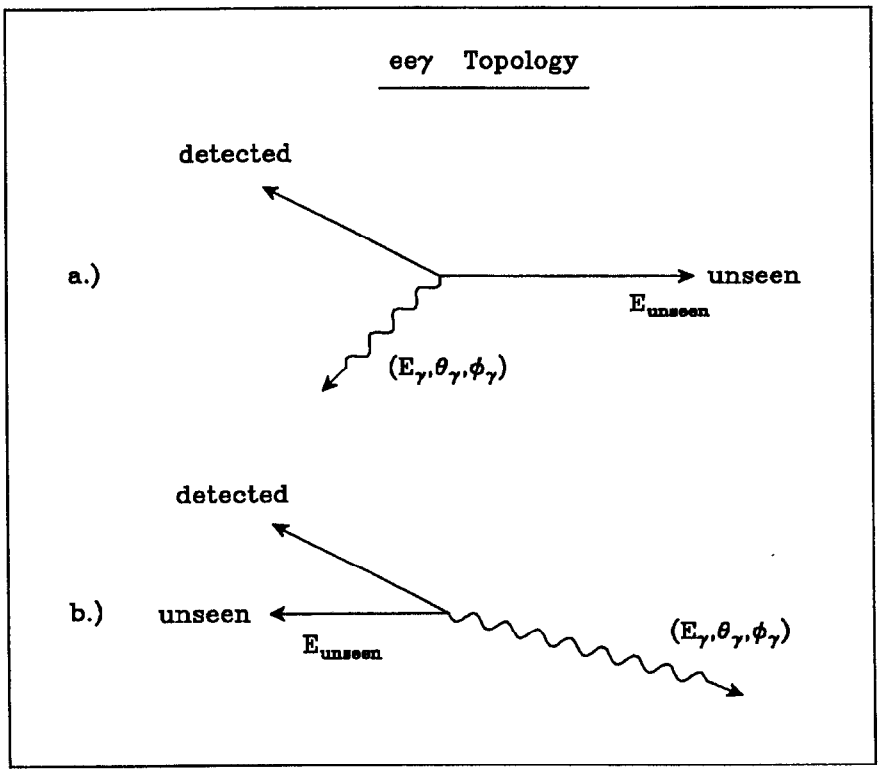

Figure 6.7. $ee\gamma$ Event Topology. The three body final states for $e^+e^- \rightarrow ee\gamma$ events are shown here. We are concerned only with the subset of these events where one of the electrons is detected and the other is undetected because it escapes out the beam pipe. These events are further classified according to whether the two electrons are in opposite hemispheres, case a.), or in the same hemisphere, case b.).

6.2.2 $ee\gamma$ Kinematics

The three body kinematics of the $ee\gamma$ events, together with the confinement of the unseen electron to within 2° of the beam axis, allowed the gamma direction to

SPEAR. The effect of this decision on the selectron analysis could not have been foreseen at that time. It is interesting to note that the Upgrade version of the Mark II does not suffer from these deficiencies since it uses a different endcap design.

be constrained by the detected prong's energy and direction measurements. This is easily seen by just counting degrees of freedom. Suppose we consider an $ee\gamma$ three body final state where the direction of travel of the unseen electron is exactly known, and the energy and direction of the other electron has been measured, see Fig. 6.7. Then there are just four unknown quantities: the energy and angles of the photon, $(E_\gamma, \theta_\gamma, \phi_\gamma)$, and the unseen electron's energy, E_{unseen}. Since we have four kinematic equations from energy-momentum conservation we can solve exactly for these four unknowns. A more careful analysis, fully described in the appendix, shows how the unknowns and their errors are derived. The important result that concerns this analysis is that the measurement of detected electron's kinematic quantities was sufficient to locate the direction of the photon under the $ee\gamma$ hypothesis, with one proviso yet to be discussed.

Thus far we have assumed that the direction of the unseen electron was known. But as Fig. 6.7 shows, the unseen electron could escape detection by traveling out the beam pipe on either the same side or the opposite side of the detected electron. This directional ambiguity was resolved by comparing the detected electron's direction with its incident direction. If the detected electron was forward (backward) scattered, the largest QED matrix element is for the other electron to be going in the opposite (same) direction. More simply put, we have assumed that the unseen electron is always traveling along its incident direction. This is due to the dominance of the scattering amplitude by the t-channel processes when t becomes small, *i.e.* when one of the electrons is scattered through small angles. Thus, working with the $ee\gamma$ hypothesis, we can predict the photon's direction from the measured electron's kinematic quantities with a great degree of confidence. Figure 6.8 shows the lowest order Feynman graphs for radiative Bhabha scattering together with the resultant final state momentum configurations. The initial electron-positron direction is shown at the top of the figure. The experimental cuts heavily influence this association by requiring that

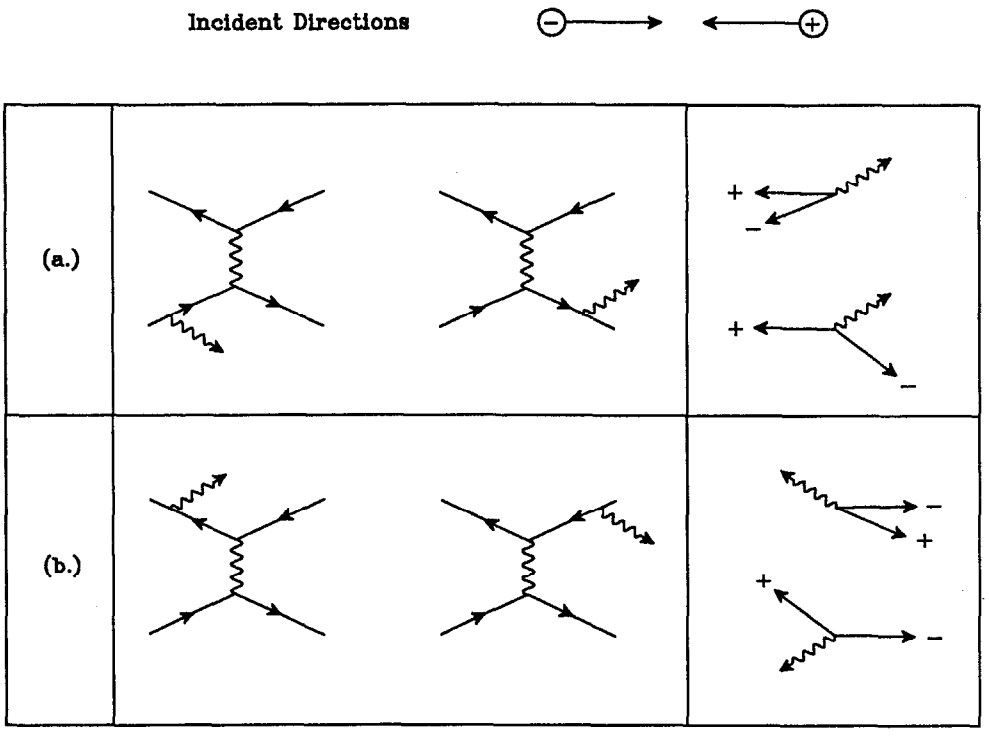

Figure 6.8. Initial and Final State Radiative Processes. Shown in this figure are the four different Feynman diagrams for t-channel scattering in $ee\gamma$ events. The final state momentum configurations which arise from these Feynman graphs are shown on the right hand side of the above figure. We have used the experimental constraint that either the electron or the positron has been scattered at large enough angles to be detected. The QED matrix element for final states where the electron is detected is dominated by the graphs where the photon is radiated off the electron, either as initial or final state radiation, as shown in (a). The positron escapes undetected traveling along its incident direction. The charge conjugate case is shown in (b). This information is important to the analysis since it was used to remove the kinematic ambiguity in locating the photon.

only one electron, with large $p_\perp$, be seen in the detector.

6.2.3 The $e\gamma$ Background Sample

The ability of the above method to predict the photon direction under the $ee\gamma$ hypothesis was of critical importance since it allowed the separation of signal events from $ee\gamma$ background events in the single electron sample. This will be discussed in greater detail in the next section. It was therefore imperative to

verify the accuracy of this method in an independent manner. Fortunately, there did exist an independent check of this technique utilizing another event topology, *i.e.* events where both an electron and a photon were detected. This event type also arose from radiative Bhabha events and shared the same kinematics as $ee\gamma$ events in the single electron sample. The $e\gamma$ events could have their photon's direction and energy predicted using only the detected electron's kinematic quantities. This prediction could then be compared to the actual measured quantities thereby providing a test of the kinematic fitting procedure.

A sample of events with a detected electron and a detected photon, hereafter referred to as the $e\gamma$ background sample, was selected from the Mark II data. This sample was selected with the same cuts as used in the selectron search sample, with the exception that one photon was required to be detected in addition to the charged track. These cuts included the DAZCUT and SAT cuts, as well as the momentum and energy cuts on the charged track. Because of the higher number of $e\gamma$ events, versus single electron events, an adequate number of $e\gamma$ events for study was obtained with a 28.8 pb^{-1} data sample. This sample modeled all the QED processes which contributed as background in the single electron search. This is due to the fact that the $e\gamma$ event would become a single electron event if the photon was lost.

A study of the deviation of the measured position of the gamma from that predicted using only the seen electron's direction and energy was used to check the three body hypothesis. Events which didn't position well under the $ee\gamma$ hypothesis, *i.e.* within 2.5σ in $\Delta\cos\theta$ and $\Delta\phi$, were handscanned according to the same criterion as the selectron sample. Those events which were found to be $\gamma\gamma$ events with a conversion were removed from the sample (they comprised 2% of the original sample). The remaining events came predominately from $ee\gamma$ and $ee\gamma\gamma$ events with one electron escaping down the beam pipe.

The deviations between the photon's energy, azimuthal and polar angles, and

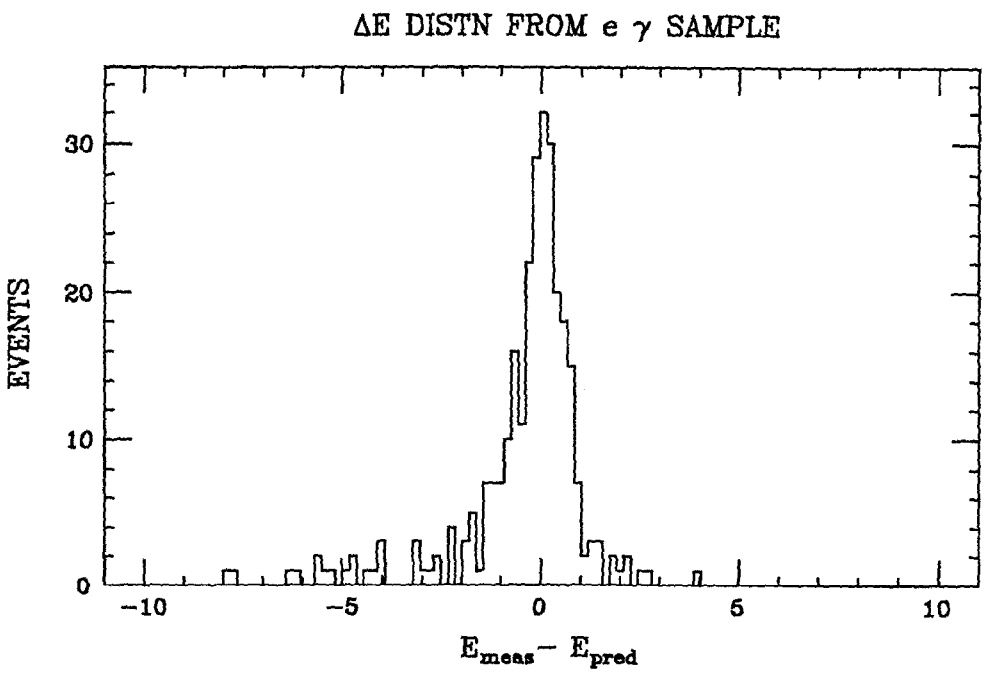

Figure 6.9. ΔE Distribution from $e\gamma$ Event Sample. This distribution shows the deviation between the measured photon energy and that predicted from the $ee\gamma$ hypothesis for 283 events. Only those events which have the photon in the LA calorimeter are considered here since the best possible energy measurement was desired.

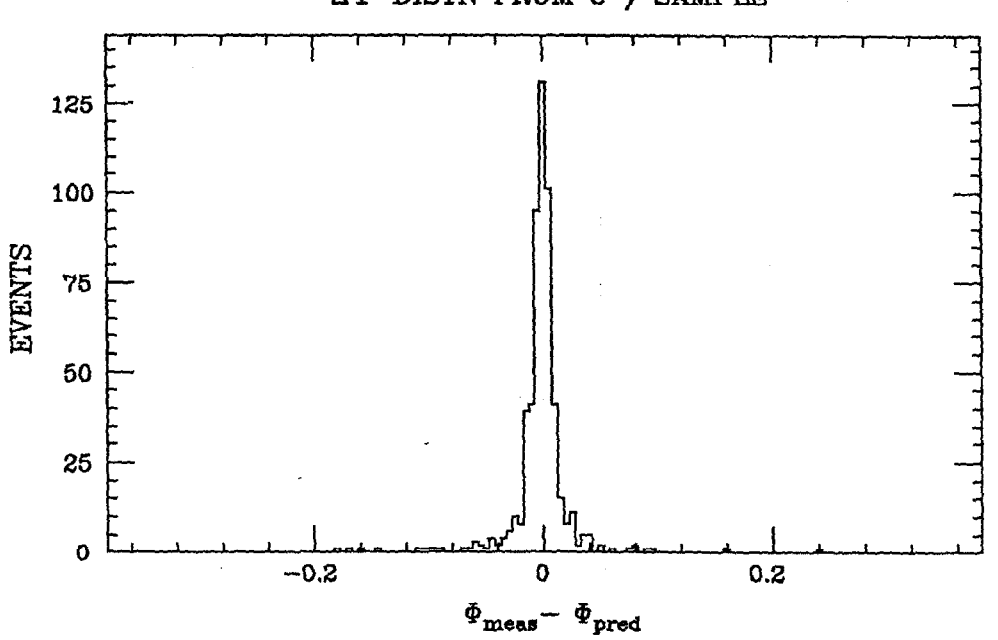

Figure 6.10. ΔΦ Distribution from $e\gamma$ Event Sample. This figure shows the distribution of the difference between the measured ϕ of the photon and that predicted from the $ee\gamma$ hypothesis. A total of 572 events are histogrammed.

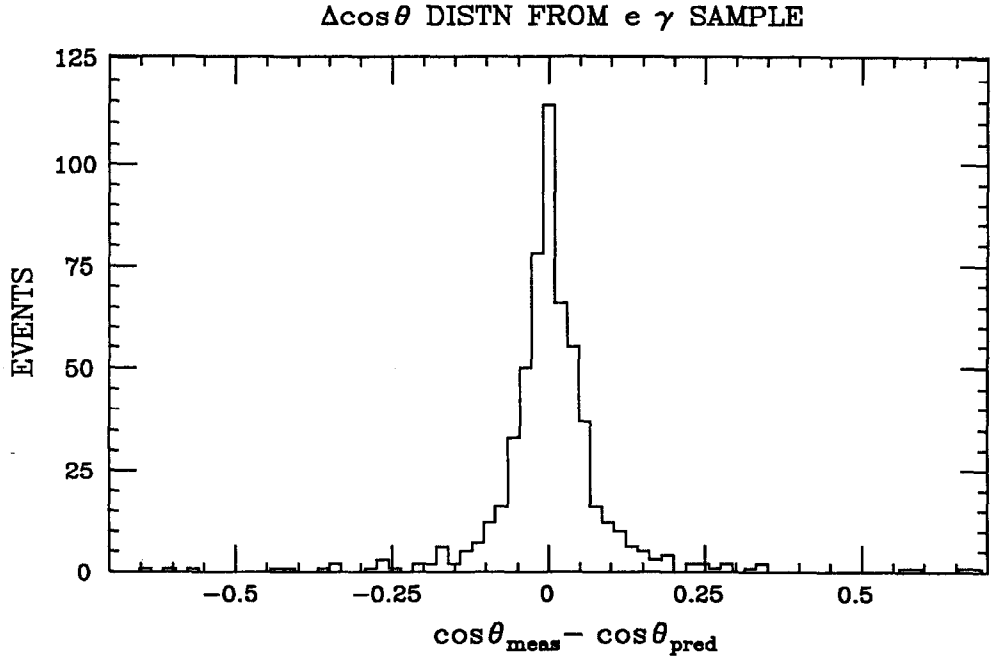

Figure 6.11. $\Delta\cos\theta$ Distribution from $e\gamma$ Event Sample. This figure shows the distribution of the difference between the measured $\cos\theta$ of the photon and that predicted from the $ee\gamma$ hypothesis. A total of 572 events are histogrammed.

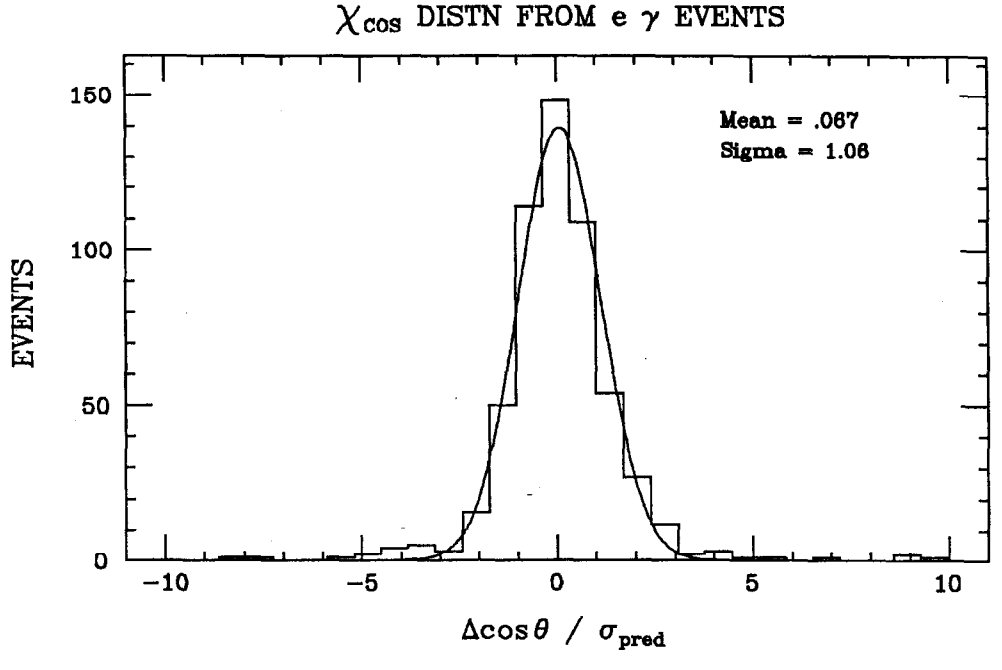

Figure 6.12. $\chi_{\cos}$ Distribution from $e\gamma$ Event Sample. This figure shows the $\chi_{\cos}$ distribution for the 572 $e\gamma$ events assuming the $ee\gamma$ hypothesis. Also shown is a fitted Gaussian. The tails were excluded from the fit since they are due to higher order radiative processes, and non-Gaussian measurement errors. See also Fig. 6.13.

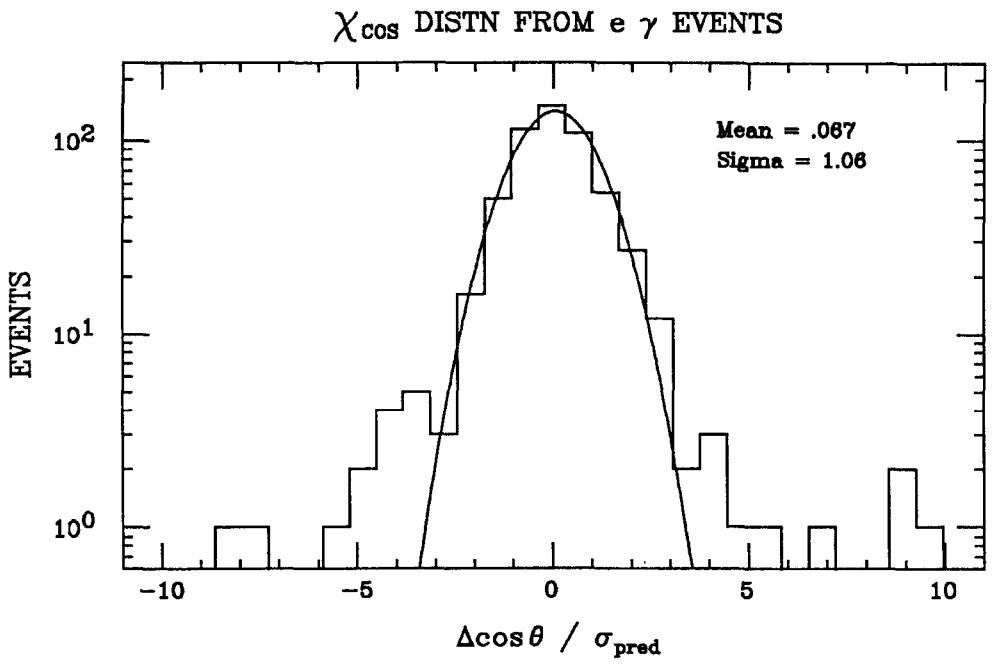

Figure 6.13. χ_{cos} Distribution from $e\gamma$ Event Sample on a Semi-Log Plot. This is the same data as presented in Fig. 6.12 but on a semi-log plot. This plot exhibits the non-Gaussian tails more prominently.

those predicted from the $ee\gamma$ hypothesis are shown in Figures 6.9–6.11. A total of 572 $e\gamma$ events were studied. The energy deviation plot, shown in Fig. 6.9, was made with the subset of $e\gamma$ events which had the photon well within the acceptance of the LA calorimeter. Those events with the photon in the endcaps were not included because of the endcap's poor energy resolution. Note that the distribution has an asymmetric low energy tail. This clearly shows that higher order radiative processes contribute to the data set. These higher order processes tend to overestimate the photon energy under the three body kinematic assumption. Fig. 6.10 shows the $\Delta\phi$ distribution. It is fortunate for this analysis that it is extremely narrow, having a FWHM† of 0.02 radians. This distribution is dictated by the requirement that $p_\perp$ balance. It is not heavily influenced by higher order radiative processes since the extra photon(s) are either collinear with the beam pipe, or with the detected electron. Photons which are collinear with the beam pipe arise from initial state radiation and tend not to carry much $p_\perp$.

† FWHM stands for Full Width Half Maximum.

Photons which are collinear with the detected electron arise from final state radiation and do not carry much momentum transverse to the electron's direction.

The polar angle deviations, shown in Fig. 6.11, are the most important of these distributions, as will be discussed in the next section. The ability to be able to predict the photon's cosine is tested by forming a $\chi_{\cos}$ distribution, where

$$\chi_{\cos} = \frac{\Delta \cos\theta}{\sigma_{\text{pred}}} = \frac{\cos\theta_{\text{meas}} - \cos\theta_{\text{pred}}}{\sigma_{\text{pred}}}.$$

Fig. 6.12 shows a plot of $\chi_{\cos}$, the normalized error distribution in the cosine of the gamma polar angle, with a Gaussian fit superimposed. The Gaussian fit shown in the figure excludes the tail of the distribution and is consistent with a mean of zero and unit width. The polar angle deviations therefore agreed well with those expected from experimental uncertainties except for the small number of events contained in the tails. The tail arose from soft radiative corrections and non-Gaussian tails in experimental resolutions. The semi-log plot shown in Fig. 6.13 shows the tail more prominently. Roughly 4% (25 of 272) of the $e\gamma$ events were in the tails of the $\chi_{\cos}$ distribution. For purposes of this analysis, we assume that the 3-body kinematic assumption provided an experimental handle on the QED background, with the realization that the tail events form an unavoidable background. Fortunately, this component of the background was small, as will be discussed later.

6.3 Single Electron Selection Cuts- Part 2

6.3.1 The $ee\gamma$ QED Background Cut

As stated above, events from the lowest order QED processes ($ee\gamma$ events) can mimic the singly produced selectron topology when the photon falls into an uninstrumented or inefficient region of the detector and one electron is within 2° of

the beam pipe. To eliminate these events we treated all single electron candidates as if they were $ee\gamma$ events. Thus, the recoil direction of the hypothetical gamma was determined for each event by assuming the unseen electron was scattered at 0°. The observed distribution of recoil angles is shown in the two scatter plots shown in Fig. 6.14. The projection of these plots onto the $|\cos\theta|$ axis is histogrammed in Fig. 6.15. This distributions are all consistent with being predominately from $ee\gamma$ events. The distribution for $ee\gamma$ events is expected to rise rapidly above a cosine of 0.70 for three reasons; first, there is an uninstrumented region between the LA and endcap calorimeters, secondly, the endcap calorimeter has a break in azimuthal coverage, and thirdly, there is a relatively large probability (2.5% as determined by a Monte Carlo simulation) that a photon will pass through the endcap undetected. The vast majority of the single electron events arise from $ee\gamma$ events where the photon has gone through the keyway. This is quite clear from the scatter plot. It should be mentioned that the cut on the detected electron's ϕ being more than 2.7° from the gaps between LA modules is responsible for the depleted population of events down a strip in the middle of the keyway.

The feedthrough of QED events into the data sample from the above sources can be eliminated by requiring that the photon recoil angle from the three body hypothesis be located well within the LA calorimeter. This final cut on the recoil angle ($\cos\theta_\gamma$) was determined by studying the sample of events which had both a detected electron and a detected photon. Fig. 6.16 shows the polar angular distribution of detected photons in the 28.1 pb^{-1} $e\gamma$ data sample. This plot is very important because the events that should have fallen in the four empty bins, with $0.7125 \leq |\cos\theta| \leq 0.7500$, represent the most difficult $ee\gamma$ background to eliminate from the selectron search. This is because the errors in locating the photon from the measurement on the electron can often put the photon inside the LA acceptance when it actually fell into the crack. Thus, some allowance for this effect must be made, resulting in an acceptance loss for real selectron events.

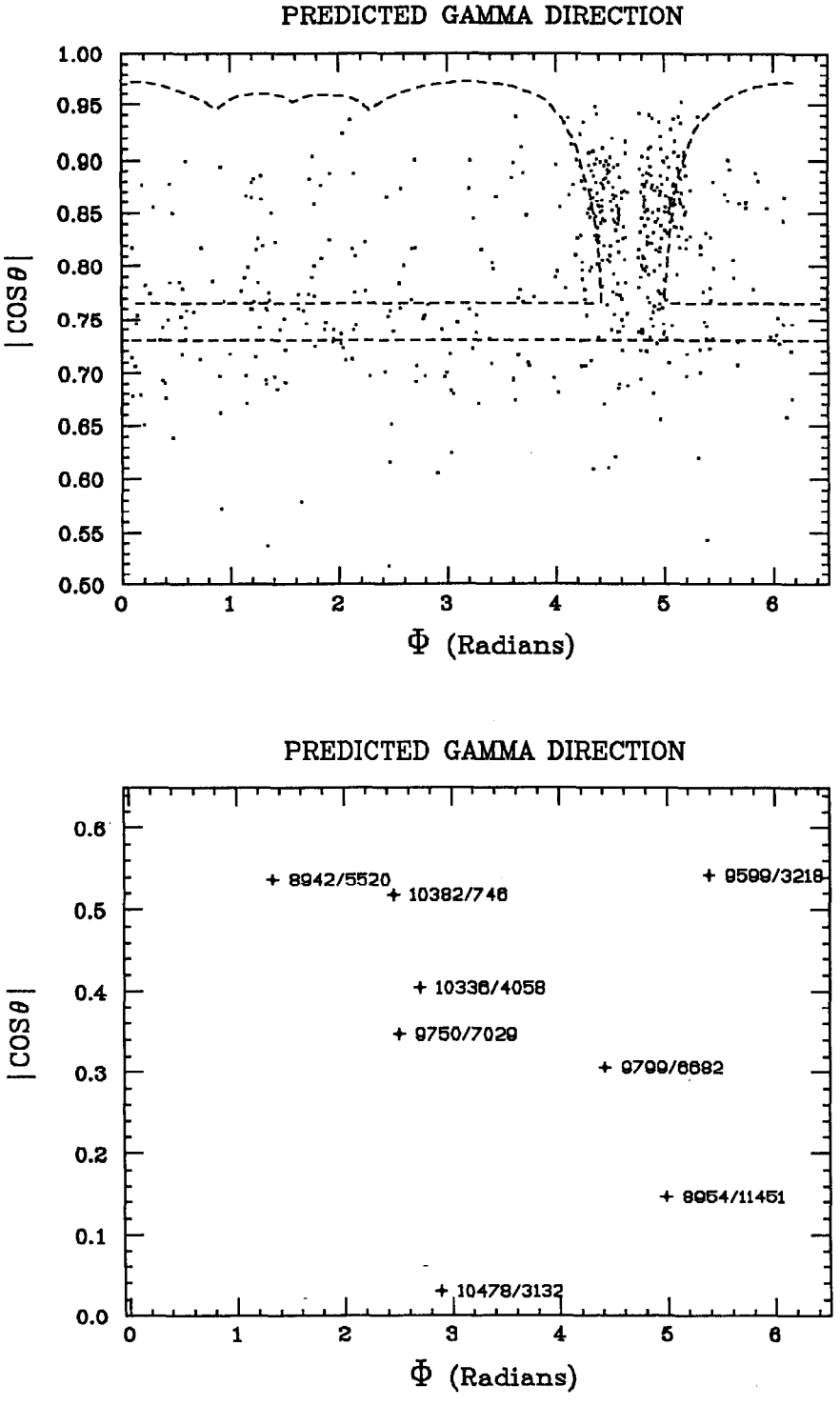

Figure 6.14. $|\cos\theta_\gamma|$ *vs.* ϕ Scatter Plot for Hypothetical Photon. The above two plots show the scatter plot of the hypothetical photon's direction for selectron events under the $ee\gamma$ hypothesis for the 123 pb^{-1} data set. The lower plot also shows the run/record number of the events with $|\cos\theta_\gamma| < 0.54$. The dotted line in the upper plot outlines the calorimetric acceptance.

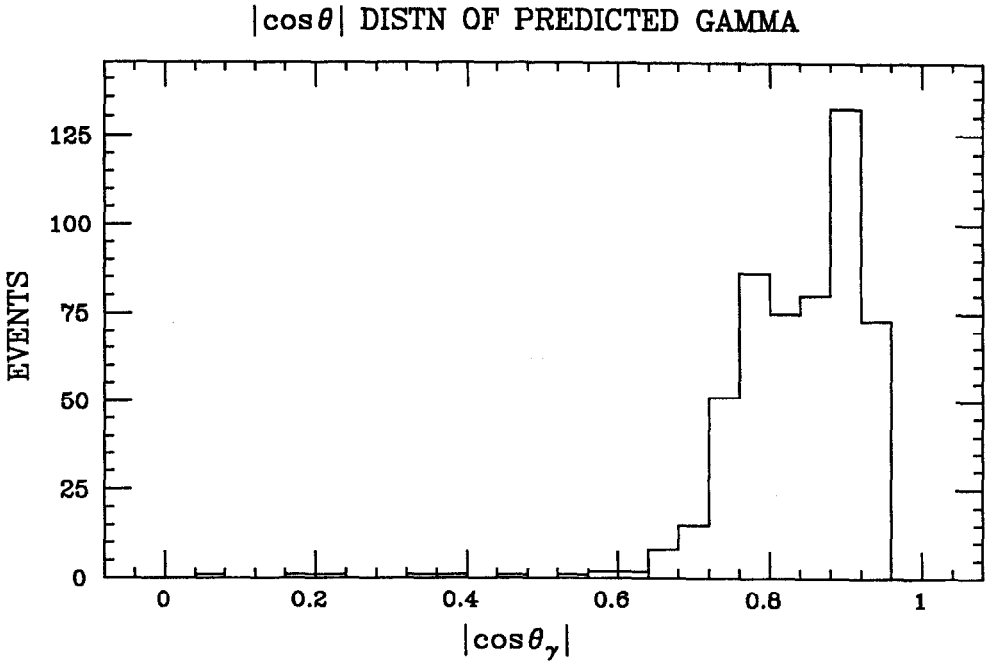

Figure 6.15. $|\cos\theta|$ Distribution of the Hypothetical Photon. Shown here is the distribution of the absolute value of the cosine of the photon under the $ee\gamma$ assumption. The data shows a strong tendency to concentrate in regions of poor photon detection efficiencies.

For the purpose of obtaining the greatest sensitivity it was desired to eliminate the QED background completely. While this could not be guaranteed in theory, we adopted the following approach in practice. We assumed that all the QED background which is not immediately rejected under the 3-body hypothesis is due to those events where the photon fell into the crack, *i.e.* the four empty bins in Fig. 6.16. From the angular distribution of the detected photons in these events, the number of events with an undetected photon falling in the region between the LA and endcap calorimeters ($\cos\theta$ between 0.72 and 0.75) was determined to be 266 ± 16 for the 123 pb^{-1} data set. Next, we assume that this number is entirely represented by $ee\gamma$ events, ignoring higher order processes for the moment. Then, we can design a cut in $\cos\theta_\gamma$ from the kinematic fit, such that only one event has a statistical chance to be below this cut. In other words, we cannot allow the errors from the 3-body kinematic fit to place photons, which fell into the crack, into the final LA acceptance. We must therefore restrict the LA acceptance to be

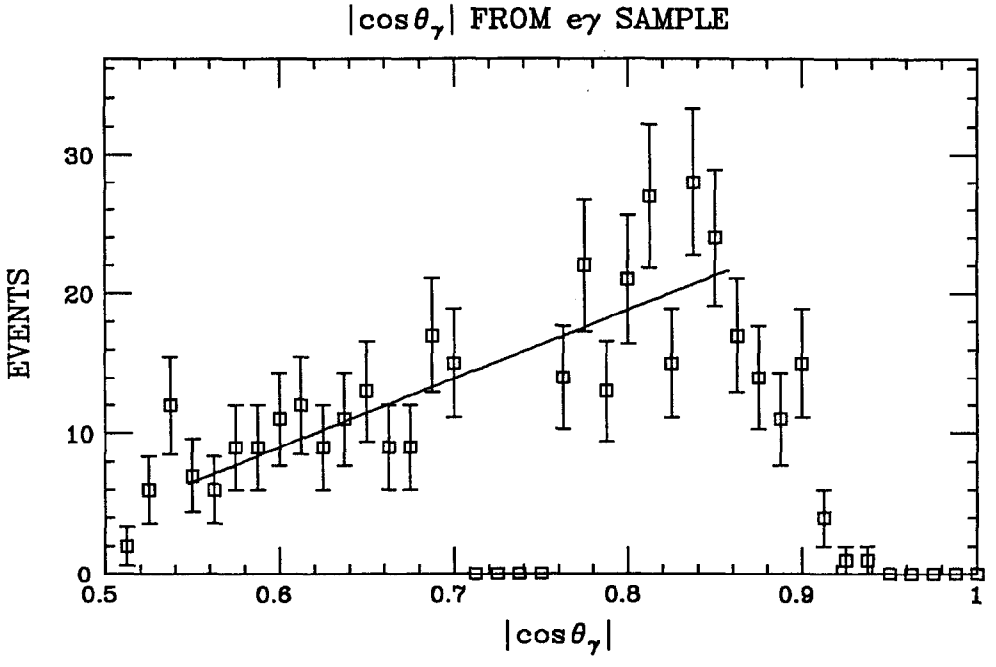

Figure 6.16. $|\cos\theta_\gamma|$ Distribution from $e\gamma$ Sample. This figure shows 383 events from the 28.1 pb^{-1} $e\gamma$ sample whose photons have $|\cos\theta| > 0.500$ in bins of 0.0125. The four zero bins with $0.7125 \leq |\cos\theta| \leq 0.7500$ are due to the crack between the LA and Endcap calorimeter. The straight line fit is the result of a linear least squares fit for the data with $0.55 \leq |\cos\theta| \leq 0.85$.

less than its fiducial volume would allow.

The actual determination of the $\cos\theta_\gamma$ cut was done by using the number of events where the photon fell into the crack, and the resolution in positioning photons when they were near the crack. Thus, we used the following formula to determine how many σ from the crack to place the cut:

$$\frac{N_{crk}}{\sqrt{2\pi\sigma^2}} e^{-(n\sigma)^2/2\sigma^2} \leq 1$$

where,

- n is number of σ away from the crack that the cut must be,
- σ is the average error in positioning $\cos\theta_\gamma$ near the crack, *i.e.* $0.65 \leq |\cos\theta_\gamma| \leq 0.75$.

Using $N_{crk} = 266$ and $\sigma = 0.045$ we arrive at $n = 3.82$, which fixes the cosine cut

at 0.54. Thus we require $\cos\theta_\gamma < 0.54$ as a definition of our selectron acceptance. And although this cut severely reduces the $ee\gamma$ background it maintains reasonable efficiency for high mass selectrons, since their angular distribution tends to be fairly flat. Thus, we may add the following item to the list of cuts:

12.) QED background cut required $\cos\theta_\gamma \leq 0.54$ for the photon under the $ee\gamma$ hypothesis.

This cut translated into a restricted acceptance in the E–$\cos\theta$ plane for the detected electron. The final acceptance is shown in Fig. 6.17. As can be seen, this acceptance has the effect of placing an overall minimum energy cut of ~ 9.40 GeV on the candidate electrons for all angles. The actual acceptance places an effective minimum energy cut that is a function of angle. This minimum increases dramatically as the electron is scattered at larger and larger angles with respect to its incident direction.

6.4 Handscan Results

The twelve cuts which have so far been described were executed entirely with a FORTRAN program run within the standard Mark II offline analysis package. All events which passed these criteria were further subjected to a handscan in order to guarantee the event cleanliness. As can be seen in the lower plot in Fig. 6.14, a total of 8 events had $\cos\theta_\gamma \leq 0.54$. These events are listed in Table 6.1.

None of the events survived the handscan. Illustrative views of 2 of these events are shown on the following pages. The most surprising of all of these rejected events is event 10478 / 3132. This event has its hypothetical photon at almost 90° with respect to the beam pipe. The probability that this is an $ee\gamma$ event with its photon falling in the crack is vanishing small. However, it was found upon visual inspection of the event that there was in reality a photon at the predicted location which was missed by the calorimetric tracking code because the photon was extremely late in converting. The raw pulse heights for the strips in this

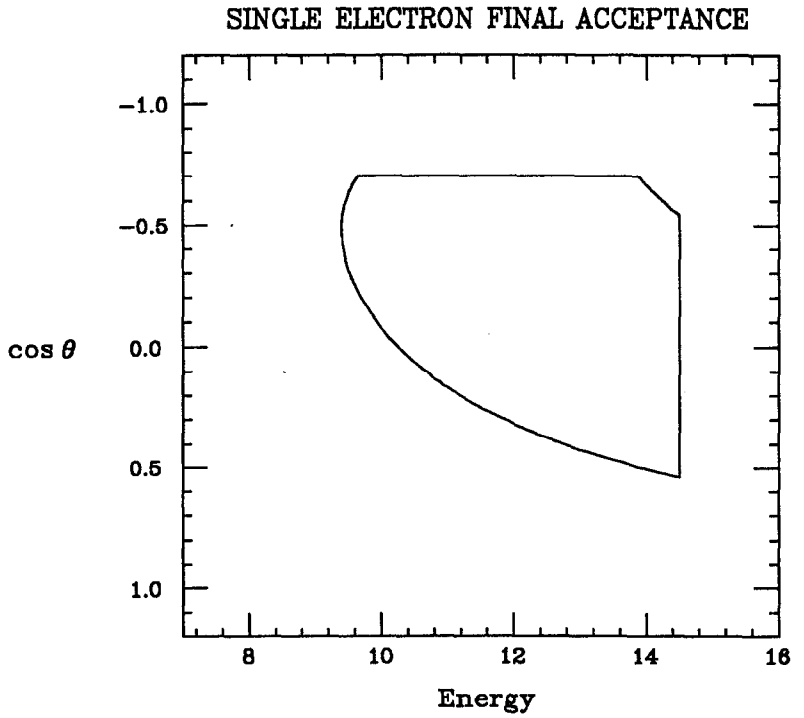

Figure 6.17. Single Electron Final Acceptance. The final acceptance in energy and $\cos\theta$ for single electrons is shown in this plot. The acceptance for positrons is the same after the mapping $\cos\theta \rightarrow -\cos\theta$. Events must fall within the closed contour.

module can be seen in Fig. 6.19. It is quite clear that a real photon converted in the last few layers of the LA module.

6.5 Background Estimates

Additional backgrounds were also expected from higher order QED processes, for example $ee\gamma\gamma$ events. These were also studied with the single prong plus photon background sample, since these events would, like the $ee\gamma$ events, become single prong candidates if the seen photon had fallen into an uninstrumented region. Since $ee\gamma\gamma$ events do not have 3-body kinematics, they are expected to populate the tails of the χ_{cos} distribution (Fig. 6.13), and also have a large missing mass. Background sample events which had a missing mass greater than 10 GeV/c^2 were called $ee\gamma\gamma$ events. An interpolation over the angular distribution of events of this type which passed the $\cos\theta_\gamma$ cut indicated a background for the selectron sample

Run	Record	E_γ	$\cos\theta_\gamma$	ϕ_γ	Comments
8942	5520	8.33	0.5368	1.3363	VC, DC
8954	11451	9.90	0.1470	4.9855	LA
9599	3218	9.09	0.5428	5.3837	LA, SAT
9750	7029	8.68	0.3467	2.5098	LA
9799	6682	11.36	0.3063	4.4204	LA
10336	4058	8.29	0.4043	2.6985	VC, LA
10382	746	11.38	0.5177	2.4562	VC, TOF
10478	3132	9.69	0.0303	2.8915	LA

Table 6.1. Single Electron Events with $|\cos\theta_\gamma| \leq 0.54$. This table lists the run/record number of single electron events whose hypothetical photon was below a cosine of 0.60. The photon's energy and angles are also listed as is the result of the handscan.

of 0.6 ± 0.5. A similar treatment applied to events with $|\chi_{cos}|$ between 2.5 and 6.0 and with missing mass less than 10 GeV/c^2 (presumably mismeasured events and $ee\gamma\gamma$ final states with one soft photon) predicted a background of 0.3 ± 0.2 events from this source. Finally, the backgrounds from two photon processes and tau production were determined by Monte Carlo studies to be 1.2 ± 1.2 and less than 0.6 respectively.

6.6 Efficiency Studies

6.6.1 Efficiencies

The set of experimental cuts outlined in the previous sections were designed to obtain as clean a sample of selectron events as possible. Unfortunately, these same cuts could also lose real selectron events. For example, the detector may not have triggered on the single electron final state, or the momentum reconstruction program, PTRAKR, could fail to track the event. The final interpretation of the

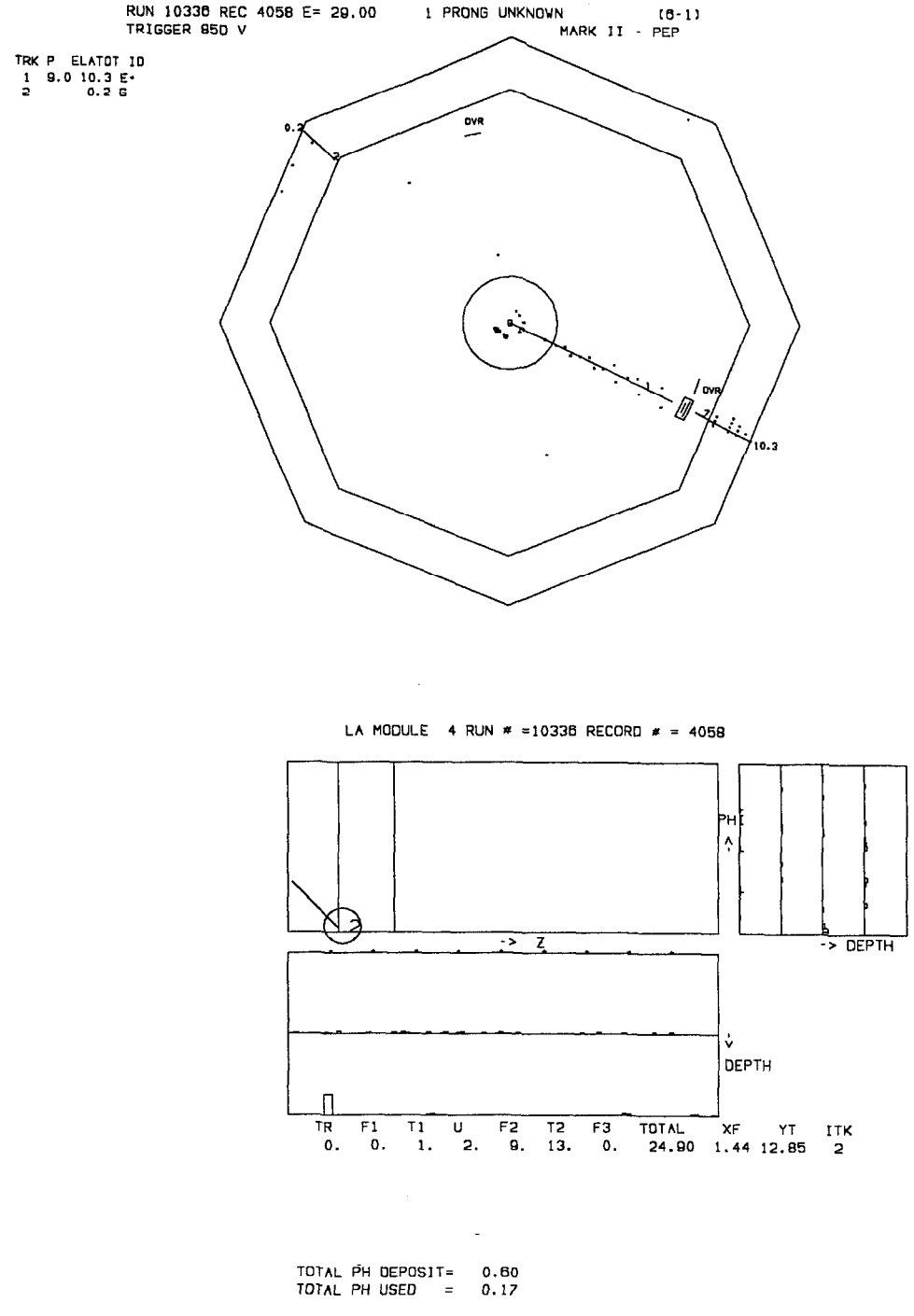

Figure 6.18. Display Plots for Event 10336 / 4058. Shown here are two plots for an event which had $\cos\theta_\gamma = 0.4043$. As can be seen the event had a large amount of activity in the VC, most probably due to backscattering from a showering particle. A very low energy photon has been found in the LA module opposite the charged track, near the edge of its acceptance. This event was rejected as a selectron candidate event.

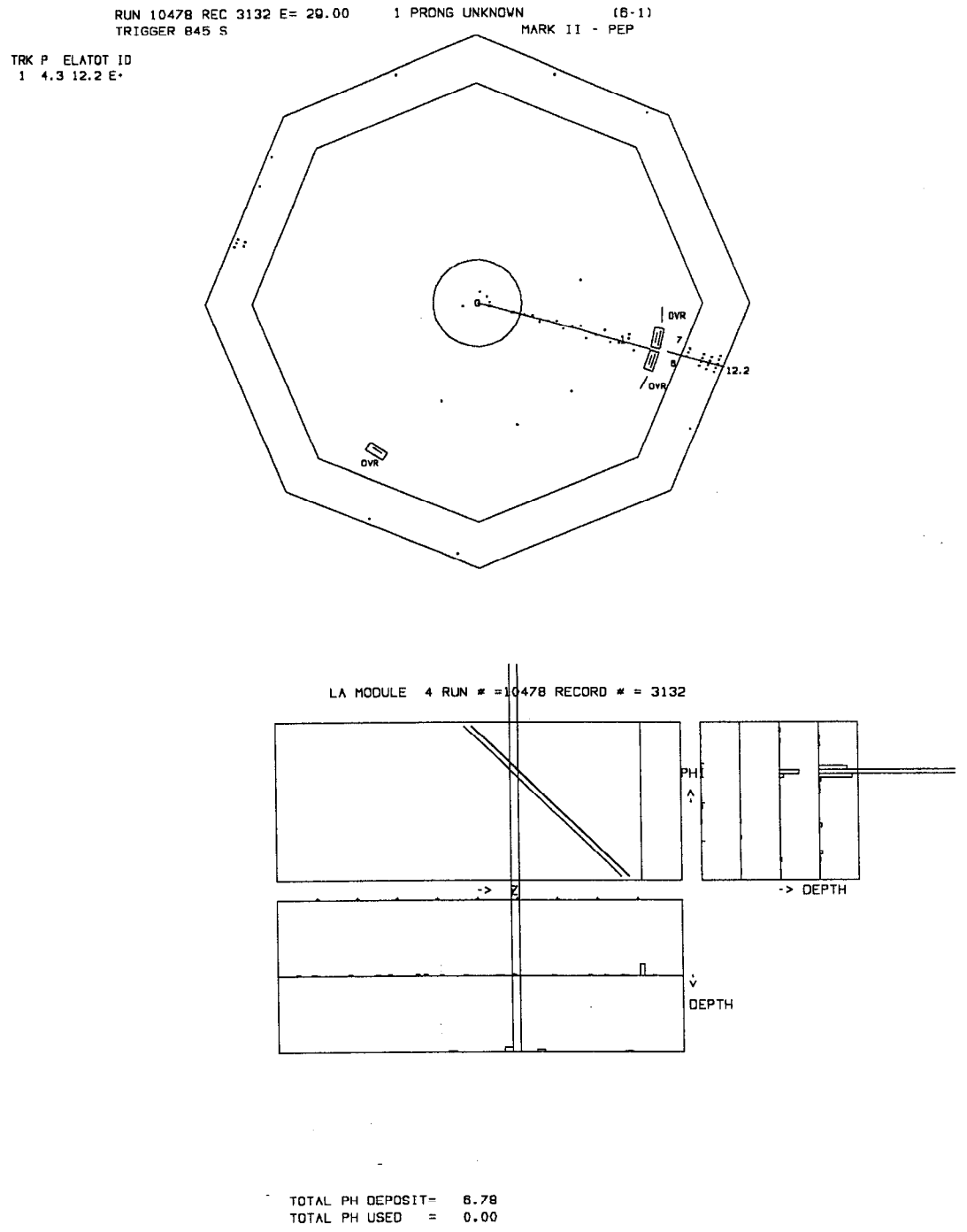

Figure 6.19. Display Plots for Event 10478 / 3132. The top plot shows the DC view of the event. Note that the LA module opposite the charged track has several hit LAZMS (hit LA strips), but no photon was found by the reconstruction program. The lower plot shows the pulse heights in this module. This plot clearly shows the presence of a late converting photon.

experiment results depended upon knowing the efficiency for selectron events to pass all the experimental cuts.

The experimental cuts can be divided into two categories; those designed to find single electron events, and those designed to reject backgrounds. The hypothetical selectron signal could therefore be lost in either two ways. First, the event could be there but not be found, either because the hardware failed to trigger or because the software did not properly reconstruct the event. Secondly, the event could be there but be rejected because of some kind of fake occupancy in a detector subsystem. An example of the latter includes a real event where the SAT system had some kind of noise pickup which gave a fake energy above the SAT energy cut of 3 GeV. Another example of a cut which was sensitive to fake occupancy is DAZCUT, which could also lose real events due to stray hits in the vertex chamber.

These efficiencies must be determined before the results of the experimental search can be meaningfully interpreted. Typically, the efficiencies of experimental cuts used in most analyzes are determined by Monte Carlo studies. This technique is reliable only in so far as the Monte Carlo programs are reliable. An alternative approach, which is not always available to the experimenter, is to use the data itself to monitor efficiencies by studying independent data samples. This latter technique was extensively used in this analysis. This was possible largely because of the simple topology of the final state signal. It is interesting to note that the very same QED processes which composed the search's primary background were in turn used to determine many of these efficiencies.

The efficiencies also needed to be studied as a function of time, or equivalently, of run number. This was necessary to account for changes in the detector over the long course, $\sim$ 2 years, of data taking. During this time many changes occurred, in both the hardware and the offline analysis. This analysis is especially sensitive to many of these changes. For instance, a trigger inefficiency of a few percent

Cuts	Efficiency (%)
A-Trigger	98.42 ± 0.08
D-Trigger	99.91 ± 0.02
CHUKIT	98.74 ± 0.01
DC Total Hit Wires	~ 100
PTRAKR	99.82 ± 0.02
SAT Energy	99.54 ± 0.04
Primary Vertex Cut	~ 100
$\delta\phi_{gap}$ Cut	94.00
DAZCUT	99.23 ± 0.03
Total Efficiency	89.98 ± 0.01

Table 6.2. Cut Efficiencies. This table shows the various cuts used for the search and their associated efficiencies.

does not affect a hadronic analysis where the typical event has a charged track multiplicity of 11. However, the selectron signal consisted of only one charged track, and so was directly sensitive to any trigger inefficiencies throughout data taking.

The actual procedures used to determine the efficiencies are outlined below. The efficiencies themselves are summarized in Table 6.2.

6.6.2 Efficiency Determination Procedures

1. *Trigger Efficiency.* The trigger efficiency was a product of two efficiencies, the charged tracking efficiency and the efficiency for an EM shower to generate a LA trigger. Both were studied with Bhabha events since Bhabha events satisfied both the 2 A-track trigger and the TED (2 D-track) trigger, in addition to the selectron trigger. Ignoring the vanishing small number of Bhabha events which fail both the A-trigger and the TED-trigger, we can

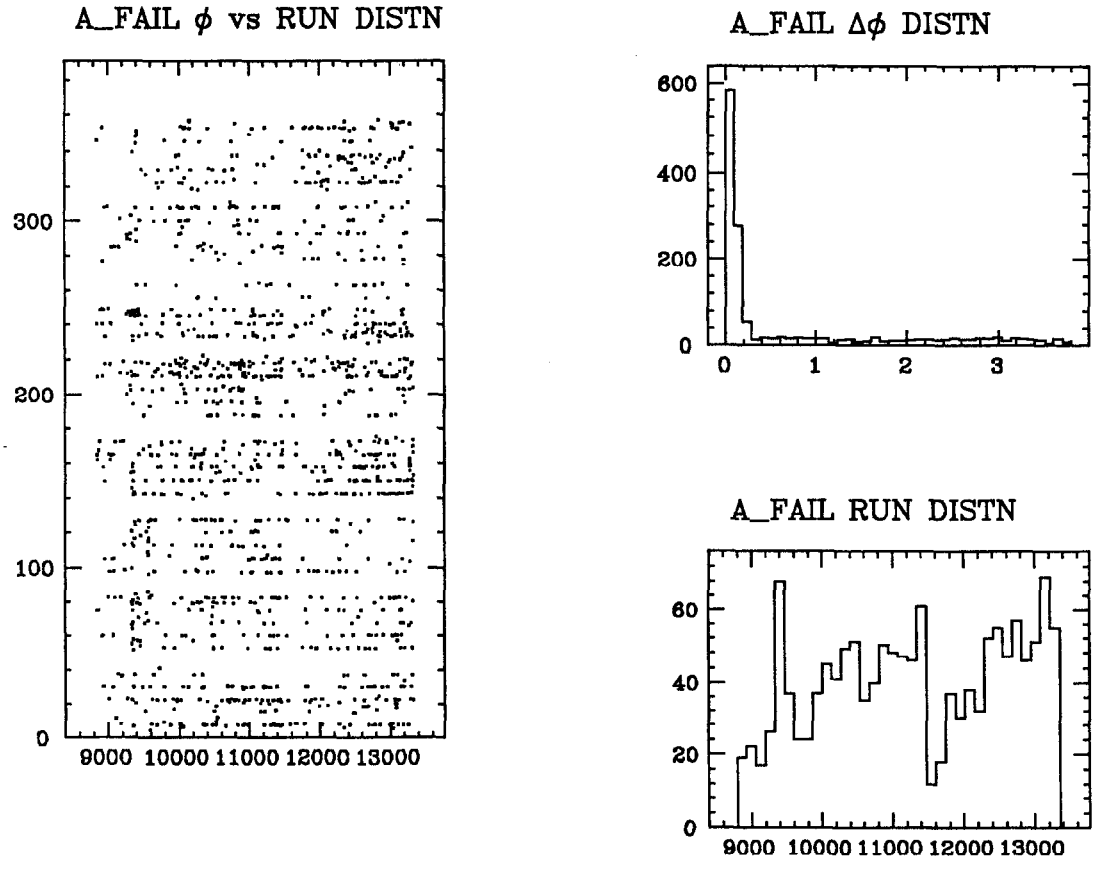

Figure 6.20. A-Trigger Efficiency. Shown here are three plots of Bhabha events which do not have an A-trigger. The scatter plot on the left shows the ϕ of the track versus its run number. The histogram of failures versus run number, *i.e.* the plot on the lower right, shows the projection. It correlates well with integrated luminosity. The plot on the upper right shows the failed event's distance, in degrees, from an edge of a TOF counter.

estimate each trigger efficiency by dividing the number of Bhabhas with the trigger by the total number of Bhabhas. A similar statement applies for measuring the TED trigger efficiency. Fig. 6.20 shows various plots of Bhabha tracks which failed the A-trigger. The inefficiency largely correlated with the cracks between TOF counters. Recall that a TOF hit is part of the A-trigger requirement. Fig. 6.21 shows various plots of Bhabha tracks which failed to have a D-trigger. There is virtually no inefficiency until run 11276. The $\cos\theta$ *vs.* ϕ scatter plot clearly shows that the inefficiency is due to hardware problems since the problem was well localized inside LA module 5. Further investigation showed that it was due to an unfortunate

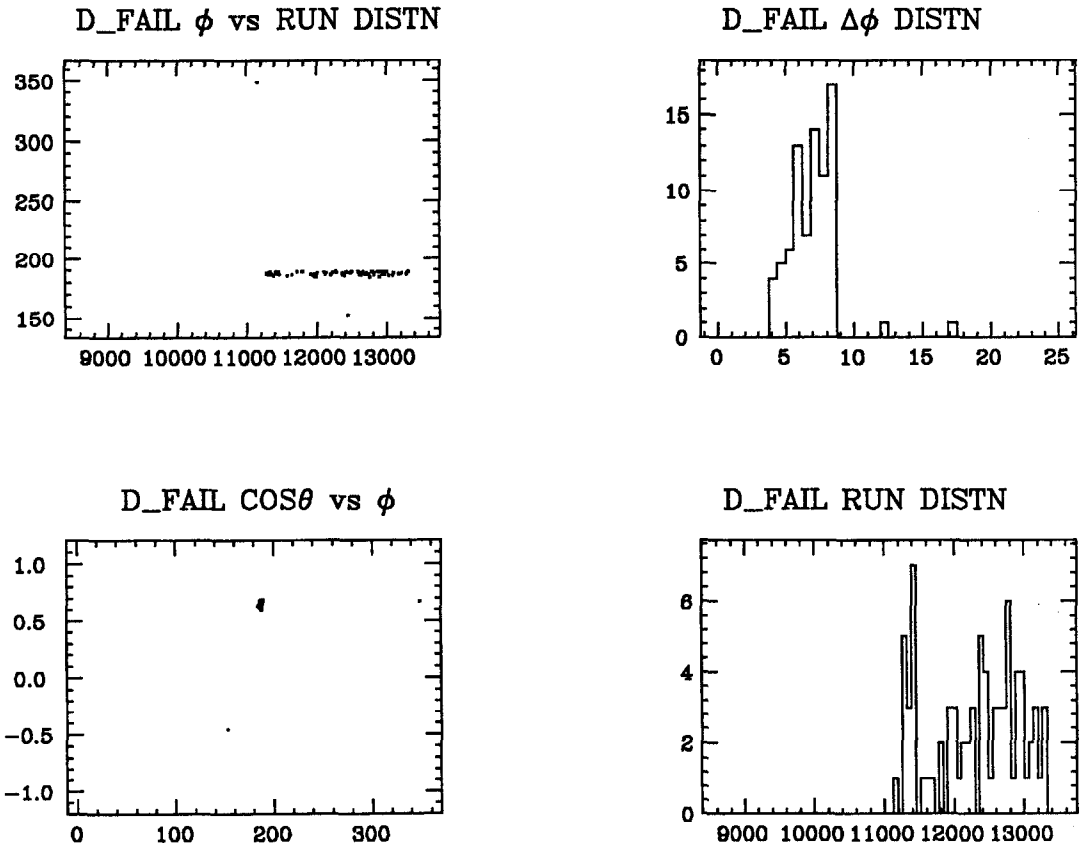

Figure 6.21. D-Trigger Efficiency. Shown here are three plots of Bhabha events which do not have a D trigger. The scatter plot on the left shows the ϕ of the track versus its run number. The histogram of failures versus run number, *i.e.* the plot on the lower right, shows the projection. The plot of failure positions, shown on the lower left, clearly show that most of the failures are localized within a LA module.

alignment of dead channels within this module.

2. *LA Energy Cut Efficiency.* The efficiency of the 5.8 GeV LA energy cut was essentially 100% over the final single electron acceptance, which had an effective energy cut of at least 9.4 GeV. The selectron Monte Carlo included the energy resolution of the LA in determining the final selectron limit.
3. *CHUKIT efficiency.* CHUKIT was a prefilter used to select events from the raw data tape for PASS2 processing. CHUKIT made a variety of cuts in an attempt to remove junk events from the data. Since CHUKIT was called before the track reconstruction programs its cuts were made strictly on the hardware information, such as the number of A-triggers counted by each

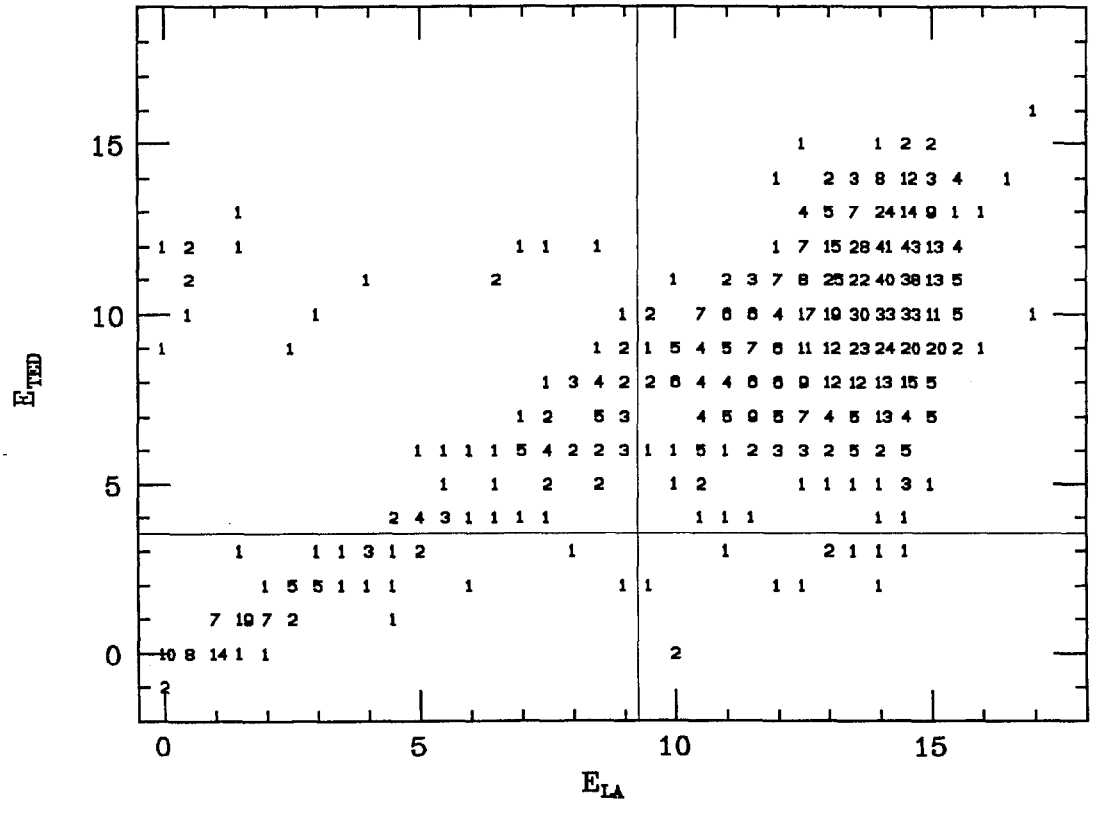

Figure 6.22. E_{TED} *vs.* E_{LA} for Charged Tracks. The LA response for an isolated (*i.e* only one track in a single module) charged track is shown here. The vertical line drawn shows the effective energy cut made by the final selectron acceptance. The horizontal cut shows the effective energy cut made on E_{TED} by CHUKIT. This plot was made by studying a sample of $ee\gamma$ events on 20 pb^{-1} of data.

curvature module. The cut most relevant to this search involved the E_{TED} hardware response of the LA system. E_{TED} was the energy sum in the front portion of module used in the D-track trigger. Each module's E_{TED} response was recorded in the raw data. CHUKIT required that the $\sum E_{TED}$ over latched LA modules be greater than 4 GeV when only 1 A-track was found in the event. This was the case for the events used in this search, since they only had one electron in the final state. In order to understand E_{TED} it is necessary to discuss the LA hardware readout in more detail. Each ganged LA strip was coupled, via transformers, to a FET output stage. The FET output voltage signal was split into two paths for strips in the front half

of a module. One path went to an amplifier circuit for subsequent readout by a SHAM, *i.e.* a Sample And Hold Module. This was the signal used by the shower reconstruction programs. The other path went to an analog summer, which summed up eight channels into what was called the ninth channel. The ninth channel signals were amplified and summed together for each module to form the E_{TED} signal. This signal caused a D-trigger if it was above threshold, or latched. The trigger signal went through entirely different electronics than the energy readout signals in order to get a faster output signal for triggering. The final shower energy, as found by the LA reconstruction program, did not use the E_{TED} signal. Instead it used the SHAM signals, including the strips from the back portion of the modules. Furthermore, the final shower energies included various corrections, such as leakage corrections, which could only be made after the shower was fully reconstructed. All these facts together imply that, even if a module contained only one showering track, its E_{TED} energy measurement rarely equaled the final energy of the shower. Thus, CHUKIT's E_{TED} energy cut required a separate study of the LA E_{TED} response. This was done by studying $ee\gamma$ events, and comparing the E_{TED} response of a module with a single charged track entering it with the final reconstructed shower energy of the charged track. A two dimensional scatter plot showing the results of this study is shown in Fig. 6.22. CHUKIT's efficiency was determined by comparing the number of tracks with $E_{TED} > 4$ GeV with the number with $E_{TED} < 4$ GeV for all tracks having $E_{LA} > 9.4$ GeV. The latter energy is the effective LA energy cut made by the final selectron acceptance.

4. *DC Total Hit Wires Cut Efficiency.* In order to eliminate cosmic shower events, a cut was made on events with 50 or more hit wires in the DC. This efficiency was studied with an $e\gamma$ data sample and was found to be essentially 100%, *i.e.* no real events were lost.

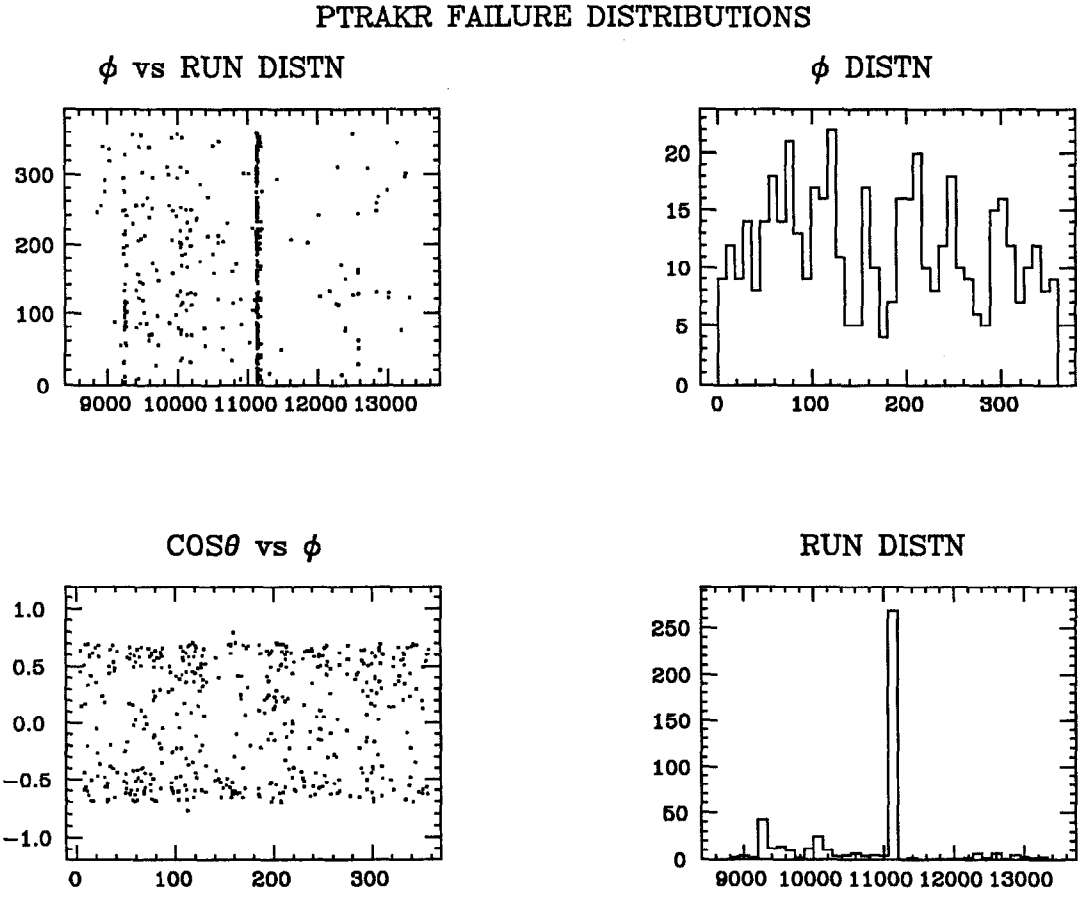

Figure 6.23. PTRAKR Tracking Efficiency. Various distributions of Bhabha events with a missing charged track are shown here. The angles were determined from the LA shower information. The cos *vs.* ϕ distribution essentially maps out the normal Bhabha distribution, *i.e.* there are no hardware associated problems. However, the run number distribution does show a period of poorer performance, for runs 11114–11473. This inefficiency was due to difficulties in operating the DC during this time (*i.e.* the wire voltages were adjusted frequently). The chamber was repaired in the summer, and the voltages raised, resulting in much better efficiencies thereafter.

5. *PTRAKR Efficiency.* PTRAKR was the reconstruction program for charged tracks. Its operation was essential for the search since it was used to find the single electron track in the wire chambers. PTRAKR was a very sophisticated program which does both pattern recognition and track fitting. Its performance was quite good, especially when the charged tracks were reasonably isolated (*i.e.* no multiple tracks in a cell). However, PTRAKR did occasionally miss tracks, thus giving rise to another search

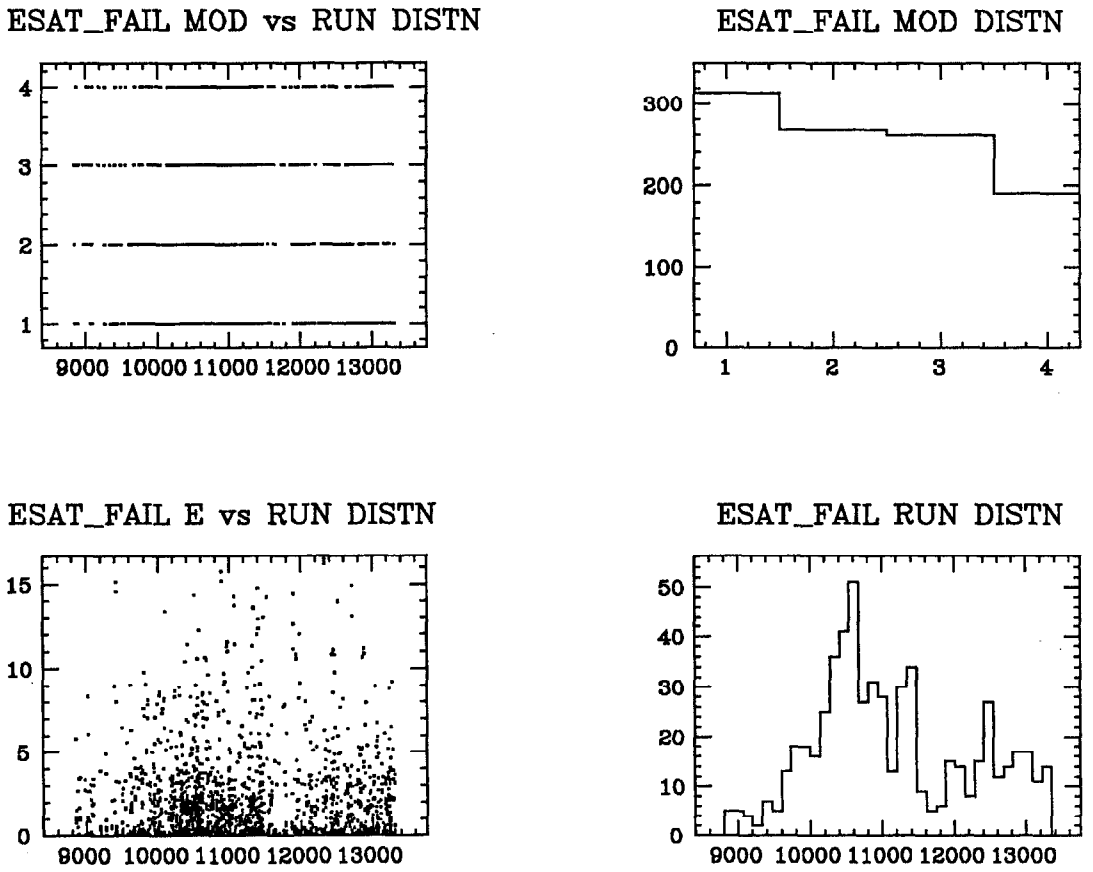

Figure 6.24. ESAT Cut Efficiency. Very collinear (< 1°) wide angle Bhabha events were used to study the occupancy of the SAT shower chambers, as shown above. Only events with a SAT latched energy sum of more than 3 GeV are plotted. The plot on the lower right shows this occupancy as a function of run number. The other plots shows the responses of the individual latched modules.

inefficiency. PTRAKR's efficiency was studied with Bhabha events, by looking for events with two good collinear showers and more than 10 hit chamber layers (VC and DC) within a 30° cone centered on the shower. As can be seen, there was a poor period of running, which was subsequently fixed. This efficiency dropped from 99.8% to ~ 90% during a 60 run period, runs 11108–11174. The efficiency averaged over all the selectron search runs was used in Table 6.2. Note that this efficiency refers to PTRAKR's ability to find isolated tracks. A different efficiency would be have to quoted for high multiplicity hadronic events, see Ref. 83.

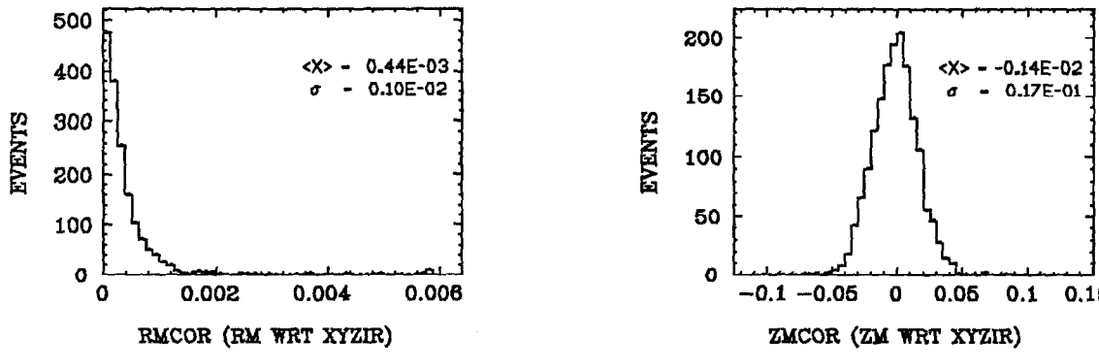

Figure 6.25. R_m and Z_m Distributions. The above shows the distance of closest approach distributions of tracks (in meters) with respect to the average beam spot. The average beam spot was determined over blocks of several runs, and was allowed to vary as running conditions changed. The point of closest approach was determined by minimizing r_m since the z tracking resolution is poorer, and because the PEP beam had a z spread much bigger than its transverse spread (which was roughly 100μ in y and 400μ in x). The analysis cuts were $r_m < 0.05$ m and $z_m < 0.15$ m.

6. *SAT Energy Cut Efficiency.* The inefficiency due to fake occupancy in the SAT chambers was studied by looking for fully reconstructed Bhabha events, with acollinearity and acoplanarity less than one degree, and examining the SAT chamber occupancy. All events which had a latched energy sum greater than 3.0 GeV were flagged.
7. *Primary Vertex Cut Efficiency.* These cuts ($r_m < 5$ cm, $z_m < 15$ cm) were quite generous and did not lose any real events. This was determined by looking at the r_m and z_m distributions of Bhabha events. Representative plots of these distributions can be found in Fig. 6.25.
8. E_{LA} *Energy Cut Efficiency.* The event sample cut of 5.8 GeV was largely arbitrary, and used only to obtain a reasonably size final data set. The true energy cut was effectively 9.4 GeV as can be seen from the final electron acceptance. Thus, it was quite reasonable to study the LA construction efficiency with Bhabha events, by looking at events with two collinear, high momentum tracks, with only one good shower.

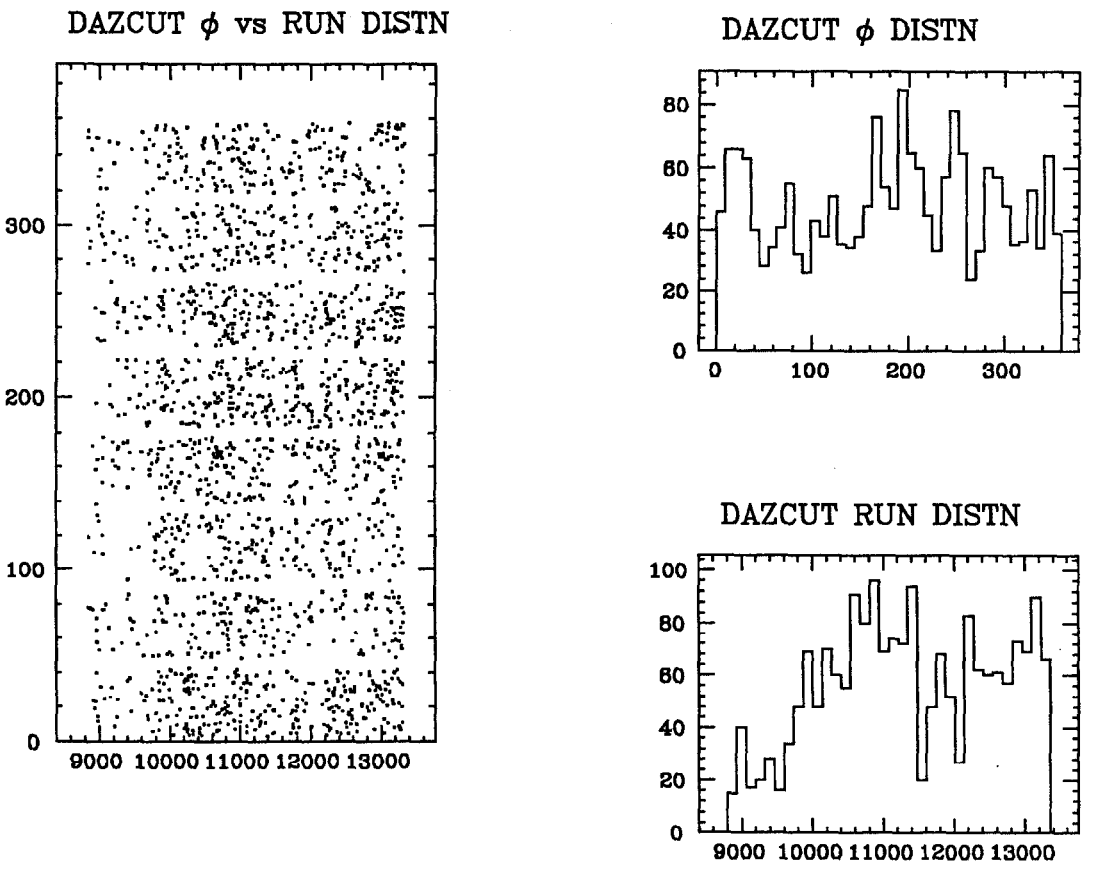

Figure 6.26. DAZCUT Cut Efficiency. DAZCUT failed Bhabha event distributions are shown in the above plots. These Bhabha events had 3 or more layers of the VC hit within a 30° cone centered perpendicular to the charged tracks. The distribution versus run number essentially follows the luminosity.

9. *The $\delta\phi_{gap}$ Cut Efficiency.* This cut was strictly a cut in fiducial volume and was therefore simply given by $8*(45-2.7)/360$. The size of $\delta\phi_{gap}$ was determined by studying the LA response for Bhabha events at SPEAR.

10. *DAZCUT Efficiency.* This cut was important for removing $ee\gamma$ background from the final data sample. It, unfortunately, also introduced an inefficiency. This inefficiency was studied with Bhabha events, by looking for extra VC dazms in a 45° cone on either side of the Bhabha pair. Alternatively, $\gamma\gamma$ events could also be subjected to DAZCUT. The efficiency determined by both methods agreed. Various distributions of DAZCUT failed events are shown in Fig. 6.26.

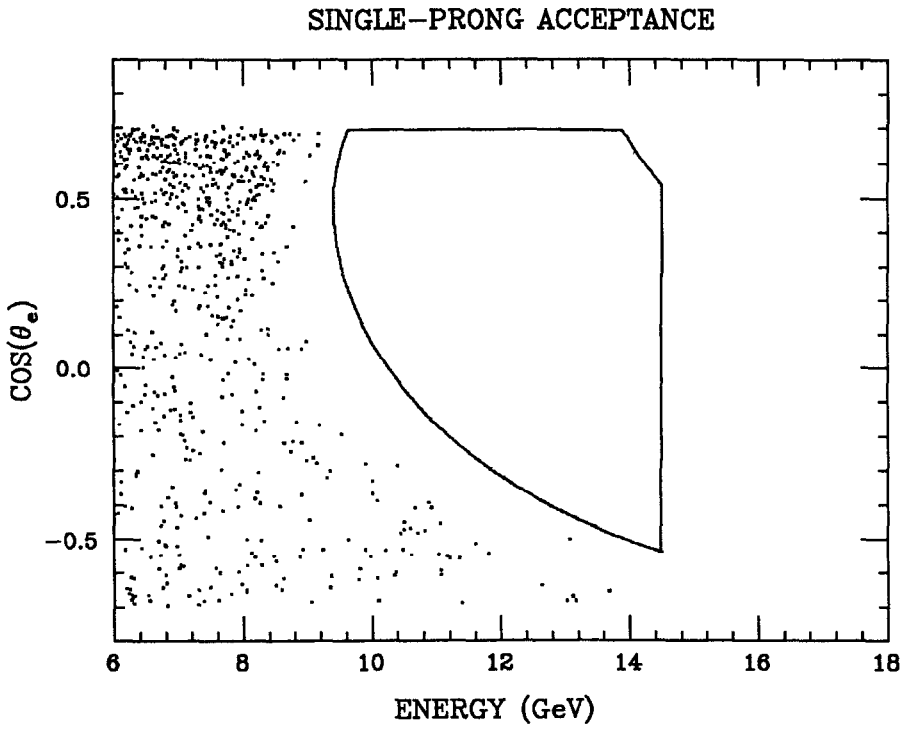

Figure 6.27. Final Single-Prong Acceptance. The enclosed contour shows the final acceptance for electron energies and angles. The same acceptance applies to positrons under the transformation $\cos\theta \rightarrow -\cos\theta$. Both electrons and positrons (with cosine mapping) are plotted above. No events fell into the final acceptance.

The final experimental answer must take in to account the efficiency of all the above cuts. The combined efficiency, given that the cuts are independent of each other, is just the product of all the individual efficiencies, ϵ_i. This essentially implies that the search had an effective integrated luminosity, L_{eff}, given by

$$L_{tot} = \epsilon_{tot} L \qquad \text{where,} \qquad \epsilon_{tot} = \prod_i \epsilon_i = 89.98 \pm 0.01\% \, .$$

6.7 Conclusions

The effect of all the cuts used in this analysis is to constrain the single measured prong to lie within the contour shown in Fig. 6.27. The acceptance is shown for negative charged prongs, and is the same for positive charged prongs except that $\cos\theta$ must be replaced by $-\cos\theta$. No single electron events were observed to fall into the selectron acceptance. Therefore, we conclude that all

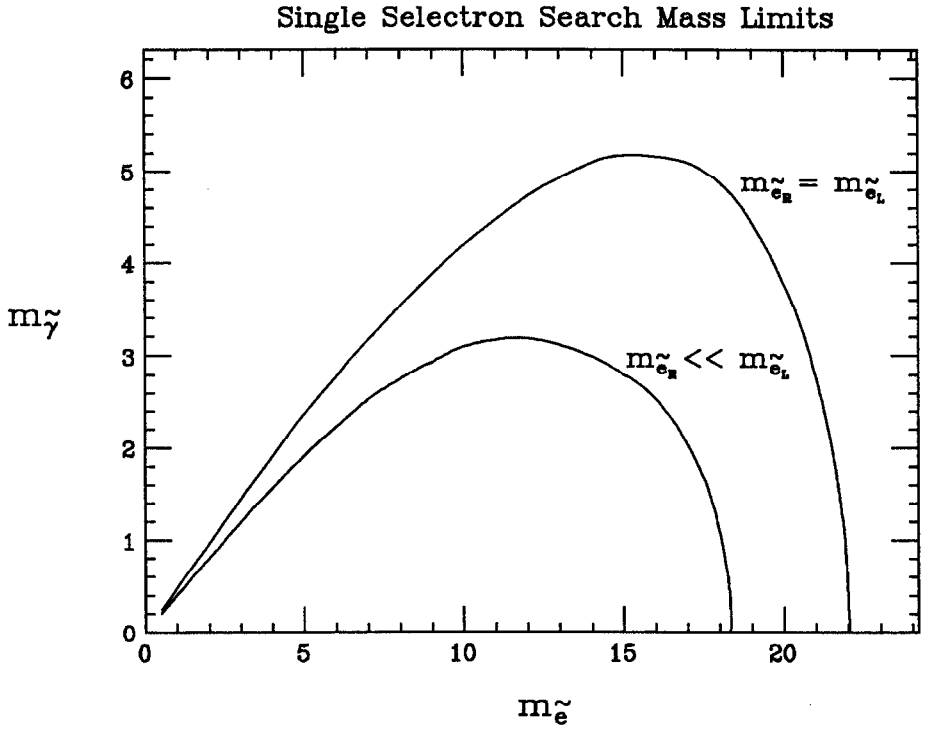

Figure 6.28. Selectron and Photino Mass Limits. The area enclosed by each curve shows the region of selectron-photino mass space ruled out at a 95% CL under two assumptions: that the left- and right-handed selectrons are degenerate in mass *or* that the left-handed selectron is above threshold, so that only the right-handed selectron was produced.

single prong events are consistent with the known background processes. Thus, the search yielded no final candidate events for an integrated luminosity of 123 pb^{-1} . This yields a 95% confidence level (CL) upper limit on the cross section within the acceptance of Fig. 6.27 of 2.4×10^{-2} pb. This cross section corresponds to 3 expected events in accordance with the 95% CL upper limit.

The selectron Monte Carlo generator described in the last chapter was used to determine the limits on selectron and photino masses. Various distributions for selectron Monte Carlo events are shown in Figures 6.29–6.30 for two different values of selectron and photino masses. The generator was run over the various values of masses, and interpolated to yield the contours shown in Fig. 6.28. These contours define the regions of selectron-photino masses which are excluded at the

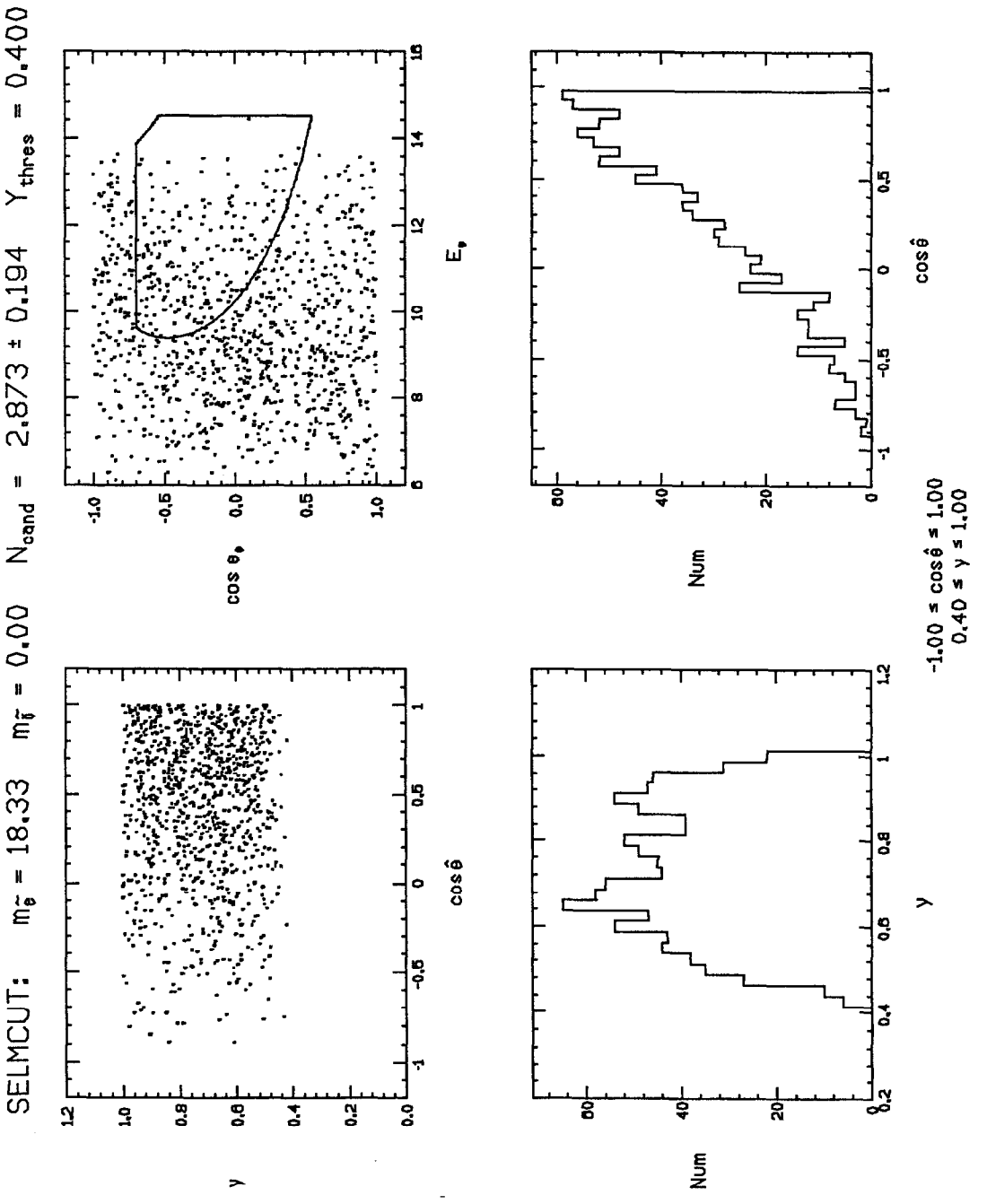

Figure 6.29. Monte Carlo Distributions for $m_{\tilde{e}} = 18.33$ GeV, $m_{\tilde{\gamma}} = 0.00$ GeV. Various distributions are shown here right-handed selectron Monte Carlo events. A total of 1000 events (equivalent to 7.73×10^4 pb^{-1}) were generated. The plot in the upper right hand corner shows the scatter plot of the decay electron's kinematic quantities $\cos\theta_e$ and E_e, in the Mark II detector. The scatter plot in the upper left hand corner shows the photon energy y *vs.* the cosine of the center of mass angle, $\cos\hat{\theta}$, of the selectron. The lower two plots show the projections of this scatter plot onto the two axes.

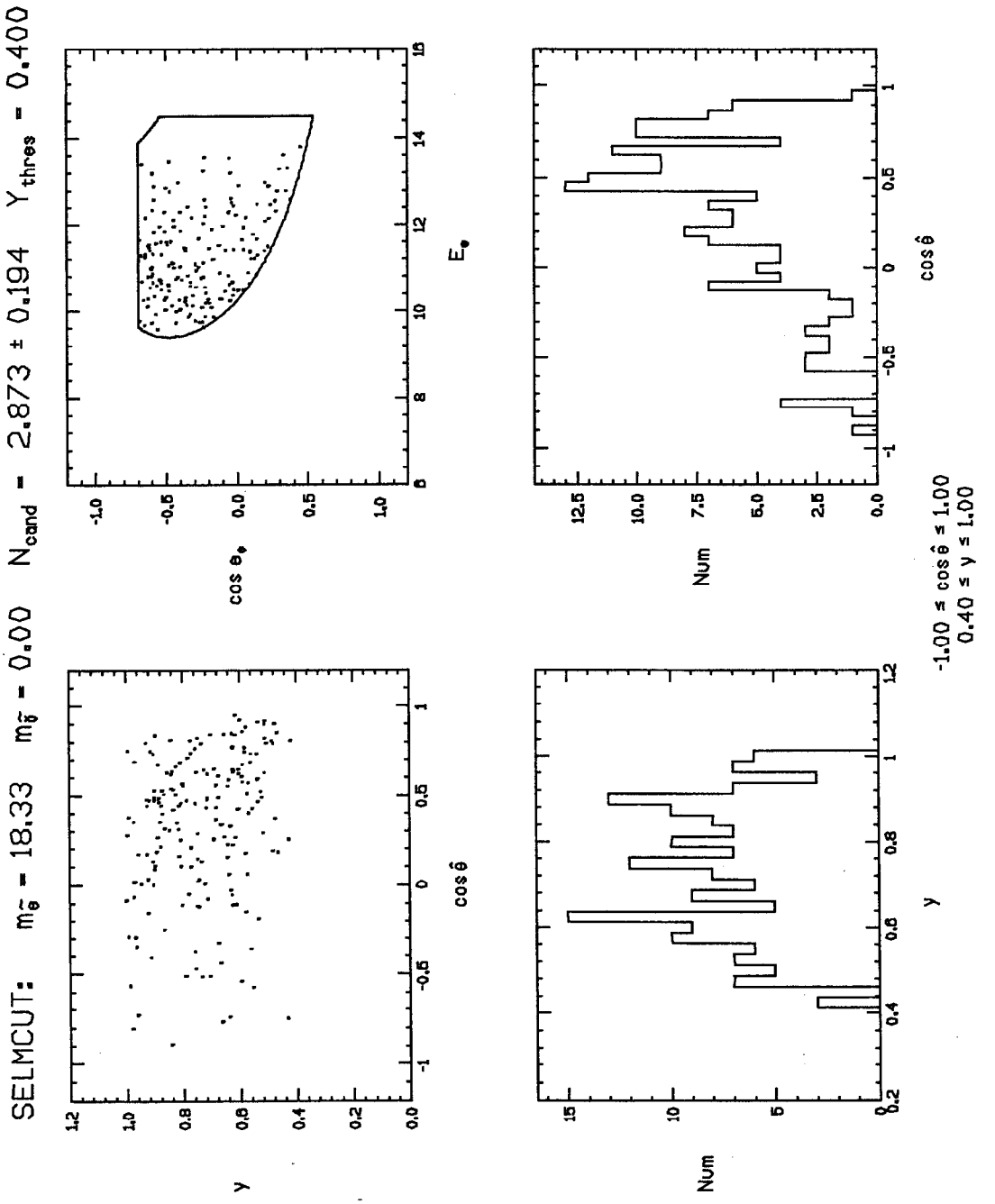

Figure 6.30. Monte Carlo Distributions for $m_{\tilde{e}} = 18.33$ GeV, $m_{\tilde{\gamma}} = 0.00$ GeV. Various distributions are shown here right-handed selectron Monte Carlo events which have a decay electron in the acceptance of the experimental search. A total of 1000 events (equivalent to 7.73×10^4 pb^{-1}) were generated, of which 180 fell into the acceptance. The plot in the upper right hand corner shows the scatter plot of the decay electron's kinematic quantities, $\cos\theta_e$ and E_e , in the Mark II detector. The scatter plot in the upper left hand corner shows the photon energy y *vs.* the cosine of the center of mass angle, $\cos\hat{\theta}$, of the selectron. The lower two plots show the projections of this scatter plot onto the two axes.

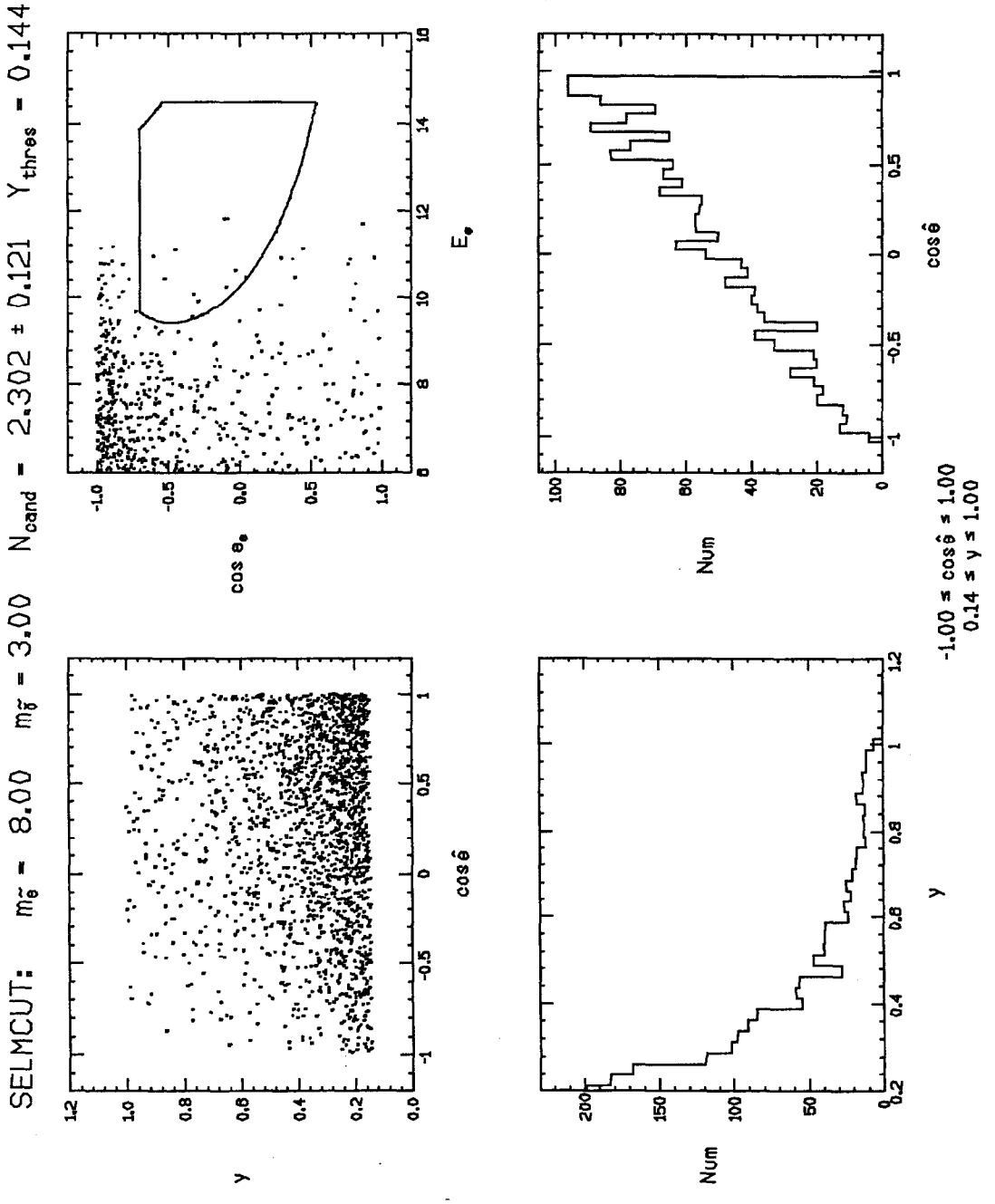

Figure 6.31. Monte Carlo Distributions for $m_{\tilde{e}} = 8.00$ GeV, $m_{\tilde{\gamma}} = 3.00$ GeV. Various distributions are shown here right-handed selectron Monte Carlo events. A total of 50,000 events (equivalent to 1.93×10^4 pb^{-1}) were generated. Only the first 2000 events were used in the above. The plot in the upper right hand corner shows the scatter plot of the decay electron's kinematic quantities, $\cos\theta_e$ and E_e , in the Mark II detector. The scatter plot in the upper left hand corner shows the photon energy y *vs.* the cosine of the center of mass angle, $\cos\hat{\theta}$, of the selectron. The lower two plots show the projections of this scatter plot onto the two axes.

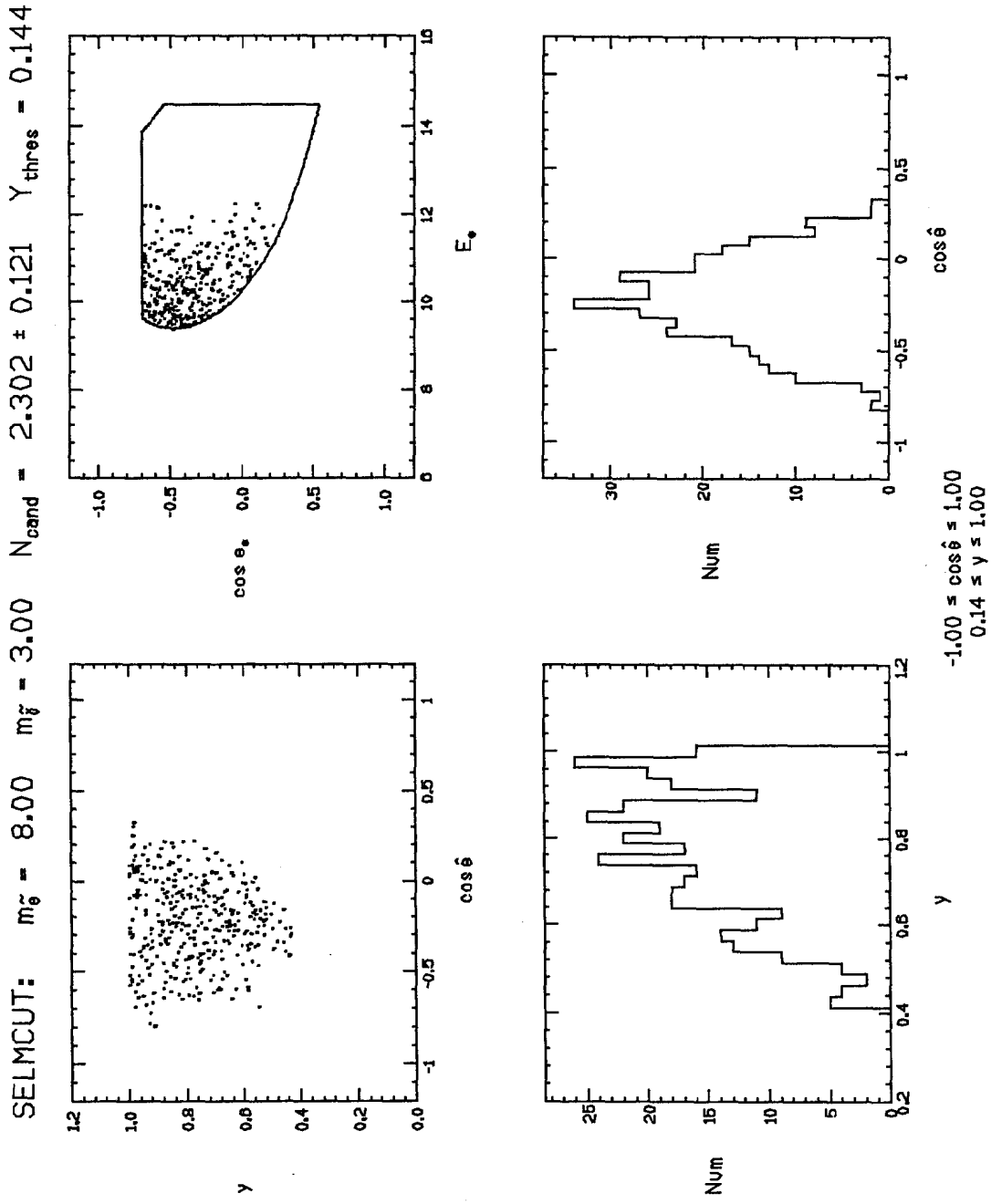

Figure 6.32. Monte Carlo Distributions for $m_{\tilde{e}} = 8.00$ GeV, $m_{\tilde{\gamma}} = 3.00$ GeV. Various distributions are shown here right-handed selectron Monte Carlo events which have a decay electron in the acceptance of the experimental search. A total of 50,000 events (equivalent to 1.93×10^4 pb^{-1}) were generated, of which 360 fell into the acceptance. The plot in the upper right hand corner shows the scatter plot of the decay electron's kinematic quantities, $\cos\theta_e$ and E_e , in the Mark II detector. The scatter plot in the upper left hand corner shows the photon energy y *vs.* the cosine of the center of mass angle, $\cos\hat{\theta}$, of the selectron. The lower two plots show the projections of this scatter plot onto the two axes.

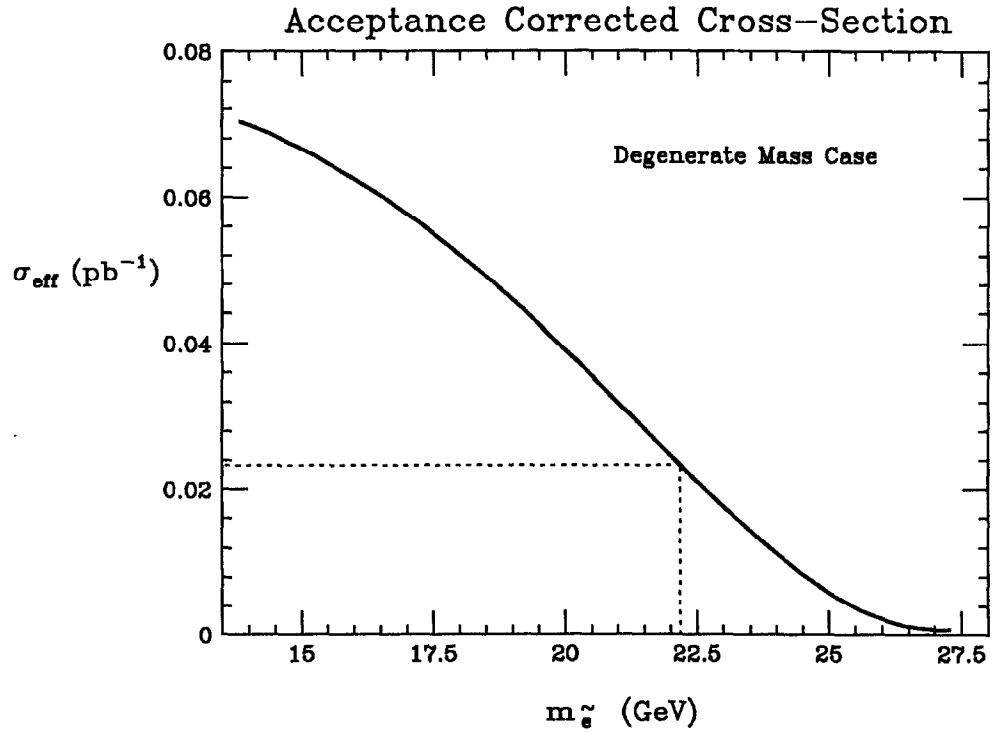

Figure 6.33. Acceptance Corrected Cross Section for Degenerate Mass Case. This plot assumes a massless photino and 14.5 GeV beam energies. The cross section has been fully corrected for acceptance and efficiencies. The dotted line shows the 95% CL limit.

95% confidence level†. Two contours are drawn for the following two limiting cases:

1. *Mass Non-Degenerate case.* Here it is assumed that the superpartner of the left-handed electron, referred to as the left-handed selectron‡, has the same mass as the right-handed selectron.
2. *Mass Degenerate case.* Here it is assumed that left- and right-handed selectrons have the same mass. Therefore, the cross section is doubled, allowing better limits to be set.

---

† If the cross-section was overestimated by 40% by the Weiszäcker-Williams approximation then this result becomes an 85% confidence level. The 95% CL limit would become 20.7 GeV for the massless photino case.

‡ With the understanding that it is a scalar, so that the "left-handed" is understood only to refer to its fermionic partner.

Consider the limit where the photino is massless, then we have the following 95% CL limits on the selectron mass

$$m_{\tilde{e}} > 22.2 \text{ GeV} \quad \text{for} \quad m_{\tilde{e}_L} = m_{\tilde{e}_R}$$
$$m_{\tilde{e}} > 18.3 \text{ GeV} \quad \text{for} \quad m_{\tilde{e}_L} \gg m_{\tilde{e}_R}$$

Both limits are well in excess of the beam energy (14.5 GeV). a plot of the acceptance corrected cross section for the mass degenerate case, and for an assumed photino mass of 0 GeV, is shown in Fig. 6.33. This figure shows that this search technique has essentially been fully exploited for the beam energy of 14.5 GeV.

This search is quite sensitive to non-zero photino masses since two photinos must be produced in the reaction (due to R-parity). Furthermore, massive photinos carry off less momentum for a given energy. This pushes the final state electron's phase space to lower momenta, so that less signal passes the $p_\perp$ cut. A useful number to quote is the largest photino mass that the search is sensitive to, which, at the 95% CL limit is:

$$m_{\tilde{\gamma}} = 5.2 \text{ GeV} \quad \text{for} \quad m_{\tilde{e}_L} = m_{\tilde{e}_R}$$
$$m_{\tilde{\gamma}} = 3.2 \text{ GeV} \quad \text{for} \quad m_{\tilde{e}_L} \gg m_{\tilde{e}_R}$$

The last conclusion which will be made in this section does not involve supersymmetry. Although supersymmetry formed the primary motivation for this search, the actual experimental result stands alone. Its essence is contained in the acceptance contour shown in Fig. 6.27. The limit of 2.4×10^{-2} pb is a very general result; it applies to any process (even ones not yet thought of) that can generate anomalous single electron events in the acceptance.

6.8 Outlook

Although this experiment yielded a negative result, it prompted other experimental searches which eventually lead to much better limits. In the few years after publication of the above results a wealth of experimental limits have been placed on supersymmetry, from both e^+e^- and $p\bar{p}$ colliders. Many limits from cosmology and beam dump searches have also been set. The reader is referred to the 1984 work of Haber and Kane[47], S. Komamiya's 1985 Lepton-Photon Conference talk[84], and M. Davier's 1986 Int. Conf. on High Energy Physics talk[4] for comprehensive reviews. A review of selectron searches based upon the same assumptions as made here can be found in 1987 thesis work of T. Lavine[85].

Despite such intense work, supersymmetry remains without experimental verification. This is not surprising based upon the earlier discussion of its theoretical motivation. If the role of supersymmetry is to alleviate the hierarchy problem, then the theory can easily accommodate masses up to the TeV scale. If supersymmetry exists at this scale the next generation of experiments should indeed be exciting. Supersymmetry not only offers experimenters a definite signal to search for, but it also serves as a road guide, telling us how to best look for new physics. At the very least, it has served to emphasize the importance of better solid angle coverage for detectors.

Supersymmetry may be a symmetry of nature entirely in its own right, without regard to problems such as SU(5) grand unification. It is quite conceivable that problems, such as the gauge hierarchy problem, are not real problems in the framework of a deeper, more correct theory. This more fundamental theory may not involve supersymmetry until energies at or above the GUT scale. This would be a sad fact for experimentalists, and most likely, for theorists as well. At least, this is what the lessons of history have taught us, for, however beautiful and abstract the mathematics of physics, it has always remained an experimental science.

Appendix A. General Kinematic Formula

A.1 Two Body Kinematics

We begin the discussion with the transformation laws for energy and momenta between reference frames S and S'. S' is moving at a velocity β with respect to S, along what is known as the boost direction. The full energy–momentum transformation properties involve components of momentum along the boost direction, and those perpendicular to it. The two perpendicular components are treated exactly alike, allowing us to treat the problem in two dimensions. Let the angle θ be measured with respect to the boost direction in frame S. Suppose that a particle of momentum p and energy $E = \sqrt{p^2 + m^2}$ is traveling at an angle θ in reference frame S. Reference frame S' sees this particle with momentum p' and energy $E' = \sqrt{p'^2 + m^2}$ at an angle θ'. The transformation equations between the two frames are given by:

$$\begin{aligned} E &= \gamma(E' + \beta p' \cos\theta') & \qquad E' &= \gamma(E - \beta p \cos\theta) \\ p\cos\theta &= \gamma(p'\cos\theta' + \beta E') & \qquad p'\cos\theta' &= \gamma(p\cos\theta - \beta E) \\ p\sin\theta &= p'\sin\theta' & \qquad p'\sin\theta' &= p\sin\theta \end{aligned}$$

where,

$$\beta = \text{velocity of } S' \text{ with respect to } S$$

and,

$$\gamma = \frac{1}{\sqrt{1-\beta^2}}\,.$$

From these equations we can also deduce the angle transformation between the two frames. It is given by:

$$\tan\theta = \frac{\beta'\sin\theta'}{\gamma(\beta + \beta'\cos\theta')}$$

where,

$$\beta' = \frac{p'}{E'} .$$

Next consider the two-body decay of a particle of mass, $\sqrt{s}$, at rest in frame S'. Thus, we will sometimes refer to S' as the center of mass frame and S as the lab frame. Suppose the particle decays into particles 1 and 2 with masses m_1 and m_2 respectively. These decay products come out with fixed momentum, p', given by:

$$p' = \frac{1}{2\sqrt{s}} \sqrt{\lambda(s, m_1^2, m_2^2)}$$

where,

$$\begin{aligned} \lambda(a,b,c) &= a^2 + b^2 + c^2 - 2(ab + bc + ca) \\ &= \left[a - (\sqrt{b} + \sqrt{c})^2\right] \left[a - (\sqrt{b} - \sqrt{c})^2\right] . \end{aligned}$$

The kinematic threshold is given by the requirement that $\lambda(s, m_1^2, m_2^2) \geq 0$, which gives the more obvious condition that $\sqrt{s} \geq m_1 + m_2$.

The Jacobian of the angle transformation, $J = J(\cos\theta) = d\cos\theta / d\cos\theta'$, is often of interest, and is found by manipulation of the following two differential transformation equations:

$$(i) \qquad dE = \gamma\beta p' \, d\cos\theta'$$

$$(ii) \qquad \cos\theta \, dp = \gamma p' \, d\cos\theta' - p \, d\cos\theta \ .$$

Dividing equation (i) by equation (ii) yields:

$$\cos\theta \frac{dp}{dE} = \frac{\gamma p' - p \, d\cos\theta / d\cos\theta'}{\gamma\beta p'}$$

and since,

$$\frac{dp}{dE} = \frac{E}{p} = \frac{1}{\beta_{lab}}$$

is the particle's velocity in the lab frame, we arrive at,

$$J = \left| \frac{d\cos\theta}{d\cos\theta'} \right| = \left| \frac{\gamma p'}{p} \left(1 - \frac{\beta}{\beta_{lab}} \cos\theta \right) \right| .$$

Notice that the Jacobian can go to zero if $\beta_{lab} < \beta$, at an angle, $\hat{\theta}$, given by:

$$\cos\hat{\theta} = \frac{\beta_{lab}}{\beta} .$$

Let us focus our discussion on particle 1. In the S' frame this particle has a fixed momentum for all angles. Then in reference frame S the transformation equations describe an ellipse in the momentum plane, which is often referred to simply as the momentum ellipse. This ellipse is conveniently parametrized by $\cos\theta'$. It has semi-major axes given by $\gamma p'$ and semi-minor axes given by p'. The center of the ellipse is offset by an amount $\gamma\beta E'$ from the origin. There are three distinct kinematic cases to consider depending on the value of $\beta' = p'/E'$, as shown in Fig. A.1.

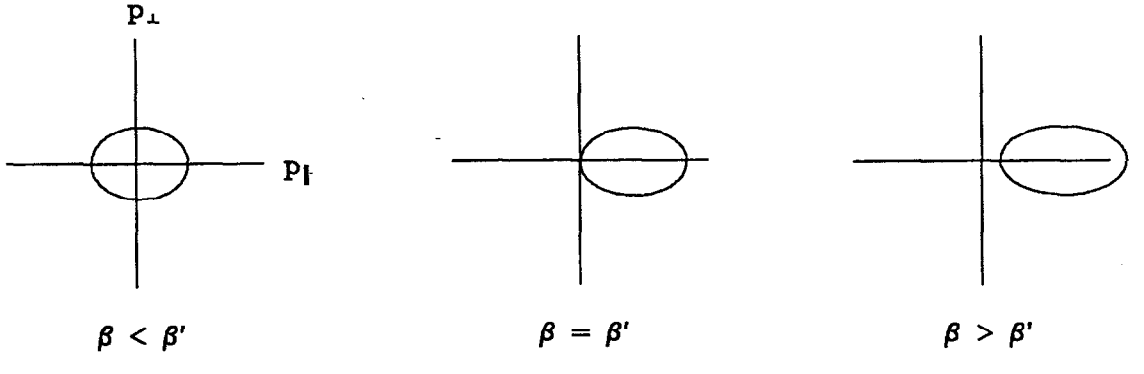

Figure A.1. Momentum Ellipses for Various Values of β. The momentum ellipse is shown for three different values of β in the three figures above.

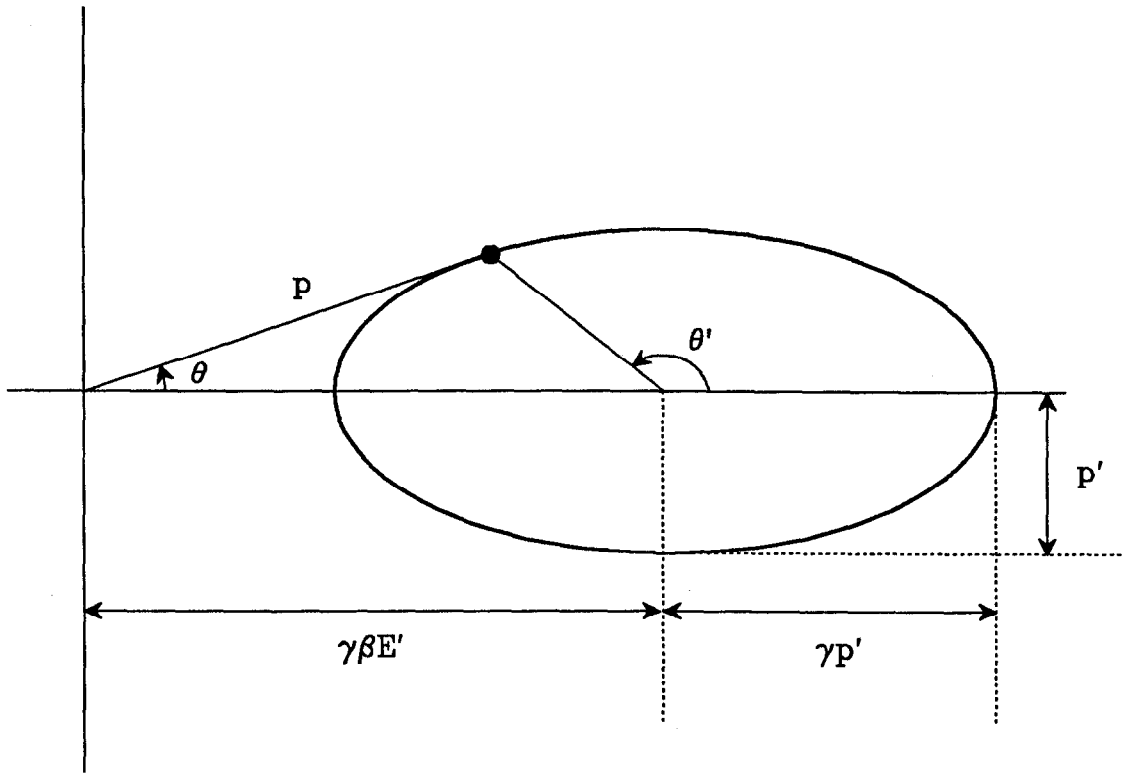

Figure A.2. Anatomy of a Momentum Ellipse. The momentum ellipse is shown here for $\beta > \beta'$. The point shown above shows the maximum allowable angle in the lab frame.

1. $\beta < \beta'$. Here the origin of the momentum axes is contained inside the momentum ellipse. All possible angles are allowed in S.
2. $\beta = \beta'$. In this case the momentum ellipse intersects the origin, so that particle 1 can be found at rest in frame S. The allowable values of angles in S are given by $-\pi/2 \leq \theta \leq \pi/2$.
3. $\beta > \beta'$. Now the momentum ellipse is entirely in the right half of the plane, and the range of angles allowed in frame S is restricted, as will be discussed below.

The anatomy of the momentum ellipse is shown in Fig. A.2 for the case where $\beta > \beta'$. This case is most interesting because of the behavior of the transformations when the momentum direction is tangent to the momentum ellipse, *i.e.* at the boundaries of allowable angles in the lab frame. We expect

that the angle Jacobian will go to zero at this point since $d\cos\theta \rightarrow 0$ at this point. We may derive an equivalent expression for this condition in terms of θ', by differentiating the angle transformation equation:

$$\frac{d\tan\theta}{d\theta'} = \frac{d}{d\theta'}\left[\frac{\beta'\sin\theta'}{\gamma(\beta+\beta'\cos\theta')}\right]$$

$$= \frac{\beta'(\beta'+\beta\cos\theta')}{\gamma(\beta+\beta'\cos\theta')^2} .$$

The derivative can only have a zero for $\beta \geq \beta'$, and denoting the S' frame angle by $\hat{\theta}'$ for this condition, we have:

$$\cos\hat{\theta}' = \frac{-\beta'}{\beta} .$$

A.2 Three and Four Body Kinematics

Suppose we are in the rest mass frame of a particle with mass, $\sqrt{s}$, which decays into three particles. We begin this discussion by counting degrees of freedom. There are initially 12 initial degrees of freedom (*i.e.* $p_i^\mu \quad \mu = 0,1,2,3 \quad i = 1,2,3$). We use the fact that the final state particles must be on mass-shell to bring us down to 9 degrees of freedom (dof). Overall energy–momentum conservation removes 4 more degrees of freedom so that only 5 are left. Two of these degrees of freedom can be used to specify the direction of any one of the particles, leaving 3 dof. We know that the event must be planar (from momentum conservation), so that the ϕ of the event plane with respect to the specified particle's direction removes one more trivial dof. Thus, a discussion of three body kinematics really has but 2 non-trivial degrees of freedom. One of these we take to be the total momentum of the particle whose direction has been specified. This is equivalent to specifying the three momentum components of this particle. Suppose we take this to be particle 1. The 3-body process can be thought

of as a 2-body in this case, where a particle of mass, $\sqrt{s}$, decays into particles of mass m_1 and m_{23}. Particle 23 is the fictitious particle whose 4-momentum is given by $p^\mu_{23} = p^\mu_2 + p^\mu_3$. Then, from the discussion in the previous section we know that particle 1's momentum is given by (note, if the greek superscripts are not present on p in this section then we are referring to $|\vec{\mathbf{p}}|$):

$$p_1 = \frac{1}{2\sqrt{s}}\sqrt{\lambda(s, m_1^2, m_{23}^2)} \; .$$

This equation can be inverted to yield m_{23}^2 as a function of p_1. A more direct approach is to note that $m_{23}^2 = (P^\mu_{tot} - p^\mu_1)^2$, where $P^\mu_{tot} = (\sqrt{s}, 0, 0, 0)$. We therefore have,

$$m_{23}^2 = s + m_1^2 - 2E_1\sqrt{s} \; .$$

Now, the requirement that $m_{23}^2 \geq (m_2 + m_3)^2$ puts an upper limit on p_1. Similar considerations hold for the maximum values of the other two momenta as well:

$$p_1^{max} = \sqrt{\frac{1}{4s}\left[s + m_1^2 - (m_2 + m_3)^2\right]^2 - m_1^2}$$

$$p_2^{max} = \sqrt{\frac{1}{4s}\left[s + m_2^2 - (m_3 + m_1)^2\right]^2 - m_2^2}$$

$$p_3^{max} = \sqrt{\frac{1}{4s}\left[s + m_3^2 - (m_1 + m_2)^2\right]^2 - m_3^2} \; .$$

The three equations are related by cyclically permuting the particle indices.

Knowing the momentum, energy, and mass of particle 23 allows us to calculate the boost of its center of mass frame (the frame in which particles 2 and 3 are back to back and have the same momentum). The boost parameters are given by:

$$\gamma\beta = \frac{p_1}{m_{23}} = \frac{p_1}{\sqrt{s + m_1^2 - 2E_1\sqrt{s}}}$$

and,

$$\beta = \frac{p_1}{E_{23}} = \frac{p_1}{\sqrt{s} - E_1} \ .$$

At this point the discussion now becomes that of the 2-body decay process dealt with above. In the center of mass frame of particle 2 and 3 they have momenta given by:

$$p_2' = p_3' = \frac{1}{2\,m_{23}} \sqrt{\lambda(m_{23}^2, m_2^2, m_3^2)} \ .$$

Therefore, both particle 2 and 3 have a momentum ellipse with the same semi-major and semi-minor axes. However, their momentum ellipses will have different offsets unless the two particles have equal masses (recall the offset is given by $\gamma\beta E'$).

We can select ${\theta_2}' = {\theta_3}' + \pi$ as our last degree of freedom. Alternatively, we could pick p_3 or p_2 as our last degree of freedom. Any one of these variables is valid. They are all equivalent to picking a point on the momentum ellipse of either particle 2 or 3. This determines the final kinematic configuration since the other particle's momentum follows from momentum conservation.

A.2.1 Three Body Kinematics Using Angles

Imagine that instead of specifying momenta, as in the previous section, that the directions of three particles are specified, so that the momenta are treated as unknowns. These directions are specified by unit vectors $\hat{\mathbf{u}}_i$, where $i = 1, 2, 3$. Because of momentum conservation the three particles must lie in a plane. This, together with momentum conservation in the event plane, requires that the allowable 3-body topologies must satisfy the following conditions:

$$\frac{\hat{\mathbf{u}}_i \times \hat{\mathbf{u}}_j}{|\hat{\mathbf{u}}_i \times \hat{\mathbf{u}}_j|} - \frac{\hat{\mathbf{u}}_k \times \hat{\mathbf{u}}_i}{|\hat{\mathbf{u}}_k \times \hat{\mathbf{u}}_i|} = 0$$

for i, j, k equal to any cyclic permutation of 1,2,3.

We denote the angles between the particles in this plane as θ_{12}, θ_{23}, and θ_{31}. The angles are defined by the following relationships:

$$\cos\theta_{ij} = \hat{\mathbf{u}}_i \cdot \hat{\mathbf{u}}_j \ .$$

Note that this implies that $0 \leq \theta_{ij} \leq \pi$ so that $\sin\theta_{ij} = \sqrt{1-\cos^2\theta_{ij}}$. Furthermore, the three angles are not all independent since we have

$$\theta_{ij} = 2\pi - \theta_{jk} - \theta_{ki}$$

for i, j, k equal to any cyclic permutation of 1,2,3.

The momentum configuration is shown in Fig. A.3. Since the overall momentum of the three particles is zero, from momentum conservation, the three vectors can be arranged to form a triangle as shown in Fig. A.4. And since $\sin(\pi - \theta) = \sin\theta$, the law of sines gives the following relationships between the momenta:

$$\frac{p_1}{\sin\theta_{23}} = \frac{p_2}{\sin\theta_{31}} = \frac{p_3}{\sin\theta_{12}} \ .$$

This allows us to solve for two of the momenta in terms of the other, provided that no two momenta are collinear. We choose to solve in terms of p_1:

$$p_2 = \left[\frac{\sin\theta_{31}}{\sin\theta_{23}}\right] p_1 \equiv \kappa_2 p_1$$

$$p_3 = \left[\frac{\sin\theta_{12}}{\sin\theta_{23}}\right] p_1 \equiv \kappa_3 p_1 \ .$$

At this point we are ready to solve the energy equation for the single variable p_1,

$$\sqrt{p_1^2 + m_1^2} + \sqrt{\kappa_2^2 p_1^2 + m_2^2} + \sqrt{\kappa_3^2 p_1^2 + m_3^2} - \sqrt{s} = 0.$$

If the particles are massless than the problem becomes linear, with simple solutions:

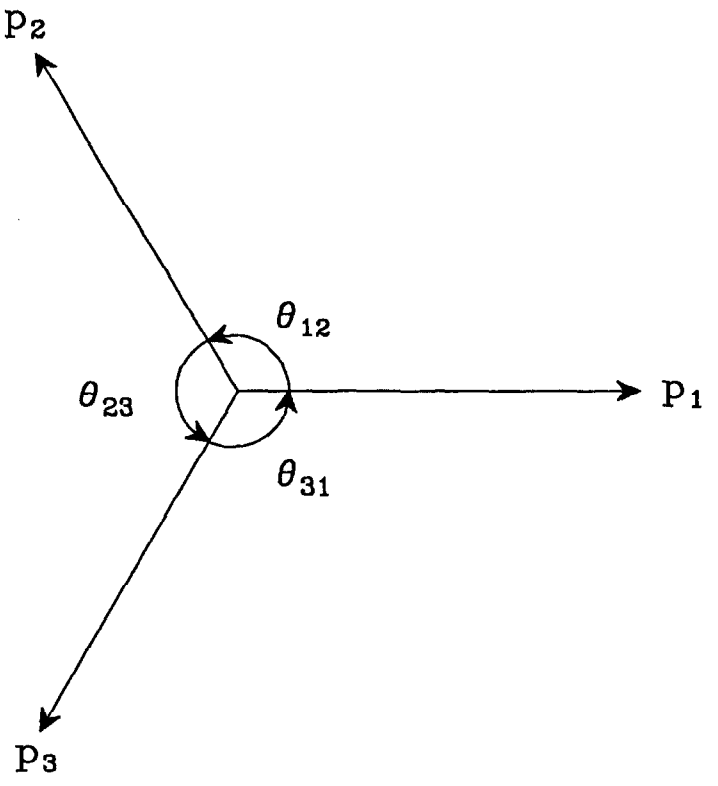

Figure A.3. Three Body Momentum Configuration. The momentum configuration, in the event plane, is shown here. The nomenclature used to label the angles is also shown.

$$p_i = \frac{\sin\theta_{jk}\sqrt{s}}{\sin\theta_{12} + \sin\theta_{23} + \sin\theta_{31}}$$

for i, j, k equal to any cyclic permutation of 1, 2, 3.

If masses are present then there exist two routes to the solution; numerical or exact. The numerical solution takes advantage of the fact that the energy function given above is monotonically increasing, so that the zero can readily be found with numerical analysis packages available on most computers†. However, the above equation can be manipulated to yield a quartic equation in E_1, so that an exact closed form solution can be found. This closed form solution is arrived

† For example, the routine ZEROIN, from the NAPL package can be used.

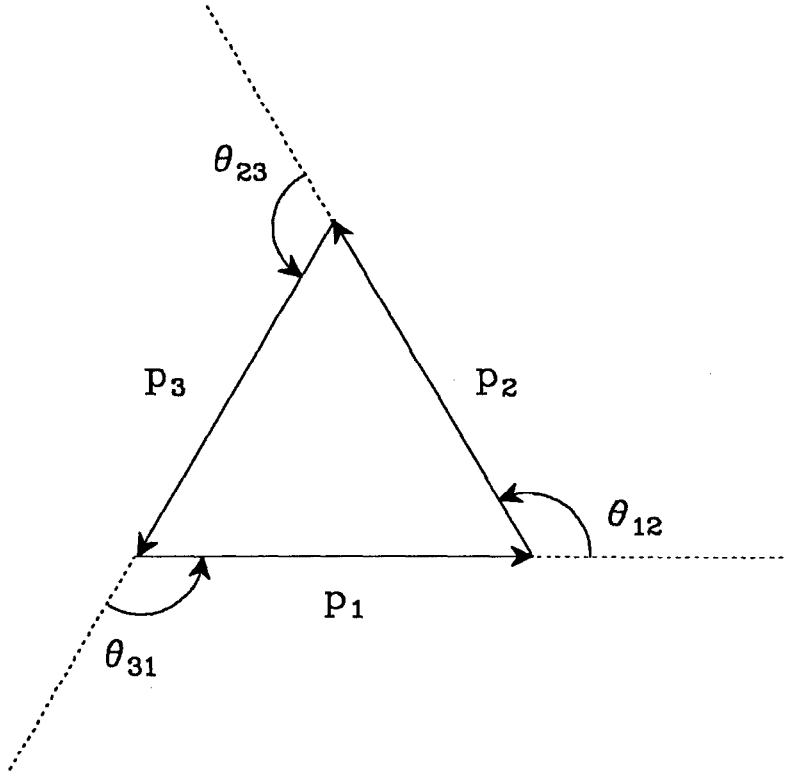

Figure A.4. The 3 Body Momentum Triangle. The momentum vectors form a triangle when their momentum sum is zero. This allows the law of sines to be used to relate the momenta.

at via the following series of substitutions.

First, we make the following definitions,

$$\alpha_2 = \kappa_2^2 \qquad \beta_2 = \frac{m_2^2 - \alpha_2 m_1^2}{s}$$

$$\alpha_3 = \kappa_3^2 \qquad \beta_3 = \frac{m_3^2 - \alpha_3 m_1^2}{s}$$

$$x_1 = E_1/\sqrt{s}$$

then the energy equation can be written as

$$x_1 + \sqrt{\alpha_2 x_1^2 + \beta_2} + \sqrt{\alpha_3 x_1^2 + \beta_3} = 1.$$

The x_1 term can be brought to the right hand side, and both sides squared. Then

the cross term on the left hand side can be isolated and squared, thereby allowing the following quartic equation to be obtained:

$$x_1^4 + ax_1^3 + bx_1^2 + cx_1 + d = 0$$

where,

$$a = -4(1 - \alpha_2 - \alpha_3)\ \mathrm{S}^{-1}$$

$$b = \Big[\, 4(1 - \alpha_2\beta_3 - \alpha_3\beta_2) + 2(1 - \alpha_2 - \alpha_3)(1 - \beta_2 - \beta_3) \,\Big]\ \mathrm{S}^{-1}$$

$$c = -4(1 - \beta_2 - \beta_3)\ \mathrm{S}^{-1}$$

$$d = \Big[(1 - \beta_2 - \beta_3)^2 - 4\beta_2\beta_3\Big]\ \mathrm{S}^{-1}$$

$$\mathrm{S} = (1 - \alpha_2 - \alpha_3)^2 - 4\alpha_2\alpha_3\ .$$

Next, by letting $x = y - a/4$ we eliminate the cubic term from the quartic equation, giving the following equations instead:

$$y^4 + py^2 + qy + r = 0 \qquad\qquad (x = y - a/4)$$

where,

$$p = b - \frac{3a^2}{8}$$

$$q = c - \frac{ab}{2} + \frac{a^3}{8}$$

$$r = d - \frac{ac}{4} + \frac{a^2 b}{16} - \frac{3a^4}{256}$$

Using this equation, we isolate the y^4 term and add $2zy^2 + z^2$ to both sides of the equation, where z is a variable that is as yet unknown. Thus, we arrive at,

$$\left(y^2 + z\right)^2 = (2z - p)y^2 - qy + (z^2 - r).$$

The variable z is now chosen to yield a perfect square on the right hand side of the equation. This yields what is known as the cubic resolute equation:

$$4(z^2 - r)(2z - p) = q^2 \ .$$

So, in the process of solving the quartic equation we will learn to solve the cubic. By making the substitution, $z = u + p/6$, we can eliminate the quadratic term, and instead have the equation,

$$u^3 + gu + h = 0 \qquad (z = u + p/6)$$

where,

$$g = -r - \frac{p^2}{12}$$

$$h = \frac{pr}{3} - \frac{p^3}{108} - \frac{q^2}{8} \ .$$

There is some hope, since we are now down to just two coefficients. From the fundamental theorem of algebra we know that 3 solutions exist. Since g and h are real, we know that if u_i is a solution to the above cubic, then so is $\bar{u}_i$. Thus, the cubic equation must always have at least one real root. This is the root which we will use to solve the quartic equation. The three solutions are found as follows†.

Letting, $\qquad A = \sqrt[3]{\frac{-h}{2} + \sqrt{\frac{h^2}{4} + \frac{g^3}{27}}} \qquad B = \sqrt[3]{\frac{-h}{2} - \sqrt{\frac{h^2}{4} + \frac{g^3}{27}}}$

the three solutions are given by following linear combinations of A and B,

---

† The solution to the cubic was first published in 1545 by Geronimo Carden, who learned of it from Niccolo Tartaglia [86] Their solution involved only $\xi_1 = 1$. It is interesting to note that this solution of the cubic involves the square root of negative numbers for the irresolute case (three different, real roots). This baffled Carden, since it preceded the development of complex numbers. Such solutions suggested that complex numbers could no longer be ignored as they could be with the quadratic equation.

$$u_n = \xi_n A + \xi_n^2 B \qquad n = 1,2,3$$

where,

$$\xi_n = \left(\sqrt[3]{1}\right)_n = e^{2i\pi(n-1)/3} \qquad n = 1,2,3.$$

All three solutions are real if the discriminant of the cubic equation, $D = 27h^2 + 4g^3$, is less than or equal to zero, with at least two degenerate roots when $D = 0$. If $D > 0$ then the only real solution is u_1. Thus, we choose the solution, u_1 for use in the quartic equation. When the discriminant is negative, the following form for the solution may be used:

$$u_n = 2\sqrt{\frac{|g|}{3}}\cos\left[\frac{\phi + 2\pi(n-1)}{3}\right] \qquad n = 1,2,3$$

where,

$$\phi = \cos^{-1}\left\{\frac{-h/2}{\sqrt{|g|^3/27}}\right\}.$$

We denote $z_i = u_i + p/6$, so that z_1 solves the cubic resolute. We therefore have the following equation to solve for the roots of the quartic equation:

$$\left(y^2 + z_1\right)^2 = \left[\sqrt{2z_1 - p}\, y - \frac{q}{|q|}\sqrt{z_1^2 - r}\right]^2.$$

Taking the square root of each side yields the following two quadratic equations in y:

$$y^2 \pm \sqrt{2z_1 - p}\, y + \left[z_1 \mp \frac{q}{|q|}\sqrt{z_1^2 - r}\right] = 0\,.$$

All four roots of the quartic equation are therefore obtained, since we have two solutions to each of the two quadratics. Only one choice is valid for the physical problem which we are dealing with here. It is gotten by choosing the plus sign in the above equation, and the plus sign in the solution to quadratic. We denote

this solution by y_1, where

$$y_1 = -\sqrt{\frac{z_1}{2} - \frac{p}{4}} + \sqrt{\frac{q}{|q|}\sqrt{z_1^2 - r} - \frac{z_1}{4} - \frac{p}{4}} \ .$$

The problem is now solved, since $x_1 = y_1 - a/4$, and $E_1 = x_1\sqrt{s}$.

This technique is useful experimentally when the experimental errors on the angles of the three final state particles give rise to smaller errors on the energies than the errors from any direct energy measurements. It is also useful for studies of the energy resolution of calorimeter systems. For instance, the study of $ee\gamma$ final states allows the calorimeter response to be studied over a much wider momentum range than from non-radiative Bhabha final states. The Mark II tracking chambers allowed the electron angles to be determined with very high accuracy, thus allowing for very accurate kinematic fitting.

Another application of three body kinematics is the study of three jet events arising from gluon radiation in hadronic events. Here the jet axes can be determined much more accurately than the jet energy could be. The determination of hadronic shower energy is extremely difficult, even for the best of hadronic detectors, due to large fluctuations in hadronic interactions, and in charged pion versus neutral pion production in the showers. Furthermore, neutrinos from semi-leptonic decays can carry away large amounts of energy without any chance of detection. The Mark II detector did not even have a hadronic calorimeter, instead, it used the momentum from the tracking chambers for determining the energy of the charged tracks. Its determination of the energy carried off by neutrals was hampered by hadronic interactions in the LA calorimeter giving rise to fake electro-magnetic energy. But since the charged energy direction correlated extremely well with the neutral energy direction, it was still possible to determinate the jet directions with good precision. This in turn allowed the jet energies to be determined. Of course we are ignoring the

important question of what masses to assign the jets, this being a difficult question in and of itself.

In both of these applications it is necessary to assess the accuracy of the kinematic formulae quoted above, given experimental uncertainties in determining the directions of the three particles (or jets). These errors involve the derivatives of the energies with respect to the angles, which in turn can be determined by the chain rule from the derivatives with respect to the κ's. The simplest procedure for finding these derivatives is to implicitly differentiate the original energy equation:

$$\frac{\partial}{\partial \kappa_{2,3}} \left(E_1 + \sqrt{\kappa_2^2 (E_1^2 - m_1^2) + m_2^2} + \sqrt{\kappa_3^2 (E_1^2 - m_1^2) + m_3^2} - \sqrt{s} \right) = 0.$$

This leads to the following equations,

$$\frac{\partial E_1}{\partial \kappa_2} = \frac{-\kappa_2 p_1^2 E_3}{E_2 E_3 + \kappa_2^2 E_1 E_3 + \kappa_3^2 E_1 E_2}$$

$$\frac{\partial E_1}{\partial \kappa_3} = \frac{-\kappa_3 p_1^2 E_2}{E_2 E_3 + \kappa_2^2 E_1 E_3 + \kappa_3^2 E_1 E_2} .$$

The next appendix contains a detailed discussion of a special 3-body kinematic problem especially relevant to the selectron experimental search.

A.2.2 Four Body Kinematics Using Angles

The four body problem can also be treated in the case where the momenta directions and particle masses are given. Here we have 4 unknown energies to determine from the 4 energy-momentum conservation equations. We can take any one of the particle's direction and write the momentum conservation condition as:

$$p_i + p_j \cos\theta_{ij} + p_k \cos\theta_{ik} + p_l \cos\theta_{il} = 0$$

for i, j, k, l equal to any cyclic permutation of 1, 2, 3 and 4.

At most only three of the above equations are independent, since there are at most 3 independent directions. The topological requirements for solution is that any

combination of three of the direction vectors must form a linearly independent basis set, and, that for every plane formed by two of the momenta, the other two momenta must be on opposite sides of the plane. This latter condition can be relaxed only if we allow the final momenta to be anti-aligned with the specified input directions.

We begin by solving for p_2, p_3, and p_4 as linear functions of p_1. We start with the following matrix equation (this approach could also have been used in the 3-body problem):

$$M \begin{pmatrix} p_2 \\ p_3 \\ p_4 \end{pmatrix} = -p_1 \begin{pmatrix} \cos\theta_{12} \\ \cos\theta_{13} \\ \cos\theta_{14} \end{pmatrix}$$

where M is the following 3×3 matrix,

$$M = \begin{pmatrix} 1 & \cos\theta_{23} & \cos\theta_{24} \\ \cos\theta_{23} & 1 & \cos\theta_{34} \\ \cos\theta_{24} & \cos\theta_{34} & 1 \end{pmatrix}.$$

Thus, provided the determinant of M is non-zero, we have:

$$\begin{pmatrix} p_2 \\ p_3 \\ p_4 \end{pmatrix} = -M^{-1} \begin{pmatrix} \cos\theta_{12} \\ \cos\theta_{13} \\ \cos\theta_{14} \end{pmatrix} p_1 \equiv \begin{pmatrix} \kappa_2 \\ \kappa_3 \\ \kappa_4 \end{pmatrix} p_1$$

where, denoting $\cos\theta_{ij}$ by c_{ij}, the $\kappa's$ are given by,

$$\kappa_2 = -\Big[c_{23}(c_{34}c_{14} - c_{13}) + c_{24}(c_{34}c_{13} - c_{14}) + c_{12}(1 - c_{34}^2)\Big]/\Delta$$

$$\kappa_3 = -\Big[c_{23}(c_{24}c_{14} - c_{12}) + c_{34}(c_{24}c_{12} - c_{14}) + c_{13}(1 - c_{24}^2)\Big]/\Delta$$

$$\kappa_4 = -\Big[c_{24}(c_{23}c_{13} - c_{12}) + c_{34}(c_{23}c_{12} - c_{13}) + c_{14}(1 - c_{23}^2)\Big]/\Delta$$

with,

$$\Delta = 1 - c_{23}^2 - c_{24}^2 - c_{34}^2 + 2\,c_{23}c_{24}c_{34}\,.$$

The κ's are required to be greater than or equal to zero, unless we allow the momenta to be anti-aligned with the specified input directions.

We then substitute the above into the energy equation, as before. Defining $\kappa_1 = 1$ allows us to write this equation in the following compact form:

$$\sum_{i=1}^{4} \sqrt{\kappa_i^2 p_1^2 + m_i^2} = \sqrt{s}\,.$$

We now consider the problem solved, leaving the above equation to be numerically solved for p_1.

Appendix B. $ee\gamma$ Kinematic Formula

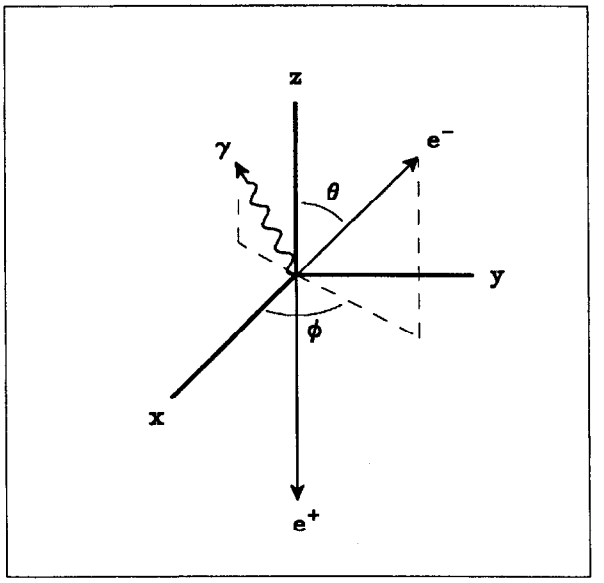

Figure B.1. Definition of $ee\gamma$ Event Geometry. This diagram shows the coordinate system used for defining the $ee\gamma$ event geometry. The electron is assumed detected, the positron is confined to a 2° cone around the beam pipe. Throughout the text the coordinate system has been rotated in ϕ so that the electron is in the y-z plane.

B.1 Simple Case- Positron at 180°

We begin our discussion by assuming the electron is detected, and that the positron escapes straight down the beam pipe undetected. The Mark II coordinate system will be used for this discussion, so that the initial particle directions are along the z-axis, with the electron initially traveling in the $+z$ direction. We also assume that both the electron and the positron are extremely relativistic, so that their rest masses can be neglected throughout our discussion. The three body final state geometry is as defined in figure B.1. The final state four momenta are then given by:

$$(B1) \qquad p_{\bar{e}} = \begin{pmatrix} \mathrm{E}_{\bar{e}} \\ 0 \\ 0 \\ -\mathrm{E}_{\bar{e}} \end{pmatrix} \qquad p_e = \begin{pmatrix} \mathrm{E}_e \\ 0 \\ \mathrm{E}_e \sin\theta_e \\ \mathrm{E}_e \cos\theta_e \end{pmatrix} \qquad p_\gamma = \begin{pmatrix} \mathrm{E}_\gamma \\ 0 \\ -\mathrm{E}_\gamma \sin\theta_\gamma \\ \mathrm{E}_\gamma \cos\theta_\gamma \end{pmatrix}.$$

One of the four energy–momentum conservation constraints has already been used in defining the planar event geometry, and we have rotated the event plane into the y-z plane for convenience. There are three remaining energy–momentum conservation equations:

(B2) Energy balance: $\mathrm{E}_e + \mathrm{E}_\gamma + \mathrm{E}_{\bar{e}} = \sqrt{s}$

(B3) p_z balance: $\mathrm{E}_e \cos\theta_e + \mathrm{E}_\gamma \cos\theta_\gamma = \mathrm{E}_{\bar{e}}$

(B4) $p_\perp$ balance: $\mathrm{E}_e \sin\theta_e = \mathrm{E}_\gamma \sin\theta_\gamma$.

Now for convenience let us adopt the following notation:

$$\chi_e = \frac{2\mathrm{E}_e}{\sqrt{s}}, \qquad c_e = \cos\theta_e, \qquad s_e = \sin\theta_e,$$

$$\chi_\gamma = \frac{2\mathrm{E}_\gamma}{\sqrt{s}}, \qquad c_\gamma = \cos\theta_\gamma, \qquad s_\gamma = \sin\theta_\gamma,$$

$$\chi_{\bar{e}} = \frac{2\mathrm{E}_{\bar{e}}}{\sqrt{s}}.$$

All the energy parameters have been scaled according to the beam energy, E_{B}, leaving the dimensionless quantities, $\chi = 2\mathrm{E}/\sqrt{s} = \mathrm{E}/\mathrm{E}_{\mathrm{B}}$.

We assume that χ_e and c_e have been measured so that there are only three unknowns: $\chi_{\bar{e}}$, χ_γ, and c_γ. The energy balance equation can be used to solve for $\chi_{\bar{e}}$ in terms of χ_e and χ_γ. Both sides of the $p_\perp$ balance equation can be squared and rewritten in terms of the cosines of the angles. These manipulations yield the following two equations:

(a) $$\chi_e c_e + \chi_\gamma c_\gamma = 2 - \chi_e - \chi_\gamma$$

(b) $$\chi_\gamma^2 c_\gamma^2 = \chi_\gamma^2 - \chi_e^2(1 - c_e^2).$$

Then the first of these equations can be used to solve for $\chi_\gamma c_\gamma$ and substituted into the second equation, leaving a linear equation in terms of χ_γ. Solving this

equation then yields:

$$(B5) \qquad \chi_\gamma = \frac{2-\chi_e(1+c_e)(2-\chi_e)}{2-\chi_e(1+c_e)}$$

$$= 1 - \frac{\chi_e(1-\chi_e)(1+c_e)}{2-\chi_e(1+c_e)}.$$

The latter form for χ_γ readily demonstrates the proper limiting behavior, for in the limit of $\chi_e \to 0$ or 1 we have $\chi_\gamma \to 1$, as expected. Furthermore, $\chi_\gamma = 1$ for $c_e = -1$ as is also expected.

Given this expression for χ_γ we can return to equation (a) above and solve for c_γ. This yields the following important equation:

$$(B6) \qquad c_\gamma = \frac{2-2\chi_e(1+\chi_e)+\chi_e^2 c_e(1+c_e)}{2-\chi_e(1+c_e)(2-\chi_e)}$$

$$= 1 - \frac{\chi_e^2(1+c_e)(1-c_e)}{2-\chi_e(1+c_e)(2-\chi_e)}.$$

This equation also has the proper limiting behavior, for in the limit of $\chi_e \to 1$ we have $c_\gamma \to -c_e$, as expected.

Of course, the unseen positron's energy can also be solved for using the original energy balance equation. This gives:

$$(B7) \qquad \chi_{\bar{e}} = \frac{2(1-\chi_e)}{2-\chi_e(1+c_e)}.$$

However, this parameter is of secondary interest, since it is the photon's position that is of paramount importance in this analysis.

B.2 Error Analysis- Part I.

Thus far, we have determined the photon's energy and position using the detected electron's kinematic quantities, together with the assumption that the

positron went dead center down the beam pipe (which is the most reasonable assumption we can make about it). The next step is to determine the error on the photon's kinematic quantities, given the error involved in measuring the electron's kinematic quantities, together with the inherent error due to our assumption that the unseen lepton was traveling at exactly 180°, straight down the beam pipe. We denote the error in locating the unseen electron as $\delta\theta_{\bar{e}} \simeq 2°$, which is where the SAT system's acceptance begins. The formulas obtained above for χ_e and c_γ represent our best estimation of the photon's kinematic quantities, given the measurement of the electron's kinematics. However, we have thus far neglected the dependence of χ_e and c_γ on $\theta_{\bar{e}}$. This will be remedied in the next section. This more accurate treatment will not provide us with a better answer of where the photon went, however. It merely allows us to better estimate our errors on these quantities. For the moment then, let us not worry about the exact form of the partial derivatives involving $\theta_{\bar{e}}$ below.

We use standard error propagation techniques to determine the error on the photon's energy and angles. This gives the following expressions for the errors:

$$(B9) \qquad \delta\phi_\gamma = \sqrt{(\delta\phi_e)^2 + \left(\frac{\partial\phi_\gamma}{\partial\theta_{\bar{e}}}\right)^2 (\delta\theta_{\bar{e}})^2}$$

$$(B10) \qquad \delta c_\gamma = \sqrt{\left(\frac{\partial c_\gamma}{\partial \mathrm{E}_e}\right)^2 (\delta \mathrm{E}_e)^2 + \left(\frac{\partial c_\gamma}{\partial\theta_e}\right)^2 (\delta\theta_e)^2 + \left(\frac{\partial c_\gamma}{\partial\theta_{\bar{e}}}\right)^2 (\delta\theta_{\bar{e}})^2}$$

$$(B11) \qquad \delta\chi_\gamma = \sqrt{\left(\frac{\partial\chi_\gamma}{\partial \mathrm{E}_e}\right)^2 (\delta \mathrm{E}_e)^2 + \left(\frac{\partial\chi_\gamma}{\partial\theta_e}\right)^2 (\delta\theta_e)^2 + \left(\frac{\partial\chi_\gamma}{\partial\theta_{\bar{e}}}\right)^2 (\delta\theta_{\bar{e}})^2} \ ,$$

where we have ignored the error in $\mathrm{E_B}$ as having a much smaller contribution to the photon's errors. Note that, with the assumption that the positron is straight down the beam pipe, the photon is directly opposite the electron in ϕ by momentum conservation. Hence, the electron's errors in ϕ contribute directly to the photon's errors in ϕ. The dependence on errors in $\theta_{\bar{e}}$ is then added in quadrature.

We can use the chain rule to convert the above into expressions involving derivatives with respect to c_e and χ_e , for example:

$$\delta c_\gamma = \sqrt{\left(\frac{\partial c_\gamma}{\partial \chi_e}\frac{d\chi_e}{d\mathrm{E}_e}\right)^2 (\delta \mathrm{E}_e)^2 + \left(\frac{\partial c_\gamma}{\partial c_e}\frac{dc_e}{d\theta_e}\right)^2 (\delta\theta_e)^2 + \left(\frac{\partial c_\gamma}{\partial s_{\bar{e}}}\frac{ds_{\bar{e}}}{d\theta_{\bar{e}}}\right)^2 (\delta\theta_{\bar{e}})^2}\,.$$

Where we have $d\chi_e/d\mathrm{E}_e = 1/\mathrm{E}_{\mathrm{B}}$, $ds_{\bar{e}}/d\theta_{\bar{e}} = c_{\bar{e}}$, and $ds_{\bar{e}}/d\theta_e = c_{\bar{e}}$.

We defer further evaluation of the above terms until after the next section.

B.3 *eeγ* Kinematics with the Positron Slightly Off Axis

At this point we must face the task of allowing the positron to *not* be traveling at exactly 180°, *i.e.* straight down the beam pipe, for purposes of error analysis. If we again rotate the event in ϕ so that the electron is in the y-z plane then the final state four momenta are now given in the more general form as:

(*B*11)
$$p_e = \chi_e \begin{pmatrix} 1 \\ 0 \\ s_e \\ c_e \end{pmatrix} \qquad p_{\bar{e}} = \chi_\gamma \begin{pmatrix} 1 \\ s_{\bar{e}}c_{\phi\bar{e}} \\ s_{\bar{e}}s_{\phi\bar{e}} \\ c_{\bar{e}} \end{pmatrix} \qquad p_\gamma = \chi_\gamma \begin{pmatrix} 1 \\ s_\gamma c_{\phi\gamma} \\ s_\gamma s_{\phi\gamma} \\ c_\gamma \end{pmatrix}.$$

Where we are using the rationalized energy variables and the compact trigonometric notation ($c_{\phi\gamma} = \cos\phi_\gamma$, $c_\gamma = \cos\theta_\gamma$, *etc.*). In these units, the center of mass four momentum has only one nonzero element, $p^0_{\mathrm{CM}} = 2$. The energy-momentum conservation equations are as follows:

(B12) Energy balance: $\chi_e + \chi_\gamma + \chi_{\bar{e}} = 2$

(B13) p_x balance: $\chi_{\bar{e}}s_{\bar{e}}c_{\phi\bar{e}} + \chi_\gamma s_\gamma c_{\phi\gamma} = 0$

(B14) p_y balance: $\chi_e s_e + \chi_{\bar{e}}s_{\bar{e}}s_{\phi\bar{e}} + \chi_\gamma s_\gamma s_{\phi\gamma} = 0$

(B15) p_z balance: $\chi_e c_e + \chi_{\bar{e}}c_{\bar{e}} + \chi_\gamma c_\gamma = 0.$

We are treating the positron angles as known throughout this part of the discussion, even though they are not known in reality, for purposes of error analysis. We wish to determine the functional dependence of the photon's kinematic quantities on $s_{\bar{e}}$ and $\phi_{\bar{e}}$. This is the whole point of this exercise, since we are attempting to determine how our lack of knowledge quantitatively affects the determination of the photon's direction and energy. Therefore, the above four equations are to be solved for the following four unknowns; $\chi_{\bar{e}}$, χ_γ, θ_γ and ϕ_γ.

We begin by isolating the terms involving ϕ_γ in equations (B13) and (B14), and then adding the squares of both equations together. This eliminates ϕ_γ, leaving us with the equation:

$$\chi_\gamma^2 s_\gamma^2 = \chi_{\bar{e}}^2 s_{\bar{e}}^2 + 2\chi_e \chi_{\bar{e}} s_e s_{\bar{e}} s_{\phi\bar{e}} + \chi_e^2 s_e^2 .$$

Then, using $\chi_\gamma^2 s_\gamma^2 = \chi_\gamma^2 - \chi_\gamma^2 c_\gamma^2$ we eliminate mention of the photon's kinematic variables by the substitutions, $\chi_\gamma = 2 - \chi_e - \chi_{\bar{e}}$ and $\chi_\gamma c_\gamma = -(\chi_e c_e + \chi_{\bar{e}} c_{\bar{e}})$. This gives us an equation in just one unknown, $\chi_{\bar{e}}$. Happily, this equation's quadratic term drops out, allowing us to obtain a simple solution for $\chi_{\bar{e}}$,

$$(B18) \qquad \chi_{\bar{e}} = \frac{2(1-\chi_e)}{2-\chi_e(1-c_e c_{\bar{e}} - s_e s_{\bar{e}} s_{\phi\bar{e}})}$$

$$= 1 - \frac{\chi_e(1+c_e c_{\bar{e}} + s_e s_{\bar{e}} s_{\phi\bar{e}})}{2-\chi_e(1-c_e c_{\bar{e}} - s_e s_{\bar{e}} s_{\phi\bar{e}})}.$$

This allows us to substitute back into the energy equation to find χ_γ:

$$(B19) \qquad \chi_\gamma = \frac{2-\chi_e(2-\chi_e)(1-c_e c_{\bar{e}} - s_e s_{\bar{e}} s_{\phi\bar{e}})}{2-\chi_e(1-c_e c_{\bar{e}} - s_e s_{\bar{e}} s_{\phi\bar{e}})}$$

$$= 1 - \frac{\chi_e(1-\chi_e)(1-c_e c_{\bar{e}} - s_e s_{\bar{e}} s_{\phi\bar{e}})}{2-\chi_e(1-c_e c_{\bar{e}} - s_e s_{\bar{e}} s_{\phi\bar{e}})}.$$

The determination of c_γ is algebraically more complicated, but straight forward. It is obtained by manipulation of equation (B15),

$$c_\gamma = \frac{-1}{\chi_\gamma}(\chi_e c_e + \chi_{\bar{e}} c_{\bar{e}}) = \frac{-(\chi_e c_e + \chi_{\bar{e}} c_{\bar{e}})}{2-\chi_e-\chi_{\bar{e}}},$$

where we have substituted in the denominator for χ_γ from the energy equation in order to simplify the algebra. The final result for c_γ is given by:

$$(B20) \qquad c_\gamma = \frac{-2c_{\bar{e}} - 2\chi_e(c_e - c_{\bar{e}}) + \chi_e^2 c_e\left[1 - c_e c_{\bar{e}} - s_e s_{\bar{e}} s_{\phi\bar{e}}\right]}{2 - \chi_e(2-\chi_e)\left[1 - c_e c_{\bar{e}} - s_e s_{\bar{e}} s_{\phi\bar{e}}\right]}$$

$$= 1 - \frac{\left\{\begin{array}{r} 2(1+c_e) - 2\chi_e\left[(1-c_e)(1-c_{\bar{e}}) - s_e s_{\bar{e}} s_{\phi\bar{e}}\right] \\ + \chi_e^2(1-c_e)(1 - c_e c_{\bar{e}} - s_e s_{\bar{e}} s_{\phi\bar{e}}) \end{array}\right\}}{2 - \chi_e(2-\chi_e)(1 - c_e c_{\bar{e}} - s_e s_{\bar{e}} s_{\phi\bar{e}})}.$$

Next we wish to determine ϕ_γ. We return to equations (B13) and (B14):

$$\cot\phi_\gamma = \frac{\chi_{\bar{e}} s_{\bar{e}} c_{\phi\bar{e}}}{\chi_e s_e + \chi_{\bar{e}} s_{\bar{e}} s_{\phi\bar{e}}}$$

$$= \frac{2(1-\chi_e) s_{\bar{e}} c_{\phi\bar{e}}}{2 s_{\bar{e}} s_{\phi\bar{e}} + 2\chi_e(s_e - s_{\bar{e}} s_{\phi\bar{e}}) - \chi_e^2 s_e(1 - c_e c_{\bar{e}} - s_e s_{\bar{e}} s_{\phi\bar{e}})}.$$

We know that $\phi_\gamma \to 3\pi/2$ as $s_{\bar{e}} \to 0$. Thus, using the identity:

$$\cot(x+y) = \frac{1 - \tan x \tan y}{\tan x + \tan y},$$

we have $\cot(3\pi/2 + y) = -\tan y$. This allows us to obtain the following expression for ϕ_γ:

$$(B21) \qquad \phi_\gamma = \frac{3\pi}{2} - \tan^{-1}\left\{\frac{2(1-\chi_e) s_{\bar{e}} c_{\phi\bar{e}}}{2 s_{\bar{e}} s_{\phi\bar{e}} + 2\chi_e(s_e - s_{\bar{e}} s_{\phi\bar{e}}) - \chi_e^2 s_e(1 - c_e c_{\bar{e}} - s_e s_{\bar{e}} s_{\phi\bar{e}})}\right\}.$$

We have now solved the problem for the case where the positron is off axis. Note that in the limit of $s_{\bar{e}} \to 0$ we recover all the results of the previous section. In fact, we can expand all the kinematic quantities out in terms of $s_{\bar{e}}$. Thus, keeping only terms out to first order (such that $\circ\left[s_{\bar{e}}^2\right] \to 0$ and $c_{\bar{e}} \to -1$), we have:

$$(B23) \qquad \chi_\gamma \simeq \chi_\gamma^0 + \chi_\gamma^1$$

$$(B25) \qquad \chi_\gamma^0 = 1 - \frac{\chi_e(1-\chi_e)(1+c_e)}{2-\chi_e(1+c_e)}$$

$$(B27) \qquad \chi_\gamma^1 = \frac{2(1-\chi_e)\chi_e s_e s_{\bar{e}} s_{\phi\bar{e}}}{[2-\chi_e(1+c_e)]^2}$$

$$(B24) \qquad c_\gamma \simeq c_\gamma^0 + c_\gamma^1$$

$$(B26) \qquad c_\gamma^0 = 1 - \frac{\chi_e^2(1+c_e)(1-c_e)}{2-\chi_e(1+c_e)(2-\chi_e)}$$

$$(B28) \qquad c_\gamma^1 = \frac{-2\chi_e(1-\chi_e)\left[2-\chi_e(1+c_e)\right] s_e s_{\bar{e}} s_{\phi\bar{e}}}{[2-\chi_e(2-\chi_e)(1+c_e)]^2}$$

$$(B29) \qquad \phi_\gamma \simeq \phi_\gamma^0 + \phi_\gamma^1$$

$$(B30) \qquad \phi_\gamma^0 = \frac{3\pi}{2}$$

$$(B31) \qquad \phi_\gamma^1 = \frac{-2(1-\chi_e)s_{\bar{e}} c_{\phi\bar{e}}}{\chi_e s_e \left[2-\chi_e(1+c_e)\right]} .$$

We have only written the photon terms here since they are of greatest interest, but note that $\chi_{\bar{e}}^1 = -\chi_\gamma^1$, which follows from energy conservation.

B.4 Error Analysis Part II.

Now we can return to the discussion of error propagation. We take the lowest order calculations from the first section for the partial derivatives of the photon's kinematic quantities with respect to χ_e, c_e, and ϕ_e. The last section contains the dependencies on the unseen positron's angles. So, using equations (B6) and (B28) we have,

$$(B29) \qquad \frac{\partial c_\gamma}{\partial \chi_e} = \frac{-2\chi_e s_e^2(2-\chi_e[1+c_e])}{\left[2-\chi_e(1+c_e)(2-\chi_e)\right]^2}$$

$$(B30) \qquad \frac{\partial c_\gamma}{\partial c_e} = \frac{\chi_e^2[4c_e - \chi_e(2-\chi_e)(1+c_e)^2]}{\left[2-\chi_e(1+c_e)(2-\chi_e)\right]^2}$$

$$(B31) \qquad \frac{\partial c_\gamma}{\partial s_{\bar{e}}} = \frac{2\chi_e(1-\chi_e)\left[2-\chi_e(1+c_e)\right] s_e c_{\bar{e}} s_{\phi\bar{e}}}{[2-\chi_e(2-\chi_e)(1+c_e)]^2}$$

while from equations (B5) and (B28) we have,

$$(B32) \qquad \frac{\partial \chi_\gamma}{\partial \chi_e} = \frac{-(1+c_e)\left[2(1-2\chi_e)+\chi_e^2(1+c_e)\right]}{\left[2-\chi_e(1+c_e)\right]^2}$$

$$(B33) \qquad \frac{\partial \chi_\gamma}{\partial c_e} = \frac{-2\chi_e(1-\chi_e)}{\left[2-\chi_e(1+c_e)\right]^2}$$

$$(B34) \qquad \frac{\partial \chi_\gamma}{\partial s_{\bar{e}}} = \frac{2(1-\chi_e)\chi_e s_e c_{\bar{e}} s_{\phi\bar{e}}}{\left[2-\chi_e(1+c_e)\right]^2}$$

and from equation (B18) we get,

$$(B35) \qquad \frac{\partial \phi_\gamma}{\partial s_{\bar{e}}} = \frac{-2(1-\chi_e)c_{\bar{e}}c_{\phi\bar{e}}}{\chi_e s_e\left[2-\chi_e(1+c_e)\right]}\,.$$

We have thus far still carried the $\phi_{\bar{e}}$ dependence. Of course we are completely ignorant of what its exact value is. The constraint that the positron go down the beam pipe restricts the value of $\theta_{\bar{e}}$ only, not the variable $\phi_{\bar{e}}$. Thus, $\theta_{\bar{e}}$ is taken to be 180°, but $\phi_{\bar{e}}$ can have any value between 0 and 2π. We are therefore forced to average over all allowable values of $\phi_{\bar{e}}$ for the squared error terms due to $\delta\theta_{\bar{e}}$. This approach, although admittedly nonexact, is quite reasonable given the tight confinement of the positron down the beam pipe. The ϕ averages are as follows:

$$(g) \qquad \left\langle (s_{\phi\bar{e}})^2 \right\rangle = \frac{1}{2\pi}\int_0^{2\pi} s_{\phi\bar{e}}^2\, d\phi_{\bar{e}} = \frac{1}{2}$$

and,

$$(h) \qquad \left\langle (c_{\phi\bar{e}})^2 \right\rangle = \frac{1}{2\pi}\int_0^{2\pi} c_{\phi\bar{e}}^2\, d\phi_{\bar{e}} = \frac{1}{2}\,.$$

Thus, we can eliminate all mention of the unseen positron's angle by substituting the following in equations (B31), (B34), and (B35):

$$(B36) \qquad c_{\bar{e}} \to -1, \qquad c_{\phi\bar{e}} \to \sqrt{\frac{1}{2}}, \qquad s_{\phi\bar{e}} \to \sqrt{\frac{1}{2}}\,.$$

Our derivation is now complete, and the above expressions can be substituted into equations (B9)–(B11). We will not brother to recopy the results.

At this point we need only the actual expressions for the measurement error's: $\delta\theta_{\bar{e}}$, $\delta\theta_e$, and $\delta \mathrm{E}_e$. These are as follows:

$$\delta \mathrm{E}_e = 0.145\sqrt{\mathrm{E}_e} \tag{B37}$$

$$\delta\theta_e = 0.003 \tag{B38}$$

$$\delta\theta_{\bar{e}} = 0.035, \tag{B39}$$

where the angles are in radians, and the energies are in GeV.

REFERENCES

1. See, for example, C. Quigg, *Gauge Theories of the Strong, Weak, and Electromagnetic Interactions*, Benjamin/Cummings, Reading, Massachusetts, 1983, or,

   E. Leader and E. Predazzi, *An Introduction to Gauge Theories and the "New Physics"*, Cambridge University Press, Cambridge England, 1982.

   Both contain references to the original literature in addition to a presentation of the standard model.

2. See, for example, H. Harrai, "Electroweak Interactions — Standard and Beyond", *Proc. of the Fourteenth SLAC Summer Inst. on Particle Physics*, Edited by E. Brennan, 1987, or,

   R. Peccei, "Phenomenological Aspects of Unified Theories", *Proc. of the XXIII International Conf. on High Energy Physics*, Edited by S. Loken, World Scientific, Singapore, 1986, or,

   S. Wojcicki, "Particle Physics — Recent Successes and Future Prospects", *Proc. of the Sante Fe Meeting*, Edited by T. Goldman and M. Nieto, World Scientific, Singapore, 1984.

3. Many comprehensive reviews of supersymmetry exist, the following are representative, not exhaustive,

   P. Fayet and S. Ferrara, "Supersymmetry", Physics Report **32**, No. 5, 1977, p 249-334, and also,

   "Supersymmetry", *Proc. of the Thirteenth SLAC Summer Inst. on Particle Physics*, Edited by E. Brennan, 1985.

   Also see the review paper by Haber and Kane (Ref. 47).

4. M. Davier, "Searches for New Particles", *Proc. of the XXIII International Conf. on High Energy Physics*, Edited by S. Loken, World Scientific, Singapore, 1986.

5. P.A.M. Dirac, "The Quantum Theory of the Electron", Proc. Roy. Soc. A **117**, p. 610, 1928.

6. Original papers by these authors can be found in, *Selected Papers on Quantum Electrodynamics*, Edited by J. Schwinger, Dover Publications, New York, 1958.

7. This quote is attributed to I.I. Rabi, see D. Griffiths, *Introduction to Elementary Particles*, Harper & Row, New York, 1987, p 29.

8. D.B. Lichtenberg, *Unitary Symmetry and Elementary Particles*, Chapter 1, Academic Press, New York, 1978, p 3.

9. E.P. Wigner, *Group Theory*, Academic Press, New York, 1959.

10. M. Gell-Mann and Y. Ne'eman, *The Eightfold Way* , Benjamin, New York, 1964.

11. M. Gell-Mann, "A Schematic Model of Baryons and Mesons", Phys. Lett. **8**, 214, 1964.

12. G. Zwieg, "An SU(3) Model for Strong Interaction Symmetry and its Breaking", CERN preprint 8409/Th. 412, 1964, unpublished.

13. G. Zwieg, in *Symmetries in Elementary Particle Physics* , Edited by A. Zichini, Academic Press, New York, 1965.

14. T.D. Lee and C.N. Yang, "Question of Parity Conservation in Weak Interactions", Phys. Rev. **104**, 254, 1956.

15. C.S. Wu, *et. al.*, "Experimental Test of Parity Conservation in Beta Decay", Phys. Rev. **105**, 1413, 1957.

16. E.C.G. Sudarshan and R. Marshak, "Chirality Invariance and the Universal Fermi Interaction", Phys. Rev. **109**, 1860, 1958.

17. R.P. Feynman and M. Gell-Mann, "Theory of the Fermi Interaction" Phys. Rev. **109**, 193, 1958.

18. V.L. Fitch, *et. al.*, "Evidence for the Constructive Interference between Coherently Regenerated and CP-Nonconserving Amplitudes", Phys. Rev. Lett. **15**, 73, 1965.

19. K. Moriyasu, *An Elementary Primer for Gauge Theory*, Section 6.4, World Scientific, Singapore, 1983.

20. C.N. Yang and R. Mills, "Conservation of Isotopic Spin and Isotopic Gauge Invariance", Phys. Rev. **96**, 191, 1954.

21. S.L. Glashow, "Partial Symmetries of Weak Interactions", Nucl. Phys. **22**, 579, 1961.

22. S. Weinberg, "A Model of Leptons", Phys. Rev. Lett. **19**, 1264, 1967.

23. A. Salam and J.C. Ward, "Electromagnetic and Weak Interactions", Phys. Lett. **13**, 168, 1964.

24. J. Blietschau, *et. al.*, "Determination of the Neutral to Charged Current Inclusive Cross-section Ratio for Neutrino and Anti-neutrino Interactions in the 'Gargamelle' Experiment", Nucl. Phys. **B118**, 218, 1976.

25. C.Y. Prescott, *et. al.*, "Parity Nonconservation in Inelastic Electron Scattering", Phys. Lett. **77B**, 347, 1978.

26. G. Arnison, *et. al.*, "Experimental Observation of Lepton Pairs of Invariant Mass Around 95 GeV/c^2 at the CERN SPS Collider", Phys. Lett. **126B**, 398, 1983.

27. P. Bagnaia, *et. al.*, "Evidence for $Z^\circ \rightarrow e^+e^-$ at the CERN $p\bar{p}$ Collider", Phys. Lett. **129B**, 130, 1983.

28. G. Arnison, *et. al.*, "Experimental Observation of Isolated Large Transverse Energy Electrons with Associated Missing Energy at $\sqrt{s} = 540$ GeV", Phys. Lett. **122B**, 103, 1983.

29. M. Banner, *et. al.*, "Observation of Single Isolated Electrons of High Transverse Momentum in Events with Missing Transverse Energy at the CERN $p\bar{p}$ Collider", Phys. Lett. **122B**, 476, 1983.

30. P.W.B. Higgs, "Broken Symmetries, Massless Particles and Gauge Fields", Phys. Lett. **12**, 132, 1964, and,

    P.W.B. Higgs, "Broken Symmetries and the Masses of Gauge Bosons", Phys. Lett. **13**, 508, 1964, and,

    G.S. Guralnik, C.R. Hagen and T.W.B. Kibble, Phys. Rev. Lett. **13**, 585, 1964, and,

    P.W.B. Higgs, "Spontaneous Symmetry Breakdown without Massless Bosons", Phys. Rev. **145**, 1156, 1966.

31. M. Kobayashi and T. Maskawa, "CP Violation in the Renormalizable Theory of the Weak Interaction", Prog. Theor. Phys. Japan **49**, 652, 1973.

32. J.L. Rosner, "Grand Unified Theories: an Update", Chicago preprint EFI-87-08-CHICAGO, Feb 1987.

33. An introduction to grand unified theories can be found in G.G. Ross, *Grand Unified Theories*, Benjamin/Cummings, Menlo Park, Ca., 1984.

    A review paper on the subject is given by P. Langacker, "Grand Unified Theories and Proton Decay", Phys. Rept. **72**, 185, 1981.

34. J.C. Pati and A. Salam, "Unified Lepton–Hadron Symmetry and a Gauge Theory of the Basic Interactions", Phys. Rev. D **8**, 1240, 1973.

35. H. Georgi and S.L. Glashow, "Unity of All Elementary–Particle Forces", Phys. Rev. Lett. **32**, 438, 1974.

36. M. Goldhaber, "Non-Accelerator Experiments", *Proc. of the XXIII Int. Conf. on High Energy Physics*, Edited by S. Loken, World Scientific, Singapore, 1987, p 248.

37. A review of monopoles in unified theories can be found in P. Goddard and D. Olive, "Magnetic Monopoles in Gauge Field Theories", Rep. Prog. Phys. **41**, 1357, 1978.

38. P. Ramond, "Dual Theory for Free Fermions", Phys. Rev. D **3**, 2415, 1971.

39. A. Neveu and J.H. Schwarz, "Factorizable Dual Model of Pions', Nucl. Phys. **B31**, 86, 1971.

40. Y.A. Golfand and E.P. Likhtman, "Extension of the Algebra of Poincairè Group Generators and Violation of P Invariance", JETP Letters **13**, 323, 1971.

41. D.V. Volkov and V.P. Akulov, "Is the Neutrino a Goldstone Particle", Phys. Lett. **46B**, 109, 1973.

42. J. Wess and B. Zumino, "A Lagrangian Model Invariant Under Supergauge Transformations", Phys. Lett. **49B**, 52, 1974.

43. P. Fayet, "Higgs Model and Supersymmetry", Il Nuovo Cimento, Vol 31 A, N. 4., p 626, 1976.

44. S. Coleman and J. Mandula, "All Possible Symmetries of the S-Matrix", Phys. Rev. **159**, 1251, 1967.

45. The following contains reprints of many of the original particles in string theory,

    Superstring Theory, Edited by M.B. Green, J.H. Schwarz and E. Witten, Cambridge Univ. Press, Cambridge, England, 1987.

46. See, for example, *Cosmology and Particle Physics*, Edited by I. Hinchliffe, World Scientific, Singapore, 1987.

47. H.E. Haber and G.L. Kane, "The Search for Supersymmetry: Probing Beyond the Standard Model", Phys. Rep. **117**, 75, 1985.

48. G.R. Farrar and P. Fayet, "Searching for the Spin-0 Leptons of Supersymmetry", Phys. Lett. **89B**, 191, 1980.

49. M.K. Gaillard, I. Hinchliffe, and L. Hall, "Hunting for the Selectron", Phys. Lett. **166B**, 279, 1982.

50. D. Dupen, "The Story of Stanford's Two-Mile Long Accelerator", SLAC-REPORT-62, May 1966.

51. Z.D. Farkas, H.A. Hogg, G.A. Loew, and P.B. Wilson, "SLED: A Method of Doubling SLAC's Energy", *Proc. of the IXth Int. Conf. on High Energy Accelerators*, National Technical Information Service, U.S. Department of Commerce, Springfield, Virginia, May, 1974, p. 576-583.

52. *The Stanford Two-Mile Accelerator*, Edited by R.B. Neal, W.A. Benjamin, Inc., N.Y., 1968.

53. D. Möhl, C. Pellegrini, J. Rees, B. Richter, M. Schwartz, A. Sessler, "A High Energy Proton-Electron-Positron Colliding Beam System", *Proc. of the VIIIth Int. Conf. on High Energy Accelerators*, CERN, 1971, p 153.

54. Numerous articles on PEP exist in the literature, see for example,
J. Rees, *et. al.*, "The Positron–Electron Project: PEP", *Particle Accelerator Conference 1977*, Chicago, 1977, p 1836.

55. R. Helm, *et. al.*, "Recent Improvements in Luminosity at PEP", IEEE Trans., Vol **NS-30**, No. 4, 1, 1983.

56. "Proposal for the Mark II at SLC", SLAC-PUB-3561, January 1985.

57. J.L. Siegrist, Ph.D. Thesis, "Hadron Production by e^+e^- Annihilation at Center of Mass Energies Between 2.6 and 7.8 GeV", SLAC-REPORT-225.

58. W. Davies-White, *et. al.*, "A Large Cylindrical Drift Chamber for the Mark II Detector at SPEAR", NIM **160**, 1979, p. 227-238.

59. J. A. Jaros, in *Proc. of the Int. Conf. on Instrumentation for Colliding Beam Physics*, SLAC-REPORT-250, Edited by W. Ash, Stanford, Ca., 1982, p. 29.

60. G. Hansen, "The New Drift Chamber for the Mark II Detector at the Stanford Linear Collider", SLAC-PUB-3880, Feb. 1986. Presented at the Wire Chamber Conf., Vienna, Austria, Feb. 25-28, 1986.

61. D.H. Perkins, *Introduction to High Energy Physics*, Chapter 2, Addison-Wesley, Mass. 1982.

62. M. Breidenbach,"The Mark II Data Acquisition and Trigger System", SLAC-PUB-3353, June 1984.

63. M. Breidenbach, *et. al.*, "Semi-Autonomous Controller for Data Acquisition, The Brilliant ADC", IEEE Transactions on Nuclear Science, Vol. **NS-25**, No. 1, Feb. 1978.

64. R. Schindler, Ph.D. Thesis, "Charmed Meson Production and Decay Properties at the $\psi(3770)$" SLAC-REPORT-219, May 1979.

65. G.S. Abrams, *et. al.*, "The Lead-Liquid Argon Shower Counter Systems of the SPEAR Mark II Detector", IEEE Transactions on Nuclear Science, Vol. **NS-25**, No. 1, Feb. 1978.

66. J.R. Smith, Ph.D. Thesis, "Two-Photon Production of the f^0 Meson", University of California, Davis, 1983, Unpublished.

67. D.L. Burke, *et. al.*, "A Precision Measurement of Luminosity", SLAC MEMORANDUM (internal memo), Dec. 1981.

68. J.D. Fox and M.E.B. Franklin, "A Luminosity Monitor at PEP", SLAC-PUB-2691, Feb. 1981.

69. T.M. Himel, Ph.D. Thesis, "Decays of the $\psi'(3684)$ to other Charmonium States", SLAC-REPORT-223, Oct. 1979.

70. H. Brafman, *et. al.*, "Fast Track Finding Trigger Processor for the SLAC/LBL Mark II Detector", SLAC-PUB-2033, Oct. 1977.

71. J.E. Grund, "A High Speed Trigger System for Total Deposited Energy Measurement in a Liquid Argon Calorimeter", SLAC-PUB-2216, Oct. 1978.

72. M.E. Nelson, Ph.D. Thesis, "Inclusive Lepton Production in Hadronic Events from e^+e^- Annihilation at 29 GeV", LBL-16724, Oct. 1983.

73. A. Boyarski,"Mark II Software Documentation", Mark II Report (internal report), Feb. 1986.

74. A.D. Johnson and G.H. Trilling, "Orbit Reconstruction Program for SPEAR Mark II Detector: Arcs", TG-301 (LBL internal report), Sept. 1978.

75. C.A. Blocker, Ph.D. Thesis, "Decays of the Heavy Lepton, $\tau(1785)$", LBL-10801, April 1980.

76. R.L. Ford, W.R. Nelson, "The EGS Code System: Computer Programs for the Monte Carlo Simulation of Electromagnetic Cascade Showers (Version 3)", SLAC-PUB-0210, Jun. 1978.

77. L. Gladney, R. Hollebeek, B. LeClaire, *et. al.*, "A Search for Supersymmetric Electrons" Phys. Rev. Lett. **51**, 2253 (1983).

78. T. Kobayashi and M. Kuroda, "Mass of Photino and Scalar Lepton Production in e^+e^- Annihilation", Phys. Lett. **134B**, 271, 1984.

79. The initial groundwork for this approximation can be found in, E. Fermi, Zeit. Physik **29**, 315, 1924.

    The one proper reference for this approximation, according to J.D. Jackson, is, E.J. Williams, "Correlation of Certain Collision Problems with Radiation Theory", Kgl. Danske Videnskab. Selskab Mat.-fys. Medd., **XIII**, No. 4, 1935.

    For historical completeness, see also, C.F. von Weizsäcker, Zeit. Physik **88**, 612, 1934.

80. E. Eilam and E. Reya, "Production of Single Charged Gauginos via $e^+e^- \to e^\pm \tilde{\nu} \widetilde{W}^\mp$", Phys. Lett. **145B**, 145, 1984.

81. G. Bonneau and F. Martin, "Invariant Spectrum for the Equivalent-Photon Method", Il Nuovo Cimento, Vol. **21A**, N. 3, 611, 1974.

82. J.H. Bolstad, *et. al.*, "Numerical Analysis Program Libary User's Guide: NAPLUG", SLAC-SCIP-USER-NOTE-082, June 1979.

83. M.E. Levi, Ph.D. Thesis, "Measurement of Electroweak Parameters in Leptonic Processes", Harvard, Jan. 1984, Unpublished.

84. P.C. Rowson, Ph.D. Thesis, "Properties of Heavy Quark Jets Produced by e^+e^- Annihilation at 29 GeV", University of California, Berkeley, LBL-20463, 1985.

85. S. Komamiya, "Search for New Particles in e^+e^- Annihilation", Int. Symp. on Lepton and Photon Int. at High Energies, *Lepton/Photon Symp.*, 1985.

86. T. Lavine, "Search for Single-Photons from Radiative Production of Supersymmetric Particles or Neutrinos", University of Wisconson–Madison, Report No. WISC-EX-86/275, Dec. 1986.

87. C.B. Boyer, *A History of Mathematics*, Princeton University Press, Princeton New Jersy, 1968.